

July 2018

Connected Autonomous Vehicles: Capacity Analysis, Trajectory Optimization, and Speed Harmonization

Amir Ghiasi

University of South Florida, a.ghiasi88@gmail.com

Follow this and additional works at: <https://scholarcommons.usf.edu/etd>



Part of the [Civil Engineering Commons](#), and the [Urban Studies and Planning Commons](#)

Scholar Commons Citation

Ghiasi, Amir, "Connected Autonomous Vehicles: Capacity Analysis, Trajectory Optimization, and Speed Harmonization" (2018).
Graduate Theses and Dissertations.
<https://scholarcommons.usf.edu/etd/7295>

This Dissertation is brought to you for free and open access by the Graduate School at Scholar Commons. It has been accepted for inclusion in Graduate Theses and Dissertations by an authorized administrator of Scholar Commons. For more information, please contact scholarcommons@usf.edu.

Connected Autonomous Vehicles:
Capacity Analysis, Trajectory Optimization, and Speed Harmonization

by

Amir Ghiasi

A dissertation submitted in partial fulfillment
of the requirements for the degree of
Doctor of Philosophy in Civil Engineering
Department of Civil and Environmental Engineering
College of Engineering
University of South Florida

Major Professor: Xiaopeng Li, Ph.D.
Fred Mannering, Ph.D.
Robert Bertini, Ph.D.
Changhyun Kwon, Ph.D.
Kaiqi Xiong, Ph.D.
Xiaobo Qu, Ph.D.

Date of Approval:
June 15, 2018

Keywords: CAV, Mixed Traffic, Traffic Control,
Traffic Smoothing, Trajectory Prediction

Copyright © 2018, Amir Ghiasi

DEDICATION

I dedicate this dissertation to my beautiful wife, lovely parents, and my brothers for their encouragement and support. This work is also dedicated to my kind mother-in-law, father-in-law, and sister-in-law who have loved me unconditionally.

ACKNOWLEDGEMENT

I would like to express my gratitude and appreciation to my advisor Dr. Xiaopeng Li for his guidance during my studies. Without his assistance, this dissertation would not have been completed. I am also thankful to my doctoral committee members Dr. Fred Mannering, Dr. Robert Bertini, Dr. Changhyun Kwon, Dr. Kaiqi Xiong and Dr. Xiaobo Qu for their invaluable advices and constructive comments.

TABLE OF CONTENTS

LIST OF TABLES	iii
LIST OF FIGURES	iv
ABSTRACT	vii
CHAPTER 1: INTRODUCTION	1
1.1 Background	1
1.2 Contribution Statement	3
1.3 Dissertation Organization	7
CHAPTER 2: LITERATURE REVIEW	8
2.1 Review of Capacity Analysis and CAV Headway Studies	8
2.2 Review of Trajectory Optimization Studies	12
2.3 Review of Signal Optimization Studies	15
2.4 Review of Speed Harmonization Studies	16
CHAPTER 3: CAPACITY ANALYSIS	18
3.1 Markov Chain Model	19
3.2 Capacity Formulation	23
3.2.1 Approximate Capacity	24
3.2.2 CAV Penetration Rate and Platooning Intensity Effects	31
3.3 Numerical Analyses	37
3.4 Chapter Summary	43
CHAPTER 4: TRAJECTORY OPTIMIZATION	45
4.1 Problem Statement	45
4.1.1 Original Formulation	45
4.1.2 Simplified Model Formulation	50
4.2 Solution Approach.....	60
4.2.1 Theoretical Properties	60
4.2.2 Optimization Algorithm	64
4.3 Numerical Examples	72
4.3.1 Algorithm Performance	72
4.3.2 Signalized Segment	77
4.3.3 Non-stop Intersection	80
4.4 Queuing Propagation Analysis	83
4.5 Chapter Summary	88

CHAPTER 5: JOINT TRAJECTORY AND SIGNAL OPTIMIZATION	90
5.1 Problem Setting	90
5.2 Primary Optimization (PO)	92
5.2.1 Model Formulation	92
5.3 Simplified Macroscopic Optimization (SMO)	95
5.3.1 Model Formulation	96
5.3.1.1 Near-optimum Trajectory Construction	96
5.3.1.2 Macroscopic Fuel Consumption Function	102
5.3.1.3 SMO Formulation	102
5.3.2 Analytical Solution	103
5.4 Numerical Experiments	105
5.5 Chapter Summary	113
CHAPTER 6: SPEED HARMONIZATION	115
6.1 Problem Setting	115
6.2 Algorithm Design	117
6.2.1 Information Update	118
6.2.2 Trajectory Prediction	120
6.2.2.1 Boundary Condition Estimation	121
6.2.2.2 Sensor-based Prediction	123
6.2.2.3 Probe-based Prediction	128
6.2.2.4 Prediction Integration	132
6.2.3 Shooting Heuristic	133
6.2.3.1 CAV Shooting Equations	135
6.2.3.2 Feasibility Constraints	140
6.2.3.3 α_i Solution	140
6.2.4 Damping Control	141
6.3 Numerical Experiments	142
6.4 Chapter Summary	153
CHAPTER 7: CONCLUSION	155
REFERENCES	159
APPENDIX A: COPYRIGHT PERMISSIONS	172

LIST OF TABLES

Table 2.1 A list of the reviewed studies proposing models for headway distributions	11
Table 3.1 Headway distributions for numerical analyses in the single-lane problem	38
Table 4.1 Comparison of objective values for signalized segments	80
Table 4.2 Comparison of objective values for non-stop intersections	82
Table 5.1 Simulation quantitative results.....	108
Table 6.1 Comparison of the evaluation measures for different sensor settings	148
Table 6.2 Comparison of the evaluation measures for different v^f values	148

LIST OF FIGURES

Figure 3.1 Illustrative examples for vehicle distributions	20
Figure 3.2 Illustration of headways in mixed traffic	24
Figure 3.3 Illustrative examples for different platooning intensities	39
Figure 3.4 ε for different N values	40
Figure 3.5 Numerical examples to test how $\hat{c}(P_1, O, h)$ changes with P_1	42
Figure 3.6 Numerical examples to test how $\hat{c}(P_1, O, h)$ changes with O i) default headways ii) $\bar{h}_{11} = 1.30$ s	43
Figure 4.1 Illustration of the constraints	46
Figure 4.2 Illustration of platoon decomposition	51
Figure 4.3 Illustration of the piece-wise quadratic form of trajectory x_n (a) with a stop section and (b) without a stop section	52
Figure 4.4 Illustration of $\Delta_{n(n-1)}$	58
Figure 4.5 Illustration of a feasible set of trajectories to Problem STO	59
Figure 4.6 Illustration of lead vehicles $\{\hat{n}_i(\varphi)\}$, where each cross marks the time of t_{n4}	65
Figure 4.7 Solution times for different problem instances	74
Figure 4.8 Performances of PSA and NSG-SH	76
Figure 4.9 Trajectories produced by PSA and NSG-SH (the crosses separate quadratic pieces)	77
Figure 4.10 Signalized segment results: (a) trajectory plot for extreme accelerations (EA); and (b) optimal trajectory (OT) plot	79
Figure 4.11 Non-stop intersection results: (a) trajectory plot for extreme accelerations (EA); and (b) optimal trajectory (OT) plot (red triangles mark the exit times of vehicles from the other approach)	81

Figure 4.12 (a) Illustration of $\delta_1^*(\varphi)$ vs. φ when $\beta_1 > 0$; (b) $\delta_1^*(\varphi)$ vs. φ for the default instance	86
Figure 4.13 Trajectories for φ^0 vs. φ^E at the default parameter values (where the dashed yellow line marks the end of the queue)	87
Figure 4.14 Results for instances with varying N : (a) N vs. β_1 ; and (b) β_1 vs. $\delta_1^*(\varphi^0)$ and $\delta_1^*(\varphi^E)$	88
Figure 5.1 Problem statement	91
Figure 5.2 An illustration to $D_i(\mathcal{S})$ calculation	94
Figure 5.3 An illustration to the piecewise quadratic trajectory function form	97
Figure 5.4 An illustration to $x_{in}^s(t)$ and $x_{in}^{s,offset}(t)$	99
Figure 5.5 An illustration to a_{in} derivation	101
Figure 5.6 $F_i^{marginal}(R_i)$ vs. R_i	103
Figure 5.7 Analytical solution to SMO	105
Figure 5.8 Simulation results for a signalized intersection	107
Figure 5.9 Simulation results for a signalized intersection with a fixed \mathcal{S}	107
Figure 5.10 Simulation results for a signalized intersection with no control	108
Figure 5.11 Simulation results for a signalized work-zone	109
Figure 5.12 Sensitivity analysis results on $\lambda_i, i = 1,2$	111
Figure 5.13 Sensitivity analysis results on $l_i, i = 1,2$ and l^C	112
Figure 5.14 Sensitivity analysis results on \bar{v}	113
Figure 6.1 Problem setting	117
Figure 6.2 Algorithm flowchart	119
Figure 6.3 Information update	120
Figure 6.4 Boundary index estimation	123
Figure 6.5 Sensor-based prediction: backward wave lower-bound index prediction	124
Figure 6.6 Sensor-based prediction: trajectory reconstruction for (a) free-flow traffic, (b) congested traffic	125

Figure 6.7 Sensor-based prediction: an illustration of trajectory reconstruction for (a) $s = 1$, (b) $s = 2$, (c) $s = S$, and (d) exit state prediction	126
Figure 6.8 Sensor-based trajectory: prediction smoothing	128
Figure 6.9 Probe-based prediction: an illustration to offset trajectories	130
Figure 6.10 Probe-based prediction: an illustration to (a) triangular fundamental diagrams and v^B derivation and (b) the revised offset trajectories	131
Figure 6.11 Prediction integration	134
Figure 6.12 Shooting heuristic: case 1	136
Figure 6.13 Shooting heuristic: case 2	137
Figure 6.14 Shooting heuristic: case 3	138
Figure 6.15 Shooting heuristic: case 4	139
Figure 6.16 Simulation results	145
Figure 6.17 Simulation results: comparing the human-driven benchmark traffic with the implemented control	146
Figure 6.18 Simulation results: random distribution	149
Figure 6.19 Sensitivity analyses on the D values	151
Figure 6.20 Sensitivity analyses on the P_1 and P_2 values	152

ABSTRACT

Emerging connected and autonomous vehicle technologies (CAV) provide an opportunity to improve highway capacity and reduce adverse impacts of stop-and-go traffic. To realize the potential benefits of CAV technologies, this study provides insightful methodological and managerial tools in microscopic and macroscopic traffic scales. In the macroscopic scale, this dissertation proposes an analytical method to formulate highway capacity for a mixed traffic environment where a portion of vehicles are CAVs and the remaining are human-driven vehicles (HVs). The proposed analytical mixed traffic highway capacity model is based on a Markov chain representation of spatial distribution of heterogeneous and stochastic headways. This model captures not only the full spectrum of CAV market penetration rates but also all possible values of CAV platooning intensities that largely affect the spatial distribution of different headway types. Numerical experiments verify that this analytical model accurately quantifies the corresponding mixed traffic capacity at various settings. This analytical model allows for examination of the impact of different CAV technology scenarios on mixed traffic capacity. We identify sufficient and necessary conditions for the mixed traffic capacity to increase (or decrease) with CAV market penetration rate and platooning intensity. These theoretical results caution scholars not to take CAVs as a sure means of increasing highway capacity for granted but rather to quantitatively analyze the actual headway settings before drawing any qualitative conclusion.

In the microscopic scale, this study develops innovative control strategies to smooth highway traffic using CAV technologies. First, it formulates a simplified traffic smoothing

model for guiding movements of CAVs on a general one-lane highway segment. The proposed simplified model is able to control the overall smoothness of a platoon of CAVs and approximately optimize traffic performance in terms of fuel efficiency and driving comfort. The elegant theoretical properties for the general objective function and the associated constraints provides an efficient analytical algorithm for solving this problem to the exact optimum. Numerical examples reveal that this exact algorithm has an efficient computational performance and a satisfactory solution quality. This trajectory-based traffic smoothing concept is then extended to develop a joint trajectory and signal optimization problem. This problem simultaneously solves the optimal CAV trajectory function shape and the signal timing plan to minimize travel time delay and fuel consumption. The proposed algorithm simplifies the vehicle trajectory and fuel consumption functions that leads to an efficient optimization model that provides exact solutions. Numerical experiments reveal that this algorithm is applicable to any signalized crossing points including intersections and work-zones. Further, the model is tested with various traffic conditions and roadway geometries. These control approaches are then extended to a mixed traffic environment with HVs, connected vehicles (CVs), and CAVs by proposing a CAV-based speed harmonization algorithm. This algorithm develops an innovative traffic prediction model to estimate the real-time status of downstream traffic using traffic sensor data and information provided by CVs and CAVs. With this prediction, the algorithm controls the upstream CAVs so that they smoothly hedge against the backward deceleration waves and gradually merge into the downstream traffic with a reasonable speed. This model addresses the full spectrum of CV and CAV market penetration rates and various traffic conditions. Numerical experiments are performed to assess the algorithm performance with different traffic conditions and CV and CAV market penetration rates. The results show significant improvements in damping traffic oscillations and reducing fuel consumption.

CHAPTER 1: INTRODUCTION

1.1 Background

Highway traffic congestion and stop-and-go movements are almost inevitable experiences in highway traffic due to intrinsic limitations in human driving behavior and information access (Li and Ouyang, 2011; Li et al., 2012; Jiang et al., 2015). These phenomena are linked to a number of adverse impacts from highway traffic, including excessive fuel consumption, extra safety hazards, and increased travel delay. Among a number of potential solutions to stop-and-go traffic (e.g., variable speed limits (Lu and Shladover, 2014), ramp metering (Hegyi et al., 2005a), merging traffic control (Spiliopoulou et al., 2009), and signal coordination (Day et al., 2010)), the connected automated vehicle (CAV) technologies have received increasing attention recently. These technologies are expected to improve highway traffic efficiency, safety, and environment through sensing local environment, sharing information, and applying appropriate control measures. Out of many benefits these technologies can offer, two most important ones are their capabilities of increasing highway capacity and smoothing traffic.

Due to communication and automated control technologies (e.g., platooning), CAVs can largely improve highway traffic capacity by reducing time headways between consecutive vehicles. With CAV platooning, a pair of CAVs are similar to two concatenated cars in a train and thus shall have much less time headway compared with a pair of disconnected human-driven vehicles (HVs). Therefore, we envision that highway capacity will be maximized in the far future when all vehicles are platooned CAVs, as predicted by a number of studies on

pure automated traffic with computer simulation (Ioannou and Chien, 1993) and analytical models (Kanaris et al., 1997; Swaroop et al., 1994; Fernandes and Nunes, 2012; Amoozadeh et al., 2015). Besides the consensus on pure automated traffic, it is not yet completely clear how highway capacity is affected by CAVs in mixed traffic containing both CAVs and HVs, which expects to last for a relatively long transitional period.

In addition to possibility of highway capacity improvement, CAV technologies can also offer the possibilities of controlling vehicle trajectories and modifying driving behavior (Ma et al., 2016). Therefore, with a proper control algorithm, we may be able to significantly dampen traffic oscillations and thus reduce stop-and-go traffic. Various studies have been conducted to utilize CAV to improve traffic smoothness on both uninterrupted freeways and signalized arterials. Most of these studies are essentially centered on a vehicle trajectory optimization problem. Simply speaking, this problem determines the optimal shapes for interdependent vehicle trajectories constrained by their boundary conditions, physical limits and safety risks. Despite the efforts taken in this area, most existing trajectory optimization models either require quite some computational resources and sophistication in algorithm design (Von Stryk and Bulirsch, 1992; Wei et al., 2016) or rely on a numerical algorithm that does not ensure solution optimality and may need many iterations to converge (Zhou et al., 2017; Ma et al., 2017).

Another important factor that impacts traffic performance measures near signalized crossing points is to have optimal signal timing plan that could serve approaches based on their demands. Numerous studies have been conducted to optimize signal timing plans for traditional human-driven traffic. Recently, a number of studies are performed to design suitable signal timing plans with CAV technologies (e.g., Goodall et al. 2013; Feng et al. 2015; Pourmehrabad et al. 2017). Although, these studies provide useful tool to improve traffic performance near signalized intersections, without implementing proper trajectory control approaches, potential benefits may significantly be compromised.

One well-known approach to dampen traffic oscillation is speed harmonization that aims to reduce temporal and spatial variations of traffic speed by applying certain control approaches (Ma et al., 2016). Traditionally, variable speed limit (VSL) and speed advisory messages approaches are used to minimize traffic speed variations. While these studies provide valuable insights into speed harmonization techniques, most of the existing studies can only advise or enforce human drivers to adjust their speed. However, the unpredictable nature of human behaviors may compromise or even fail these approaches. Moreover, most of these studies rely on limited fixed traffic sensors (e.g., loop detector, Remote Traffic Microwave Sensor (RTMS), etc.) deployed on highways. Although these infrastructure units can provide useful traffic information when there is not enough information sources, the data received from most of these sensors are low in resolution and related to certain sets of fixed locations. As a result, the data captured from the fixed deployed traffic sensors may not provide effective resources for advanced speed harmonization techniques. Therefore, it might be impossible to significantly smooth traffic speeds using the traditional speed harmonization control strategies. Fortunately, emerging CAV technologies allow human drivers to be replaced with robots that can precisely execute well-designed driving algorithms with complete information from vehicle-to-vehicle (V2V) and vehicle-to-infrastructure (V2I) communications, and therefore may improve highway traffic efficiency, fuel and environmental efficiency, and safety (Ghiasi et al., 2017; Wu et al., 2011; Chen and Du, 2017; Kamrani et al., 2017; Azizi et al., 2018). This brings us inspiring opportunities for achieving speed harmonization with controllable CAVs.

1.2 Contribution Statement

The contents of this dissertation are generally categorized into two scales: macroscopic and microscopic. In the macroscopic scale, to address the lack of analytical analysis on effects of emerging CAV technologies on highway capacity, an analytical formulation to highway

capacity is proposed in a mixed traffic environments with CAVs. In the microscopic scale, we aim to use CAV technologies to dampen traffic oscillations and smooth traffic. For this task, first a simplified trajectory optimization model is proposed for a pure-automated traffic where all vehicles are assumed to be CAVs. This concept is then extended is to a joint trajectory and signal optimization model to simultaneously design CAV trajectories and signal timing plan near signalized crossing points. Finally, the proposed trajectory optimization concept is extended to a mixed traffic environment by proposing a mixed traffic speed harmonization algorithm. This dissertation makes the following contributions to the literature.

First, this dissertation proposes an analytical stochastic formulation for highway capacity in a mixed traffic environment with CAVs. We propose a novel Markov chain model to describe spatial headway distributions of mixed traffic along a highway segment. With this creative modeling structure, we are able to capture complex stochastic headway with different types of distributions (e.g., headway between two CAVs, headway of a CAV following an HV, headway of an HV following a CAV, and headway between two HVs) and unify a full spectrum of CAV penetration rates and platooning intensities in a parsimonious analytical capacity formulation. This formulation well approximates the maximum rate of traffic that the corresponding highway can process, and we conduct both theoretical analysis and numerical simulation to show that this approximation is very close to the ground-truth capacity at various temporal and spatial scales. Further, to test the conventional assumption that highway capacity always increases with CAV market penetration rate and platooning intensity, we analyze how mixed traffic capacity changes across all possible values of these two factors. Theoretical results reveal that only certain conditions of headway settings can justify this assumption. Otherwise, contrary to the conventional assumption, greater CAV market penetration rate and platooning intensity may actually compromise mixed traffic capacity when these conditions are not satisfied, which is likely the case under certain conservative CAV technology scenarios.

Second, this dissertation aims to address the existing challenges found in (Zhou et al., 2017; Ma et al., 2017) by investigating a further simplified trajectory optimization model. This simplified model confines each trajectory to consist of no more than five quadratic sections. Further, this simplified model assumes that all vehicles arrive at the same speed. This is a reasonable assumption for cases when the upstream traffic is well controlled in a similar manner. While the new model preserves the main features of the shooting heuristic (e.g., yielding overall smooth trajectories) only with these minor simplifications, it has a number of appealing theoretical and algorithmic properties that were not found in (Zhou et al., 2017; Ma et al., 2017). We discover elegant theoretical relationships between a general objective function and its associated variables and constraints. These findings enable development of an analytical solution algorithm that efficiently solves the exact solution to this simplified problem. This analytical exact algorithm makes a significant methodological contribution to the CAV trajectory optimization literature that has mostly relied on numerical and heuristic algorithms in the past. Numerical studies are conducted to verify the solution efficiency and quality compared with the existing approach and illustrate applications of the proposed model to signalized highways and non-stop intersections. Further, to examine the intuitive conjecture that traffic smoothing leads to longer queue propagation, we investigate a homogeneous yet representative case and find analytical conditions for this conjecture to fail. Interestingly, we find that trajectory smoothing may not always cause longer queue propagation but instead may mitigate queue propagation with appropriate settings.

Third, the trajectory concept is extended to a joint trajectory and signal optimization model to simultaneously design CAV trajectories and signal timing plan near signalized crossing points. Instead of solving the original complex optimization functions, this dissertation develops a simplified optimization model based on two modifications. First, the trajectory functions are confined into no more than five quadratic sections. Second, the highly nonlinear instantaneous fuel consumption function is approximated with a very simple quadratic

function of signal red interval. The results of a regression analysis reveal that the proposed macroscopic fuel consumption function can approximate the true fuel consumption very accurately. These two simplifications lead to an optimization model that can efficiently be solved to the exact solution. Numerical experiments indicate that the proposed joint optimization model can be applied to any signalized crossing points including intersections and signalized work-zones.

Finally, to extend the proposed trajectory optimization concept to a mixed traffic environment, this dissertation proposes a speed harmonization algorithm that addresses mixed traffic freeways with various CV and CAV market penetration rate. Contrary to most speed harmonization models, the proposed algorithm uses real-time traffic sensor data as well as the real-time information provided by CVs and CAVs for adjusting and correcting the CAV controls. These two sets of information are integrated and used by our innovative prediction algorithm to estimate the traffic downstream to each CAV. The prediction outcomes then enable the algorithm to plan the future CAV trajectories as smooth as possible to improve performance of a freeway traffic stream. To quantify the benefits, four most important measures of effectiveness in traffic flow analyses are considered: throughput, traffic speed variations, fuel consumption and emission, and surrogate safety measures. Numerical experiments are performed to evaluate the performance of the algorithm and to test the algorithm with various parameter values. The results show that the proposed speed harmonization model can produce much smoother trajectories for CAVs and their following vehicles than the benchmark case, and thus improves the overall smoothness of the traffic stream in different traffic conditions. We would like to note that although the proposed algorithm considers a single-lane freeway where no lane changing and vehicle taking-over happen, the proposed control strategy could be applied to a multi-lane highway by forming a wall of CAVs or managed lanes where lane-changing maneuvers are restricted (Ghiasi et al., 2017; Chen et al., 2017; Hussain et al., 2016). Overall, this speed harmonization algorithm can

provide a methodological bridge to more advanced control strategies in future CAV mixed traffic.

1.3 Dissertation Organization

This proposal is organized as follows. CHAPTER 2 reviews relevant literature and explains how this dissertation can contribute to the existing literature. CHAPTER 3 describes the Markov chain model and the proposed capacity formulation for a mixed traffic highway. Further, numerical analyses are performed to verify the analytical formulations. CHAPTER 4 proposes the simplified trajectory optimization model, investigates its theoretical properties, and proposes an exact analytical solution. Further, numerical examples are provided to test the solution algorithm efficiency and illustrate applications of this algorithm. CHAPTER 5 develops the trajectory and signal joint optimization problem formulation and conducts numerical experiments to evaluate the algorithm and to test it with various parameter settings. Finally, CHAPTER 6 proposes the speed harmonization algorithm, followed by the simulation analyses to evaluate its performance.

CHAPTER 2: LITERATURE REVIEW¹

This chapter provides literature review for the three research tasks. First, a review of capacity analysis models and CAV headway studies are presented in Section 2.1. Then, Section 2.2 presents a literature review of existing trajectory optimization models. Finally, Section 2.4 reviews the existing speed harmonization literature.

2.1 Review of Capacity Analysis and CAV Headway Studies

Capacity analysis is an essential component of transportation studies. An accurate capacity estimation enables transportation planners to make proper decisions to maximize highway traffic performance. Numerous studies have been conducted to analyze highway capacity at various conditions (e.g., geometrical, weather, etc.). Minderhoud et al. (1997) presents a relatively comprehensive review to traditional highway capacity estimation methods. All these traditional capacity estimation models consider human-driven traffic and the corresponding headway distributions. With the advent of new CAV technologies, vehicle headway distributions may significantly change, and thus can directly affect highway capacity. This highlights the need for a highway capacity model for a mixed traffic environment where a portion of vehicles are CAVs and the remaining are HVs.

A number of studies conducted capacity analyses for mixed traffic, most of them relying on computer simulation (e.g., Van Arem et al., 1997; Shladover et al., 2001; Vander Werf et al., 2002; Van Arem et al., 2006; Kesting et al., 2008, 2010; Shladover et al., 2012). There

¹Portions of this chapter have been previously published in Ghiasi et al. (2017). Permission is included in Appendix.

are only a limited number of studies attempting building analytical models to characterize capacity of mixed traffic. Tientrakool et al. (2011) evaluates the impact of Adaptive Cruise Control (ACC) and Cooperative Adaptive Cruise Control (CACC) vehicles with deterministic headway rules on highway capacity. Levin and Boyles (2015) propose a link capacity model as a function of automated vehicles (AV) penetration rate and deterministic headway values. This model is extended by Levin and Boyles (2016) by considering different vehicle classes, while headways settings are uniform across all vehicles in each class. While these studies provide valuable quantitative results and insights into the benefits of CAVs in improving mixed traffic capacity, most of them consider deterministic time headways in a specific technology scenario. However, in reality, time headways between consecutive vehicles are highly stochastic. The effect of headway stochasticity on highway capacity is not captured in studies assuming deterministic headways. Further, headway distributions in mixed traffic highly depend on CAV technologies that are yet to be fully developed and thus may have quite some uncertainties.

Table 2.1 provides a literature review of headway distributions in different types of traffic, i.e., including traditional pure human-driven, mixed, and pure automated traffic. Since there are comprehensive literature reviews available for HV headway distributions (e.g., Minderhoud et al. (1997)), this section only presents a few representative studies with bounded uniform distributions as quantitative benchmarks. Whereas much fewer studies investigated headway distributions for mixed and pure CAV traffic. To complement studies on headways distribution of HV traffic, we provide a comprehensive review on headway distributions in mixed and pure CAV traffic for all possible vehicle pair combinations, i.e., between two CAVs, for a CAV following an HV, for an HV following a CAV, and between two HVs. This information later supplies the numerical analyses in CHAPTER 3. Note that some studies use different terms (e.g., Adaptive Cruise Control (ACC) and Cooperative

Adaptive Cruise Control (CACC)²) for automated driving. Since all these terms refer to automated longitudinal control of vehicles, we refer them as CAV to unify the notation in this presentation. Basically, we see that the headway values between two HVs range from 0.7 to 2.4 seconds, those for a CAV following an HV from 0.5 to 2.6 seconds, those for an HV following a CAV from 0.6 to 2.6 seconds, and those between two CAVs from 0.3 through 2 seconds. In these results, we observe wide variabilities within the same type of headways and between different types of headways, and different studies may assume quite different realizations of CAV technologies in terms of headway distributions (e.g., a conservative technology scenario yield a CAV-to-CAV headway as long as 2 seconds whereas an aggressive technology scenario only takes 0.3 second for the same headway). These discrepancies may significantly affect corresponding capacity analysis outcomes. This highlights the need for an analytical capacity modeling framework incorporating headway stochasticities for the same type of vehicle pairs, discrepancies between different vehicle types, and different realization scenarios of future technologies.

Existing studies also pointed out that the CAV market penetration is a critical factor that affects the highway capacity in mixed traffic. Results from both simulation (Kesting et al., 2008; Shladover et al., 2012; Arnaout and Arnaout, 2014; Ntousakis et al., 2015) and analytical modeling (Levin and Boyles, 2015; van den Berg and Verhoef, 2016) show that highway capacity increases significantly with market penetration rate. However, another important factor that also largely affects traffic capacity yet receives less attention is the CAV platooning intensities. CAV platooning refers to the technology that reduces the headway between consecutive CAVs with vehicle-to-vehicle (V2V) communications and automated control (e.g., Stevens et al. 1996; Zhao and Sun 2013; Amoozadeh et al. 2015). Even at the same market penetration rate, different CAV platooning intensities may result in quite

²We treat headway between an ACC vehicle and a HV the same as that between a CACC vehicle and a HV since no communication happens in either case, whereas for headways between two CAVs, we only report results from CACC vehicles because communication is necessary.

Table 2.1: A list of the reviewed studies proposing models for headway distributions.

Studies	Headway between HVs		Headway for a CAV following an HV		Headway for an HV following a CAV		Headway between CAVs	
	Distri - bution	Range (sec)	Distri - bution	Range (sec)	Distri - bution	Range (sec)	Distri - bution	Range (sec)
Neubert et al. (1999)	Uniform	0.8 – 1.8						
Fancher et al. (2001)	Uniform	1.0 – 2.0						
VanderWerf et al. (2001)			Uniform	1.0 – 2.0			Uniform	0.5 – 1.4
Bose and Ioannou (2003)	Uniform	0.7 – 2.2	Uniform	0.5 – 1.5				
Nowakowski et al. (2010)			Uniform	1.1 – 2.2			Uniform	0.6 – 1.1
Schakel et al. (2010)			Gaussian	$1.2 \pm 0.15 / 1.2 \pm 0.3$			Gaussian	$1.2 \pm 0.15 / 1.2 \pm 0.3$
Calvert et al. (2012)							Uniform	0.3 – 1.4
Larsson (2012)			Uniform	1.0 – 2.6				
Altay et al. (2013)			Uniform	0.6 – 2.0			Uniform	0.6 – 2.0
Zhao and Sun (2013)			Fixed	1.4			Fixed	0.5
Allam Ahmed et al. (2014)	Uniform	1.3 – 2.4						
Arnaout and Bowling (2014)	Uniform	1.0 – 1.8	Uniform	0.8 – 1.0	Uniform	1.0 – 1.8	Fixed	0.5
Shladover et al. (2014)					Uniform	0.6 – 2.2		
Gao et al. (2015)					Uniform	0.6 – 2.6		
Nikolos et al. (2015)			Uniform	0.8 – 2.2				
Roncoli et al. (2015)			Uniform	0.5 – 2.0				
Wang et al. (2015b)			Uniform	0.5 – 2.0				

different traffic capacities. For example, if CAVs are more scattered across the highway, there will be fewer long platoons of CAVs with reduced headways and thus the improvement of traffic capacity becomes less salient. On the other hand, if CAVs are better clustered, highway capacity will increase as a result of longer CAV platoons with reduced headways. Only limited studies investigated the impact of vehicle platooning on traffic capacity in mixed traffic with simulation and claimed that a higher platooning intensity ensures a higher capacity (e.g., Rao and Varaiya, 1993; Zhao and Sun, 2013; Harwood and Reed, 2014). It remains a challenge to reveal analytical insights into how both market penetration and CAV platooning intensity jointly affect mixed traffic capacity.

2.2 Review of Trajectory Optimization Studies

Several studies have focused on trajectory optimization methods in different modes of transportation including ground (e.g., Mensing et al., 2011; Li and Wang, 2006; Zhou et al., 2017), rail (e.g., Lu et al., 2013; Xu et al., 2017), and air (e.g., Wickramasinghe et al., 2012). This section focuses on reviewing CAV trajectory optimization models on two major transportation network segments: uninterrupted freeways and signalized arterials. Various studies have been conducted to utilize CAV to improve traffic smoothness and throughputs on both these two segments.

Studies on the freeway side focus on guiding vehicle trajectories for minimum speed oscillations and minimum conflicts in lane changes and merges. Van Arem et al. (2006) investigates traffic stability and efficiency at a merge point. Ahn et al. (2013) proposed a rolling-horizon model for an individual CAV control strategy that minimizes fuel consumption and emissions at different grades. Yang and Jin (2014) studied a vehicle speed control strategy to reduce vehicle fuel consumption and emissions. Wang et al. (2014a; 2014b) proposed optimal control models to determine optimal accelerations of a platoon of CAVs to minimize a variety of objective cost functions in a rolling horizon manner. Later, Wang et al.

(2016) investigated distributed CAV acceleration control methods to mitigate formation and propagation of moving jams.

Studies on the signalized arterial side concern the problem of coordinating and scheduling vehicle trajectories to avoid conflicts at crossing points while improving traffic performance measures. Some studies focus on scheduling of vehicles arrival and departure times at an intersection and aim to minimize stops and delay at the intersection. Li and Wang (2006) studied CAV scheduling and trajectory planning for a two-lane intersection, using spanning tree and simulation techniques. Dresner and Stone (2008) investigated a similar non-stop intersection problem and proposed a heuristic control algorithm that processes vehicles as a queuing system. Lee and Park (2012) proposed a nonlinear optimization model to optimize trajectories for CAVs approaching and passing a non-stop intersection. Zohdy and Rakha (2014) proposed a nonlinear optimization model that integrates an embedded car-following rule and an intersection communication protocol for non-stop intersection management. Other studies consider how to control vehicle trajectories in compliance with existing traffic signal timing at intersections. Trayford et al. (1984a; 1984b) proposed to use speed advice to reduce fuel consumption for vehicles approaching an intersection. Later studies further investigated car-following dynamics (Sanchez et al., 2006), in-vehicle traffic light assistance (Iglesias et al., 2008; Wu et al., 2010), multi-intersection corridors (Mandava et al., 2009; Guan and Frey, 2013; De Nunzio et al., 2013), scaled-up simulation (Tielert et al., 2010), and electric vehicles (Wu et al., 2015). These studies mainly concerned control of vehicle speeds but ignored acceleration detail, which however could cause significant errors in estimating fuel consumption and emissions and practical difficulties for real vehicles to follow these trajectories with speed jumps. To address this issue, Kamalanathsharma et al. (2013) considered acceleration detail in optimizing an individual vehicle trajectory. Li’s team (Zhou et al., 2017; Ma et al., 2017) proposed a parsimonious shooting heuristic to simultaneously optimize trajectories of a stream of CAVs approaching an intersection.

Most studies on using CAVs to smooth traffic are essentially centered on a vehicle trajectory optimization problem that aims to determine the optimal shapes for interdependent vehicle trajectories constrained by their boundary conditions, physical limits and safety risks. However, this problem in a general form is very complex and difficult to solve due to several computational challenges. First, each trajectory is essentially an infinite-dimensional object since every point along it can be a variable, and thus this problem deals with an infinite number of decision variables. Second, the optimization objective often involves highly non-linear components such as fuel consumption and emissions. Third, problem constraints can be quite complex due to vehicle interactions (e.g., two consecutive vehicles have to maintain a safe headway all the time) and boundary conditions (e.g., vehicles can only pass an intersection during a green light). Directly solving this problem, even a quite simple version, requires quite some computational resources and sophistication in algorithm design (Von Stryk and Bulirsch, 1992; Wei et al., 2016). Instead of solving the original trajectory problem, Li’s team (Zhou et al., 2017; Ma et al., 2017) opted to investigate a reduced problem where a trajectory is broken into a small number of quadratic sections and only a few acceleration levels are used to control the overall smoothness of the stream of vehicle trajectories. Although this reduced problem may not necessarily solve the true optimal solution to the original problem, it can yield a stream of trajectories with appealing overall smoothness and performance measures that much outperform the benchmark case without trajectory smoothing. Further, this simplification enables discovery of elegant theoretical properties and development of an efficient sub-gradient-based optimization algorithm for real-time applications.

Despite the breakthroughs from this previous work, there still remain a number of fundamental challenges in CAV trajectory optimization. First, the trajectory optimization method based on the shooting heuristic still relies on a numerical algorithm that does not ensure solution optimality and may need many iterations to converge. Second, one may intuitively think that since trajectory smoothing always leads to longer acceleration and

deceleration distances for vehicles (though with milder acceleration magnitudes), it shall always yield a longer queue propagation or spillback. However, this intuition has not been systematically and analytically verified. Third, the previous work only focuses on a signalized intersection and applications in other types of highway segments remain to be investigated. These challenges are addressed in the simplified trajectory optimization model proposed in Section 4.

2.3 Review of Signal Optimization Studies

Previous section provides a review of trajectory optimization studies. To serve sufficient background information for CHAPTER 5, this section complements the trajectory literature review with a review of signal optimization studies using CAV technologies.

Several studies have been conducted to optimize signal timing plans with CAV technologies. Goodall et al. (2013) proposed a predictive microscopic algorithm to predict accumulative delays within the communication range and determine the optimal timing plan that yields the minimum delays. Lee (2010) presented a similar algorithm using adaptive Kalman filter to estimate accumulative travel times. In this algorithm, the green time will be allocated to the phase that has the largest accumulative travel time. He et al. (2012) proposed a multi-modal online traffic signal control that identifies platoons and then determine the optimal signal timing using a linear programming method. This algorithm was based on a decentralized traffic signal coordination system and generally proposes no specific cycle length. He et al. (2014) conducted a follow-up study, in which a mixed integer model for a multi-modal traffic signal control optimization was proposed. Feng et al. (2015) proposed a bi-level adaptive traffic signal control algorithm to optimize both phase sequences and phase duration. This algorithm is one of the core algorithms of Multi-Modal Intelligent Traffic Safety System (MMITSS) (Ahn et al., 2016).

These studies provide useful models to optimize signal timing plans with CV, or CAV technologies. However, most of these studies predict when vehicles arrive at the signalized crossing point, and then coordinate the signal timing plans accordingly. As noted before, with CAV technologies, detailed vehicle trajectory shapes could be efficiently controlled. This brings an opportunity to join both signal and trajectory controls to further improve traffic performance. Some recent studies have started investigating benefits of joint optimization of trajectories and signal control. Kathis (2016) proposed a joint trajectory and signal algorithm for an isolated intersection. However, the proposed algorithm could not be implemented in the real-world applications due to the required heavy computational efforts. Pourmehrab et al. (2017) proposed an iterative algorithm to optimize intersection signal timing plan and AV trajectories. Despite these breakthroughs, these algorithms are based on heuristic solutions that require a substantial computational efforts to converge and thus may not be applicable to future CAV traffic. Therefore, an efficient joint trajectory and signal optimization model is yet to be discovered.

2.4 Review of Speed Harmonization Studies

Speed harmonization techniques aim to eliminate or reduce traffic oscillation by reducing the variations of traffic speed. Traditionally, variable speed limit (VSL) and speed advisory messages approaches are used to minimize traffic speed variations. Numerous studies have been conducted on VSL approaches. Many of these studies focus on VSL simulation or optimization studies with different objective functions. Alessandri et al. (1999) develops an optimization model to determine the appropriate variable-speed that results in the minimum travel time. Due to the complex nature of this optimization problem, this model relies on numerical solutions to obtain the solutions. Hegyi et al. (2002) proposes a network-wide optimization problem to minimize total time spent in the network and abrupt changes in the control signal. Later, Hegyi et al. (2005b) develops a VSL strategy to suppress shock waves.

The objective of this model is also to minimize total travel time. Lin et al. (2004) proposes a VSL control strategy to maximize throughput. Their results indicate that VSL can also improve safety and emissions. Hadiuzzaman and Qiu (2013) develops an analytical model based cell transition method (CTM) to maximize throughput. In this model, the optimal speed limit is determined using a numerical optimization technique. On the empirical side, a number of efforts are taken to adopt VSL approaches that were able to improve traffic performance (e.g., Ulfarsson et al., 2005; Bertini et al., 2005, 2006; Chang et al., 2011; Weikl et al., 2013). Eco-driving is another speed harmonization strategy that has recently attracted research attentions and includes driving techniques to reduce fuel consumption and emissions (e.g., Barth and Boriboonsomsin, 2009; Saboohi and Farzaneh, 2009; Mensing et al., 2011).

Despite the improvements that these approaches offer, due to the lack of sufficient and accurate information and the unpredictable nature of human behaviors, these traditional control approaches are not able to completely smooth traffic speeds. Fortunately, the advent of CAV technologies enables vehicle and infrastructure units to share high-resolution information in real-time. Further, these technologies eliminate human error and allow vehicles to be controlled by precise and fast-responding robots. Therefore, with these technologies, speed harmonization goals can be fully achieved. A number of studies have been conducted to apply these technologies in speed harmonization. Ma et al. (2016) presents a relatively comprehensive review on recent speed harmonization studies using connected, automated, or CAV technologies. Most of these studies either focus on only sharing information with connected systems (e.g., Talebpour et al., 2013; Yang and Jin, 2014; Lu et al., 2015) or controlling individual CAVs (e.g., Wang et al., 2015a). Further, most existing studies either consider pure-automated traffic or make simple simple assumptions about human behavior (Ma et al., 2016). Thus a CAV-based speed harmonization algorithm that could be applied to whole traffic stream as one system and can be adapted based on real-time updated information is yet to be discovered.

CHAPTER 3: CAPACITY ANALYSIS¹

This chapter aims to model mixed traffic (including both CAVs and HVs) on a one-lane highway segment. To capture real-world stochasticity and uncertainties, we allow vehicle types to be distributed stochastically and vehicle headways to follow random distributions depending on the corresponding vehicle types. Yet the overall traffic pattern can be characterized by two exogenous parameters that largely affect highway capacity. The first parameter, denoted by P_1 , describes the percentage of CAVs in the mixed traffic. We would expect that due to reduced CAV headway, traffic capacity shall grow with P_1 that is predicted to grow rapidly in the following decades (Bansal and Kockelman, 2017; Chen et al., 2016; Lavasani et al., 2016). The second parameter, denoted by O , indicating the CAV platooning intensity, i.e., the strength of CAV clustering in the mixed traffic. Addressing different CAV platooning intensities is a valid concern, because different CAV technologies and highway management strategies can significantly affect how CAV are platooned and how much the corresponding traffic capacity is. For example, if CAVs are individual units that are not much coordinated during operations, they could be just randomly distributed in mixed traffic with weak platooning, and the improvement to traffic capacity is limited. Otherwise, if they are run as fleets by coordinated and centralized operators (Fernandes and Nunes, 2012), CAVs may form platoons with significant lengths, which expects to significantly improve traffic capacity. Further, proper traffic management strategies (e.g., exclusive CAV lanes and pricing) could be applied to encourage CAVs platooning. This chapter describes the proposed analytical model that incorporates these random aspects and reveals fundamental

¹This chapter has been previously published in Ghiasi et al. (2017). Permission is included in Appendix.

impacts of market penetration rates and platooning intensities on mixed traffic capacity. Section 3.1 presents a Markov chain model to describe a class of vehicle spatial distributions along the mixed traffic stream incorporating the whole spectra of CAV penetration rates and platooning intensities. Section 3.2 formulates the expected capacity for the mixed traffic characterized by this Markov chain model. Finally, Section 3.3 provides numerical examples to verify the presented theoretical analyses and to demonstrate the accuracy of the proposed capacity formulation.

3.1 Markov Chain Model

We consider a stream of N vehicles indexed as $n \in \mathcal{N} := \{1, 2, \dots, N\}$ moving along the highway segment. Let $A_n \in \{0, 1\}$ denote whether vehicle n is CAV or HV; i.e., $A_n = 1$ if vehicle n is a CAV and $A_n = 0$ if vehicle n is an HV. Penetration rate P_1 is defined as the expected percentage of CAVs among all vehicles, i.e.,

$$P_1 := \mathbb{E} \left(\sum_{n \in \mathcal{N}} A_n / N \right). \quad (3.1)$$

For notation convenience, we also define the corresponding percentage of HVs among all vehicles as

$$P_0 := \mathbb{E} \left(\sum_{n \in \mathcal{N}} (1 - A_n) / N \right) = 1 - P_1.$$

The following analysis treats P_0 and $1 - P_1$ interchangeably, and P_0 is used only for formulation compactness. Note that the same P_1 value could correspond to different distributions of vehicle types or platooning intensities of CAVs. For example, when $P_1 = 0.5$, one extreme case is that every CAV always follows an HV (as illustrated by Fig. 3.1(a)), the other extreme case is that the first half set of vehicles are all CAVs and the remaining vehicles are all HVs (as illustrated by Fig. 3.1(b)), and a case in between is that CAVs are clustered somehow but occasionally disrupted by HVs (as illustrated by Fig. 3.1(c)). It is not difficult to see

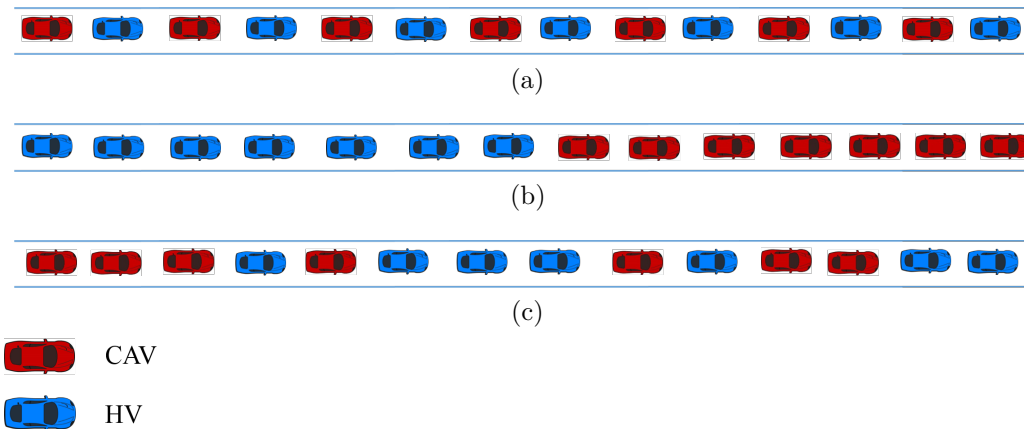


Figure 3.1: Illustrative examples for vehicle distributions.

that at the same P_1 value, there are numerous cases corresponding to different platooning intensities, and each of them could yield a different traffic throughput due to different headways between different types of vehicles. To model such general CAV platooning intensities for stochastic mixed traffic in a parsimonious way, we use a discrete Markov chain model to specify types of vehicles in \mathcal{N} sequentially from downstream to upstream as follows. In this Markov chain, A_n can be interpreted as the state variable at step n , and the state space is

$$S := \{1, 0\},$$

where 1 denotes the CAV type and 0 denotes the HV type. Let the first vehicle have a probability of P_1 to be a CAV, i.e., $\Pr(A_1 = 1) = P_1$. Therefore, the initial state is

$$\pi := [P_1, P_0]. \quad (3.2)$$

Then we define the following transition matrix:

$$T := \begin{bmatrix} t_{11} & t_{10} \\ t_{01} & t_{00} \end{bmatrix}, \quad (3.3)$$

where t_{sr} denotes the probability for a type- s vehicle to be followed by a type- r vehicle, i.e., $t_{sr} := \Pr(A_{n+1} = r \mid A_n = s), \forall n \in \mathcal{N} \setminus N, s, r \in S$. To capture general market penetration rates and platooning intensities, t_{sr} is formulated as a function P_1 and O :

$$t_{10}(P_1, O) := \begin{cases} P_0(1 - O), & O \geq 0; \\ P_0 + O \left(P_0 - \min \left\{ 1, \frac{P_0}{P_1} \right\} \right), & O < 0, \end{cases} \quad (3.4)$$

$$t_{11}(P_1, O) := 1 - t_{10}(P_1, O), \quad (3.5)$$

$$t_{01}(P_1, O) := \begin{cases} P_1(1 - O), & O \geq 0; \\ P_1 + O \left(P_1 - \min \left\{ 1, \frac{P_1}{P_0} \right\} \right), & O < 0, \end{cases} \quad (3.6)$$

$$t_{00}(P_1, O) := 1 - t_{01}(P_1, O). \quad (3.7)$$

We denote this Markov chain by $Markov(\pi, T)$. This formulation is carefully designed such that parameter O decreases from 1 to -1 as the platooning intensity decreases from maximum to minimum. This can be seen from the following special cases.

- Maximum platooning intensity ($O = 1$): All CAVs in this case are perfectly platooned into one group, similar to the case illustrated by Fig. 3.1(b). Thus, given that vehicle n is a CAV, the probability that following vehicle $n + 1$ is also a CAV converges to one. Similarly, given that vehicle n is an HV, the probability that following vehicle $n + 1$ is also an HV converges to one. Thus the elements of transition matrix T in this case are

$$t_{11}(P_1, 1) = t_{00}(P_1, 1) = 1, t_{10}(P_1, 1) = t_{01}(P_1, 1) = 0. \quad (3.8)$$

- Independent platooning ($O = 0$): In this case, CAVs and HVs are randomly mixed; i.e., a vehicle's type is independent of its preceding vehicle and is only determined by

penetration rate P_1 . Thus, the elements of transition matrix T in this case are

$$t_{11}(P_1, 0) = t_{01}(P_1, 0) = P_1, t_{10}(P_1, 0) = t_{00}(P_1, 0) = P_0.$$

- Minimum platooning intensity ($O = -1$): In this case, CAVs are at the weakest possible platooning intensity where the number of CAV platoons are maximal. Now a CAV would follow an HV if possible at all, and vice versa; i.e., t_{01} and t_{10} are set to their maximum values. Therefore, the elements of T in this case become

$$\begin{aligned} t_{10}(P_1, -1) &= \min\left\{1, \frac{P_0}{P_1}\right\}, & t_{11}(P_1, -1) &= 1 - t_{10}(P_1, -1), \\ t_{01}(P_1, -1) &= \min\left\{1, \frac{P_1}{P_0}\right\}, & t_{00}(P_1, -1) &= 1 - t_{01}(P_1, -1). \end{aligned}$$

Now we will show that this Markov chain model is consistent with P_1 definition (3.1) in the follow proposition.

Proposition 1. *The Markov chain model defined by (3.2)-(3.7) yields (3.1) as the invariant distribution probability.*

Proof. To prove this proposition, we will just show $\Pr(A_n = 1) = P_1, \forall n \in \mathcal{N}$ with induction. When $n = 1$, Equation (3.2) apparently yields $\Pr(A_1 = 1) = P_1$. Next, we set an induction assumption that for $n = k \in \mathcal{N} \setminus N$, $\Pr(A_k = 1) = P_1$. Then when $n = k + 1$, in case of $O > 0$

$$\begin{aligned} \Pr(A_{k+1} = 1) &= \Pr(A_k = 0)t_{01} + \Pr(A_k = 1)t_{11} \\ &= (1 - P_1) \cdot P_1(1 - O) + P_1 \cdot (1 - (1 - P_1)(1 - O)) \\ &= P_1, \end{aligned}$$

whereas in case of $O < 0$,

$$\begin{aligned}
\Pr(A_{k+1} = 1) &= \Pr(A_k = 0)t_{01} + \Pr(A_k = 1)t_{11} \\
&= (1 - P_1) \cdot \left(P_1 + O\left(P_1 - \min\left\{ 1, \frac{P_1}{P_0} \right\} \right) \right) + \\
&\quad P_1 \cdot \left(P_1 - O\left(1 - P_1 - \min\left\{ 1, \frac{P_0}{P_1} \right\} \right) \right) \\
&= P_1.
\end{aligned}$$

This completes the proposition. □

The above proposition verifies that the proposed Markov chain model is capable of describing stochastic mixed traffic with different CAV penetration rates and platooning intensities.

3.2 Capacity Formulation

This section aims to formulate the expected capacity of Markov chain mixed traffic model (3.2)-(3.7) by analyzing time headway between consecutive vehicles. Since our analysis focuses on traffic capacity, i.e., the maximum allowed traffic throughput, each headway investigated in this study refers to the minimum headway between the corresponding vehicles at the design speed on the investigated road segment. Let h_n denote the time headway between vehicles n and $n + 1, \forall n \in \mathcal{N} \setminus N$. We allow h_n to be a random variable that follows a positive distribution depending on vehicle types A_n and A_{n+1} with a finite mean of $\bar{h}_{A_n A_{n+1}}$ and a finite variance. Assume the variations $\{h_n\}$ values are independent across different vehicles. Note that as illustrated in Figure 3.2, there are four types of mean time headways: \bar{h}_{00} for an HV followed another HV, \bar{h}_{01} for an HV followed a CAV, \bar{h}_{10} for a CAV followed an HV, and \bar{h}_{11} for a CAV followed by another CAV. With this, the expected capacity of the mixed traffic stream can be written as:

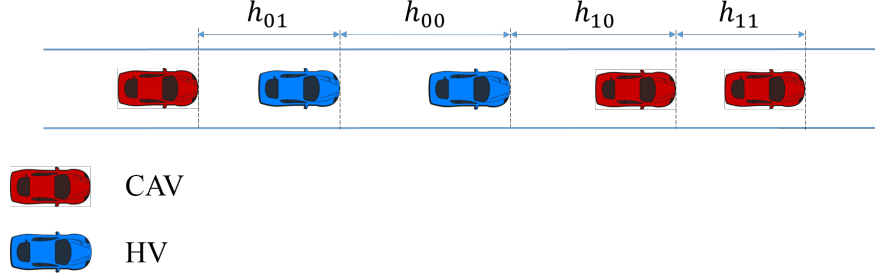


Figure 3.2: Illustration of headways in mixed traffic.

$$\bar{c} := \mathbb{E} \left(\frac{N-1}{\sum_{n=1}^{N-1} h_n} \right).$$

Due to the exponential number of vehicle type scenarios (a scenario here is a realization of all vehicles types) and random headway distributions, it is difficult to directly calculate \bar{c} . Instead, Section 3.2.1 proposes a closed-form analytical formula to approximate \bar{c} and presents theoretical analysis to show the closeness of this approximate value to the actual \bar{c} value. Next, Section 3.2.2 examines how this approximate capacity varies with CAV penetration rates and platooning intensities against the intuition that mixed traffic capacity increases with these two factors.

3.2.1 Approximate Capacity

We propose to estimate \bar{c} with an approximate capacity formulated below:

$$\hat{c} := \frac{N-1}{\sum_{n=1}^{N-1} \mathbb{E}(h_n)} = \frac{N-1}{\sum_{n=1}^{N-1} \bar{h}_{A_n A_{n+1}}}.$$

With the Markov chain model, Proposition 1 yields

$$\Pr(A_n A_{n+1} = sr) = P_s t_{sr}(P_1, O), \forall s, r \in S, n \in \mathcal{N} \setminus N.$$

Then we obtain

$$\frac{\sum_{n=1}^{N-1} \bar{h}_{A_n A_{n+1}}}{N-1} = \sum_{s \in S, r \in S} P_{st_{sr}}(P_1, O) \bar{h}_{sr}$$

and approximate capacity \hat{c} can be reformulated into a deterministic form as:

$$\hat{c}(P_1, O, h) = \frac{1}{\sum_{s \in S, r \in S} P_{st_{sr}}(P_1, O) \bar{h}_{sr}}. \quad (3.9)$$

where h is the vector of expected headways, i.e., $h := [\bar{h}_{11}, \bar{h}_{10}, \bar{h}_{01}, \bar{h}_{00}]$. Below we investigate the relationship between actual expectation \bar{c} and approximate value $\hat{c}(P_1, O, h)$.

Lemma 1. $f(h^u) := \frac{1}{\sum_{n=1}^{N-1} h_n^u}$ is a convex function of $h^u := [h_n^u \geq 0]_{\forall n}$.

Proof. Define $h^{u1} := [h_n^{u2} \geq 0]_{\forall n}$, $h^{u2} := [h_n^{u2} \geq 0]_{\forall n}$ and $h^{u3} := [h_n^{u3} := 0.5h_n^{u1} + 0.5h_n^{u2} \geq 0]_{\forall n}$. Proving function $f(\cdot)$ is convex is equivalent to showing $0.5f(h^{u1}) + 0.5f(h^{u2}) \geq f(h^{u3})$. Then we obtain:

$$\begin{aligned} \frac{0.5f(h^{u1}) + 0.5f(h^{u2})}{f(h^{u3})} &= \frac{\frac{0.5}{\sum_{n=1}^{N-1} h_n^{u1}} + \frac{0.5}{\sum_{n=1}^{N-1} h_n^{u2}}}{\frac{1}{\sum_{n=1}^{N-1} h_n^{u3}}} \\ &= \frac{\left(\sum_{n=1}^{N-1} h_n^{u3}\right)^2}{\sum_{n=1}^{N-1} h_n^{u1} \sum_{n=1}^{N-1} h_n^{u2}} \\ &= \frac{\left(\sum_{n=1}^{N-1} h_n^{u3}\right)^2}{\left(\sum_{n=1}^{N-1} h_n^{u3}\right)^2 - 0.25 \left(\sum_{n=1}^{N-1} h_n^{u1} - \sum_{n=1}^{N-1} h_n^{u2}\right)^2} \\ &\geq 1. \end{aligned}$$

This completes the proof. □

Theorem 1. $\hat{c}(P_1, O, h) \leq \bar{c}$ for any finite N .

Proof. Let \mathcal{U} denote the set of all possible vehicle type scenarios, and let p_u denote the probability of scenario $u \in \mathcal{U}$. Let A_n^u denote the realization of A_n and h_n^u denote the

headway between vehicles n and $n + 1$ in scenario u . Then we can formulate

$$\bar{c} = \sum_{u \in \mathcal{U}} p_u \mathbb{E} \left(\frac{N-1}{\sum_{n=1}^{N-1} h_n^u} \right).$$

Then based on Lemma 1 and Jensen's inequality (Jensen, 1906), we have $\mathbb{E} \left(\frac{N-1}{\sum_{n=1}^{N-1} h_n^u} \right) \geq$

$$\frac{N-1}{\sum_{n=1}^{N-1} \mathbb{E}(h_n^u)} = \frac{N-1}{\sum_{n=1}^{N-1} \bar{h}_{A_n^u A_{n+1}^u}}. \text{ This yields}$$

$$\bar{c} \geq \sum_{u \in \mathcal{U}} p_u \frac{N-1}{\sum_{n=1}^{N-1} \bar{h}_{A_n^u A_{n+1}^u}}.$$

Based on the same argument with Jensen's inequality, we obtain

$$\sum_{u \in \mathcal{U}} p_u \frac{N-1}{\sum_{n=1}^{N-1} \bar{h}_{A_n^u A_{n+1}^u}} \geq \frac{N-1}{\sum_{n=1}^{N-1} \sum_{u \in \mathcal{U}} p_u \bar{h}_{A_n^u A_{n+1}^u}} = \frac{N-1}{\sum_{n=1}^{N-1} \mathbb{E}(h_n)} = \hat{c}(P_1, O, h).$$

This indicates $\hat{c}(P_1, O, h) \leq \bar{c}$ and completes the proof. \square

The above theorem indicates that $\hat{c}(P_1, O, h)$ provides a lower bound to \bar{c} for a small stream of vehicles, which can still serve as a conservative estimation of the real capacity. Further, as the size of the traffic stream increases, the following analysis shows $\hat{c}(P_1, O, h)$ is an accurate estimation of \bar{c} .

We define an extended Markov chain where states are defined for consecutive vehicle pairs instead. We call two consecutive vehicles n and $n + 1$ vehicle pair n . Define $(X_n := A_n A_{n+1})_{n \in \mathcal{N} \setminus N}$ as the state variable for vehicle pair n , and the corresponding state space is

$$S^E := S^2 = \{(1, 1), (1, 0), (0, 1), (0, 0)\}.$$

Based on Proposition 1 and Equation (3.3), for this extended Markov chain, we can obtain the initial distribution as $\pi^E := [\pi_{sr}^E := P_s t_{sr}(P_1, O)]$, $\forall s \in S, sr \in S^E$ and the transition

matrix as

$$T^E := \begin{bmatrix} t_{1111}^E & t_{1110}^E & t_{1101}^E & t_{1100}^E \\ t_{1011}^E & t_{1010}^E & t_{1001}^E & t_{1000}^E \\ t_{0111}^E & t_{0110}^E & t_{0101}^E & t_{0100}^E \\ t_{0011}^E & t_{0010}^E & t_{0001}^E & t_{0000}^E \end{bmatrix},$$

where $t_{sr s' r'}^E$ denotes the probability for a vehicle pair of type sr to be followed by a vehicle pair of type $s' r'$, i.e.,

$$\begin{aligned} t_{sr s' r'}^E &:= \Pr(X_{n+1} = s' r' \mid X_n = sr) \\ &= \Pr(A_{n+1} A_{n+2} = s' r' \mid A_n A_{n+1} = sr), \forall n \in \mathcal{N} \setminus \{N, N-1\}, sr \in S^E. \end{aligned}$$

It is apparent that $t_{sr s' r'}^E = 0$, if $r \neq s', \forall s, r, s', r' \in S$. For other elements of T^E , based on Proposition 1 and Equation (3.3), we obtain $t_{sr r r'}^E = t_{r r'} \forall s, r, s', r' \in S$. Thus we can rewrite T^E as

$$T^E(P_1, O) = \begin{bmatrix} t_{11} & t_{10} & 0 & 0 \\ 0 & 0 & t_{01} & t_{00} \\ t_{11} & t_{10} & 0 & 0 \\ 0 & 0 & t_{01} & t_{00} \end{bmatrix}.$$

We denote this extended Markov chain by $Markov(\pi^E, T^E)$ and the following lemmas investigate its basic properties.

Lemma 2. *If $O < 1$ and $0 < P_s < 1, \forall s \in S$, then π^E is an invariant distribution for T^E .*

Proof. Based on the definition of invariant distribution (Norris, 1998), we just need to show $\pi^E T^E = \pi^E$.

$$\begin{aligned} \pi^E T^E &= [P_1 t_{11}, P_1 t_{10}, P_0 t_{01}, P_0 t_{00}] \cdot \begin{bmatrix} t_{11} & t_{10} & 0 & 0 \\ 0 & 0 & t_{01} & t_{00} \\ t_{11} & t_{10} & 0 & 0 \\ 0 & 0 & t_{01} & t_{00} \end{bmatrix} \\ &= [P_1 t_{11}^2 + P_0 t_{01} t_{11}, P_1 t_{11} t_{10} + P_0 t_{01} t_{10}, P_1 t_{10} t_{01} + P_0 t_{00} t_{01}, P_1 t_{10} t_{00} + P_0 t_{00}^2]. \end{aligned}$$

We obtain the elements of the above vector as following:

$$\begin{aligned} P_1 t_{11}^2 + P_0 t_{01} t_{11} &= P_1 t_{11}^2 + (1 - P_1) \cdot \frac{P_1}{1 - P_1} (1 - t_{11}) \cdot t_{11} = P_1 t_{11}, \\ P_1 t_{11} t_{10} + P_0 t_{01} t_{10} &= P_1 \cdot (1 - t_{10}) \cdot t_{10} + (1 - P_1) \cdot \frac{P_1}{1 - P_1} t_{10} \cdot t_{10} = P_1 t_{10}, \\ P_1 t_{10} t_{01} + P_0 t_{00} t_{01} &= (1 - P_0) \cdot \frac{P_0}{1 - P_0} t_{01} \cdot t_{01} + P_0 \cdot (1 - t_{01}) t_{01} = P_0 t_{01}, \\ P_1 t_{10} t_{00} + P_0 t_{00}^2 &= (1 - P_0) \cdot \frac{P_0}{1 - P_0} (1 - t_{00}) \cdot t_{00} + P_0 t_{00}^2 = P_0 t_{00}. \end{aligned}$$

Thus $\pi^E T^E = \pi^E$, which completes the proof. \square

Lemma 3. *If $O < 1$ and $0 < P_s < 1, \forall s \in S$, Markov(π^E, T^E) is irreducible and all states in S^E are positive recurrent.*

Proof. If $O < 1$ and $0 < P_s < 1$, then $P_{st_{sr}}(P_1, O) > 0, \forall s, r \in S$. Thus it is intuitive that

$$\Pr(X_{n+1} = s' r' \mid X_n = s s') = P_{st_{sr}}(P_1, O) > 0, \forall sr, s' s' \in S^E, \forall n \in \mathcal{N} \setminus N.$$

With this, we know

$$\Pr(X_3 = s'r' \mid X_1 = sr) \geq \Pr(X_3 = s'r' \mid X_2 = rs') \cdot \Pr(X_2 = rs' \mid X_1 = sr) > 0, \\ \forall sr, s'r' \in S^E.$$

Thus all states in S^E communicate each other, i.e., $sr \leftrightarrow s'r', \forall sr, s'r' \in S^E$. Based on Theorem 1.2.1 in Norris (1998), $Markov(\pi^E, T^E)$ is irreducible. Also, since all states in S^E form a finite closed class, Theorem 1.5.6 in Norris (1998) shows that all states in S^E are recurrent. Further, based on Lemma 2 and Theorem 1.7.7 in Norris (1998), all states in S^E are positive recurrent. This completes the proof. \square

Lemma 4. Define $N_{sr} := \sum_{n \in \mathcal{N} \setminus N} I_{sr}(X_n)$ where indicator function $I_{sr}(X_n)$ is 1 if $X_n = sr$ is true or 0 otherwise. If $O < 1$, then we obtain

$$\Pr\left(\frac{N_{sr}}{N-1} \rightarrow \pi_{sr}^E \text{ as } N \rightarrow \infty\right) = 1, \forall sr \in S^E.$$

Proof. We first investigate the cases where $Markov(\pi^E, T^E)$ is non-recurrent, i.e., $P_1 = 1$ or $P_0 = 1$ ($O < 1$). When $P_1 = 1$, Equations (3.4) and (3.5) yield $t_{11} = 1$, which indicates $sr = 11$ is an absorbing state. This further yields $\pi_{sr}^E = 1$, which indicates that all vehicles are CAVs or $N_{11} = N - 1$. Then it is easy to obtain $\frac{N_{11}}{N-1} = P_1 t_{11} = 1$. Similarly, when $P_0 = 1$, with a similar logic, we can show that $\frac{N_{00}}{N-1} = P_0 t_{00} = 1$. Further, for cases where $0 < P_s < 1, \forall s \in S$, based on Lemmas 2 and 3, $Markov(\pi^E, T^E)$ is irreducible with an invariant distribution π^E and all states in S^E are positive recurrent. Based on the definition, we obtain

$$I_{sr}(s'r') = \begin{cases} 1, & \text{if } s'r' = sr; \\ 0, & \text{otherwise.} \end{cases}$$

Theorem 1.10.2 in Norris (1998) shows that as $N \rightarrow \infty$, $\frac{1}{N-1} \sum_{n \in \mathcal{N} \setminus N} I_{sr}(X_n) \rightarrow \bar{I}_{sr}$ for all $sr \in S^{\mathbb{E}}$, where $\bar{I}_{sr} := \sum_{s'r' \in S} \mathbb{E} \left(\pi_{sr}^{\mathbb{E}} I_{sr}(s'r') \right)$. Since $\bar{I}_{sr} = \pi_{sr}^{\mathbb{E}}$, and based on the definition of N_{sr} , we obtain

$$\Pr \left(\frac{N_{sr}}{N-1} \rightarrow \pi_{sr}^{\mathbb{E}} \text{ as } N \rightarrow \infty \right) = 1, \forall sr \in S^{\mathbb{E}}.$$

This completes the proof. \square

Theorem 2. *When $O < 1$, we obtain $\Pr(\hat{c}(P_1, O, h) \rightarrow \bar{c} \text{ as } N \rightarrow \infty) = 1$.*

Proof. First we investigate the two cases when $Markov(\pi^{\mathbb{E}}, T^{\mathbb{E}})$ is non-recurrent: i.e., $P_1 = 1$ or $P_0 = 1$. When $P_1 = 1$, we obtain $A_n = 1, \forall n \in \mathcal{N}$. Then based on the definitions, $\hat{c}(P_1, O, h) = \frac{N-1}{\sum_{n=1}^{N-1} \bar{h}_{11}} = \frac{1}{h_{11}}$ and $\bar{c} = \mathbb{E} \left(\frac{N-1}{\sum_{n=1}^{N-1} h_n} \right)$. By the assumption of the independent distributions of vehicle headways and the strong law of large numbers, we obtain that the probability for $\left(\lim_{N \rightarrow \infty} \frac{N-1}{\sum_{n=1}^{N-1} h_n} = \frac{1}{h_{11}} \right)$ is one. Thus $\Pr(\bar{c} = \hat{c}(P_1, O, h) \text{ as } N \rightarrow \infty) = 1$. Similarly, we can show that when $P_0 = 1$, $\Pr \left(\lim_{N \rightarrow \infty} \frac{N-1}{\sum_{n=1}^{N-1} h_n} = \frac{1}{h_{00}} \right) = 1$, and thus $\Pr(\bar{c} = \hat{c}(P_1, O, h) \text{ as } N \rightarrow \infty) = 1$.

Now we investigate other cases for $0 < P_s < 1$. Since Lemma 3 indicates $\Pr(N_{sr} \rightarrow \infty \text{ as } N \rightarrow \infty) = 1, \forall sr \in S^{\mathbb{E}}$, based on the law of large numbers, we obtain

$$\bar{c} = \mathbb{E} \left(\frac{1}{\sum_{s \in S, r \in S} \frac{\sum_{n \in \mathcal{N}_{sr}^u} h_n}{N_{sr}} \cdot \frac{N_{sr}}{N-1}} \right) \rightarrow \mathbb{E} \left(\frac{1}{\sum_{s \in S, r \in S} \bar{h}_{sr} \cdot \frac{N_{sr}}{N-1}} \right) \text{ as } N \rightarrow \infty. \quad (3.10)$$

Further, since Lemma 4 indicates that $\Pr \left(\frac{N_{sr}}{N-1} \rightarrow \pi_{sr}^{\mathbb{E}} \text{ as } N \rightarrow \infty \right) = 1, \forall sr \in S^{\mathbb{E}}$, then we obtain

$$\Pr \left(\frac{1}{\sum_{s \in S, r \in S} \bar{h}_{sr} \cdot \frac{N_{sr}}{N-1}} \rightarrow \frac{1}{\sum_{s \in S, r \in S} \bar{h}_{sr} \pi_{sr}^{\mathbb{E}}} = \hat{c}(P_1, O, h) \text{ as } N \rightarrow \infty \right) = 1,$$

which yields,

$$\Pr \left(\mathbb{E} \left(\frac{1}{\sum_{s \in S, r \in S} \bar{h}_{sr} \cdot \frac{N_{sr}}{N-1}} \right) \rightarrow \hat{c}(P_1, O, h) \text{ as } N \rightarrow \infty \right) = 1. \quad (3.11)$$

Equations (3.10) and (3.11) indicate that $\Pr(\hat{c}(P_1, O, h) \rightarrow \bar{c} \text{ as } N \rightarrow \infty) = 1$, which completes the proof. \square

Note that the above analysis for $O < 1$ is sufficient for practical applications where the platooning intensity never reaches the extreme case with $O = 1$. Further, practical traffic capacity analysis is usually interested in a relatively long period with a large number of vehicles passing. Thus the above theorem reveals that it is reasonable to use $\hat{c}(P_1, O)$ to estimate true capacity \bar{c} in engineering practices. However, for the completeness of the analytical results, the following corollary shows the corresponding results for the extreme case with $O = 1$. The proof is straightforward and thus omitted in this presentation.

Corollary 1. *When $O = 1$, $\hat{c}(P_1, O, h) = \frac{1}{P_1 \bar{h}_{11} + P_0 \bar{h}_{00}} \leq \bar{c} = \frac{P_1}{h_{11}} + \frac{P_0}{h_{00}}$.*

3.2.2 CAV Penetration Rate and Platooning Intensity Effects

Previous studies have frequently taken for granted that highway capacity always increases with P_1 (e.g., Kesting et al., 2008; Arnaout and Arnaout, 2014; van den Berg and Verhoef, 2016) and O (Zhao and Sun, 2013; Harwood and Reed, 2014), and some claim that this increasing rate is higher at a greater P_1 value (e.g., van den Berg and Verhoef, 2016). To test this intuition, we investigate the effects of P_1 and O changes on $\hat{c}(P_1, O, h)$ with the following theorems. Define $\hat{h}_{10} := (\bar{h}_{10} + \bar{h}_{01})/2$, $\alpha := \bar{h}_{11} + \bar{h}_{00} - 2\hat{h}_{10}$ and $\beta := \hat{h}_{10} - \bar{h}_{00}$.

Theorem 3. *Define $\phi := (\rho - 1)\bar{h}_{00} + (2 - \rho)\hat{h}_{10} - \bar{h}_{11}$. $\hat{c}(P_1, O, h)$ is increasing at $P_1 \in (0, 1]$, if and only if $\phi(P_1, O, h) \geq 0$, where*

$$\rho(P_1, O) := \begin{cases} \frac{1}{(1-O)P_1 + \frac{\sigma}{2}}, & \text{if } O \in [0, 1]; \\ \frac{1}{(1+O)P_1}, & \text{if } O \in [-1, 0), p \in (0, 0.5]; \\ \frac{1}{(1+O)P_1 - O}, & \text{if } O \in [-1, 0), p \in (0.5, 1]. \end{cases}$$

Proof. Based on Equations (3.4)-(3.7) and (3.9), $\hat{c}(P_1, O, h)$ can be written as

$$\hat{c}(P_1, O, h) = \begin{cases} \frac{1}{\zeta_1 P_1^2 + \eta_1 P_1 + \theta_1} & O \in [0, 1]; \\ \frac{1}{\zeta_2 P_1^2 + \eta_2 P_1 + \theta_2}, & O \in [-1, 0), P_1 \in (0, 0.5]; \\ \frac{1}{\zeta_3 P_1^2 + \eta_3 P_1 + \theta_3} & O \in [-1, 0), P_1 \in (0.5, 1], \end{cases}$$

where $\zeta_1 := \alpha(1-O)$, $\zeta_2 := \zeta_3 := \alpha(1+O)$, $\eta_1 := \alpha O + 2\beta$, $\eta_2 := 2\beta$, $\eta_3 := -2\alpha O + 2\beta$, $\theta_1 := \theta_2 := \bar{h}_{00}$ and $\theta_3 := \alpha O + \bar{h}_{00}$.

For a certain O , we obtain $\frac{d\hat{c}}{dP_1}(P_1, O, h)$ as

$$\frac{d\hat{c}}{dP_1}(P_1, O, h) = \begin{cases} \frac{-2\zeta_1 P_1 - \eta_1}{(\zeta_1 P_1^2 + \eta_1 P_1 + \theta_1)^2}, & O \in [0, 1]; \\ \frac{-2\zeta_2 P_1 - \eta_2}{(\zeta_2 P_1^2 + \eta_2 P_1 + \theta_2)^2}, & O \in [-1, 0), P_1 \in (0, 0.5]; \\ \frac{-2\zeta_3 P_1 - \eta_3}{(\zeta_3 P_1^2 + \eta_3 P_1 + \theta_3)^2}, & O \in [-1, 0), P_1 \in (0.5, 1]. \end{cases}$$

$\hat{c}(P_1, O, h)$ is increasing at $P_1 \in (0, 1]$, if and only if $\frac{d\hat{c}}{dP_1}(P_1, O, h) \geq 0$. Since the denominators in the above equations are positive, we just need to investigate the signs of the numerators. Thus, $\frac{d\hat{c}}{dP_1}(P_1, O, h) \geq 0$ is equivalent to $-2\zeta_i P_1 - \eta_i \geq 0, \forall i = \{1, 2, 3\}$. Thus,

$\frac{d\hat{c}}{dP_1}(P_1, O, h) \geq 0$ is equivalent to

$$\begin{cases} -\alpha(2(1-O)P_1 + O) - 2\beta \geq 0, & O \in [0, 1]; \\ -2\alpha(1+O)P_1 - 2\beta \geq 0, & O \in [-1, 0), P_1 \in (0, 0.5]; \\ -2\alpha((1+O)P_1 - O) - 2\beta \geq 0, & O \in [-1, 0), P_1 \in (0.5, 1]. \end{cases}$$

Since for any $P_1 \in (0, 1]$, when $O \in [0, 1]$, $2(1-O)P_1 + O > 0$, and when $O \in [-1, 0)$, $2(1+O)P_1 > 0$, $\frac{d\hat{c}}{dP_1}(P_1, O, h) \geq 0$ is equivalent to

$$\begin{cases} \left(\frac{1}{(1-O)P_1 + \frac{O}{2}} - 1 \right) \bar{h}_{00} + \left(2 - \frac{1}{(1-O)P_1 + \frac{O}{2}} \right) \hat{h}_{10} - \bar{h}_{11} \geq 0, & O \in [0, 1]; \\ \left(\frac{1}{(1+O)P_1} - 1 \right) \bar{h}_{00} + \left(2 - \frac{1}{(1+O)P_1} \right) \hat{h}_{10} - \bar{h}_{11} \geq 0, & O \in [-1, 0), P_1 \in (0, 0.5]; \\ \left(\frac{1}{(1+O)P_1 - O} - 1 \right) \bar{h}_{00} + \left(2 - \frac{1}{(1+O)P_1 - O} \right) \hat{h}_{10} - \bar{h}_{11} \geq 0, & O \in [-1, 0), P_1 \in (0.5, 1]. \end{cases}$$

Thus, $\frac{d\hat{c}}{dP_1}(P_1, O, h) \geq 0$ is equivalent to $\phi(P_1, O, h) \geq 0$. This completes the proof. \square

Corollary 2. When $\hat{h}_{10} \leq \bar{h}_{00}$, $\phi(P_1, O, h)$ is a decreasing function of P_1 , and when $\hat{h}_{10} > \bar{h}_{00}$, $\phi(P_1, O, h)$ is an increasing function of P_1 , $\forall P_1 \in (0, 1]$.

Corollary 3. If $\hat{h}_{10} \leq \bar{h}_{00}$, $\hat{c}(P_1, O, h)$ is an increasing function of P_1 , $\forall P_1 \in (0, 1]$ if and only if $\phi(P_1 = 1, O, h) \geq 0, \forall O, h$, or equivalently

$$\begin{cases} \left(\frac{O}{2-O} \right) \bar{h}_{00} + \left(\frac{2-2O}{2-O} \right) \hat{h}_{10} - \bar{h}_{11} \geq 0, & \text{if } O \in [0, 1]; \\ \hat{h}_{10} \geq \bar{h}_{11}, & \text{if } O \in [-1, 0). \end{cases}$$

Otherwise if $\hat{h}_{10} > \bar{h}_{00}$, $\hat{c}(P_1, O, h)$ is an increasing function of P_1 , $\forall P_1 \in (0, 1]$ if and only if $\phi(P_1 = 0, O, h) \geq 0, \forall O \in [0, 1], h$, or equivalently $\left(\frac{2}{O} - 1 \right) \bar{h}_{00} + \left(2 - \frac{2}{O} \right) \hat{h}_{10} - \bar{h}_{11} \geq 0$. Further, when $\hat{h}_{10} > \bar{h}_{00}$ and $O \in [-1, 0)$, $\hat{c}(P_1, O, h)$ is not an increasing function of P_1 , $\forall P_1 \in (0, 1]$.

Corollary 4. *If $\hat{h}_{10} \leq \bar{h}_{00}$, $\hat{c}(P_1, O, h)$ is a decreasing function of P_1 , $\forall P_1 \in (0, 1]$ if and only if $\phi(P_1 = 0, O, h) \leq 0, \forall O \in [0, 1], h$, or equivalently $\left(\frac{2}{O} - 1\right)\bar{h}_{00} + \left(2 - \frac{2}{O}\right)\hat{h}_{10} - \bar{h}_{11} \leq 0$. Otherwise if $\hat{h}_{10} > \bar{h}_{00}$, $\hat{c}(P_1, O, h)$ is a decreasing function of P_1 , $\forall P_1 \in (0, 1]$ if and only if $\phi(P_1 = 1, O, h) \leq 0, \forall O, h$, or equivalently*

$$\begin{cases} \left(\frac{O}{2-O}\right)\bar{h}_{00} + \left(\frac{2-2O}{2-O}\right)\hat{h}_{10} - \bar{h}_{11} \leq 0, & \text{if } O \in [0, 1]; \\ \hat{h}_{10} \leq \bar{h}_{11}, & \text{if } O \in [-1, 0). \end{cases}$$

Further, when $\hat{h}_{10} \leq \bar{h}_{00}$ and $O \in [-1, 0)$, $\hat{c}(P_1, O, h)$ is not a decreasing function of P_1 , $\forall P_1 \in (0, 1]$.

Corollary 5. *The necessary and sufficient condition for $\hat{c}(P_1, O, h)$ to be an increasing function of $P_1, \forall P_1 \in (0, 1]$ is $\bar{h}_{11} \leq \hat{h}_{10} \leq \bar{h}_{00}$.*

Corollary 6. *The necessary and sufficient condition for $\hat{c}(P_1, O, h)$ to be a decreasing function of $P_1, \forall P_1 \in (0, 1]$ is $\bar{h}_{11} \geq \hat{h}_{10} \geq \bar{h}_{00}$.*

Theorem 3 and the associated corollaries indicate that contrary to the ubiquitous assumption that higher CAV penetration rates always yield greater mixed traffic capacity, CAV penetration may not help with capacity under certain headway settings. For example, under conservative CAV technologies with headways as specified by Corollary 6, a higher CAV penetration rate instead reduces highway capacity.

Next, to test the claim that the increasing rate of capacity is higher at a greater CAV penetration rate, we investigate the necessary and sufficient conditions in which $\hat{c}(P_1, O, h)$ is a convex function of P_1 , $\forall P_1 \in (0, 1]$.

Theorem 4. *When $O \in [0, 1]$, $\hat{c}(P_1, O, h)$ is a convex function of $P_1, \forall P_1 \in [0, 1]$ if and only if*

$$\left\{ \begin{array}{ll} \left(\sqrt{\eta_1^2 - 4\zeta_1 \cdot \theta_1} + \eta_1 + 2\zeta_1 < 0 \right) \vee (\eta_1 > 0), & \text{if } \zeta_1 > 0 \text{ and } 4\zeta_1 \cdot \theta_1 - \eta_1^2 < 0; \\ (\eta_1 + 2\zeta_1 < 0) \vee (\eta_1 > 0), & \text{if } \zeta_1 > 0 \text{ and } 4\zeta_1 \cdot \theta_1 - \eta_1^2 = 0; \\ \left(3\eta_1 + \sqrt{12\zeta_1 \cdot \theta_1 - 3\eta_1^2} + 6\zeta_1 < 0 \right) \vee \left(\eta_1 - \sqrt{\zeta_1 \cdot \theta_1} > 0 \right), & \text{if } \zeta_1 > 0 \text{ and } 4\zeta_1 \cdot \theta_1 - \eta_1^2 > 0; \\ (\eta_1 \cdot \theta_1 < -\eta_1^2) \vee (\eta_1 > 0), & \text{if } \zeta_1 = 0; \\ \sqrt{\eta_1^2 - 4\zeta_1 \cdot \theta_1} + \eta_1 + 2\zeta_1 > 0, & \text{if } \zeta_1 < 0 \text{ and } 4\zeta_1 \cdot \theta_1 - \eta_1^2 < 0; \end{array} \right.$$

if $\zeta_1 < 0$ and $4\zeta_1 \cdot \theta_1 - \eta_1^2 \geq 0$, then $\hat{c}(P_1, O, h)$ is not a convex function of $P_1, \forall P_1 \in [0, 1]$.

Proof. $\hat{c}(P_1, O, h)$ is a convex function of $P_1, \forall P_1 \in [0, 1]$, if and only if $\frac{d^2 \hat{c}}{dP_1^2}(P_1, O, h) > 0, \forall P_1 \in [0, 1]$. For a certain $O \in [0, 1]$, we obtain $\frac{d^2 \hat{c}}{dP_1^2}(P_1, O, h)$ as

$$\frac{d^2 \hat{c}}{dP_1^2}(P_1, O, h) = \frac{2(2\zeta_1 \cdot P_1 + \eta_1)^2}{(\zeta_1 \cdot P_1^2 + \eta_1 \cdot P_1 + \theta_1)^3} - \frac{2\zeta_1}{(\zeta_1 \cdot P_1^2 + \eta_1 \cdot P_1 + \theta_1)^2}.$$

Thus we obtain that $\frac{d^2 \hat{c}}{dP_1^2}(P_1, O, h) > 0$ is equivalent to $\frac{\nu(P_1)}{\delta(P_1)} > 0, \forall P_1 \in [0, 1]$ where $\delta(P_1) := \zeta_1 \cdot P_1^2 + \eta_1 \cdot P_1 + \theta_1$ and $\nu(P_1) := 3\zeta_1^2 \cdot P_1^2 + 3\zeta_1 \cdot \eta_1 \cdot P_1 - \zeta_1 \cdot \theta_1 + \eta_1^2$. Since $\hat{c}(P_1, O, h) > 0$, it is necessary that $\delta(P_1) > 0$ and for convexity, we require that $\nu(P_1) > 0, \forall P_1 \in [0, 1]$. We investigate each above condition separately as follows. If $\zeta_1 > 0$ and $4\zeta_1 \cdot \theta_1 - \eta_1^2 < 0$, $\nu(P_1)$ is always positive; however, $\delta(P_1) > 0, \forall P_1 \in [0, 1]$, if and only if $\frac{-\eta_1 + \sqrt{\eta_1^2 - 4\zeta_1 \cdot \theta_1}}{2\zeta_1} < 0$ or $\frac{-\eta_1 - \sqrt{\eta_1^2 - 4\zeta_1 \cdot \theta_1}}{2\zeta_1} > 1$. Thus, $\left(\sqrt{\eta_1^2 - 4\zeta_1 \cdot \theta_1} + \eta_1 + 2\zeta_1 < 0 \right) \vee (\eta_1 > 0)$. If $\zeta_1 > 0$ and $4\zeta_1 \cdot \theta_1 - \eta_1^2 = 0$, $\delta(P_1), \nu(P_1) > 0, \forall P_1 \in [0, 1]$, if and only if $\frac{-\eta_1}{2\zeta_1} < 0$ or $\frac{-\eta_1}{2\zeta_1} > 1$. Therefore, $(\eta_1 + 2\zeta_1 < 0) \vee (\eta_1 > 0)$. If $\zeta_1 > 0$ and $4\zeta_1 \cdot \theta_1 - \eta_1^2 < 0$, $\delta(P_1)$ is always positive; however, $\nu(P_1) > 0, \forall P_1 \in [0, 1]$, if and only if $\frac{-\eta_1 + \sqrt{12\zeta_1 \cdot \theta_1 - 3\eta_1^2}/3}{2\zeta_1} < 0$ or $\frac{-\eta_1 - \sqrt{12\zeta_1 \cdot \theta_1 - 3\eta_1^2}/3}{2\zeta_1} > 1$ that is equivalent to $\left(3\eta_1 + \sqrt{12\zeta_1 \cdot \theta_1 - 3\eta_1^2} + 6\zeta_1 < 0 \right) \vee \left(\eta_1 - \sqrt{\zeta_1 \cdot \theta_1} > 0 \right)$. When $\zeta_1 = 0$, $\delta(P_1) >$

0, $\forall P_1 \in [0, 1]$, if and only if $\frac{-\theta_1}{\eta_1} < 0$ or $\frac{-\theta_1}{\eta_1} > 1$. Thus, $(\eta_1 \cdot \theta_1 < -\eta_1^2) \vee (\eta_1 \cdot \theta_1 > 0)$. If $\zeta_1 < 0$ and $4\zeta_1 \cdot \theta_1 - \eta_1^2 < 0$, $\nu(P_1)$ is always positive; however, $\delta(P_1) > 0, \forall P_1 \in [0, 1]$, if and only if $\frac{-\eta_1 + \sqrt{\eta_1^2 - 4\zeta_1 \cdot \theta_1}}{2\zeta_1} < 0$ and $\frac{-\eta_1 - \sqrt{\eta_1^2 - 4\zeta_1 \cdot \theta_1}}{2\zeta_1} > 1$ that is equivalent to $\sqrt{\eta_1^2 - 4\zeta_1 \cdot \theta_1} + \eta_1 + 2\zeta_1 > 0$. Finally, If $\zeta_1 < 0$ and $4\zeta_1 \cdot \theta_1 - \eta_1^2 \geq 0$, $\delta(P_1), \nu(P_1) \leq 0, \forall P_1 \in [0, 1]$ and $\hat{c}(P_1, O, h)$ is not a convex function of $P_1, \forall P_1 \in [0, 1]$. \square

Theorem 4 states a set of additional headway settings in which highway capacity is a convex function of CAV market penetration rate. For example, based on this theorem, for independent platooning intensity ($O = 0$), if the average interfacing headway between a CAV and an HV is equal to to the geometric mean of the expected values of headways between two CAVs and two HVs ($\hat{h}_{10} = \sqrt{\bar{h}_{00}\bar{h}_{11}}$), then with the conditions in Corollary 5, highway capacity convexly increases with CAV penetration rate. Thereafter, taking these settings into consideration on top of the previous settings will further enhance the highway capacity. Note that since the convexity conditions for $O < 0$ are so complex, these conditions are provided only for $O \geq 0$, which is sufficient for practical applications because the platooning intensity rarely reaches worse than the random intensity with $O = 0$.

Now, to examine the claim that highway capacity increases with CAV platooning intensity, we present the necessary and sufficient condition in which $\hat{c}(P_1, O, h)$ is an increasing function of $O, \forall O \in [-1, 1]$.

Theorem 5. $\hat{c}(P_1, O, h)$ is an increasing function of $O, \forall O \in [-1, 1]$ if and only if $\bar{h}_{11} + \bar{h}_{00} \leq 2\hat{h}_{10}$.

Proof. Based on equations (3.4)-(3.7) and (3.9), $\hat{c}(P_1, O, h)$ can be rewritten as

$$\hat{c}(P_1, O, h) = \begin{cases} \frac{1}{\alpha P_1(1-P_1)O + \alpha P_1^2 + 2\beta P_1 + \bar{h}_{00}} & O \in [0, 1]; \\ \frac{1}{\alpha P_1^2 O + \alpha P_1^2 + 2\beta P_1 + \bar{h}_{00}}, & O \in [-1, 0), P_1 \in [0, 0.5]; \\ \frac{1}{\alpha(1-P_1)^2 O + \alpha P_1^2 + 2\beta P_1 + \bar{h}_{00}} & O \in [-1, 0), P_1 \in (0.5, 1]. \end{cases}$$

For a certain P_1 , we obtain $\frac{d\hat{c}}{dO}(P_1, O, h)$ as

$$\frac{d\hat{c}}{dO}(P_1, O, h) = \begin{cases} \frac{-\alpha P_1(1-P_1)}{(\alpha P_1(1-P_1)O + \alpha P_1^2 + 2\beta P_1 + \bar{h}_{00})^2} & O \in [0, 1]; \\ \frac{-\alpha P_1^2}{(\alpha P_1^2 O + \alpha P_1^2 + 2\beta P_1 + \bar{h}_{00})^2}, & O \in [-1, 0), P_1 \in [0, 0.5]; \\ \frac{-\alpha(1-P_1)^2}{(\alpha(1-P_1)^2 O + \alpha P_1^2 + 2\beta P_1 + \bar{h}_{00})^2} & O \in [-1, 0), P_1 \in (0.5, 1]. \end{cases}$$

Thus $\bar{h}_{11} + \bar{h}_{00} \leq 2\hat{h}_{10}$ is necessary and sufficient to $\frac{d\hat{c}}{dO}(P_1, O, h) \geq 0$ which implies that $\hat{c}(P_1, O, h)$ is an increasing function with of O . This completes the proof. \square

Theorem 5 indicates that despite the common assumption that higher CAV platooning yield greater highway capacity, in certain CAV headway settings, a higher CAV platooning intensity could reduce highway capacity. For example, for CAV technologies in which the average interfacing headway between a CAV and an HV (\hat{h}_{10}) is less than the average of headways between two CAVs and two HVs ($\frac{\bar{h}_{11} + \bar{h}_{00}}{2}$), CAV platooning intensity may not help with highway capacity.

From the above analysis, we see that these conventional assumptions that have been frequently taken for granted may not always hold in various conditions, especially under certain conservative technology scenarios. Therefore, in order to take full advantage of emerging CAV technologies, traffic planners and managers have to be fully aware of all possible impacts of different technology scenarios on mixed traffic capacity and be cautious in using these commonly accepted assumptions. These insights will be demonstrated by numerical examples in the following section.

3.3 Numerical Analyses

This section presents numerical examples to illustrate stochastic vehicle distribution patterns in the proposed Markov chain model. Thereafter, we verify the analytical theorems

Table 3.1: Headway distributions for numerical analyses in the single-lane problem.

h_{11}	h_{10}	h_{01}	h_{00}
$Uniform(0.6, 1.1)$	$Uniform(0.8, 2.2)$	$Uniform(0.7, 1.5)$	$Uniform(0.8, 2.2)$

presented in Section 3.2.1, and show the accuracy of the approximate capacity formulation. Finally, we show the impacts of CAV penetration rate and platooning intensity changes on mixed traffic capacity, which also verify the presented theorems in Section 3.2.2. To perform these numerical analyses, we define a set of default headway distributions in Table 3.1. For simplicity, the numerical studies only consider uniform distributions where $Uniform(a, b)$ denotes a uniform distribution with lower bound a and upper bound b and the parameter values are extracted from the comprehensive literature review (see Table 2.1). Note that in general the proposed methods can be applied to other general distribution patterns in the same way.

Fig. 3.3 shows a number of simulation results to illustrate stochastic vehicle spatial distributions for different platooning intensities. All h_{sr} values are stochastically distributed, $\forall sr \in S^E$. The maximum platooning intensity ($O = 1$) is illustrated in Fig. 3.3(a) and 3.3(b). With Equation (3.8), $\pi^E = [P_1, 0, 0, 1 - P_1]$, and thus at this intensity, in each simulation scenario, the first vehicle has a probability of $1 - P_1$ to be an HV (Fig. 3.3(a)) and a probability of P_1 to be a CAV (Fig. 3.3(b)), and all following vehicles are of the same type as the first vehicle. Fig. 3.3(c) and 3.3(d) show examples for the independent platooning intensity ($O = 0$) for $P_1 = 0.5$ and $P_1 = 0.75$, respectively. We see that CAVs and HVs are randomly distributed. Note that based on Theorem 2, the CAV percentage converges to P_1 as $N \rightarrow \infty$. Fig. 3.3(e) and 3.3(f) illustrate examples for the minimum platooning intensity ($O = -1$) for $P_1 = 0.5$ and $P_1 = 0.75$, respectively. We see that at this platooning intensity, the vehicle spatial distribution at $P_1 = 0.5$ yields a strict CAV-to-HV alternating pattern (Fig. 3.3(e)) that has the maximum segregation between CAVs and HVs. If P_1 is not equal to 0.5, due to the asymmetry of CAV and HV numbers, the spatial distribution does not exhibit the

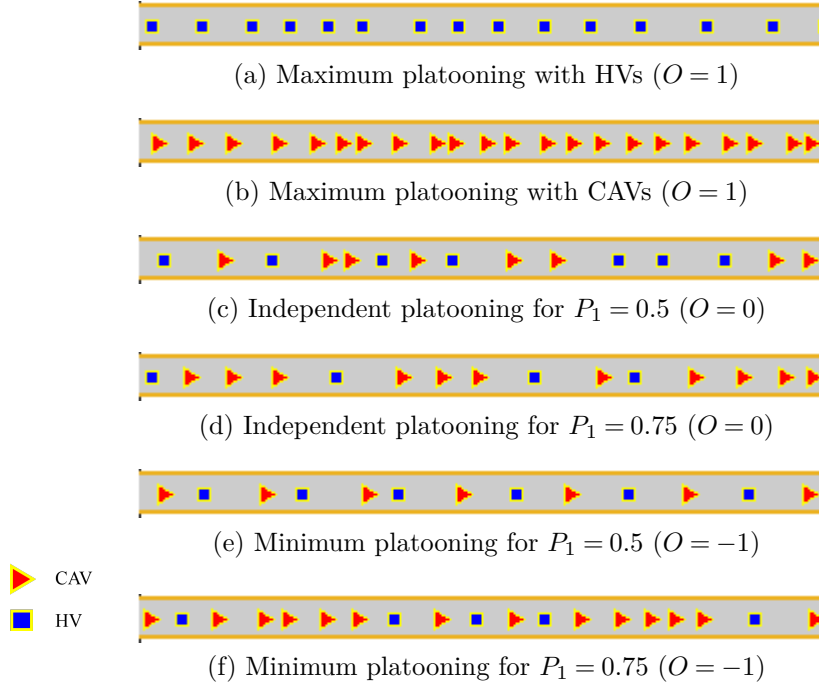


Figure 3.3: Illustrative examples for different platooning intensities

perfect CAV-to-HV alternating pattern, but it as well yields the maximum possible segregation between CAVs and HVs (Fig. 3.3(f)). These examples demonstrates the capability of the proposed Markov chain model in describing stochastic headway distributions across the full spectrum of platooning intensities in realistic mixed traffic.

Next, we verify the analytical theorems in Section 3.2.1 and test the accuracy of the proposed approximate capacity model with numerical instances. We perform numerical instances with various N values. To compare $\hat{c}(P_1, O, h)$ with \bar{c} , we define a capacity error measure as $\varepsilon := \frac{\hat{c} - \bar{c}}{\bar{c}} \times 100$ (%), and calculate it for different N values. To approximate \bar{c} values for a certain N , we run $Markov(\pi^E, T^E)$ 1000 times, and set \bar{c} equal to the average of the observed capacities. In this analysis, we set $P_1 = 0.5$ and $O = 0$. Fig. 3.4 shows ε values for different N values. The results indicate that for all N values, $\varepsilon \leq 0$ and thus $\hat{c}(P_1, O, h) \leq \bar{c}$, which verifies Theorem 1. Further, we see as N increases, $\varepsilon \rightarrow 0$, and thus $\hat{c}(P_1, O, h) \rightarrow \bar{c}$, which verifies Theorem 2. Actually, note that even with very low N values (e.g., around

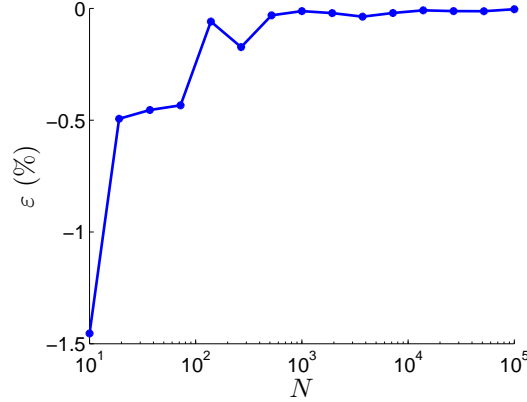


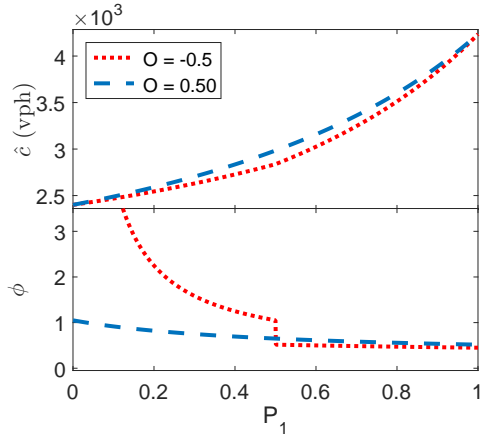
Figure 3.4: ε for different N values.

10), $|\varepsilon|$ does not even exceed 1.5%, which means across all realistic N values, approximate capacity $\hat{c}(P_1, O, h)$ is no more than a couple of percent from ground truth capacity \bar{c} that is otherwise hard to quantify. Therefore, this test confirms that the approximate capacity is accurate and suitable for engineering practices.

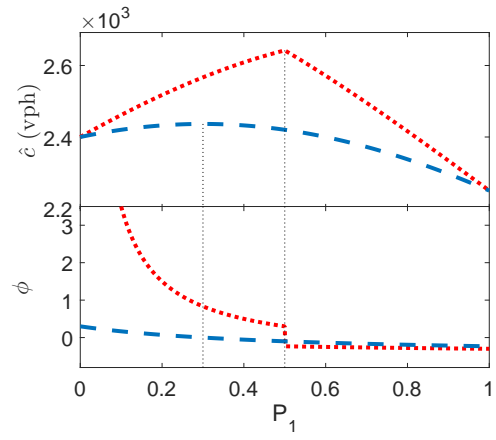
Now we test the impacts of CAV penetration rate and platooning intensity on highway capacity. Theorem 3 provides the necessary and sufficient conditions on which $\hat{c}(P_1, O, h)$ is increasing at $P_1, \forall P_1 \in (0, 1]$. The numerical results are shown in Fig. 3.5. In each sub-figure, the upper and lower half figures show how $\hat{c}(P_1, O, h)$ changes with P_1 and the corresponding $\phi(P_1, O, h)$, respectively. The analyses are performed for $O = -0.5$ and $O = 0.5$ as representative negative and positive O values, respectively. Fig. 3.5(a) shows the results for the default headways defined in Table 3.1. This headway setting yields $h = [0.85, 1.50, 1.10, 1.50]$, which leads to $\phi(P_1, O, h) > 0, \forall P_1 \in (0, 1]$ for $O \in \{-0.5, 0.5\}$. Then Theorem 3 indicates that $\hat{c}(P_1, O, h)$ is an increasing function of P_1 over $P_1 \in (0, 1]$ for $O \in \{-0.5, 0.5\}$, which is consistent with the results in Fig. 3.5(a). To verify this theorem for other CAV technology scenarios, we change h vector elements as shown in each sub-figure. For example, in Fig. 3.5(b), we set $\bar{h}_{11} = 1.60$ seconds while keeping the remaining headways at their default values (i.e., $h = [1.60, 1.50, 1.10, 1.50]$). The results indicate that

$\hat{c}(P_1, O, h)$ changes corresponds to $\phi(P_1, O, h)$ signs, i.e., if $\phi(P_1, O, h) > 0$, then $\hat{c}(P_1, O, h)$ is increasing at P_1 , and if $\phi(P_1, O, h) < 0$, then $\hat{c}(P_1, O, h)$ is decreasing at $P_1, \forall P_1 \in (0, 1]$. Note that in Fig. 3.5(a)- 3.5(c), $\bar{h}_{00} \geq \hat{h}_{10}$, and $\phi(P_1, O, h)$ is a decreasing function of P_1 . Thus, if $\phi(P_1 = \mathbf{p}) = 0$ for some $\mathbf{p} \in (0, 1]$, then $\hat{c}(P_1, O, h)$ is an increasing function over $P_1 \in (0, \mathbf{p}]$ and a decreasing function over $P_1 \in [\mathbf{p}, 1]$. On the other hand, in Fig. 3.5(d)- 3.5(f), since $\bar{h}_{00} < \hat{h}_{10}$, $\phi(P_1, O, h)$ is an increasing function of P_1 . Thus, if $\phi(P_1 = \mathbf{p}) = 0$ for some $\mathbf{p} \in (0, 1]$, then $\hat{c}(P_1, O, h)$ is a decreasing function over $P_1 \in (0, \mathbf{p}]$ and an increasing function over $P_1 \in [\mathbf{p}, 1]$. These numerical analyses reveal that the common assumption that highway capacity always increases with CAV market penetration rate is not necessarily true, but rather, it depends on CAV technologies. If CAV technologies are aggressive (e.g., as the default parameters in Fig. 3.5(a) specifies), CAV market penetration rate helps with highway capacity. Otherwise, capacity may decrease at some market penetration rate values, or even always decreases at any market penetration rate (see Fig. 3.5(f)).

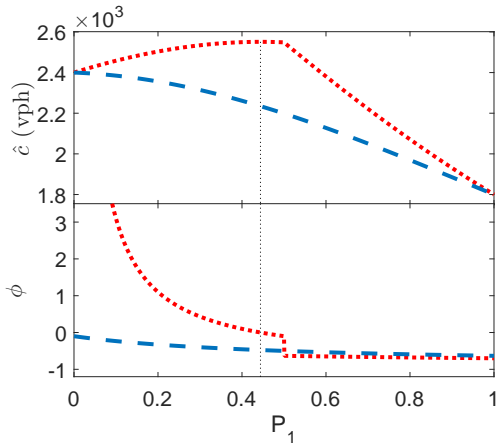
Next, we show how highway capacity is affected by different CAV platooning intensities. Theorem 5 provides the necessary and sufficient condition on which $\hat{c}(P_1, O, h)$ is an increasing function of $O, \forall O \in [-1, 1]$. In addition to the presented analytical theorem, we provide numerical examples with two cases as shown in Fig. 3.6 to test this condition. In these examples, we set $P_1 = 0.5$ for both cases. In the first case with the default headways, since $\bar{h}_{11} + \bar{h}_{00} < 2\hat{h}_{10}$, $\hat{c}(P_1, O, h)$ is an increasing function of O over $O \in [-1, 1]$. In the second case, we set $\bar{h}_{11} = 1.30$ seconds while keeping the remaining headways at their default values. Therefore, $\bar{h}_{11} + \bar{h}_{00} > 2\hat{h}_{10}$, and \hat{c} is a decreasing function of O over $O \in [-1, 1]$. These examples, besides the analytical theorem, show that the usual assumption that highway capacity always increases with CAV platooning intensity is not necessarily true; rather, it depends on CAV technologies.



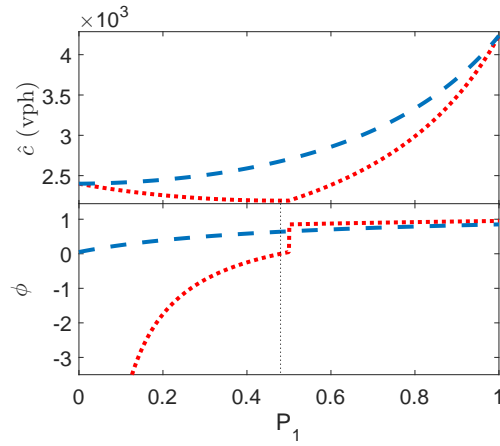
(a) Default headways



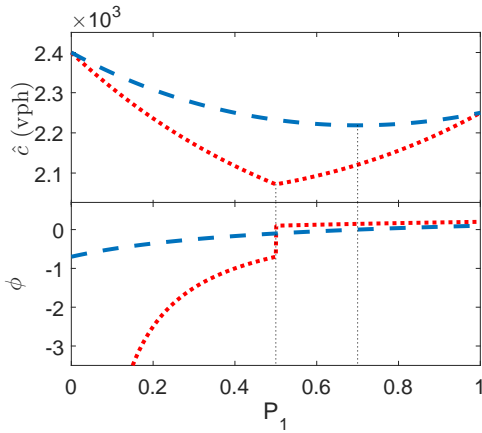
(b) $\bar{h}_{11} = 1.60$ s



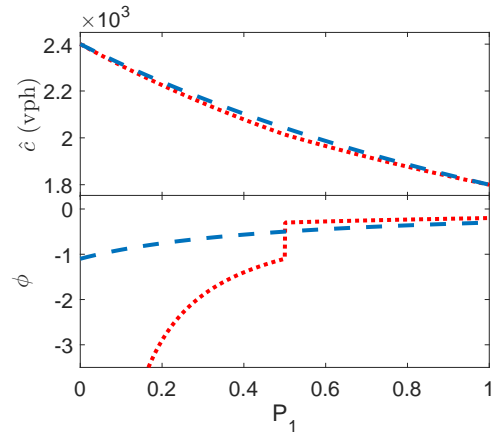
(c) $\bar{h}_{11} = 2.00$ s



(d) $\hat{h}_{10} = 1.80$ s



(e) $\hat{h}_{10} = 1.80$ s, $\bar{h}_{11} = 1.60$ s



(f) $\hat{h}_{10} = 1.80$ s, $\bar{h}_{11} = 2.00$ s

Figure 3.5: Numerical examples to test how $\hat{c}(P_1, O, h)$ changes with P_1 .

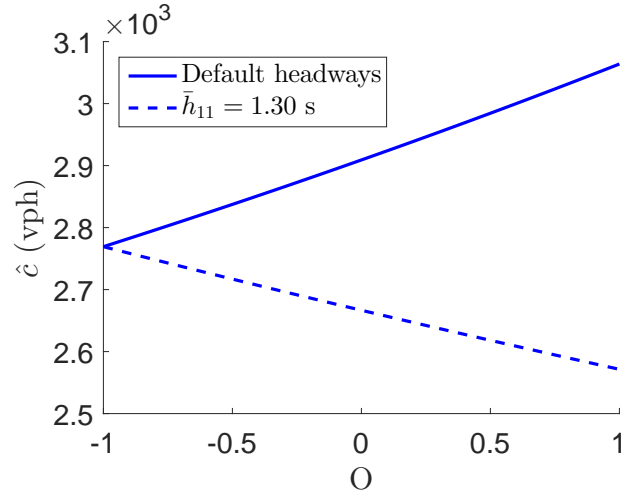


Figure 3.6: Numerical examples to test how $\hat{c}(P_1, O, h)$ changes with O i) default headways ii) $\bar{h}_{11} = 1.30$ s.

3.4 Chapter Summary

This chapter proposes an analytical stochastic formulation for mixed traffic highway capacity as a function of three critical factors: CAV penetration rate, CAV platooning intensity, and mixed traffic headway settings. We first conduct a review of the literature on headway distributions for mixed and pure CAV traffic (see Section 2.1), and the outcomes are used in the numerical analyses in which we evaluate hypothetical CAV technology scenarios with different headway distributions. We propose a Markov chain model to analytically formulate mixed traffic capacity under stochastic and heterogeneous headway settings across the full spectra of CAV market penetration rates and platooning intensities in mixed traffic. Both theoretical and numerical analyses show that the proposed Markov chain model can efficiently and accurately quantify mixed traffic capacity. Moreover, our analytical analyses reveal that contrary to the ubiquitous assumption that higher CAV penetration rates and platooning intensities always yield greater mixed traffic capacity, these two factors may not always help improve highway capacity. Therefore, as CAV market penetration rate (Bansal and Kockelman, 2017; Chen et al., 2016; Lavasani et al., 2016) and platooning intensity

increase in the future, traffic operators have to be aware of possible impacts of different CAV technologies on capacity.

CHAPTER 4: TRAJECTORY OPTIMIZATION¹

This chapter proposes a simplified trajectory optimization model that can address the challenges in the existing trajectory optimization models. The proposed trajectory optimization model is described as follows.

4.1 Problem Statement

4.1.1 Original Formulation

This study investigates the far-future scenario where all vehicles are controllable CAVs. Figure 4.1 illustrates the studied problem. Consider a one-lane highway segment starting at location 0 upstream and ending at location L downstream. A number of N CAVs, indexed as $n \in \mathcal{N} = \{1, 2, \dots, N\}$, consecutively arrive at location 0, drive through the segment and exit this segment at location L . This problem assumes that with advanced information system, vehicle n 's arrival time at location 0 can be accurately estimated as t_n^- . Without much loss of generality, we assume that each vehicle arrives at a maximum cruising speed \bar{v} for the maximum system throughput². This problem also assumes that the traffic control protocol is given, and vehicle n 's departure at location L is scheduled at time t_n^+

¹This chapter is submitted for publication: Li, X., Ghiasi, A., Xu, Z., Qu, X., 2018. A piecewise trajectory optimization model for connected automated vehicles: exact optimization algorithm and queue propagation analysis.

²The problem in Zhou et al. (2017) allows vehicles to arrive at different speeds, which however only affects the initial part of the trajectories but does not change much overall trajectory patterns. Further, when all vehicles are CAVs, arrival vehicles at this segment shall be departure vehicles from the upstream segments, and the proposed control shall ensure that all vehicles exit from the upstream segments at speed \bar{v} , which is equivalent to arrival speed \bar{v} at this segment.

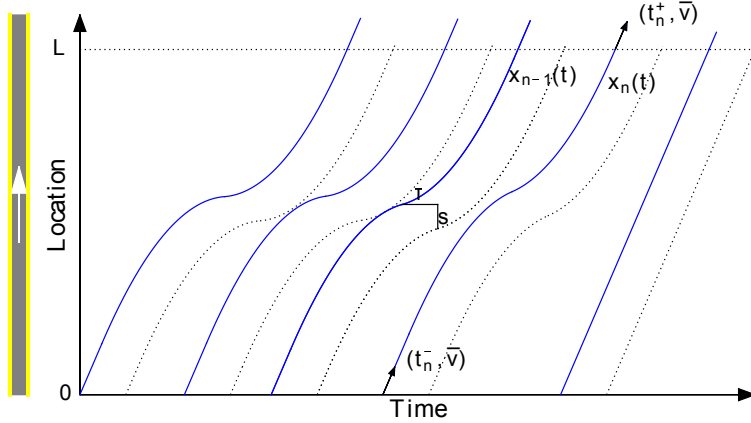


Figure 4.1: Illustration of the constraints.

in advance³. One example is that the CAV traffic control protocol is a fixed-timing traffic signal, and every vehicle is scheduled to depart as early as possible, which yields a fixed departure time for each vehicle. Another example is the first-in-first-out control policy at a non-stop intersection (or a merge point), and each vehicle’s departure time is essentially determined by the arrival times of all vehicles that have already arrived. To achieve the maximum system throughput, as discussed in Zhou et al. (2017), we postulate that each vehicle departs the segment at speed \bar{v} . We use $x_n(t), \forall t \in [t_n^-, t_n^+]$ to denote the trajectory of vehicle n , i.e., the location of vehicle n at every time point t . Define trajectory vector $\mathbf{x} = [x_n]_{n \in \mathcal{N}}$, which shall satisfy the following constraints.

- Entry boundary constraints: Vehicle n is cruising at speed \bar{v} at location 0 at time t_n^- , i.e.,

$$x_n(t_n^-) = 0, \forall n \in \mathcal{N}, \tag{4.1}$$

$$\dot{x}_n(t_n^-) = \bar{v}, \forall n \in \mathcal{N}, \tag{4.2}$$

³Note that the problem in Ma et al. (2017) does not fix a vehicle’s exit time t_n^+ but rather lets the optimization result determine it. Nonetheless, the numerical experiments in Ma et al. (2017) show that exit time t_n^+ does not change much from the theoretical minimum value in the optimal results. Thus fixing the exit times will not much affect the generality of CAV trajectory optimization at the highway segment level.

- Exit boundary constraints: Based on the CAV control protocol, each vehicle n shall exit location L at cruising speed \bar{v} at a predetermined time t_n^+ , i.e.,

$$x_n(t_n^+) = L, \forall n \in \mathcal{N}, \quad (4.3)$$

$$\dot{x}_n(t_n^+) = \bar{v}, \forall n \in \mathcal{N}. \quad (4.4)$$

- Speed constraints: Vehicle n cannot back up any time and cannot go beyond cruising speed \bar{v} , i.e.,

$$0 \leq \dot{x}_n(t) \leq \bar{v}, \forall t \in [t_n^-, t_n^+], n \in \mathcal{N}. \quad (4.5)$$

- Acceleration constraints: Vehicle n 's acceleration is bounded between minimum acceleration (or maximum deceleration) $\underline{a} < 0$ and maximum acceleration $\bar{a} > 0$, i.e.,

$$\underline{a} \leq \ddot{x}_n(t) \leq \bar{a}, \forall t \in [t_n^-, t_n^+], n \in \mathcal{N}. \quad (4.6)$$

We require $\ddot{x}_n(t)$ to be a piecewise second-order differentiable function. At a joint between two pieces, $\ddot{x}_n(t)$ is defined as the left differential.

- Safety constraints: For every two consecutive vehicles $n-1$ and n , their trajectories have to maintain certain safety headway to ensure

$$x_{n-1}(t - \tau) - x_n(t) = s, \forall t \in [t_{n-1}^- + \tau, t_n^+], \forall n \in \mathcal{N} \setminus \{1\}, \quad (4.7)$$

where τ is the minimum time headway and s is the minimum space headway. The value of τ depends on CAV communication and control delay, and the value of s depends on the CAV size and the reserved safety buffer.

Each trajectory x_n is associated with an operational cost, formulated as the cost function below

$$c(x_n) := \int_{t_n^-}^{t_n^+} e(\dot{x}_n(t), \ddot{x}_n(t)) dt, \forall n \in \mathcal{N} \quad (4.8)$$

where function $e(\dot{x}_n(t), \ddot{x}_n(t))$ measures the instantaneous cost of x_n at time point t . This study considers a general class of e functions as follows,

$$e(\dot{x}, \ddot{x}) = \sum_{p=1}^P A_p |\ddot{x}|^p + \sum_{q=1}^Q B_q \dot{x}^q + \sum_{r=-\infty}^{\infty} C_r \dot{x}^r \ddot{x}, \quad (4.9)$$

where power index P can be any positive integer, $Q \in \{1, 2, 3, 4\}$ and all coefficients $A_p, B_q, C_r \geq 0$. The reason we use this function form as the optimization objective is two-fold. First, it is a closed-form function suitable for analytical studies. More importantly, several commonly used instantaneous vehicle performance measures can be written as special forms of this function. For example, one special case is vehicle specific power (Frey et al., 2002), which is approximately proportional to vehicle fuel consumption and positively correlated with emissions, i.e.,

$$e^{\text{VSP}}(\dot{x}, \ddot{x}) = \xi \dot{x} \ddot{x} + \psi \dot{x} + \zeta \dot{x}^3. \quad (4.10)$$

where ξ, ψ and ζ are positive coefficients. Another special case is squared acceleration (Smith et al., 1978), which has been frequently used to indicate driving comfort, i.e.,

$$e^{\text{SA}}(\dot{x}, \ddot{x}) = \ddot{x}^2. \quad (4.11)$$

With formula (4.9), vehicle cost (4.8) can be rewritten as

$$c(x_n) = \sum_{p=1}^P A_p \int_{t_n^-}^{t_n^+} |\ddot{x}_n(t)|^p dt + \sum_{q=1}^Q B_q \int_{t_n^-}^{t_n^+} \dot{x}_n(t)^q dt. \quad (4.12)$$

Note that the third item is dropped because $\int_{t_n^-}^{t_n^+} \dot{x}_n(t)^r \ddot{x}_n(t) dt = \frac{1}{r+1} \dot{x}_n(t)^{r+1} \Big|_{t_n^-}^{t_n^+}$ is always equal to zero for any $r \in \mathbb{R}$ since $\dot{x}_n(t_n^-) = \dot{x}_n(t_n^+) = \bar{v}$. Then the system performance is measured by the average cost per vehicle

$$C(\mathbf{x}) := \sum_{n \in \mathcal{N}} c(x_n)/N.$$

Now the primary trajectory optimization problem can be formulated as follows,

$$\text{PTO} : \min_{\mathbf{x}} C(\mathbf{x}) \tag{4.13}$$

subject to Constraints (4.1)—(4.7).

In order for problem PTO to be feasible, parameters should satisfy the following conditions. Since vehicles shall satisfy safety constraints (4.7), then $\{t_n^-\}$ values shall satisfy

$$t_n^- - t_{n-1}^- \geq \tau + s/\bar{v}, \forall n \in \mathcal{N} \setminus \{1\}. \tag{4.14}$$

Since vehicles can only exit the highway segment consequentially, safety constraints (4.7) imply that $\{t_n^+\}$ should satisfy a similar relationship,

$$t_n^+ - t_{n-1}^+ \geq \tau + s/\bar{v}, \forall n \in \mathcal{N} \setminus \{1\}. \tag{4.15}$$

Further, since vehicles only have a limited speed \bar{v} , the following constraints shall be satisfied

$$t_n^+ - t_n^- \geq L/\bar{v}, \forall n \in \mathcal{N}. \tag{4.16}$$

4.1.2 Simplified Model Formulation

It is difficult to solve PTO to the exact optimal due to infinite-dimensional variables, highly nonlinear objective and vehicle dependency in the constraints. By adapting the simplification approach in Ma et al. (2017), instead of directly analyzing PTO, this study formulates a simplified model that restricts each trajectory to consist of no more than five quadratic segments and trajectories in each platoon (platoon will be defined in the next paragraph) have identical acceleration and deceleration magnitudes. Although this restriction may slightly sacrifice the solution optimality since it reduces the feasible region of the trajectories, we believe that the restricted solution shall be close to the true optimum for the following two reasons. First, since a realistic vehicle cost function (4.12) shall be optimal with a smooth vehicle trajectory that does not frequently decelerate and accelerate, using piecewise quadratic approximation shall not bring too much error to the optimal trajectory shape. Second, since these vehicles closely follow each other in a platoon, they optimal trajectories shall have similar acceleration and deceleration levels, and thus assuming them sharing identical acceleration and deceleration magnitudes will not much compromise the optimality. While it is interesting to verify this conjecture with theoretical analysis and numerical experiments, it is beyond the scope of this study. This study will focus on formulating, analyzing and testing this simplified model, and this section will present the formulation of this model.

First, we want to note that safety constraints (4.7) will not be activated for two consecutive vehicles n and $n + 1$ if vehicle n 's departure time is not much later than vehicle $n + 1$'s arrival time, i.e.,

$$t_n^+ + \tau + s/\bar{v} \leq t_{n+1}^- + L/\bar{v}.$$

If this inequality holds, the optimization problem can be decomposed into two sub-problems, one for vehicles up to n and the other for vehicles from $n + 1$ on. Such decomposition can be repeated for other vehicles satisfying this condition. Eventually, vehicles will be decomposed

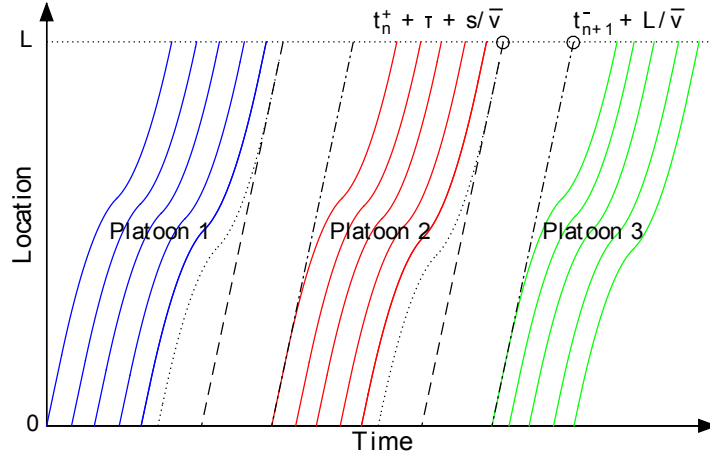


Figure 4.2: Illustration of platoon decomposition.

into a number of platoons such that only two vehicles in the same platoon can possibly activate safety constraints (4.7). This is illustrated in Figure 4.2. Vehicle platoons can be identified by the following platooning algorithm (PA).

- PA-0: Set platoon collection $\mathbb{M} = \emptyset$. Set current vehicle $n = 1$, and initialize current platoon vector $\mathcal{M} = [1]$.
- PA-1: Check whether $t_n^+ + \tau + s/\bar{v} > t_{n+1}^- + L/\bar{v}$ holds. If yes, then vehicles n and $n+1$ belong to the same platoon, append $n+1$ to the end of \mathcal{M} . Otherwise, vehicles n and $n+1$ shall be in different platoons, and then add \mathcal{M} to \mathbb{M} and start a new platoon $\mathcal{M} = [n+1]$;
- PA-2: If $n = N$, add \mathcal{M} to \mathbb{M} and end the algorithm. Otherwise, set $n = n+1$, got to Step PA-1.

With this, we can decompose the trajectory optimization into a set of subproblems, each for one platoon separately. Then the following analysis only focuses on the optimization of a generic non-trivial platoon (i.e., having two or more trajectories), for which we index vehicles with $\mathcal{M} = \{1, 2, \dots, M\}$ without lose of generality.

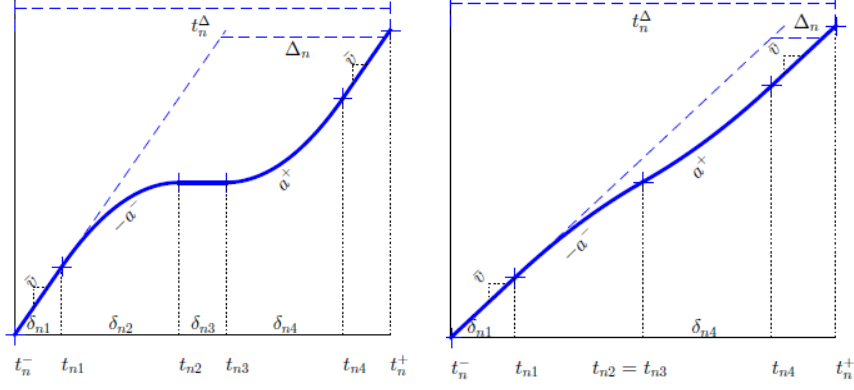


Figure 4.3: Illustration of the piece-wise quadratic form of trajectory x_n (a) with a stop section and (b) without a stop section.

The remainder of this section presents the simplified trajectory optimization model (STO) for vehicles in \mathcal{M} . Basically, STO restricts that each trajectory x_n has at most 5 consecutive quadratic sections, as illustrated in Figure 4.3. Each section is with acceleration $-a^- \in [a, 0]$, 0 or $a^+ \in [0, \bar{a}]$ where a^- and a^+ are the acceleration variables that determine the overall smoothness of the whole platoon. Let $t_{n1} \leq t_{n2} \leq t_{n3} \leq t_{n4} \in [t_n^-, t_n^+]$ denote the joint time points between these sections. The first section of x_n during time interval $[t_n^-, t_{n1}]$ cruises at speed \bar{v} . The second section during time interval $(t_{n1}, t_{n2}]$ decelerates at a constant deceleration rate of $-a^-$. Note that the third section during time interval $(t_{n2}, t_{n3}]$ exists (i.e. $t_{n2} < t_{n3}$) only if x_n has to make a stop from time t_{n2} to t_{n3} (as illustrated in Figure 4.3(a)). Otherwise, $t_{n2} = t_{n3}$, $\dot{x}_n(t) > 0, \forall t \in [t_n^-, t_n^+]$, and this third section does not exist (as illustrated in Figure 4.3(b)). The fourth section during time $(t_{n3}, t_{n4}]$ accelerates at a constant acceleration rate of a^+ . Note that these three intermediate sections form a reversed “S-shaped” transitional part that fits trajectory $x_n(t)$ for arrival time t_n^- and exit time t_n^+ . Then the fifth section during time $(t_{n4}, t_n^+]$ cruises at speed \bar{v} and reaches exit location L at exit time t_n^+ .

Note that trajectory x_n in this piecewise quadratic form is determined by three variables, i.e., initial cruising time $\delta_{n1} := t_{n1} - t_n^-$ and deceleration magnitude a^- and acceleration

magnitude a^+ . Given these variables, each trajectory x_n can be formulated in the following way. For mathematical convenience, define $\Delta_n := t_n^+ - t_n^- - L/\bar{v}$ (note that Δ_n has to be positive or otherwise vehicle n itself is a trivial platoon), and $t_n^\Delta = t_n^+ - t_n^-$, as illustrated in Figure 4.3. Note that t_n^Δ is the travel time for vehicle n on this segment, and Δ_n can be interpreted as the corresponding travel delay. Instead of investigating the two acceleration variables directly, we investigate two auxiliary variables $\phi := \frac{a^- a^+}{a^- + a^+}$ and $\lambda := a^- / (a^- + a^+)$, because these auxiliary variables much simplify the following formulations (which will be explained in a later remark). Although the physical meanings of these two auxiliary variables are not as intuitive, one can simply consider ϕ as an indication of the overall acceleration/deceleration magnitude, and λ as a weight of deceleration magnitude. Since $a^- \in [0, -\underline{a}]$ and $a^+ \in [0, \bar{a}]$, then ϕ and λ shall fall in the following ranges: $\phi \in [0, \bar{\phi}]$ where $\bar{\phi} := \frac{-a\bar{a}}{a-\bar{a}}$ and $\lambda \in [\frac{\phi}{\bar{a}}, 1 + \frac{\phi}{\underline{a}}]$. Note that for given values of (ϕ, λ) except for trivial singular points where $\lambda = 0$ or 1 , the corresponding acceleration values can be obtained uniquely as $a^- = \phi / (1 - \lambda)$ and $a^+ = \phi / \lambda$. With this, we can formulate the time joints with variables $\{\delta_{n1}\}, a^-, a^+$ as follows,

$$t_{n1} = t_n^- + \delta_{n1}, \quad (4.17)$$

$$t_{ni} = t_{n(i-1)} + \delta_{ni}(\phi, \lambda), \forall i = 2, 3, 4 \quad (4.18)$$

where

$$\delta_{n2}(\phi, \lambda) = \begin{cases} \sqrt{\frac{2\bar{v}\Delta_n}{\phi}}(1 - \lambda), & \text{if } \phi \leq \frac{\bar{v}}{2\Delta_n}; \\ \frac{\bar{v}(1-\lambda)}{\phi}, & \text{otherwise,} \end{cases}$$

$$\delta_{n3}(\phi) = \begin{cases} 0, & \text{if } \phi \leq \frac{\bar{v}}{2\Delta_n}; \\ \Delta_n - \frac{\bar{v}}{2\phi}, & \text{otherwise,} \end{cases}$$

and

$$\delta_{n4}(\phi, \lambda) = \begin{cases} \sqrt{\frac{2\bar{v}\Delta_n}{\phi}}\lambda, & \text{if } \phi \leq \frac{\bar{v}}{2\Delta_n}; \\ \frac{\bar{v}\lambda}{\phi}, & \text{otherwise.} \end{cases}$$

Then we obtain the time duration for the transitional part as,

$$\delta(\phi, \Delta_n) := \sum_{i=2}^4 \delta_{ni}(\phi, \lambda) = \begin{cases} \sqrt{\frac{2\bar{v}\Delta_n}{\phi}}, & \text{if } \phi \leq \frac{\bar{v}}{2\Delta_n}; \\ \Delta_n + \frac{\bar{v}}{2\phi}, & \text{otherwise.} \end{cases}$$

Note that function $\delta(\phi, \Delta_n)$ is differentiable with respect to ϕ and Δ_n ; i.e.,

$$\frac{d\delta(\phi, \Delta_n)}{d\phi} = \max \left\{ -\sqrt{\frac{\bar{v}\Delta_n}{2}}\phi^{-1.5}, -\frac{\bar{v}}{2}\phi^{-2} \right\}$$

which is negative, increasing with ϕ and decreasing with Δ_n , and

$$\frac{d\delta(\phi, \Delta_n)}{d\Delta_n} = \max \left\{ \sqrt{\frac{\bar{v}}{2\phi\Delta_n}}, 1 \right\}$$

which is positive and decreasing with Δ_n and ϕ . These results also suggest that $\delta(\phi, \Delta_n)$ decreases with ϕ and increases with Δ_n .

Note that time duration $\delta(\phi, \Delta_n)$ is essentially determined by variable ϕ but independent of λ . Thus the effects of variables ϕ and λ on the shape of x_n are separated: ϕ decreases with the duration of the transitional part, and λ affects the skewness of the transitional part between acceleration and deceleration. This separation, which cannot be achieved by original variables a^- and a^+ , much facilitates the following analysis. This is the reason why we use auxiliary variables ϕ and λ instead of original variables a^- and a^+ .

Now the corresponding acceleration function can be formulated as

$$\ddot{x}_n(t) = \begin{cases} 0, & \text{if } t \in [t_n^-, t_{n1}]; \\ -\frac{\phi}{1-\lambda}, & \text{if } t \in (t_{n1}, t_{n2}]; \\ 0, & \text{if } t \in (t_{n2}, t_{n3}]; \\ \frac{\phi}{\lambda}, & \text{if } t \in (t_{n3}, t_{n4}]; \\ 0, & \text{if } t \in (t_{n4}, t_n^+]. \end{cases} \quad (4.19)$$

The corresponding speed function is

$$\dot{x}_n(t) = \begin{cases} \bar{v}, & \text{if } t \in [t_n^-, t_{n1}]; \\ \bar{v} - \frac{\phi}{1-\lambda}(t - t_{n1}) & \text{if } t \in (t_{n1}, t_{n2}]; \\ 0 & \text{if } t \in (t_{n2}, t_{n3}]; \\ \bar{v} + \frac{\phi}{\lambda}(t - t_{n4}), & \text{if } t \in (t_{n3}, t_{n4}]; \\ \bar{v}, & \text{if } t \in (t_{n4}, t_n^+]. \end{cases} \quad (4.20)$$

The corresponding location function is

$$x_n(t) = \begin{cases} \bar{v}(t - t_n^-), & \text{if } t \in [t_n^-, t_{n1}]; \\ \bar{v}(t - t_n^-) - 0.5\frac{\phi}{1-\lambda}(t - t_{n1})^2 & \text{if } t \in (t_{n1}, t_{n2}]; \\ \bar{v}(t_{n2} - t_n^-) - 0.5\frac{\phi}{1-\lambda}\delta_{n2}^2(\phi, \lambda) & \text{if } t \in (t_{n2}, t_{n3}]; \\ \bar{v}(t - t_{n3} + t_{n2} - t_n^-) - 0.5\frac{\phi}{1-\lambda}\delta_{n2}^2(\phi, \lambda) - 0.5\frac{\phi}{\lambda}(t - t_{n4})^2, & \text{if } t \in (t_{n3}, t_{n4}]; \\ \bar{v}(t - t_{n3} + t_{n2} - t_n^-) - 0.5\lambda\frac{\phi}{1-\lambda}\delta_{n2}^2(\phi, \lambda) - 0.5\frac{\phi}{\lambda}\delta_{n4}^2(\phi, \lambda), & \text{if } t \in (t_{n4}, t_n^+]. \end{cases} \quad (4.21)$$

With this simplification, cost function (4.12) can be rewritten into a closed-form expression without integrals as follows,

$$\bar{c}_n(\phi, \lambda) = \sum_{p=1}^P A_p F_n^A(\phi, \lambda, p) + \sum_{q=1}^Q B_q F_n^V(\phi, q) \quad (4.22)$$

where

$$F_n^A(\phi, \lambda, p) := \int_{t_n^-}^{t_n^+} |\ddot{x}_n(t)|^p dt = \min \left(\sqrt{2\bar{v}\Delta_n\phi}, \bar{v} \right) \cdot (\lambda^{1-p} + (1-\lambda)^{1-p}) \phi^{p-1} \quad (4.23)$$

and

$$F_n^V(\phi, q) := \int_{t_n^-}^{t_n^+} \dot{x}_n^q(t) dt = L\bar{v}^{q-1} - \begin{cases} (q-1)\Delta_n\bar{v}^q + \frac{\bar{v}^{q+1}}{q+1} \sum_{i=3}^{q+1} \binom{q+1}{i} \left(-\sqrt{\frac{2\Delta_n}{\bar{v}}} \right)^i \phi^{i/2-1}, & \text{if } \phi \leq \frac{\bar{v}}{2\Delta_n}; \\ \left(\frac{1}{2} - \frac{1}{q+1} \right) \bar{v}^q \frac{1}{\phi}, & \text{otherwise.} \end{cases} \quad (4.24)$$

Note that after this simplification, cost function c_n is only dependent on ϕ and λ but independent of $\{\delta_{n1}\}$.

Next, we investigate how to simplify the corresponding constraints. We denote the five sections of x_n in the following form: initial cruising section $x_n(t_n^- : t_{n1})$, deceleration section $x_n(t_{n1} : t_{n4})$, stopping section $x_n(t_{n2} : t_{n3})$, accelerating section $x_n(t_{n3} : t_{n4})$, and final cruising section $x_n(t_{n4} : t_n^+)$ (where operator $:$ separates the starting and ending time of a trajectory section). The length of initial cruising section is simply

$$|x_n(t_n^- : t_{n1})| = \bar{v}\delta_{n1}.$$

Length $|x_n(t_{n1} : t_{n4})|$ is a function ϕ and Δ_n as follows,

$$|x_n(t_{n1} : t_{n4})| = \begin{cases} \bar{v} \left(\frac{\sqrt{2\bar{v}\Delta_n}}{\sqrt{\phi}} - \Delta_n \right), & \text{if } \phi \leq \frac{\bar{v}}{2\Delta_n}; \\ \frac{\bar{v}^2}{2\phi}, & \text{otherwise.} \end{cases}$$

Length $|x_n(t_{n4} : t_{n5})|$ is also a function of ϕ as follows,

$$|x_n(t_{n4} : t_{n5})| = L - \bar{v} \left(\delta_{n1} + \begin{cases} \frac{\sqrt{2\bar{v}\Delta_n}}{\sqrt{\phi}} - \Delta_n, & \text{if } \phi \leq \frac{\bar{v}}{2\Delta_n}; \\ \frac{\bar{v}^2}{2\phi}, & \text{otherwise.} \end{cases} \right)$$

In order for x_n to satisfy constraints (4.1)-(4.6), we actually only need to impose

$$|x_n(t_n^- : t_{n1})|, |x_n(t_{n4} : t_{n5})| \geq 0, \text{ i.e.,}$$

$$0 \leq \delta_{n1} \leq \tilde{\delta}_{n1}(\phi) := t_n^\Delta - \delta(\phi, \Delta_n). \quad (4.25)$$

Note that in order for $\tilde{\delta}_{n1}(\phi)$ to be no greater than 0 for all n , the value of ϕ should satisfy

$$\phi \geq \underline{\phi} := \begin{cases} \max_{n \in \mathcal{M}} \frac{2\bar{v}\Delta_n}{(L/\bar{v} + \Delta_n)^2}, & \text{if } \Delta_n \leq \frac{2L}{\bar{v}}; \\ \frac{\bar{v}^2}{2L}, & \text{otherwise.} \end{cases} \quad (4.26)$$

where $\underline{\phi}$ can be taken as a lower bound for ϕ , which is tighter than 0.

Now we discuss how to select variables $a^-, a^+, \{\delta_{n1}\}_{\forall n}$ to comply with safety constraints (4.7). Define a shadow trajectory of $x_n(t)$ as

$$x_n^S(t) := x_n(t - \tau) - s.$$

Then safety constraints (4.7) essentially mean that x_n is always below or at maximum tangent to x_{n-1}^S . Note that this condition is equivalent to $x_n(t_{n1} : t_{n4})$ is always below or at maximum tangent to $x_{n-1}^S(t_{(n-1)1} + \tau : t_{(n-1)4} + \tau)$. We investigate the critical condi-

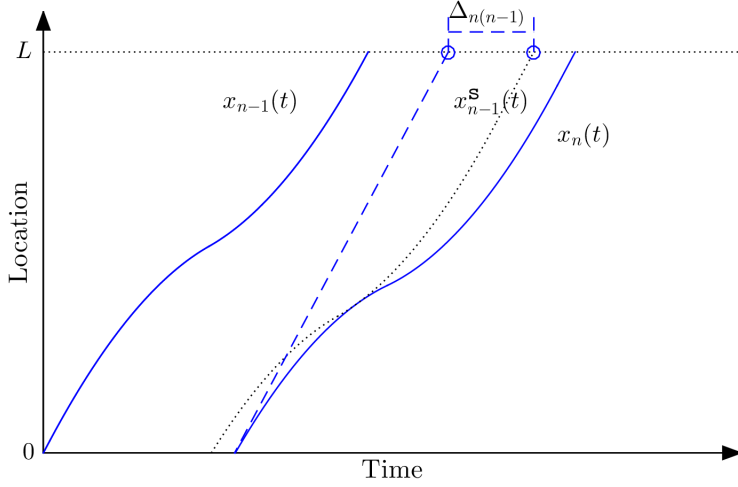


Figure 4.4: Illustration of $\Delta_{n(n-1)}$.

tion when $x_n(t_{n1} : t_{n4})$ gets tangent to $x_{n-1}^S(t_{(n-1)1} + \tau : t_{(n-1)4} + \tau)$, and we denote the corresponding critical δ_{n1} value as function $\hat{\delta}_{n1}(\delta_{(n-1)1}, \phi)$. For formulation convenience, define $\Delta_{(n-1)n} := t_{n-1}^+ + \tau + s/\bar{v} - t_n^- - L/\bar{v}$ as illustrated in Figure 4.4, which can be interpreted as the potential time headway conflict between vehicles n and $n-1$. Note that $\Delta_{(n-1)n} \leq \Delta_{n-1}$ since $t_n^- \geq t_{n-1}^- + \tau + s/\bar{v}$, and $\Delta_{(n-1)n} \leq \Delta_n$ since $t_{n-1}^+ + \tau + s/\bar{v} \leq t_n^+$. Then function $\hat{\delta}_{n1}(\delta_{(n-1)1}, \phi)$ can be formulated as

$$\hat{\delta}_{n1}(\delta_{(n-1)1}, \phi) := \delta_{(n-1)1} + \delta(\phi, \Delta_{n-1}) + t_{n-1}^- + \tau - t_n^- - \delta(\phi, \Delta_{n(n-1)}). \quad (4.27)$$

Then safety constraints (4.7) are essentially equivalent to $\delta_{n1} \leq \hat{\delta}_{n1}(\delta_{(n-1)1}, \phi), \forall n \in \mathcal{M} \setminus \{1\}$. This together with Equation (4.25) yields

$$0 \leq \delta_{n1} \leq \begin{cases} \tilde{\delta}_{n1}(\phi), & \text{if } n = 1; \\ \min\{\tilde{\delta}_{n1}(\phi), \hat{\delta}_{n1}(\delta_{(n-1)1}, \phi)\}, & \text{otherwise,} \end{cases} \quad \forall n \in \mathcal{M}. \quad (4.28)$$

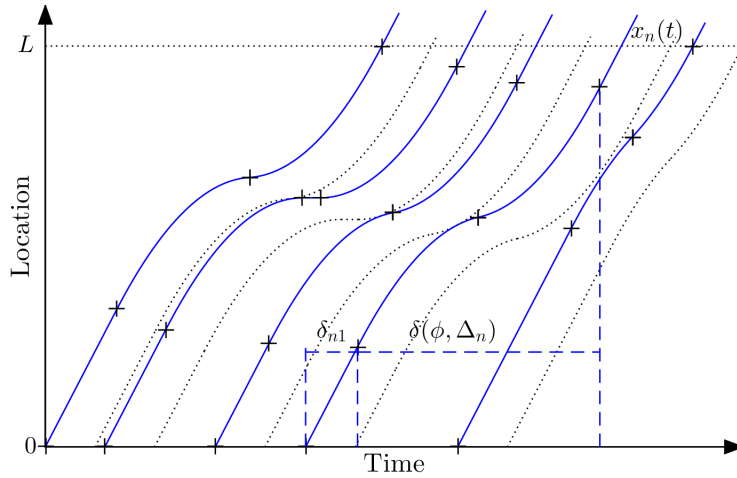


Figure 4.5: Illustration of a feasible set of trajectories to Problem STO.

Now the simplified trajectory optimization model (STO) that this study investigates is formulated as

$$\text{STO: } \min_{\{\delta_{n1}\}, \phi, \lambda} \bar{C}(\phi, \lambda) := \sum_{n=1}^N \bar{c}_n(\phi, \lambda) / N \quad (4.29)$$

where cost function \bar{c}_n is defined in (4.22), subject to (4.28) and

$$\underline{\phi} \leq \phi \leq \bar{\phi}, \quad (4.30)$$

and

$$\frac{\phi}{\underline{a}} \leq \lambda \leq 1 + \frac{\phi}{\underline{a}}. \quad (4.31)$$

Note that Model STO only has $N + 2$ independent variables, which is a dramatic simplification compared with PTO. Figure 4.5 illustrates a set of feasible trajectories to STO.

4.2 Solution Approach

This section analyzes the structure of STO and aims to find an exact solution approach to this problem. Section 4.2.1 investigates certain theoretical properties on how the variable values affect the STO objective and the constraints. Based on these theoretical results, Section 4.2.2 proposes an exact analytical algorithm to solve the optimal solution to STO.

4.2.1 Theoretical Properties

Note that objective function (4.29) of STO is independent of the $\{\delta_{n1}\}$ values. Rather, the $\{\delta_{n1}\}$ values affect the feasible region of STO through constraints (4.28), (4.30) and (4.31). Therefore, to solve STO, we can first set $\{\delta_{n1}\}$ to values that are the least restrictive to the feasible region of variables ϕ and λ , which leads to the following proposition.

Proposition 2. *For given ϕ and λ values, if STO has at least one feasible solution to $\{\delta_{n1}\}$, then $\{\delta_{n1} = \delta_{n1}^*(\phi)\}$ must be feasible to STO as well, where*

$$\delta_{n1}^*(\phi) := \begin{cases} \tilde{\delta}_{n1}(\phi), & \text{if } n = 1; \\ \min\{\tilde{\delta}_{n1}(\phi), \hat{\delta}_{n1}(\delta_{(n-1)1}^*(\phi), \phi)\}, & \text{otherwise,} \end{cases} \quad \forall n \in \mathcal{M}. \quad (4.32)$$

Proof. Let $\{\delta'_{n1}\}$ denote an feasible solution to $\{\delta_{n1}\}$. Then $\{\delta'_{n1}\}$ shall satisfy constraints (4.28) as follows

$$0 \leq \delta'_{n1} \leq \begin{cases} \tilde{\delta}_{n1}(\phi), & \text{if } n = 1; \\ \min\{\tilde{\delta}_{n1}(\phi), \hat{\delta}_{n1}(\delta'_{(n-1)1}, \phi)\}, & \text{otherwise;} \end{cases} \quad \forall n \in \mathcal{M}.$$

Then first $\delta_{11}^*(\phi) = \tilde{\delta}_{11}(\phi) \geq \delta'_{11} \geq 0$ is apparently feasible to constraints (4.28) as well. Now we will use induction to show that $\delta_{n1}^*(\phi)$ is feasible for $n \in \mathcal{M}/\{1\}$. Assume $0 \leq \delta'_{k1} \leq \delta_{k1}^*(\phi)$ and $\delta_{k1}^*(\phi)$ satisfies constraints (4.28), which is obviously true for $k = 1$. Then for

$n = k + 1$, by definition (4.32), $\delta_{n1}^*(\phi) = \min \left\{ \tilde{\delta}_{n1}(\phi), \hat{\delta}_{n1}(\delta_{(n-1)1}^*(\phi), \phi) \right\}$, which obviously satisfies constraints (4.28). Further, by definition $\hat{\delta}_{n1}(\delta_{(n-1)1}(\phi), \phi)$ apparently increases with the $\delta_{(n-1)1}(\phi)$ value, which indicates $\delta_{n1}^*(\phi) \geq \delta'_{n1} \geq 0$. This completes the induction proof. \square

Note that in the above proposition, $\{\delta_{n1} = \delta_{n1}^*(\phi)\}$ essentially means that the transitional part of each trajectory is pushed downstream all the way until either $t_{n4} = t_n^+$ or safety constraint (4.7) is activated. The above proposition indicates that $\{\delta_{n1}\}$ values can be just fixed to $\{\delta_{n1}^*(\phi)\}$ without affecting the optimal objective of STO. Further, denote

$$\delta_1^*(\phi) := \min_{n \in \mathcal{M}} \{\delta_{n1}^*(\phi)\}. \quad (4.33)$$

Note that $\{\delta_{n1} = \delta_{n1}^*(\phi)\}$ are feasible to constraints (4.28) if and only if $\delta_1^*(\phi) \geq 0$. With this, STO essentially reduces to the following restricted STO (RSTO).

$$\text{RSTO: } \min_{\phi, \lambda} \bar{C}(\phi, \lambda) \quad (4.34)$$

subject to (4.30), (4.31) and

$$\delta_1^*(\phi) \geq 0. \quad (4.35)$$

Note that RSTO further reduces this problem to one with only two variables, ϕ and λ , which further simplifies the problem. The following analysis only investigates RSTO since RSTO's optimal solution also solves STO. Now we investigate the relationships between the cost objective function and the decision variables ϕ and λ .

Lemma 5. *For any $p \geq 1$, function $F_n^A(\phi, \lambda, p)$ increases with $\phi > 0$.*

Proof. Based on Equation (4.23), if $\phi \leq \frac{\bar{v}}{2\Delta_n}$,

$$F_n^A(\phi, \lambda, p) = \sqrt{2\bar{v}\Delta_n} (\lambda^{1-p} + (1-\lambda)^{1-p}) \phi^{p-0.5},$$

which apparently increases with $\phi > 0$ when $p \geq 1$. Otherwise, if $\phi > \frac{\bar{v}}{2\Delta_n}$,

$$F_n^A(\phi, \lambda, p) = \bar{v} (\lambda^{1-p} + (1-\lambda)^{1-p}) \phi^{p-1},$$

which again increases with $\phi > 0$ when $p \geq 1$. This completes the proof. \square

Lemma 6. For any $p \geq 1$, function $F_n^A(\phi, \lambda, p)$ is symmetric with respect to $\lambda = 0.5$, decreasing with $\lambda \in (0, 0.5]$ and increasing with $\lambda \in [0.5, 1)$.

Proof. Equation (4.23) apparently shows that $F_n^A(\phi, \lambda, p)$ is symmetric with respect to $\lambda = 0.5$. Further,

$$\frac{dF_n^A(\phi, \lambda, p)}{d\lambda} = \min\left(\sqrt{2\bar{v}\Delta_n\phi}, \bar{v}\right) \cdot \phi^{p-1}(q-1) \left((1-\lambda)^{-p} - \lambda^{-p}\right),$$

which apparently is no greater than 0 when $\lambda \in (0, 0.5]$ and no less than 0 when $\lambda \in [0.5, 1)$.

This completes the proof. \square

Lemma 7. For $q \in \{1, 2, 3, 4\}$, function $F_n^V(\phi, q)$ increases with $\phi > 0$.

Proof. This lemma trivially holds when $q = 1$ since $F_n^V(\phi, 1)$ equals constant L . Then we only investigate the cases for $q = 2, 3, 4$. Based on formulation (4.24), if $\phi \leq \frac{\bar{v}}{2\Delta_n}$,

$$\frac{dF_n^V(\phi, q)}{d\phi} = -\frac{\bar{v}^{q+1}}{(q+1)\phi^2} \sum_{i=3}^{q+1} \binom{q+1}{i} (i/2-1) \left(-\sqrt{\frac{2\Delta_n\phi}{\bar{v}}}\right)^i.$$

Since $\frac{2\Delta_n\phi}{\bar{v}} \leq 1$ holds in this case, it is easy to verify that $\frac{dF_n^V(\phi, q)}{d\phi} \geq 0$ for $q = 2, 3, 4$.

Otherwise if $\phi > \frac{\bar{v}}{2\Delta_n}$,

$$\frac{dF_n^V(\phi, q)}{d\phi} = \left(\frac{1}{2} - \frac{1}{q+1} \right) \bar{v}^{q+1} \frac{1}{\phi^2}$$

which is greater than 0 for all $q > 1$. This completes the proof. \square

These lemmas lead to the following relationship between the optimization objective and the decision variables.

Theorem 6. *Objective function $\bar{C}(\phi, \lambda)$ increases with $\phi > 0$, is symmetric with respect to $\lambda = 0.5$, decreases with $\lambda \in (0, 0.5]$ and increases with $\lambda \in [0.5, 1)$.*

The proof of this theorem directly follows Lemmas 5-7. With this property, the optimal solution to RSTO can be obtained as the following theorem states.

Theorem 7. *For RSTO, the optimal solution to ϕ , if existing, is*

$$\phi^* = \min_{\phi} \left\{ \phi \mid \underline{\phi} \leq \phi \leq \bar{\phi}, \delta_1^*(\phi) \geq 0 \right\}, \quad (4.36)$$

and the optimal solution to λ , if existing, is

$$\lambda^* = \min \left(\max \left(0.5, \frac{\phi^*}{\underline{a}} \right), 1 + \frac{\phi^*}{\underline{a}} \right). \quad (4.37)$$

Proof. First, if ϕ^* exists and is given, based on the relationship between $\bar{C}(\phi^*, \lambda)$ and λ stated in Theorem 7 and constraints (4.31), it is easy to see that λ^* can be solved by (4.37). Note that with Equation (4.37), as ϕ^* decreases, $\frac{\phi^*}{\underline{a}}$ shall decrease and $1 + \frac{\phi^*}{\underline{a}}$ shall increase. Therefore, as ϕ^* reduces, λ^* will be always feasible, and $|\lambda^* - 0.5|$ decreases as well. Therefore, based on Theorem 7, a further decrease of ϕ^* will not affect the feasibility of λ^* while improving the objective. Therefore, Equation (4.36) holds. This completes the proof. \square

The optimal solution stated in Theorem 7 can be intuitively interpreted as to stretch all trajectories as smooth as the transitional parts reach the upstream end of the investigated segment (or $\delta_1^*(\phi) = 0$) and the acceleration and deceleration magnitudes are maximally balanced (or λ^* gets as close to 0.5 as the feasibility allows). For most problem instances with realistic settings, the optimal acceleration and deceleration shall be mild and shall not activate their respective bounds. In this case, λ^* is just set to 0.5, indicating the same deceleration and acceleration magnitudes. Theorem 7 essentially further reduces RSTO into a one dimensional search problem where we only need to find the minimal $\phi \in [\underline{\phi}, \bar{\phi}]$ satisfying $\delta_1^*(\phi) \geq 0$. This result can be further narrowed as follows.

Corollary 7. *For RSTO, the optimal solution to ϕ , if existing, is*

$$\phi^* = \min_{\phi} \left\{ \phi \mid \underline{\phi} \leq \phi \leq \bar{\phi}, \delta_1^*(\phi) = 0 \right\}, \quad (4.38)$$

Proof. Based on the definition of $\delta_{n1}^*(\phi)$ with Equations (4.25), (4.27) and (4.32), we find that $\delta_{n1}^*(\phi)$, is continuous with ϕ . Then it is easy to see with Equation (4.33) that $\delta_1^*(\phi)$ is continuous with ϕ as well. Further, we shall see that $\delta_1^*(\underline{\phi}) \leq \min_{n \in \mathcal{M}} \tilde{\delta}_{n1}(\underline{\phi}) = 0$. Then if $\delta_1^*(\underline{\phi}) = 0$, then apparently, $\phi^* = \underline{\phi}$. Otherwise, $\delta_1^*(\underline{\phi}) < 0$. Then if $\delta_1^*(\phi) < 0, \forall \phi \in [\underline{\phi}, \bar{\phi}]$, ϕ^* does not exist. Otherwise, based on the intermediate value theorem, Equations (4.36) and (4.38) are equivalent. This completes the proof. \square

4.2.2 Optimization Algorithm

Theorem 7 and Corollary 7 indicate that the key to solving RSTO is finding the minimum feasible solution to $\delta_1^*(\phi) \geq 0$ in a finite range $[\underline{\phi}, \bar{\phi}]$. Although $\delta_1^*(\phi)$ may not have simple monotonicity that justifies a bisection search algorithm, we notice that $\delta_1^*(\phi)$ is essentially a piece-wise quadratic function, and thus $\delta_1^*(\phi) = 0$ can be solved analytically at each piece with the following customized algorithm.

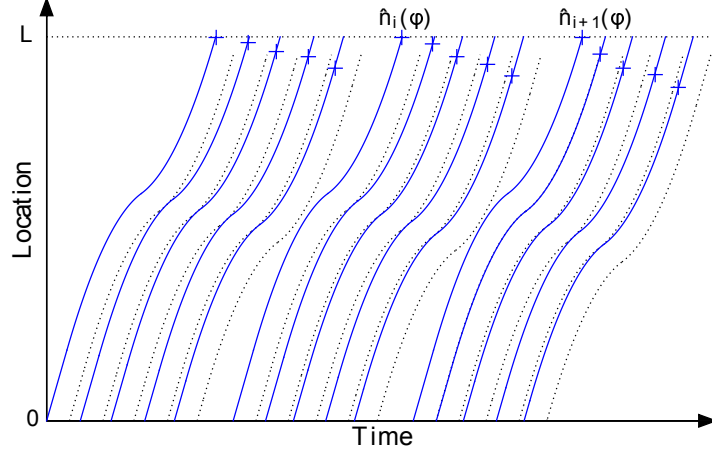


Figure 4.6: Illustration of lead vehicles $\{\hat{n}_i(\phi)\}$, where each cross marks the time of t_{n4} .

Define $\delta_{n1}^\Delta(\phi) := \tilde{\delta}_{n1}(\phi) - \hat{\delta}_{n1}(\delta_{(n-1)1}^*, \phi), \forall n \in \mathcal{M}$, and $\hat{\mathcal{M}}(\phi) := \{1\} \cup \{n \mid \delta_{n1}^\Delta(\phi) \leq 0, n \in \mathcal{M} \setminus \{1\}\}$. Note that $\delta_{n1}^\Delta(\phi) \leq 0$ actually indicates $t_{n4} = t_n^+$ while $\delta_{n1}^\Delta(\phi) > 0$ indicates $t_{n4} < t_n^+$. Index elements in $\hat{\mathcal{M}}(\phi)$ consecutively with $\{\hat{n}_1(\phi) < \hat{n}_2(\phi) < \dots < \hat{n}_{\hat{M}(\phi)}(\phi)\}$ where $\hat{M}(\phi) := |\hat{\mathcal{M}}(\phi)|$. For notation convenience, define $\hat{n}_{\hat{M}(\phi)+1}(\phi) = M + 1$. Note that vehicles in $\hat{\mathcal{M}}(\phi)$ are essentially the trajectories where safety constraints (4.7) are not activated for a given ϕ value. Then in the neighborhood of ϕ , $\delta_{\hat{n}_i(\phi)1}^*(\phi)$ does not depend on vehicle $\hat{n}_i(\phi) - 1$. Rather, $\delta_{\hat{n}_i(\phi)1}^*(\phi)$ depends on vehicles $\hat{n}_i(\phi), \hat{n}_i(\phi) + 1, \dots, n - 1, \forall n \in [\hat{n}_i(\phi) + 1, \hat{n}_{i+1}(\phi) - 1]$. Therefore, each vehicle in $\hat{\mathcal{M}}(\phi)$ can be regarded as a lead vehicle. Specifically, we call $\hat{n}_i(\phi)$ the lead vehicle for all $n = \hat{n}_i(\phi), \hat{n}_i(\phi) + 1, \dots, \hat{n}_{i+1}(\phi) - 1$, and denote this as

$$\hat{n}(n, \phi) := \hat{n}_i(\phi), \forall n = \hat{n}_i(\phi), \hat{n}_i(\phi) + 1, \dots, \hat{n}_{i+1}(\phi) - 1.$$

Lead vehicles $\{\hat{n}_i(\phi)\}$ are illustrated in Figure 4.6. For a given $\phi > 0$, $\hat{\mathcal{M}}(\phi)$ can be easily identified with the following iterative algorithm (IA).

- IA-1: Set $\hat{n}_1(\phi) = \hat{n}(1, \phi) = 1$, $i = 2$ and $n = 2$.

- IA-2: This step verifies whether $\hat{n}(n, \phi) = \hat{n}(n-1, \phi)$ holds. If it holds, then $\delta_{n1}^{\Delta}(\phi) = \hat{\delta}_{n1}^{\Delta}(\phi)$ as defined below.

$$\hat{\delta}_{n1}^{\Delta}(\phi) := t_n^+ - (n - \hat{n}(n-1, \phi))\tau - t_{n-1}^+ + \sum_{n'=\hat{n}(n-1, \phi)+1}^n \left(\delta(\phi, \Delta_{n'(n'-1)}) - \delta(\phi, \Delta_{n'}) \right) \quad (4.39)$$

Note that calculation of $\hat{\delta}_{n1}^{\Delta}(\phi)$ can be further expedited since $\hat{\delta}_{n1}^{\Delta}(\phi) = \hat{\delta}_{(n-1)1}^{\Delta}(\phi) + \delta(\phi, \Delta_{n-1}) - \delta(\phi, \Delta_{n(n-1)})$.

- IA-3: If $\hat{\delta}_{n1}^{\Delta}(\phi) > 0$, the above assumption holds, and then set $\hat{n}(n, \phi) = \hat{n}(n-1, \phi)$. Increase $n = n+1$ and go to Step IA-2. Otherwise, go to the next step.
- IA-4: Set $\hat{n}(n, \phi) = n$ and $\hat{n}_i(\phi) = n$. If $n < M$, increase $i = i+1$, $n = n+1$, and go to Step IA-2. Otherwise, go to the next step.
- IA-5: Return $\hat{\mathcal{M}}(\phi) = \{\hat{n}_1(\phi), \hat{n}_2(\phi), \dots, \hat{n}_i(\phi)\}$.

Note that the computational complexity of the IA algorithm is $o(M)$. Once $\hat{\mathcal{M}}(\phi)$ is obtained, $\hat{\delta}_{n1}(\delta_{(n-1)1}^*, \phi)$ can be denoted as a closed form function $\hat{\delta}_{n1}^{\text{lead}}(\hat{n}(n, \phi^*), \phi)$ as defined below

$$\hat{\delta}_{n1}^{\text{lead}}(\hat{n}(n, \phi^*), \phi) := t_{\hat{n}(n, \phi^*)}^+ + (n - \hat{n}(n, \phi^*))\tau - t_n^- - \delta(\phi, \Delta_{n(n-1)}) \quad (4.40)$$

$$+ \sum_{n'=\hat{n}(n, \phi^*)+1}^{n-1} \left[\delta(\phi, \Delta_{n'}) - \delta(\phi, \Delta_{n'(n'-1)}) \right]. \quad (4.41)$$

Then based on Corollary 7, if there exists an optimal solution ϕ^* , it should be the minimum value satisfying the following conditions

$$\hat{\delta}_{n1}^{\text{lead}}(\hat{n}(n, \phi^*), \phi^*) \geq 0, \forall n \in \mathcal{M} \setminus \hat{\mathcal{M}}(\phi^*), \quad (4.42)$$

and constraint (4.30) for the feasible range of ϕ .

Then the sketch of the exact solution algorithm is to first identify $\hat{\mathcal{M}}(\phi^*)$ and then solve the above equations by analytically solving a set of piecewise quadratic functions. We first analyze the property of $\hat{\mathcal{M}}(\phi)$.

Proposition 3. $\hat{\mathcal{M}}(\phi) = \{1\}$ as $\phi \rightarrow \infty$ and $\hat{\mathcal{M}}(\phi_1) \supseteq \hat{\mathcal{M}}(\phi_2), \forall \phi_1 < \phi_2 \in \mathbb{R}^+$.

Proof. First as $\phi \rightarrow \infty$, $\hat{n}(n, \phi)$ has to be less than n , and thus $\delta_{n1}^\Delta(\phi) = t_n^+ - (n - \hat{n}(n, \phi))\tau - t_{\hat{n}(n, \phi)}^+ > 0, \forall n \in \mathcal{M}$, and thus $\hat{\mathcal{M}}(\phi) = \{1\}$. Then we only need to show as ϕ increases, if a lead vehicle n leaves $\hat{\mathcal{M}}(\phi)$, it should not come back to $\hat{\mathcal{M}}(\phi)$ and become a lead vehicle again. When vehicle n just leaves $\hat{\mathcal{M}}(\phi)$, then we have

$$\delta_{n1}^\Delta(\phi) = t_n^+ - (n - \hat{n}(n-1, \phi))\tau - t_{\hat{n}(n-1, \phi)}^+ + \sum_{n'=\hat{n}(n-1, \phi)+1}^n \left(\delta(\phi, \Delta_{n'(n'-1)}) - \delta(\phi, \Delta_{n'}) \right) \geq 0, \forall n \in \mathcal{M} \setminus \{1\}.$$

As ϕ increases, when $\hat{n}(n-1, \phi)$ does not change, $\sum_{n'=\hat{n}(n-1, \phi)+1}^n \left(\delta(\phi, \Delta_{n'(n'-1)}) - \delta(\phi, \Delta_{n'}) \right)$ shall increase and $\delta_{n1}^\Delta(\phi)$ shall remain non-negative. If $\hat{n}(n-1, \phi)$ changes, it has to decrease based on the formulation of $\delta_{\hat{n}(n-1, \phi)1}^\Delta(\phi)$. Thus $\delta_{n1}^\Delta(\phi)$ shall remain non-negative, too. This completes this proof. \square

Corollary 8. $\delta_{n1}^\Delta(\phi)$ increases with $\phi > 0$. If $\delta_{n1}^\Delta(\phi^-) \leq 0$ for some $\phi^- > 0$, $\delta_{n1}^\Delta(\phi)$ strictly increases with ϕ from ϕ^- to some ϕ^+ with $\delta_{n1}^\Delta(\phi^+) > 0$. In this case, $\delta_{n1}^\Delta(\phi) = 0$ has a unique solution.

We omit the proof to this corollary because this property is apparent following Proposition 3 and the formulation structure of $\delta_{n1}^\Delta(\phi)$. The above analysis indicates that as ϕ increases, the elements of $\hat{\mathcal{M}}(\phi)$ will only drop out but never grow. We can use the following

algorithm to evaluate which index of $\hat{\mathcal{M}}(\phi)$ will first drop out as ϕ increases from a given value $\hat{\phi}$.

- DROP-1: Given $\hat{\phi}$ and $\hat{\mathcal{M}}(\hat{\phi})$ (which could be obtained with the IA algorithm), set $i = 2$.
- DROP-2: Then this algorithm checks at which ϕ value as $\hat{\phi}$ increases to, $\hat{n}_i(\hat{\phi})$ will be dropped out from $\hat{\mathcal{M}}(\hat{\phi})$, i.e., solving $\hat{\delta}_{\hat{n}_i(\hat{\phi})_1}^{\Delta}(\phi) = 0$. Based on Corollary 8, since $\hat{\delta}_{\hat{n}_i(\hat{\phi})_1}^{\Delta}(\hat{\phi}) < 0$, $\hat{\delta}_{\hat{n}_i(\hat{\phi})_1}^{\Delta}(\phi) = 0$ has a unique solution in $[\hat{\phi}, \infty)$. For mathematical convenience, we equivalently investigate $F_{\hat{\phi}_i}(\sqrt{\phi}) := \hat{\delta}_{\hat{n}_i(\hat{\phi})_1}^{\Delta}(\phi) \cdot \phi = 0$. Note that $F_{\hat{\phi}_i}(\sqrt{\phi})$ is essentially a piecewise quadratic function of $\sqrt{\phi}$, and its joint points between consecutive pieces can be obtained in the following way. Define

$$\phi_n^{\text{crit1}} := \frac{\bar{v}}{2\Delta_n}, \phi_n^{\text{crit2}} := \frac{\bar{v}}{2\Delta_{n(n-1)}}, \forall n. \quad (4.43)$$

Then define $\Phi_i^{\text{crit}}(\hat{\phi}) = \{\hat{\phi}, \infty\} \cup \{\phi_n^{\text{crit1}}, \phi_n^{\text{crit2}}\}_{n=\hat{n}_{i-1}(\hat{\phi}), \dots, \hat{n}_i(\hat{\phi})-1}$. Then delete all elements in $\Phi_i^{\text{crit}}(\hat{\phi})$ less than $\hat{\phi}$ and then sort these elements in an ascending order. Denote the sorted elements as $\Phi_i^{\text{crit}}(\hat{\phi}) = [\phi_{i1}^{\text{crit}}, \phi_{i2}^{\text{crit}}, \dots, \phi_{iK_i}^{\text{crit}}]$ where $K_i := |\Phi_i^{\text{crit}}(\hat{\phi})|$. Now $\Phi_i^{\text{crit}}(\hat{\phi})$ contains all the joints between consecutive pieces of $F_{\hat{\phi}_i}(\sqrt{\phi})$. Then we iterate all these pieces, starting with $k = 1$.

- DROP-3: This step makes a guess that the solution to $F_{\hat{\phi}_i}(\sqrt{\phi}) = 0$ falls in $[\phi_{ik}^{\text{crit}}, \phi_{i(k+1)}^{\text{crit}}]$. Based on the definition, we know when $\phi \in [\phi_{ik}^{\text{crit}}, \phi_{i(k+1)}^{\text{crit}}]$, $F_{\hat{\phi}_i}(\sqrt{\phi})$ is a quadratic function in the form of $A\phi + B\sqrt{\phi} + C = 0$, and coefficients A, B, C can be obtained in the following way. Initially, set $A = t_{\hat{n}_i(\hat{\phi})}^+ - (\hat{n}_i(\hat{\phi}) - \hat{n}_{i-1}(\hat{\phi}))\tau - t_{\hat{n}_{i-1}(\hat{\phi})}^+, B = 0, C = 0$. Set $n = \hat{n}_{i-1}(\hat{\phi}) + 1$.
- DROP-4: If $\phi_{i(k+1)}^{\text{crit}} \leq \frac{\bar{v}}{2\Delta_n}$, update $B = B - \sqrt{2\Delta_n\bar{v}}$; otherwise, update $C = C - \bar{v}/2$, $A = A - \Delta_n$. If $\phi_{i(k+1)}^{\text{crit}} \leq \frac{\bar{v}}{2\Delta_{n(n-1)}}$, update $B = B + \sqrt{2\Delta_{n(n-1)}\bar{v}}$; otherwise, update

$C = C + \bar{v}/2$, $A = A + \Delta_{n(n-1)}$. If $n < \hat{n}_i(\hat{\phi})$, update $n = n + 1$ and repeat this step; otherwise, go to the next step.

- DROP-5: Solve the roots to $A\phi + B\sqrt{\phi} + C = 0$. There should be no more than one solution to ϕ falling in $[\phi_{ik}^{\text{crit}}, \phi_{i(k+1)}^{\text{crit}}]$. If such a solution exists, then the guess at Step DROP-3 is correct, and we record it as $\phi_{\hat{n}_i(\hat{\phi})}^{\text{next}}(\hat{\phi})$ and go to the next step; otherwise, update $k = k + 1$, and go to Step DROP-3.
- DROP-6: If $i < \hat{M}(\hat{\phi})$, update $i = i + 1$ and go to Step DROP-2. Otherwise, go to the next step.
- DROP-7: Solve $n^{\text{next}}(\hat{\phi}) = \arg \min_{n \in \hat{\mathcal{M}}(\hat{\phi}) \setminus \{1\}} \phi_n^{\text{next}}(\hat{\phi})$. Then $n^{\text{next}}(\hat{\phi})$ will be the first element to be dropped from $\hat{\mathcal{M}}(\phi)$ as ϕ increases from $\hat{\phi}$ to $\phi_{n^{\text{next}}(\hat{\phi})}^{\text{next}}(\hat{\phi})$. Return $n^{\text{next}}(\hat{\phi})$ and $\phi_{n^{\text{next}}(\hat{\phi})}^{\text{next}}(\hat{\phi})$.

Note that the computational complexity of the DROP algorithm is $o(M^2)$. The DROP algorithm can help identify an interval $[\hat{\phi}, \phi_{n^{\text{next}}(\hat{\phi})}^{\text{next}}(\hat{\phi})]$ where $\hat{\mathcal{M}}(\phi)$ can be treated as the same $\hat{\mathcal{M}}(\hat{\phi})$ ⁴. We call such an interval a stationary interval. With this, we will search stationary intervals consecutively in an ascending order between $\underline{\phi}$ and $\bar{\phi}$. In each stationary interval, we try to find the minimum ϕ that satisfies conditions (4.42). This process is described in the following piece-wise search algorithm (PSA).

- PSA-1: Initially, set $\phi^- = \underline{\phi}$, call the DROP algorithm to solve $\phi^+ = \phi_{n^{\text{next}}(\phi^-)}^{\text{next}}(\phi^-)$.
- PSA-2: Call the IA algorithm to solve $\hat{\mathcal{M}}(\phi^-)$. Then this algorithm tries to find the region for constraints (4.42) to be feasible within $[\phi^-, \phi^+]$. We initially set the candidate feasible region $\mathcal{R}^{\text{feas}} = [\phi^-, \phi^+]$, then we narrow it down by iteratively

⁴Note that strictly speaking, $\hat{\mathcal{M}}(\phi_{n^{\text{next}}(\hat{\phi})}^{\text{next}}(\hat{\phi}))$ compared with $\hat{\mathcal{M}}(\hat{\phi})$ has one more element, $n^{\text{next}}(\hat{\phi})$, but deleting $n^{\text{next}}(\hat{\phi})$ does not change the validity of all proposed equations

checking feasible regions for all n in $\mathcal{M} \setminus \hat{\mathcal{M}}(\phi^-)$. We start the feasibility checking from the the first index in $\mathcal{M} \setminus \hat{\mathcal{M}}(\phi^-)$, denoted by n .

- PSA-2: Initially set the feasibility region $\mathcal{R}_n^{\text{feas}} = \emptyset$. Note that

$$\forall \phi \in [\phi^-, \phi^+], \hat{\delta}_{n1}^{\text{lead}}(\hat{n}(n, \phi), \phi) = \hat{\delta}_{n1}^{\text{lead}}(\hat{n}(n, \phi^-), \phi).$$

Then for mathematical convenience, we define $G_{n\phi^-}(\sqrt{\phi}) := \phi \cdot \hat{\delta}_{n1}^{\text{lead}}(\hat{n}(n, \phi^-), \phi)$, which is a piecewise quadratic function of $\sqrt{\phi}$. Similar to Step DROP-2, we will first identify the joints between consecutive pieces. Define $\Phi_n^{\text{crit}} = \{\phi^-, \phi^+\} \cup \{\phi_{n'}^{\text{crit}1}, \phi_{n'}^{\text{crit}2}\}_{n'=\hat{n}(n, \phi^-)+1, \dots, n}$ and drop all elements less than ϕ^- or greater than ϕ^+ from Φ_n^{crit} , where $\phi_{n'}^{\text{crit}1}, \phi_{n'}^{\text{crit}2}$ are defined in Equation (4.43). Then sort all elements in Φ_n^{crit} in an ascending order, and denote them as $\Phi_n^{\text{crit}} = [\phi_{n1}^{\text{crit}}, \phi_{n2}^{\text{crit}}, \dots, \phi_{nK_n}^{\text{crit}}]$ where $K_n = |\Phi_n^{\text{crit}}|$. Now Φ_n^{crit} contains all the joints between consecutive pieces of $G_{n\phi^-}(\sqrt{\phi})$ during $[\phi^-, \phi^+]$ in an ascending order. Then will iterate through all these pieces, starting with $k = 1$.

- PSA-3: This step will find the feasible region that $G_{n\phi^-}(\sqrt{\phi}) \geq 0$ (or $\hat{\delta}_{n1}^{\text{lead}}(\hat{n}(n, \phi^-), \phi) \geq 0$) during interval $[\phi_{nk}^{\text{crit}}, \phi_{n(k+1)}^{\text{crit}}]$, where $G_{n\phi^-}(\sqrt{\phi})$ is a quadratic function in the form of $A\sqrt{\phi} + B\phi + C$, where coefficients A, B, C can be obtained in the following iterative approach. Initially, set $A = t_{\hat{n}(n, \phi^-)}^+ + (n - \hat{n}(n, \phi^-))\tau - t_n^-$, $B = 0$ and $C = 0$, then update these coefficients according to the following pseudo code:

For $n' = \hat{n}(n, \phi^-) + 1$ to $n - 1$

$$\text{If } \phi_{n(k+1)}^{\text{crit}} \leq \frac{\bar{v}}{2\Delta_{n'}}$$

$$\text{Update } B = B + \sqrt{2\bar{v}\Delta_{n'}}.$$

Else

$$\text{Update } A = A + \Delta_{n'}, C = C + \bar{v}/2.$$

For $n' = \hat{n}(n, \phi^-) + 1$ to n

If $\phi_{n(k+1)}^{\text{crit}} \leq \frac{\bar{v}}{2\Delta_{n'(n'-1)}}$
 Update $B = B - \sqrt{2\bar{v}\Delta_{n'(n'-1)}}$.

Else

Update $A = A - \Delta_{n'(n'-1)}$, $C = C - \bar{v}/2$.

- PSA-4: It is easy to solve the subset $\mathcal{R}_{nk}^{\text{feas}}$ in $[\phi_{nk}^{\text{crit}}, \phi_{n(k+1)}^{\text{crit}}]$ such that $G_{n\phi^-}(\sqrt{\phi}) = A\phi + B\sqrt{\phi} + C \geq 0$ with the following pseudo code:

If $A = 0$

If $B = 0$

If $C \geq 0$, return $\mathcal{R}_{nk}^{\text{feas}} = [\phi_{nk}^{\text{crit}}, \phi_{n(k+1)}^{\text{crit}}]$.

Else, return $\mathcal{R}_{nk}^{\text{feas}} = \emptyset$.

Else if $B > 0$, return $\mathcal{R}_{nk}^{\text{feas}} = \left[\max\left\{\phi_{nk}^{\text{crit}}, \frac{C^2}{B^2}\right\}, \phi_{n(k+1)}^{\text{crit}} \right]$.

Else, return $\mathcal{R}_{nk}^{\text{feas}} = \left[\phi_{nk}^{\text{crit}}, \min\left\{\phi_{n(k+1)}^{\text{crit}}, \frac{C^2}{B^2}\right\} \right]$.

Else

If $B^2 - 4AC < 0$, return $\mathcal{R}_{nk}^{\text{feas}} = [\phi_{nk}^{\text{crit}}, \phi_{n(k+1)}^{\text{crit}}]$ if $A > 0$ or return $\mathcal{R}_{nk}^{\text{feas}} = \emptyset$

otherwise.

Solve $\phi_{nk}^1 = \left(\frac{-B - \sqrt{B^2 - 4AC}}{2A}\right)^2$, $\phi_{nk}^2 = \left(\frac{-B + \sqrt{B^2 - 4AC}}{2A}\right)^2$.

If $A > 0$, return $\mathcal{R}_{nk}^{\text{feas}} = [\phi_{nk}^{\text{crit}}, \phi_{n(k+1)}^{\text{crit}}] \cap \{(-\infty, \min\{\phi_{nk}^1, \phi_{nk}^2\}) \cup [\max\{\phi_{nk}^1, \phi_{nk}^2\}, \infty)\}$.

Else, return $\mathcal{R}_{nk}^{\text{feas}} = [\phi_{nk}^{\text{crit}}, \phi_{n(k+1)}^{\text{crit}}] \cap [\min\{\phi_{nk}^1, \phi_{nk}^2\}, \max\{\phi_{nk}^1, \phi_{nk}^2\}]$.

Then update $\mathcal{R}_n^{\text{feas}} = \mathcal{R}_n^{\text{feas}} \cup \mathcal{R}_{nk}^{\text{feas}}$. If $k+1 < K_n$, update $k = k+1$ and go to Step PSA-3 to check the next piece. Otherwise, $\mathcal{R}_n^{\text{feas}}$ is all the feasible region for $G_{n\phi^-}(\sqrt{\phi}) \geq 0$ in $[\phi^-, \phi^+]$, and we go to the next step.

- PSA-5: Set $\mathcal{R}^{\text{feas}} = \mathcal{R}^{\text{feas}} \cap \mathcal{R}_n^{\text{feas}}$. If n is not the last element in $\mathcal{M} \setminus \hat{\mathcal{M}}(\phi^-)$, update n to be the next element in $\mathcal{M} \setminus \hat{\mathcal{M}}(\phi^-)$ and go to Step PSA-2 to find the feasible

region for this new vehicle. Otherwise, $\mathcal{R}^{\text{feas}}$ is exactly the feasible region in $[\phi^-, \phi^+]$ such that Constraints (4.42) holds, and then go to the next step.

- PSA-5: If $\mathcal{R}^{\text{feas}} \neq \emptyset$, then the optimal solution is found and return $\phi^* = \min \{ \phi \in \mathcal{R}^{\text{feas}} \}$. Otherwise, if $\hat{\mathcal{M}}(\phi^-) = \{1\}$, then there is no feasible solution. Otherwise, $|\hat{\mathcal{M}}(\phi^-)| > 1$, and we set $\phi^- = \phi^+$ and go to Step PSA-2.

The PSA yields the exact optimal solution ϕ^* to problem RSTO. Note that the computational complexity of the PSA is $o(M^3)$. This is because each vehicle n needs to check no more than M pieces, and at each piece, it takes no more than M steps to solve the feasible region for each $G_{n\phi^-}(\sqrt{\phi}) \geq 0, \forall n \in \mathcal{M} \setminus \hat{\mathcal{M}}(\phi^-)$. Note that the most complex operation is just to solve a quadratic equality. It is expected that the PSA can be very efficiently solved with modern computers.

4.3 Numerical Examples

This section conducts numerical examples to test the solution efficiency of the proposed algorithm and the application of this trajectory optimization model. Section 4.3.1 reports the solution times of the PSA for different instances and concludes that this proposed algorithm has appealing computational efficiency for real-time applications. The proposed trajectory optimization model can actually be applied to a general highway segment under different control strategies. For illustration purposes, Sections 4.3.2 and 4.3.3 show its applications for signalized segments and non-stop intersections, respectively.

4.3.1 Algorithm Performance

The computation experiments are conducted on a PC with 2.6 GHz CPU and 16 GB RAM. The parameters are set in the following way. The vehicle arrival times are generated

as

$$t_n^- = \begin{cases} 0, & \text{if } n = 1; \\ t_{n-1}^- + (\tau + s/\bar{v}) \left(1 + \left(\frac{1}{r} - 1\right) [(1 - \alpha) + \alpha\xi_n]\right), & \text{otherwise,} \end{cases} \quad (4.44)$$

where $r \in (0, 1]$ indicates traffic saturation rate, parameter $\alpha \in [0, 1]$ controls the dispersion of arrival time headway (greater α indicates higher dispersion), ξ_n is a uniformly distributed random number over $[0, 2]$, and ξ_n values are independent across different n values. We generate arrival times in this way so that they are feasible to Equation (4.14) and we can control traffic volume with r and arrival randomness with α . Similarly, we set vehicle departure times as

$$t_n^+ = \begin{cases} L/\bar{v} + \Delta^S, & \text{if } n = 1; \\ \max \left\{ t_{n-1}^+ + (\tau + s/\bar{v}) \left(1 + \left(\frac{1}{r} - 1\right) [(1 - \alpha) + \alpha\xi'_n]\right), t_n^- + L/\bar{v} \right\}, & \text{otherwise,} \end{cases}$$

where $\Delta^S \geq 0$ is a time shift (e.g., due to a downstream bottleneck) and ξ'_n again is a uniformly and independently distributed random number over $[0, 2]$. This formulation ensures feasible conditions (4.15) and (4.16) hold. In the experiments, we purposefully set L to a large value, 8000m. Although this value may not be realistic for all applications, it ensures that each tested problem instance is feasible (i.e., there exist solutions not causing queue spillback) even for large N values. The examples in this section set $\underline{a} = -3.5\text{m/s}^2$, $\bar{a} = 2\text{m/s}^2$, $\bar{v} = 16\text{m/s}$ ($\approx 35\text{mph}$), $s = 7\text{m}$ and $\tau = 1.5\text{s}$. To test instances of different input sizes, we vary N between 50 and 1000. Further, we try $r \in \{0.3, 0.5, 0.7, 0.9\}$, $\alpha \in \{0.5, 1\}$ and $\Delta^S \in \{20, 50\}$ to create different scenarios. The solution times of all these instances are reported in Figure 4.7. We see that the solution times are less than 3 seconds for most instances and less than 10 seconds for all these instances, which are suitable for real-time engineering practices where a few hundred vehicles would take tens of minutes to arrive. Overall, as the increase of r , α or

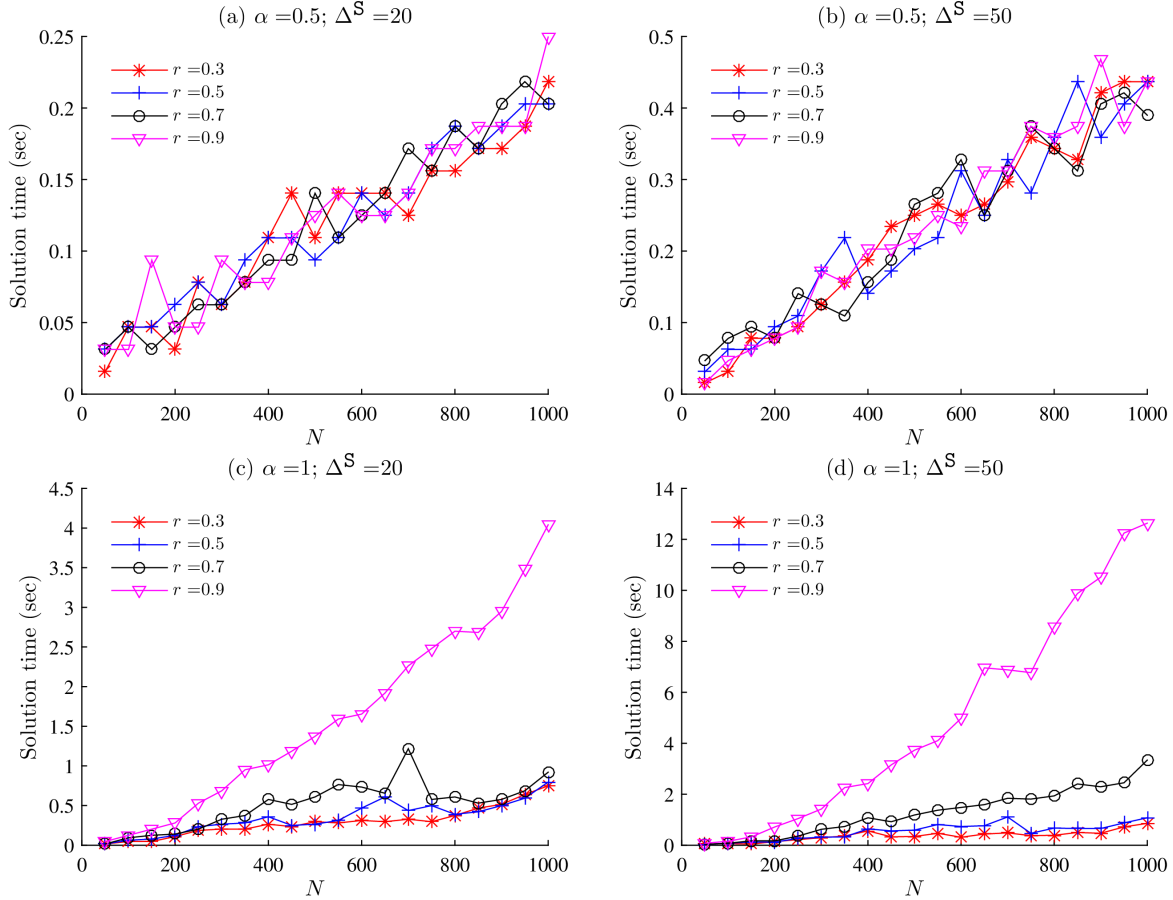


Figure 4.7: Solution times for different problem instances.

Δ^S , the solution time in general increases. This is because when these variable increases, the average size of a platoon shall increase and the interactions between consecutive trajectories become stronger. Therefore, the PSA likely needs to check more pieces and thus the solution time generally increases. For most instances, the solution time increases almost linearly with the instance size (or the N value). For some instances with relatively large r and α , the solution time increase exhibits a super-linear trend when N gets large. This is probably due to the increased interactions between consecutive trajectories as mentioned above. Yet the super-linear increasing trend looks less than that of a cubic function, and thus the actually solution times are likely less than the theoretical cubic time complexity bound as discussed in the end of Section 4.2.2.

To further investigate the performance of PSA, the following analysis compares the results from PSA and those from the numerical sub-gradient algorithm (NSG) with an slightly adapted shooting heuristic (SH)⁵ proposed by Ma et al. (2017). Basically, compared with the proposed trajectory construction model (4.21), a feasible SH solution also contains piecewise quadratic trajectories, which however may have more than five pieces. Compared with the analytical PSA approach, the NSG-SH approach contains more acceleration variables, but it is numerical and may not guarantee to find the optimal solution. For the algorithm detail, please refer to Ma et al. (2017). Figure 4.8 shows the comparison results with the same parameter values as Figure 4.7 (d). Figures 4.8 (a) and (b) show the ratio of the PSA solution time over the NSG-SH solution time for the VSP and SA objectives, respectively, as N increases at different r values. We can see that for all instances, the PSA solution time is less than 3.5% of the NSG-SH solution time. This ratio generally drops as r decreases. This verifies that the analytical PSA algorithm is much more efficient than the numerical NSG-SH algorithm, though the latter’s solution time is already reasonable for practical applications. Figures 4.8 (c) and (d) show the ratio of the PSA objective value over the NSG-SH objective value for VSP and SA, respectively. We see that for VSP, both PSA and NSG-SH have very close objective values while most PSA objectives are slightly less than the NSG-SH objectives. Whereas for SA, the PSA objectives are much better than the NSG-SH objectives: all PSA objectives are less than 2% of their NSG-SH counterparts, and the ratio in general further drops as r increases. These results indicate that the PSA solutions, though generated from a more restrictive model with fewer quadratic pieces and less variables, are no worse than those from the NSG-SH objectives. Overall, we see that compared with the previously proposed NSG-SH approach, the PSA approach much improves the solution efficiency with-

⁵We made the following minor adaptations to SH to fit our problem. The backward shooting process for each vehicle n now starts at its fixed exit time t_n^- instead of being regulated by signal timing. The objective function is VSP (4.10) or SA (4.11). The speed variable v is fixed to speed limit \bar{v} .

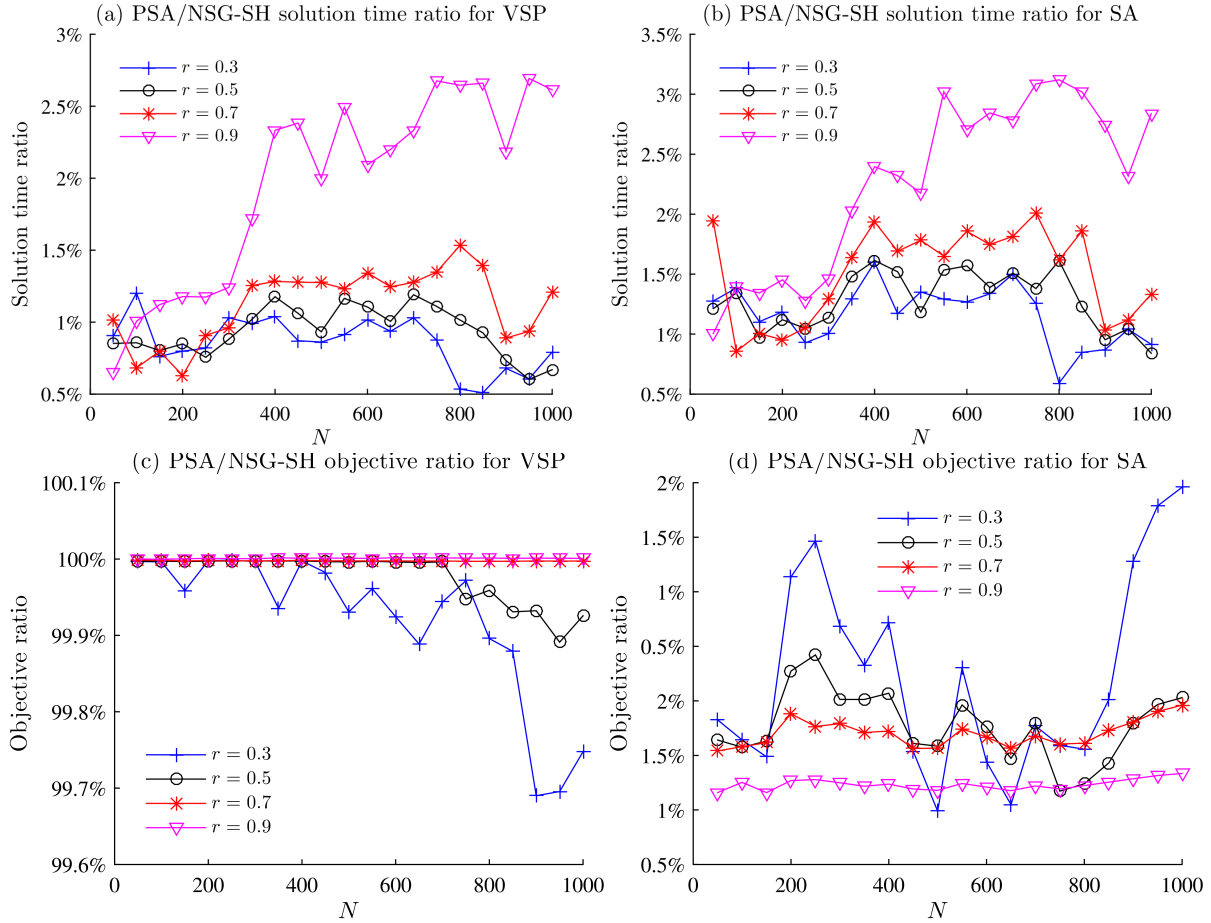


Figure 4.8: Performances of PSA and NSG-SH.

out compromising the solution quality (actually the solution quality is improved for most instances).

Next we compare the shapes of trajectories produced by PSA and NSG-SH. For clarity of the plot, we investigate a shorter segment with less vehicles, where we set $L = 300\text{m}$, $N = 20$, $r = 0.9$, $\alpha = 0.5$ and $\Delta^S = 10\text{s}$ and keep the remaining settings the same. Figure 4.9 compares the trajectory solutions from PSA and NSG-SH for this instance, where crosses mark the ends of quadratic pieces. We can see that the PSA solution contains less quadratic pieces and appears smoother compared with the NSG-SH solution. and therefore the PSA trajectories may be easier to implement in real-time control. Whereas as N increases, a NSG-SH trajectory could contain quite a number of quadratic pieces including repeated

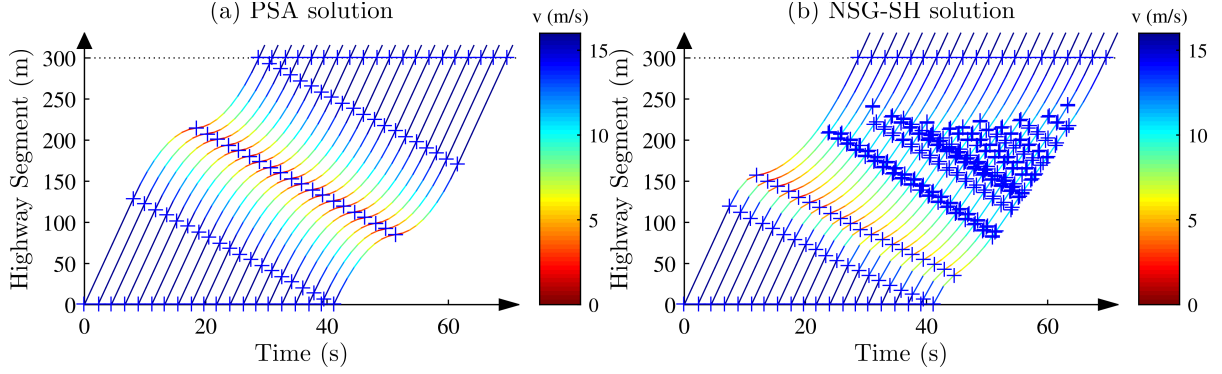


Figure 4.9: Trajectories produced by PSA and NSG-SH (the crosses separate quadratic pieces).

deceleration-acceleration cycles, though at mild acceleration magnitudes. This would add some control difficulty and slightly compromise driving comfort.

4.3.2 Signalized Segment

This section investigates a highway section where a fixed-timing signal controls exit location L . Assume that the effective green starts at time 0 and has a duration of G , and the effective red time has a duration of R . For illustration purposes, we set $G = R = C/2$ in the following experiments, where $C = R + G$ is the cycle length. The vehicle arrival times are again generated by Equation (4.44). Further, we apply Proposition 1 in Ma et al. (2017) to obtain exit times t_n^+ as the earliest time when vehicle n can exit this segment, formulated as follows

$$t_n^+ = \begin{cases} \mathcal{G}(t_n^- + L/\bar{v}), & \text{if } n = 1; \\ \mathcal{G}(\max\{t_n^- + L/\bar{v}, t_{n-1}^+ + \tau + s/\bar{v}\}), & \text{otherwise,} \end{cases}$$

where function

$$\mathcal{G}(t) := \begin{cases} t, & \text{if } \text{mod}(t, R+G) \in [0, G) \text{ (or the light is green at time } t\text{);} \\ \lceil t/(R+G) \rceil \cdot (R+G), & \text{otherwise,} \end{cases}$$

which pushes time t to the beginning of the next green phase if it is in a red phase. We set the default parameter values as: $L = 500\text{m}$, $C = 60\text{s}$, $N = 50$, $\underline{a} = -3.5\text{m/s}^2$, $\bar{a} = 2\text{m/s}^2$, $\bar{v} = 16\text{m/s}$ ($\approx 35\text{mph}$), $s = 7\text{m}$, $\tau = 1.5\text{s}$, $\alpha = 0.5$ and $r = 0.4$. With this, all the input parameters are ready. The trajectory optimization approach first breaks the traffic stream into independent platoons with the PA algorithm and then applies the PSA algorithm to each platoon to smooth the corresponding trajectories.

Figure 4.10 shows the trajectory results in the time-space diagram for two cases. The first case (Figure 4.10(a)), referred as the extreme acceleration (EA) case, is a feasible solution to RSTO where the acceleration variables are set to their extreme values, i.e., $a^- = -\underline{a}$ and $a^+ = \bar{a}$. This solution is regarded as the benchmark without optimally smoothing the trajectories. The second case (Figure 4.10(b)), referred as the optimal trajectory case, is the optimal trajectories (OT) obtained with the PSA algorithm. We can see that the trajectories in the EA case have relatively sharp accelerations and decelerations, and vehicles are forced to stop before passing this intersection. Whereas the OT result exhibits smooth trajectories and completely eliminates stops. Therefore we expect that the OT result has better performance compared with the benchmark EA case.

Table 4.1 compares the EA objective values with the optimal OT objective values. Nine different instances are tested, and in each instance at most one parameter value is changed and the remaining parameters stay at their default values. Both VSP function (4.10) and SA function (4.11) are tested in the objective. For VSP function (4.10), we set $\xi = 5.5043$, $\psi = 0.2953$ and $\zeta = 0.00338$ by converting the coefficients from Frey et al. (2002)

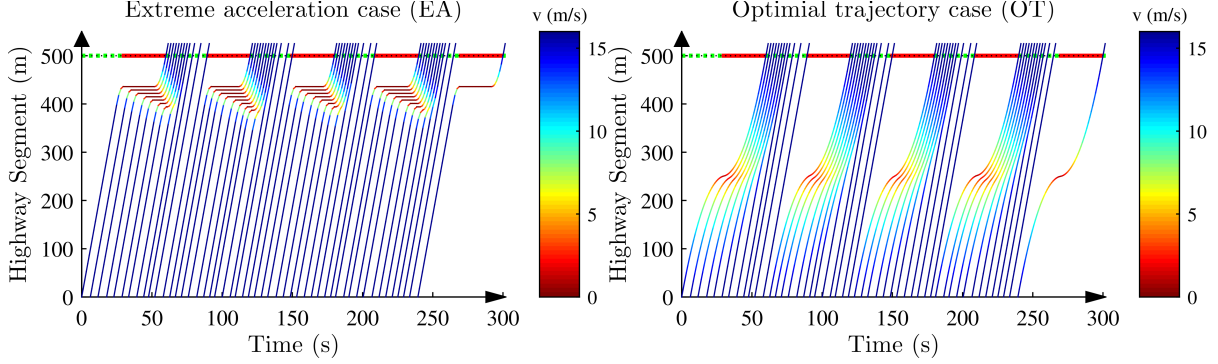


Figure 4.10: Signalized segment results: (a) trajectory plot for extreme accelerations (EA); and (b) optimal trajectory (OT) plot.

to fit the metric units. Denote the EA objectives for VSP and SA with C_{EA}^{VSP} and C_{EA}^{SA} , respectively, and denote the OT objectives for VSP and SA with C_{OT}^{VSP} and C_{OT}^{SA} , respectively. The corresponding objectives are compared between EA and OT. The improvement from EA to OT for the VSP objective is denoted by $\varepsilon^{VSP} := (C_{EA}^{VSP} - C_{OT}^{VSP}) / C_{EA}^{VSP}$, and the improvement for the SA objective is $\varepsilon^{SA} := (C_{EA}^{SA} - C_{OT}^{SA}) / C_{EA}^{SA}$. We see from Table 4.1 that for both VSP and SA objectives, the OT results yield significantly better performance than the benchmark EA results. We see both ε^{VSP} and ε^{SA} are insensitive to vehicle number N . Note that at the default values, the vehicle arrival rate is less than the intersection capacity, and thus no queue remains at the end of a green phase. This indicates vehicles arriving in different cycles shall belong to different platoons and the number of arrival vehicles does not much affect the average platoon size. This explains why ε^{VSP} and ε^{SA} are insensitive to N . As L increases, ε^{VSP} does not change much, which indicates that the saving of fuel consumption from trajectory smoothing is not much affected by the segment length. But ε^{SA} increases significantly as L increases, this is because a longer segment provides more space for trajectory smoothing and thus shall further reduce acceleration magnitudes. We see ε^{VSP} increases with C . This is probably because a longer signal cycle may force EA trajectories to stop for a longer time and thus cause more fuel consumption, while the OT trajectories may still have room to glide through without full stops. However, ε^{SA} decreases

Table 4.1: Comparison of objective values for signalized segments.

Parameter values	C_{EA}^{VSP} (kJ/ton)	C_{OT}^{VSP} (kJ/ton)	ε^{VSP}	C_{EA}^{SA} (m ² /s ⁴)	C_{OT}^{SA} (m ² /s ⁴)	ε^{SA}
Default	547.9	468.8	14%	63.2	7.9	88%
$N = 25$	549.1	473.1	14%	60.9	7.6	88%
$N = 75$	546.6	462.2	15%	65.9	8.4	87%
$L = 250\text{m}$	256.1	230.6	10%	66.6	25.5	62%
$L = 750\text{m}$	836.4	710.0	15%	66.8	4.2	94%
$C = 30\text{s}$	549.0	498.3	9%	58.3	3.9	93%
$C = 90\text{s}$	545.6	449.0	18%	69.1	11.8	83%
$r = 0.2$	552.4	477.7	14%	55.1	7.2	87%
$r = 0.6$	535.4	514.2	4%	89.7	49.7	45%

as C increases, which indicates a longer cycle increases the acceleration magnitudes of the smoothed trajectories. As r goes above 0.5, both ε^{VSP} and ε^{SA} decrease dramatically. Note when $r > 0.5$, the intersection capacity is less than the arrival vehicle rate, and thus more and more vehicles will be queued over cycles. An increasing queue occupies much of the segment space and diminishes the room for trajectory smoothing, and thus the trajectory smoothing effect is not as salient in this case.

4.3.3 Non-stop Intersection

This section investigates a one-lane non-stop intersection where trajectories of approaching vehicles are coordinated such that they all can pass the intersection without stops (Li and Wang, 2006; Dresner and Stone, 2008). We consider this intersection has two identical approaches of vehicles crossing at the intersection. The segment length of each approach is identical to L , and each approach has N vehicles and their arrival times are again generated by Equation (4.44). We rank these $2N$ vehicles from both approaches by their arrival times in an ascending order, denoted as n_1, n_2, \dots, n_{2N} . Assume the exit times of vehicles from both approaches follow a first-in-first-out (FIFO) protocol, i.e., $t_{n_1}^+ < t_{n_2}^+ < \dots < t_{n_{2N}}^+$, and all vehicles enter the intersection at speed \bar{v} so as to maximize the intersection throughput.

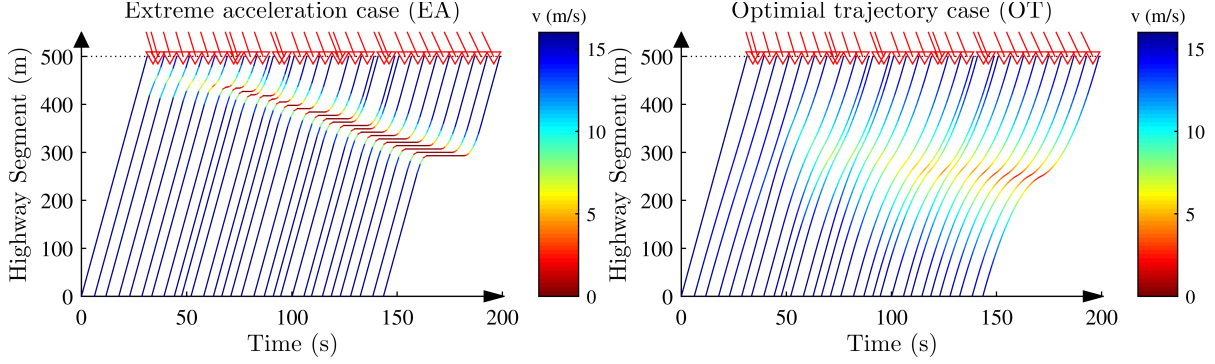


Figure 4.11: Non-stop intersection results: (a) trajectory plot for extreme accelerations (EA); and (b) optimal trajectory (OT) plot (red triangles mark the exit times of vehicles from the other approach).

Then for every two consecutive vehicles n_{i-1} and n_i , if they are from the same approach, then the separation of their exit times should be no less than $\tau + s/\bar{v}$ due to safety constraints (4.7). Otherwise, if n_{i-1} and n_i are from different approaches, we assume the separation of their exit times should be no less than a minimum switching headway h^S for safe crossing. With this FIFO protocol, vehicle exit times can be fixed as

$$t_{n_i}^+ = \begin{cases} 0, & \text{if } i = 1; \\ \max \left\{ t_{n_i}^- + L/\bar{v}, t_{n_{i-1}}^+ + \tau + s/\bar{v} \right\}, & \text{if vehicles } i \text{ and } i-1 \\ & \text{are from the same approach;} \\ \max \left\{ t_{n_i}^- + L/\bar{v}, t_{n_{i-1}}^+ + h^S \right\}, & \text{if vehicles } i \text{ and } i-1 \\ & \text{are from different approaches.} \end{cases}$$

The default parameters are set the same as those in the previous section except for $N = 30$ (which is for the clearance of trajectory plots in Figure 4.11), and in addition, h^S is set to 3s. For illustration purposes, we only investigate one approach. Figure 4.11 compares the trajectories between the benchmark EA case and the OT case. We see that the OT trajectories are much smoother than the EA trajectories and minimize the need for stops.

Table 4.2: Comparison of objective values for non-stop intersections.

Changed parameter	C_{EA}^{VSP} (kJ/ton)	C_{OT}^{VSP} (kJ/ton)	ε^{VSP}	C_{EA}^{SA} (m ² /s ⁴)	C_{OT}^{SA} (m ² /s ⁴)	ε^{SA}
Default	545.3	441.0	19%	81.0	8.5	90%
$N = 15$	548.3	481.5	12%	72.1	3.5	95%
$N = 45$	544.8	436.8	20%	83.1	13.1	84%
$L = 250\text{m}$	255.3	245.5	4%	81.0	57.0	30%
$L = 750\text{m}$	835.5	697.3	17%	81.0	4.0	95%
$r = 0.2$	578.8	575.9	0.5%	9.5	0.04	99.5%
$r = 0.6$	543.9	446.5	18%	86.1	21.1	75%

Table 4.2 compares results between the benchmark EA case and the OT case for problem instances with different parameters. The setting follows Table 4.1. For most instances, the improvement from EA to OT is significant for both the VSP and SA objectives. We see that as N increases, ε^{VSP} increases yet ε^{SA} decreases. Note that with the default saturation rate, the queue grows with the vehicle number and thus more upstream trajectories in the EA case would have higher speed variations or longer stop sections. The improvement of these upstream queued vehicles shall dominate ε^{VSP} and ε^{SA} values as N increases. As L grows, ε^{VSP} first increases and then decreases, which indicates there would be some intermediate segment length range best for fuel consumption saving. ε^{SA} consistently increases as L grows, which again is because a longer segment provides more room for smoother trajectories. When r is very low, the improvement of VSP is not apparent because traffic is anyway close to free flow. As r increases to a certain level at which traffic gets congested, ε^{VSP} seems to be insensitive as r further grows. Whereas ε^{SA} increases as r drops, which is because lower r provides more room to smooth trajectories closer to straight lines with near-zero accelerations.

4.4 Queuing Propagation Analysis

Intuitively, it may be easy to arrive at a conjecture that traffic smoothing would cause vehicles queued (or slowing down) at more upstream locations, or even cause further queue spillback. This section will investigate this conjecture by rigorously analyzing a special case of the studied problem with homogeneous settings. We assume that the entry headway and the exit headway between every two vehicles is the same, i.e.,

$$t_1^1 = 0, t_n^- = (n-1)(\tau + s/\bar{v})/r, \forall n \in \mathcal{M} \setminus \{1\}, \quad (4.45)$$

$$t_1^+ = L/\bar{v} + \Delta^S, t_n^+ = t_1^+ + (n-1)(\tau + s/\bar{v})/r, \forall n \in \mathcal{M} \setminus \{1\}. \quad (4.46)$$

where again parameter $r \in (0, 1]$ is the traffic saturation rate and $\Delta^S \geq 0$ is the phase shift (e.g., due to being blocked by a red light or coordination with the downstream segment). For the conciseness of the formulations, define $\gamma := \tau + s/\bar{v}$. With this, we obtain.

$$\Delta_n = \Delta^S, \forall n \in \mathcal{M},$$

$$\Delta_{n(n-1)} = \Delta^S - \gamma \left(\frac{1}{r} - 1 \right), \forall n \in \mathcal{M} \setminus \{1\}.$$

Note that for all vehicles in \mathcal{M} , we have $\Delta_{n(n-1)} > 0$. For each vehicle n , since the impact of trajectory smoothing starts at time $\delta_{n1}^*(\phi)$, we will investigate how $\delta_1^*(\phi)$, which marks the end of the trajectory-smoothing-induced queue, changes as ϕ varies. If the above-mentioned conjecture is true, $\delta_1^*(\phi)$ shall always decrease (or the trajectories always get smoother) as ϕ drops. This is to say, $\delta_1^*(\phi)$ increases with $\phi, \forall \phi \in (0, \infty)$. The following analysis will check whether this is true.

Define

$$\hat{\sigma}_n(\phi, \Delta^{\mathbf{S}}) = \hat{\delta}_{n1}^* \left(\delta_{(n-1)1}^*(\phi), \phi \right) - \delta_{(n-1)1}^*(\phi) = \alpha + \delta(\phi, \Delta_{n-1}) - \delta(\phi, \Delta^{\mathbf{S}}).$$

where $\alpha := -\tau \left(\frac{1}{r} - 1 \right) - \frac{s}{\bar{v}}$ for the conciseness of the formulation. This can be expanded as

$$\hat{\sigma}(\phi, \Delta^{\mathbf{S}}) = \alpha + \begin{cases} \sqrt{\frac{2\bar{v}}{\phi}} \left(\sqrt{\Delta^{\mathbf{S}}} - \sqrt{\Delta^{\mathbf{S}} - \gamma \left(\frac{1}{r} - 1 \right)} \right), & \text{if } \phi \leq \frac{\bar{v}}{2\Delta^{\mathbf{S}}}; \\ \Delta^{\mathbf{S}} + \frac{\bar{v}}{2\phi} - \sqrt{\frac{2\bar{v}}{\phi}} \sqrt{\Delta^{\mathbf{S}} - \gamma \left(\frac{1}{r} - 1 \right)}, & \text{if } \frac{\bar{v}}{2\Delta^{\mathbf{S}}} < \phi \leq \frac{\bar{v}}{2\Delta^{\mathbf{S}} - \gamma \left(\frac{1}{r} - 1 \right)}; \\ \gamma \left(\frac{1}{r} - 1 \right), & \text{if } \phi > \frac{\bar{v}}{2\Delta^{\mathbf{S}} - \gamma \left(\frac{1}{r} - 1 \right)}. \end{cases} \quad (4.47)$$

Note that $\hat{\sigma}_n(\phi, \Delta^{\mathbf{S}})$ indicates the difference between $\delta_{(n-1)1}^*(\phi)$ and $\delta_{n1}^*(\phi)$ as

$$\delta_{n1}^*(\phi) - \delta_{(n-1)1}^*(\phi) = \begin{cases} \hat{\sigma}_n(\phi, \Delta^{\mathbf{S}}), & \text{if } \hat{\sigma}_n(\phi, \Delta^{\mathbf{S}}) < 0; \\ 0, & \text{otherwise.} \end{cases}$$

With this formulation, we see that when $r = 1$, $\hat{\sigma}(\phi, \Delta_{n-1}) = -s/\bar{v}, \forall \phi$, and $\delta_1^* = t_n^\Delta - \delta(\phi, \Delta^{\mathbf{S}}) - (M-1)\underline{d}/\bar{v}$, which shall always increase with ϕ . Thus the conjecture trivially holds for this case. The following analysis will investigate the non-trivial case when $r \in (0, 1)$. In this case, we see that $\hat{\sigma}(\phi, \Delta^{\mathbf{S}})$ decreases with ϕ , $\lim_{\phi \rightarrow 0} \hat{\sigma}(\phi, \Delta^{\mathbf{S}}) = \infty$ and $\hat{\sigma}(\phi, \Delta^{\mathbf{S}}) = -s/\bar{v}, \forall \phi \geq \frac{\bar{v}}{2\Delta^{\mathbf{S}} - \gamma \left(\frac{1}{r} - 1 \right)}$. Since $\hat{\sigma}(\phi, \Delta^{\mathbf{S}})$ is apparently continuous with ϕ , then there must exist an $\phi^0 < \frac{\bar{v}}{2\Delta^{\mathbf{S}} - \gamma \left(\frac{1}{r} - 1 \right)}$ such that $\hat{\sigma}(\phi, \Delta^{\mathbf{S}}) > 0, \forall \phi \in (0, \phi^0)$ and $\hat{\sigma}(\phi, \Delta^{\mathbf{S}}) \leq 0, \forall \phi > \phi^0$. As ϕ increases from 0 to ϕ^0 , note that $\hat{\sigma}(\phi, \Delta^{\mathbf{S}}) \geq 0$ and thus $\delta_1^*(\phi) = \delta_{11}^*(\phi) = L/\bar{v} + \Delta^{\mathbf{S}} - \delta(\phi, \Delta^{\mathbf{S}})$, which shall increase with ϕ . Then we consider two cases:

- Case-1: If $\phi^0 < \frac{\bar{v}}{2\Delta^S}$. When $\phi \in \left[\phi^0, \frac{\bar{v}}{2\Delta^S}\right]$,

$$\begin{aligned}\delta_1^*(\phi) &= t_n^\Delta - \delta(\phi, \Delta^S) + (M-1)\hat{\sigma}(\phi, \Delta^S) \\ &= t_n^\Delta - (M-1)\alpha + \beta_1\phi^{-0.5},\end{aligned}$$

where

$$\beta_1 := \left[(M-2)\sqrt{2\bar{v}\Delta^S} - (M-1)\sqrt{2\bar{v}\left(\Delta^S - \gamma\left(\frac{1}{r} - 1\right)\right)} \right]. \quad (4.48)$$

If $\beta_1 \leq 0$, $\delta_1^*(\phi)$ continues to increase with $\phi \in \left[\phi^0, \frac{\bar{v}}{2\Delta^S}\right]$. Otherwise if $\beta_1 > 0$, $\delta_1^*(\phi)$ decreases with ϕ . Next, when $\phi \in \left[\frac{\bar{v}}{2\Delta^S}, \frac{\bar{v}}{2\left(\Delta^S - \gamma\left(\frac{1}{r} - 1\right)\right)}\right]$,

$$\delta_1^*(\phi) = t_n^\Delta - (M-1)\alpha + \beta_2(\phi).$$

where $\beta_2(\phi) := (M-2)\left(\Delta^S + \frac{\bar{v}}{2\phi}\right) - (M-1)\sqrt{2\bar{v}\left(\Delta^S - \gamma\left(\frac{1}{r} - 1\right)\right)}\phi^{-0.5}$. We can obtain

$$\frac{d\beta_2(\phi)}{d\phi} = \left[-(M-2)\frac{\bar{v}}{2\sqrt{\phi}} + (M-1)\sqrt{\frac{\bar{v}\left(\Delta^S - \gamma\left(\frac{1}{r} - 1\right)\right)}{2}} \right] \phi^{-1.5}$$

Therefore, if $\beta_1 \leq 0$, it is easy to see that $\frac{d\beta_2(\phi)}{d\phi} \geq 0$, and $\delta_1^*(\phi)$ will continue to increase

with ϕ . Otherwise if $\beta_1 > 0$, we shall have $\frac{d\beta_2\left(\frac{\bar{v}}{2\Delta^S}\right)}{d\phi} > 0$ and $\frac{d\beta_2\left(\frac{\bar{v}}{2\Delta^S - \gamma\left(\frac{1}{r} - 1\right)}\right)}{d\phi} < 0$.

Therefore, there exists a $\phi^E \in \left[\frac{\bar{v}}{2\Delta^S}, \frac{\bar{v}}{2\left(\Delta^S - \gamma\left(\frac{1}{r} - 1\right)\right)}\right]$ such that $\delta_1^*(\phi)$ decreases

with $\phi \in \left[\frac{\bar{v}}{2\Delta^S}, \phi^E\right]$ and increases with $\phi \in \left[\phi^E, \frac{\bar{v}}{2\left(\Delta^S - \gamma\left(\frac{1}{r} - 1\right)\right)}\right]$. Further, when $\phi > \frac{\bar{v}}{2\left(\Delta^S - \gamma\left(\frac{1}{r} - 1\right)\right)}$,

$$\delta_1^*(\phi) = t_n^\Delta - \delta(\phi, \Delta^S) - (M-1)s/\bar{v},$$

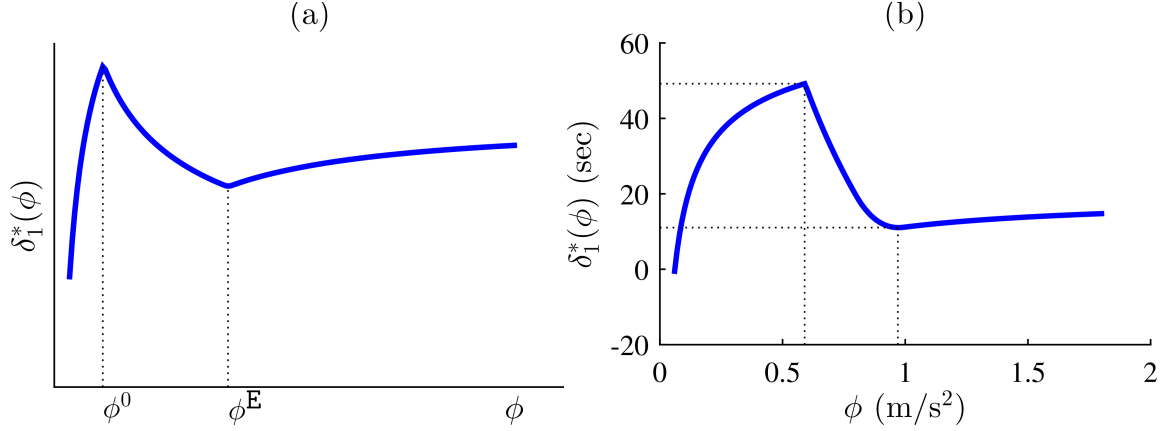


Figure 4.12: (a) Illustration of $\delta_1^*(\phi)$ vs. ϕ when $\beta_1 > 0$; (b) $\delta_1^*(\phi)$ vs. ϕ for the default instance.

which apparently increases with ϕ .

- Case-2: If $\phi^0 > \frac{\bar{v}}{2\Delta^S}$, the analysis for $\phi \in \left[\phi^0, \frac{\bar{v}}{2(\Delta^S - \gamma(\frac{1}{r} - 1))} \right]$ is the same as that for $\phi \in \left[\frac{\bar{v}}{2\Delta^S}, \frac{\bar{v}}{2(\Delta^S - \gamma(\frac{1}{r} - 1))} \right]$ in the previous case, and the analysis for $\phi > \frac{\bar{v}}{2(\Delta^S - \gamma(\frac{1}{r} - 1))}$ is the same as the previous case, too.

In both cases, if $\beta_1 \leq 0$, then $\delta_1^*(\phi)$ increases all the way with ϕ , which is consistent with the initial conjecture. However, if $\beta_1 > 0$, then $\delta_1^*(\phi)$ first increases with ϕ during $[0, \phi^0]$, then decreases with ϕ during $[\phi^0, \phi^E]$, and finally increases with ϕ during $[\phi^E, \infty)$, which is illustrated in Figure 4.12(a). This is contradictory to the initial conjecture, such that when $\phi \in [\phi^0, \phi^E]$, further decreasing ϕ (or smoothing the trajectories) actually helps reduce the length of the queue. This finding suggests that traffic smoothing does not always worsen queue spillback. Instead, it may help alleviate queuing if the smoothing is done appropriately.

To illustrate this analysis result, we show some examples in the following presentation. The default parameters are set as $L = 1000\text{m}$, $N = 100$, $\bar{v} = 16\text{m/s}$, $s = 7\text{m}$, $\tau = 1.5\text{s}$, $r = 0.5$, $\Delta^S = 10\text{m}$. With this setting, there is only one platoon in this traffic stream (i.e., $M = N$). Further, we obtain $\beta_1 = 162.9\text{m}^{0.5}$, $\phi^0 = 0.59\text{m/s}^2$, $\phi^E = 0.97\text{m/s}^2$, $\delta_1^*(\phi^0) = 49.2\text{s}$ and $\delta_1^*(\phi^E) = 11.0\text{s}$. The complete $\delta_1^*(\phi)$ to ϕ curve for this default instance is shown in Figure

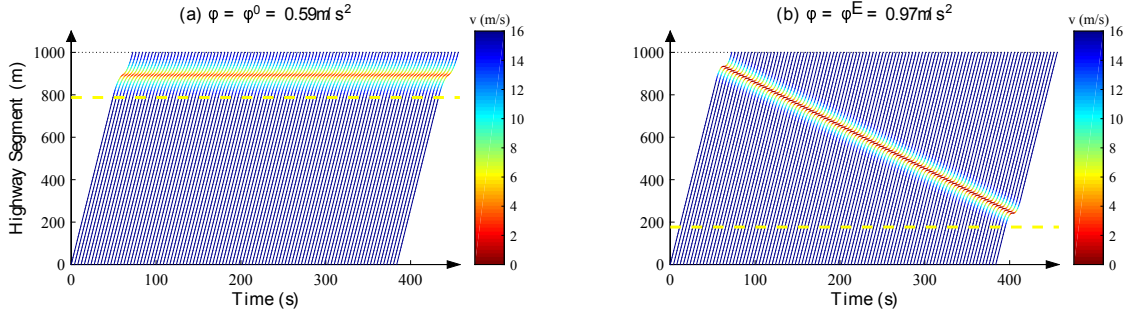


Figure 4.13: Trajectories for ϕ^0 and ϕ^E at the default parameter values (where the dashed yellow line marks the end of the queue).

4.12(b), which is consistent with the previous conclusion that $\beta_1 > 0$ indicates that $\delta_1^*(\phi)$ decreases on $[\phi^0, \phi^E]$. This also indicates that the end of queue is at 787.4m for $\phi = \phi^0$ and at 176.7m for $\phi = \phi^E$. The trajectories for these two cases are shown in Figure 4.13.

Next, we vary the N value and investigate its impact on the queue length. As illustrated in Figure 4.14(a), β_1 value increases linearly with N when there is only one platoon (or $M = N$). This can be also seen from the definition of β_1 in Equation (4.48). Figure 4.14(b) plots the values of $\delta_1^*(\phi^0)$ and $\delta_1^*(\phi^E)$ as β_1 increases (e.g., as a result of the increase of N). We see that $\delta_1^*(\phi^0)$ remains the same across different N value for the following reasons. Note that based on Equation (4.47) and the definition, ϕ^0 shall remain the same at 0.59 regardless of N or β_1 . Further, when $\phi = \phi_0$, no shock wave propagates backwards and the effect of traffic smoothing stays in a local area regardless of the N value. When $\beta_1 > 0$, ϕ^E shall split from ϕ^0 , and as a result we see that $\delta_1^*(\phi^E)$ decreases as β_1 increases from 0. Note that $(\delta_1^*(\phi^0) - \delta_1^*(\phi^E)) \cdot \bar{v}$ implies the queue distance that traffic smoothing can reduce by lowering ϕ from ϕ^E to ϕ^0 , which increases with β_1 (and thus N). Interestingly, this result indicates that even without modification of macroscopic traffic characteristics, backward propagation of stopping shock waves could be hampered by proper traffic smoothing, which only adjusts vehicle trajectories in a local area independent of the number of incoming vehicles (as long as the saturation rate remains the same). Further, as the number of incoming vehicles in

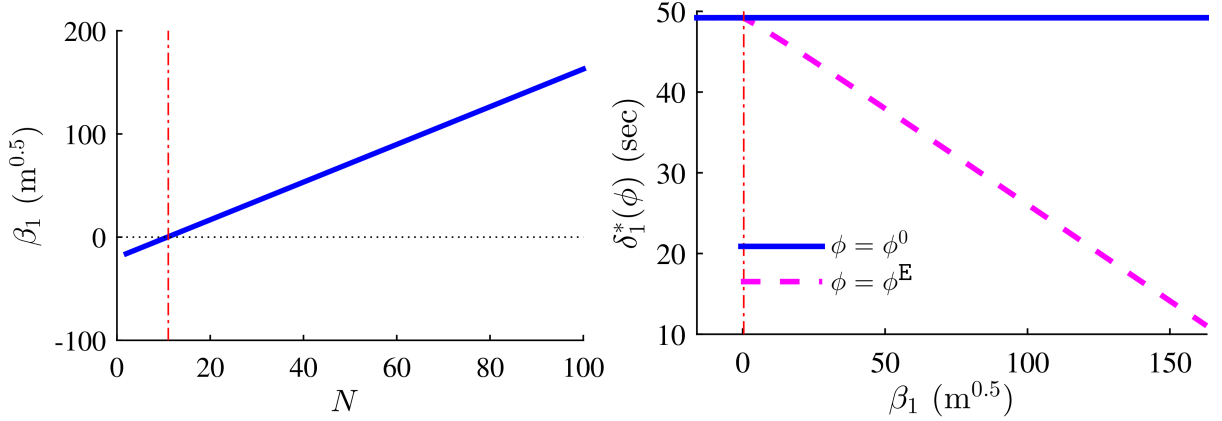


Figure 4.14: Results for instances with varying N : (a) N vs. β_1 ; and (b) β_1 vs. $\delta_1^*(\phi^0)$ and $\delta_1^*(\phi^E)$.

a platoon increases, there actually could be more potential to reduce the queue length by traffic smoothing.

4.5 Chapter Summary

This chapter investigates a trajectory smoothing problem for a general one-lane highway segment with pure CAVs and provides elegant theoretical insights and efficient algorithmic methods. Inspired by previous studies from Co-author Li’s research team, this problem is simplified to one where each vehicle’s trajectory is approximated with no more than five pieces of consecutive quadratic functions and all trajectories share identical acceleration and deceleration rates in the same platoon. This simplified problem is shown to have elegant theoretical properties in the objective shape and the feasible region. These properties lead to the development of an exact solution algorithm that efficiently solves the true optimum to this problem with only a series of analytical operations. The optimal solution can be intuitively interpreted as stretching all trajectories as smooth as the feasibility allows. Numerical examples reveal that the proposed analytical exact algorithm solves the problem much faster with the same or better solution quality compared with its numerical predecessor proposed earlier in Ma et al. (2017). They also illustrate the applications of this algorithm

to various CAV trajectory smoothing problems, e.g., on signalized segments and at non-stop intersections. Further, by constructing a homogeneous special case, we analyze how traffic smoothing affects propagation of the vehicle queue. We find that counter-intuitively, proper traffic smoothing may reduce the queue length or confine traffic slowdown within a local area without further propagation.

CHAPTER 5: JOINT TRAJECTORY AND SIGNAL OPTIMIZATION

This chapter proposes a joint trajectory and signal optimization model for signalized crossing points. The proposed optimization model is described as follows.

5.1 Problem Setting

We consider a two-way signalized conflict zone (e.g., an intersection) connecting two directions indexed by $i \in \mathcal{I} := \{1, 2\}$, and let l_i and l^C denote the length of the highway section at each direction $i, \forall i \in \mathcal{I}$ and the crossing point, respectively. For each direction i , a longitudinal coordinate system is defined along the highway that increases toward the intersection. A traffic signal is installed at the conflict zone with the signal timing plan of $\mathcal{S} := \{R_1, R_2, C\}$, where R_i is the effective red interval for direction $i, \forall i \in \mathcal{I}$, and C denotes the signal cycle time. This study considers a pure-automated traffic where all vehicles are controllable CAVs. At each direction i , a stream of CAVs moves toward the crossing point that are indexed as $n \in \mathcal{N}_i := \{1, 2, \dots, N_i\}, \forall i \in \mathcal{I}$. We assume that the traffic at both directions are homogeneous and denote the traffic arrival rate at direction i by $\lambda_i, \forall i \in \mathcal{I}$. With the homogeneity assumption and for simplicity, problem can be investigated during only one C , and then the obtained control outcomes can be applied to the following cycles. Given C , N_i is calculated as $N_i = \lfloor C\lambda_i \rfloor, \forall i \in \mathcal{I}$. It is assumed that CAVs at each direction can be controlled by a centralized controller in a control zone. Let τ denote the CAV communication and control delay.

Let $\mathcal{X}_i := \{x_{in}(t)\}$ be the set of CAV trajectory functions at direction i , where $x_{in}(t)$ is the location of vehicle n at direction i at time t . $\dot{x}_{in}(t)$ and $\ddot{x}_{in}(t)$ represent first and

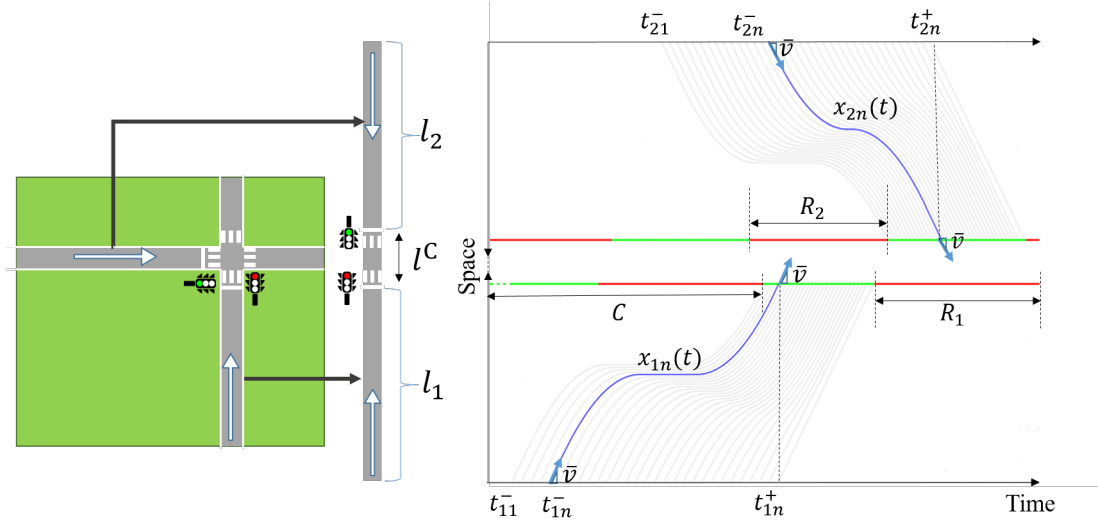


Figure 5.1: Problem statement.

second order differential that indicate the instantaneous speed and acceleration of vehicle n at direction i at time t , respectively. The speed limit on this freeway section is denoted by \bar{v} , and the minimum and maximum accelerations for all CAVs at any time are denoted by \underline{a} and \bar{a} , respectively. Let t_{in}^- and t_{in}^+ denote the arrival and departure times of vehicle n at direction i to/from the control zone for $\forall i \in \mathcal{I}$, respectively. Note that t_{in}^- can be accurately estimated with the advanced CAV technologies, and thus considered as predetermined in this study. However, t_{in}^+ is a variable that is determined by the signal timing plan \mathcal{S} . It is assumed that CAVs arrive and depart the control zone with the maximum speed of \bar{v} . Without much loss of generality, both crossing point are assumed to have the same saturation flow rate of $\mu := \frac{1}{\tau+s/\bar{v}}$. Let $\gamma_i := (1/\lambda_i - 1/\mu)$ define the arrival and exit time headway difference, for all $i \in \mathcal{I}$, respectively. Figure 5.1 illustrates the problem setting for a two-way signalized intersection. Note that for visualization purposes, we rotate the plot for direction 2 as shown in this figure.

5.2 Primary Optimization (PO)

This section presents the primary optimization problem formulation and proposes a heuristic solution approach.

5.2.1 Model Formulation

This section formulates the PO problem. This model is formulated considering t_{i1}^- as a reference point for each $i \in \mathcal{I}$. With this and the homogeneity assumption, we obtain $t_{in}^- = t_{i1}^- + \frac{n-1}{\lambda_i}, \forall i \in \mathcal{I}$. Each CAV trajectory in $\mathcal{X}_i, i \in \mathcal{I}$ shall satisfy the following constraints.

- Entry boundary constraints: At each direction i , CAV n arrives location 0 at speed of \bar{v} at a predetermined time t_{in}^- , i.e.,

$$x_{in}(t_{in}^-) = 0, \forall n \in \mathcal{N}_i, i \in \mathcal{I}, \quad (5.1)$$

$$\dot{x}_{in}(t_{in}^-) = \bar{v}, \forall n \in \mathcal{N}_i, i \in \mathcal{I}. \quad (5.2)$$

- Exit boundary constraints: At each direction i , each CAV n shall exit location l_i at speed of \bar{v} at time t_{in}^+ , i.e.,

$$x_{in}(t_{in}^+) = l_i, \forall n \in \mathcal{N}_i, i \in \mathcal{I}, \quad (5.3)$$

$$\dot{x}_{in}(t_{in}^+) = \bar{v}, \forall n \in \mathcal{N}_i, i \in \mathcal{I}, \quad (5.4)$$

$$t_{in}^+ = t_{in}^- + \frac{l_i}{\bar{v}} + \max(0, R_i - (n-1)\gamma_i). \quad (5.5)$$

- Speed constraint: We do not allow the CAVs to back up, and they cannot go beyond the speed limit \bar{v} , i.e.,

$$\dot{x}_{in}(t) \in [0, \bar{v}], \forall t \in [t_{in}^-, t_{in}^+], n \in \mathcal{N}_i, i \in \mathcal{I}. \quad (5.6)$$

- Acceleration constraint: We set the CAV acceleration values bounded by \underline{a} and \bar{a} , i.e.,

$$\ddot{x}_{in}(t) \in [\underline{a}, \bar{a}], \forall t \in [t_{in}^-, t_{in}^+], n \in \mathcal{N}_i, i \in \mathcal{I}. \quad (5.7)$$

- Safety constraint: The trajectories of every two consecutive CAVs shall maintain a certain safety headway. We require that this the distance gap between vehicle n 's location and $(n-1)$'s location a communication delay τ ago at each direction i is no less than a jam spacing s_0 at any time $t \in [t_{in}^-, t_{i(n-1)}^+]$, i.e.,

$$x_{i(n-1)}(t-\tau) - x_{in}(t) \geq s_0, \forall t \in [t_{in}^-, t_{i(n-1)}^+], n \in \mathcal{N}_i \setminus \{1\}, i \in \mathcal{I}. \quad (5.8)$$

Each trajectory in $\mathcal{X}_i, i \in \mathcal{I}$ is associated to two operational costs as follows.

- Travel time delay: The travel time delay of each CAV at both directions is affected by the signal timing plan \mathcal{S} . We let $D_i(\mathcal{S})$ denote the total unit-time travel time delay for direction $i, \forall i \in \mathcal{I}$, which can be determined by summing over the delays of all CAVs that depart from the signal within one C period. Figure 5.2 illustrates the calculation of $D_i(\mathcal{S})$. This figure plots the CAV trajectories that could pass the signal within one C period. The gray-colored trajectories represent the non-delayed imaginary trajectories corresponding to the real trajectories shown as blue curves. The non-delayed trajectories are determined assuming that the signal light is always green and thus continue with the constant speed of \bar{v} . As a result of the signal red interval,

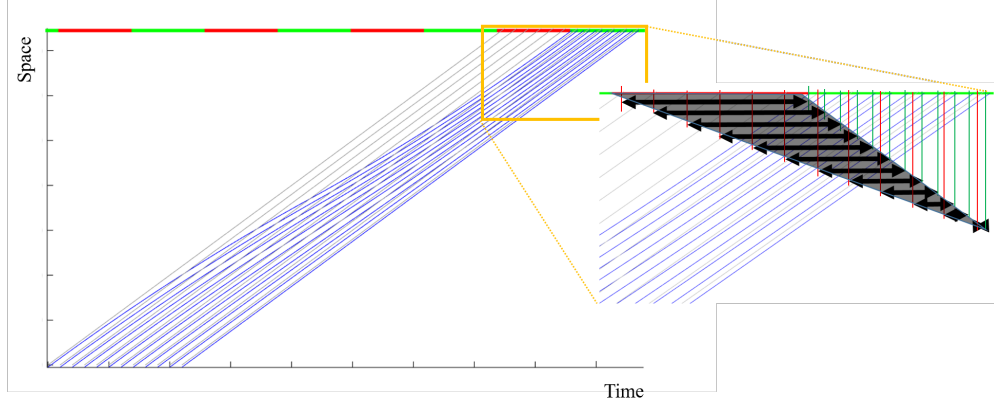


Figure 5.2: An illustration to $D_i(\mathcal{S})$ calculation.

each trajectory is delayed and the amount of these delays are shown as double-arrows in the inset figure. $D_i(\mathcal{S})$ can be determined by summing over all of these delays. This microscopic point of view to travel time delay leads us a macroscopic measure formulated as

$$D_i(\mathcal{S}) = \frac{R_i^2}{2C \left(1 - \frac{\lambda_i}{\mu}\right)}, \forall i \in \mathcal{I}.$$

- Fuel consumption: Fuel consumption of each CAV n is a function of the instantaneous speed and acceleration values between the arrival time t_{in}^- and the departure time t_{in}^+ . Thus this measure is affected by both the trajectory shapes, i.e., \mathcal{X}_i at each direction i and the signal timing plan \mathcal{S} (\mathcal{S} would determines $t_{in}^+, \forall n \in \mathcal{N}_i, i \in \mathcal{I}$). We let $F_i(\mathcal{X}_i, \mathcal{S})$ denote the unit-time fuel consumption function for direction $i, \forall i \in \mathcal{I}$, which can be determined by summing over the fuel consumption values of all CAVs that depart from the signal within one C period, as formulated below

$$F_i(\mathcal{X}_i, \mathcal{S}) := \frac{1}{C} \sum_{n=1}^{N_i} \int_{t_{in}^-}^{t_{in}^+} e(\dot{x}_{in}(t), \ddot{x}_{in}(t)) dt, \forall i \in \mathcal{I}, \quad (5.9)$$

where $e(\dot{x}_{in}(t), \ddot{x}_{in}(t))$ is the instantaneous cost function of $x_{in}(t)$ at time point t that could implement any instantaneous fuel consumption model in the literature (e.g., CMEM (Barth et al., 2000), VT-micro (Ahn, 1998), MOVES (Koupal et al., 2002), etc.).

Now, the primary trajectory optimization problem is formulated as

$$\text{PO} : \min_{\mathcal{X}_i, \mathcal{S}} O^{\text{PO}}(\mathcal{X}_i, \mathcal{S}) := \sum_i (D_i(\mathcal{S}) + wF_i(\mathcal{X}_i, \mathcal{S})), \quad (5.10)$$

subject to Constraints (5.1)-(5.8). In Equation (5.10), w is a coefficient factor that determines the importance of $F_i(\mathcal{X}_i, \mathcal{S})$ compared to $D_i(\mathcal{S})$ in the objective function.

5.3 Simplified Macroscopic Optimization (SMO)

The PO problem formulated in Sub-section 5.2.1 is hard to be solved to the exact optimal due the infinite-dimensional variables, highly non-linear objectives and vehicle dependency in the constraints. Instead, this study formulates a simplified model that modifies the PO problem in two ways. The first adaptation that is based on the approach proposed by Li et al. (2017) restricts each CAV trajectory to consist of no more than five quadratic segments. According to Li et al. (2017), this simplified function reduces the feasible region of the optimization problem and yet the obtained solutions are very close to the true optimum. Second, instead of the highly non-linear function of the instantaneous fuel consumption in Equation (5.9), this study proposes a simplified macroscopic fuel consumption function that can be solved to the exact optimal. This section presents the model formulation and the analytical solution to this problem.

5.3.1 Model Formulation

This sub-section formulates the simplified macroscopic optimization (SMO) problem. The signalized control allows a number of CAVs to pass the crossing point during each cycle time C , and thus separates CAVs into several platoons. In this study, a CAVs platoon is referred to the stream of CAVs that pass the crossing point during a cycle length C . The following SMO model formulations are also presented for one C cycle.

5.3.1.1 Near-optimum Trajectory Construction

SMO restricts that each CAV trajectory $x_{in}(t)$ has at most five quadratic segments. Let a_{in} denote the acceleration magnitude of trajectory $x_{in}(t)$ that is bounded to $[\underline{a}, \bar{a}]$, $\forall n \in \mathcal{N}_i, i \in \mathcal{I}$, and $t_{in}^1 \leq t_{in}^2 \leq t_{in}^3 \leq t_{in}^4 \in [t_{in}^-, t_{in}^+]$ denote the joint time points between these sections. At a joint between two pieces, $x_{in}(t)$ is defined as the left differential, $\forall n \in \mathcal{N}_i, i \in \mathcal{I}$. The first segment of $x_{in}(t)$ during time interval $[t_{in}^-, t_{in}^1]$ cruises at the constant speed of \bar{v} . Let $\delta_n^i := (t_{in}^1 - t_{in}^-) \bar{v}, \forall n \in \mathcal{N}_i, i \in \mathcal{I}$ denote the length of this segment. Note that this segment does not necessarily exist for all trajectories. If this segment does not exist, then we set $t_{in}^1 = t_{in}^-$ and thus $\delta_{in} = 0$. The way to determine δ_{in} is explained later in this section of the study. The second time interval $(t_{in}^1, t_{in}^2]$ decelerates at a constant deceleration rate of $-a_{in}$. The third segment during time interval $(t_{in}^2, t_{in}^3]$ exists only if $x_{in}(t)$ has to make a stop. Otherwise, $t_{in}^3 = t_{in}^2$, and this segment does not exist. The fourth segment during time interval $(t_{in}^3, t_{in}^4]$ accelerates at a constant rate of a_{in} . Finally, the last segment during time interval $(t_{in}^4, t_{in}^+]$ cruises at speed \bar{v} and reaches the signal location L at exit time t_{in}^+ . Figure 5.3 illustrates the trajectory function shape and its segments for a two directional signalized intersection.

The proposed near-optimum piecewise quadratic trajectory function form is determined by two variables: acceleration magnitude a_{in} and initial cruising length δ_{in} ,

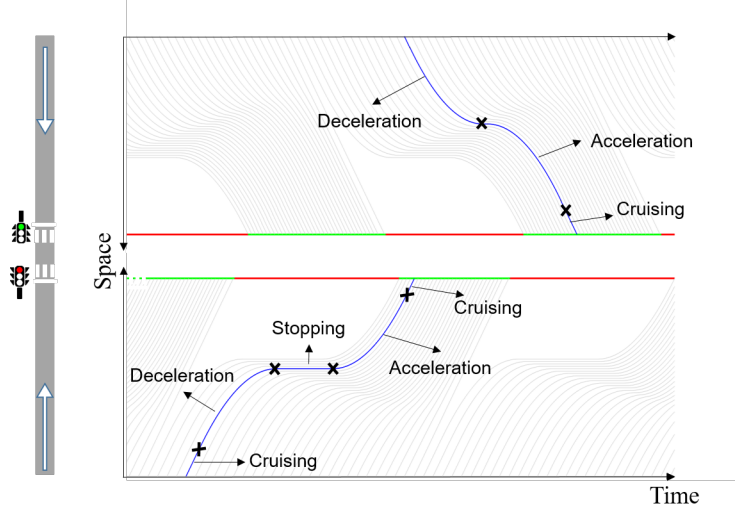


Figure 5.3: An illustration to the piecewise quadratic trajectory function form.

$\forall n \in \mathcal{N}_i, i \in \mathcal{I}$. Let $\mathcal{X}_i^{\text{NO}}$ be the set of the near-optimum CAV trajectory functions at direction i . Given a_{in} and δ_{in} , each $x_{in}(t) \in \mathcal{X}_i^{\text{NO}}$ is formulated as:

$$x_{in}(t) = \begin{cases} \delta_{in}, & \text{if } t \in [t_{in}^-, t_{in}^1]; \\ \delta_{in} + \bar{v}(t - t_{in}^1) - 0.5a_{in}(t - t_{in}^1)^2, & \text{if } t \in (t_{in}^1, t_{in}^2]; \\ \delta_{in} + \bar{v}(t - t_{in}^2) - 0.5a_{in}^i(t - t_{in}^2)^2, & \text{if } t \in (t_{in}^2, t_{in}^3]; \\ \delta_{in} + \bar{v}(t_{in}^2 - t_{in}^1) - 0.5a_{in}(t_{in}^2 - t_{in}^1)^2 + \\ (\bar{v} - a_{in}(t_{in}^2 - t_{in}^1))(t - t_{in}^3) + 0.5a_{in}(t - t_{in}^3)^2, & \text{if } t \in (t_{in}^3, t_{in}^4]; \\ l_i - \bar{v}(t_{in}^+ - t), & \text{if } t \in (t_{in}^4, t_{in}^+]; \end{cases}, \forall n \in \mathcal{N}_i, i \in \mathcal{I}. \quad (5.11)$$

As noted before, infinite number of variables associated to CAV trajectories have to be solved in the original PO problem. Now, with this simplification, the number of variables is significantly reduced to only two for $x_{in}(t) \in \mathcal{X}_i^{\text{NO}}$, which makes the SMO problem

much more tractable. Next, we investigate how to determine decision variables a_{in} and δ_{in} , $\forall n \in \mathcal{N}_i, i \in \mathcal{I}$. Let Δ_{in} and T_{in} denote the length of the last cruising segment and total duration of $x_{in}(t)$, $\forall n \in \mathcal{N}_i, i \in \mathcal{I}$, respectively. For the first trajectory, we set $\Delta_{i1} = 0$ and obtain $T_{i1} = l_i/\bar{v} + \max(0, R_i - 1/\lambda_i + 1/2\mu)$, $\forall i \in \mathcal{I}$. Then the number of CAV trajectories that are delayed during one C , denoted by N_i^d , is determined as:

$$N_i^d = \left\lfloor \frac{T_{i1} - l_i/\bar{v}}{1/\lambda_i - 1/\mu} + 1 \right\rfloor, \forall i \in \mathcal{I}.$$

Then, for any CAV trajectory after N_i^d , safety constraint (5.8) is not activated and thus they move with constant maximum \bar{v} , i.e.,

$$\begin{aligned} \Delta_{in} &= 0, \forall n \in \{N_i^d + 1, \dots, N_i\}, \\ a_{in} &= 0, \forall n \in \{N_i^d + 1, \dots, N_i\}. \end{aligned}$$

Let $x_{in}^s(t)$ define a shadow trajectory of $x_{in}(t)$ as:

$$x_{in}^s(t) := x_{in}(t - \tau) - s_0, \forall n \in \mathcal{N}_i, i \in \mathcal{I}.$$

According to safety constraint (5.8), $x_{in}(t)$ should be always below or at maximum tangent to $x_{i(n-1)}^s(t)$. Therefore, $x_{in}(t_{in}^1 : t_{in}^4)$ is always below or at maximum tangent to $x_{i(n-1)}^s(t_{i(n-1)}^1 + \tau : t_{i(n-1)}^4 + \tau)$. To set $x_{in}(t_{in}^1 : t_{in}^4)$ as close as possible to $x_{i(n-1)}^s(t_{i(n-1)}^1 + \tau : t_{i(n-1)}^4 + \tau)$ and ensure the maximum throughput at the crossing point, we require that $x_{in}(t)$ get tangent to $x_{i(n-1)}^s(t)$ at $t = t_{in}^4$, for all $n \in \mathcal{N}_i \setminus \{1\} \cup \{N_i^d + 1, \dots, N_i\}$, $i \in \mathcal{I}$. Therefore, we obtain

$$t_{in}^4 - t_{in'}^4 = \tau(n - n'), \forall n, n' \in \mathcal{N}_i \setminus \{N_i^d + 1, \dots, N_i\}, i \in \mathcal{I}, \quad (5.12)$$

$$x_{in'}(t_{in'}^4) - x_{in}(t_{in}^4) = s_0(n - n'), \forall n, n' \in \mathcal{N}_i \setminus \{N_i^d + 1, \dots, N_i\}, i \in \mathcal{I}. \quad (5.13)$$

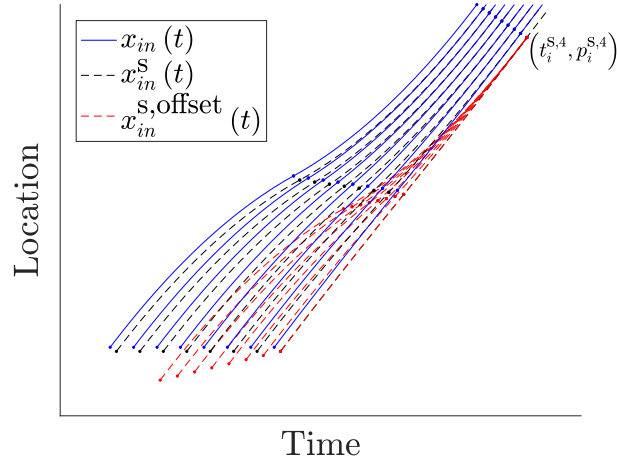


Figure 5.4: An illustration to $x_{in}^s(t)$ and $x_{in}^{s,offset}(t)$.

Equations (5.12)-(5.13) yield

$$\Delta_{in} = s_0(n-1), \forall n \in \mathcal{N}_i \setminus \{N_i^d + 1, \dots, N_i\}, i \in \mathcal{I}. \quad (5.14)$$

Let $x_{in}^{s,offset}(t)$ define an offset shadow trajectory of $x_{in}(t)$ as:

$$x_{in}^{s,offset}(t) := x_{in}^s(t - (N_i^d - n)\tau) - (N_i^d - n)s_0, \forall n \in \mathcal{N}_i \setminus \{N_i^d + 1, \dots, N_i\}, i \in \mathcal{I}. \quad (5.15)$$

According to Equations (5.12)-(5.13) and (5.15), all $x_{in}^{s,offset}(t)$ at each direction $i \in \mathcal{I}$, get tangent at the same point $(t_i^{s,4}, p_i^{s,4}) := (t_{i1}^+ - N_i^d\tau, l_i - N_i^d s_0)$, $\forall i \in \mathcal{I}$. Figure 5.4 illustrates $x_{in}^s(t)$ and $x_{in}^{s,offset}(t)$.

According to safety constraint (5.8), $x_{in}^{s,offset}(t)$ should be always below or at maximum tangent to $x_{i(n-1)}^{s,offset}(t)$. To meet this constraint and at the same time set $x_{i(n-1)}^{s,offset}(t)$ as close as possible to $x_{in}^{s,offset}(t)$ for all $n \in \mathcal{N}_i \setminus \{N_i^d + 1, \dots, N_i\}, i \in \mathcal{I}$, a_{in} and δ_{in} are found such that a_{in} is not an increasing function of vehicle index n . Let $f_i^0(n)$ denote the acceleration

function assuming that $\delta_{in} = 0, \forall n \in \mathcal{N}_i \setminus \{N_i^d + 1, \dots, N_i\}, i \in \mathcal{I}$ that is determined as:

$$f_i^0(n) := \begin{cases} \frac{\bar{v}^2}{l_i - s_0(n-1)}, & n \leq 1 + \frac{T_{i1}\bar{v} - 2l_i}{\gamma_i\bar{v} - s_0}; \\ \frac{4\bar{v}^2(-\gamma_i\bar{v}n + (T_{i1} + \gamma_i)\bar{v} - l_i)}{((- \gamma_i\bar{v} - s_0)n + (T_{i1} + \gamma_i)\bar{v} + s_0)^2}, & n > 1 + \frac{T_{i1}\bar{v} - 2l_i}{\gamma_i\bar{v} - s_0}; \end{cases}, \forall n \in \mathcal{N}_i \setminus \{N_i^d + 1, \dots, N_i\}, i \in \mathcal{I}, \quad (5.16)$$

where the first and the second function pieces determine the acceleration for the trajectories with and without stopping sections, respectively. Let $a_i^{\text{cr}} := \max(f_i^0(n))$ and $n_i^{\text{cr}} := f_i^{0-1}(a_i^{\text{cr}})$ denote the maximum acceleration and the corresponding vehicle index, respectively. a_i^{cr} is calculated as:

$$a_i^{\text{cr}} = \max\left(\frac{\bar{v}^2(\gamma_i\bar{v} - s_0)}{l_i(\gamma_i\bar{v} + s_0) - T_{i1}\bar{v}s_0}, \frac{\gamma_i^2\bar{v}^4}{(\gamma_i\bar{v} + s_0)(l_i(\gamma_i\bar{v} + s_0) - T_{i1}\bar{v}s_0)}\right), \forall i \in \mathcal{I}. \quad (5.17)$$

Then, to make a_{in} a decreasing function of n , we set $a_{in} = a_i^{\text{cr}}, \forall n \leq n_i^{\text{cr}}$ and $a_{in} = f_i^0(n), \forall n > n_i^{\text{cr}}$, i.e.,

$$a_{in} = \begin{cases} a_i^{\text{cr}}, & n \leq n_i^{\text{cr}}; \\ f_i^0(n), & n > n_i^{\text{cr}}; \end{cases}, \forall n \in \mathcal{N}_i \setminus \{N_i^d + 1, \dots, N_i\}, i \in \mathcal{I}. \quad (5.18)$$

Figure 5.5 illustrates the a_{in} derivation.

Given a_{in} , δ_{in} is calculated such that $x_{in}^{\text{s,offset}}(t)$ gets tangent to $x_{i(n-1)}^{\text{s,offset}}(t)$ for all $n \in \mathcal{N}_i \setminus \{\{1\} \cup \{N_i^d + 1, \dots, N_i\}\}, i \in \mathcal{I}$. Let $T_{in}^{\text{s,offset}} = T_{i1} - \gamma_i(n-1) - \Delta_{in}/\bar{v}$ and $l_{in}^{\text{s,offset}} := l_i - s_0(n-1)$ denote the duration and length of $x_{in}^{\text{s,offset}}(t), \forall n \in \mathcal{N}_i \setminus \{N_i^d + 1, \dots, N_i\}, i \in \mathcal{I}$. To determine δ_{in} , first assume that no stopping section is required. Let δ_{in}^{ns} be the obtained δ_{in} without a stopping section. Given a_{i1} and T_{i1} , δ_{i1}^{ns} is determined as

$$\delta_{i1}^{\text{ns}} = T_{i1}^{\text{s,offset}}\bar{v} - \frac{2\bar{v}\sqrt{-a_{i1}(l_i - T_{i1}^{\text{s,offset}}\bar{v})}}{a_{i1}}, \forall i \in \mathcal{I}. \quad (5.19)$$

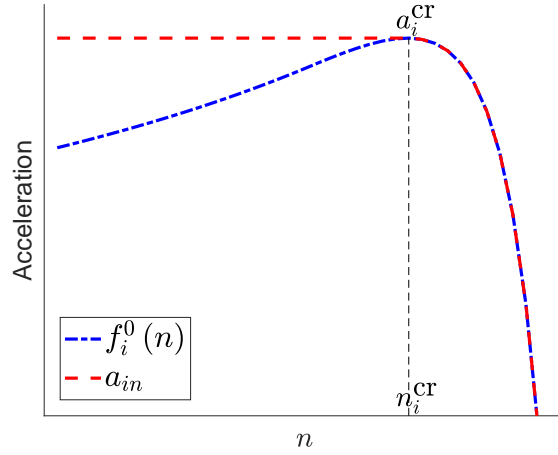


Figure 5.5: An illustration to a_{in} derivation.

Further, for each $n > 1$, a local coordinate system is set at the origin of $x_{i(n-1)}^{s, \text{offset}}(t)$, and find the tangent to $x_{i(n-1)}^{s, \text{offset}}(t)$. With this, δ_{in}^{ns} is calculated as:

$$\delta_{in}^{\text{ns}} = T_{in}^{s, \text{offset}} \bar{v} - \frac{2\bar{v} \sqrt{a_{in} (T_{in}^{s, \text{offset}} \bar{v} + s_0 - l_{i(n-1)}^{s, \text{offset}})}}{a_{in}}, \forall n \in \mathcal{N}_i \setminus \{1\} \cup \{N_i^d + 1, \dots, N_i\}, i \in \mathcal{I}. \quad (5.20)$$

Given δ_{in}^{ns} , we check if any stopping section is required for $x_{in}^{s, \text{offset}}(t)$. Define $v_{in}^m := \bar{v} - a_{in} (T_{in}^{s, \text{offset}} - \delta_{in}^{\text{ns}} / \bar{v}) / 2, \forall n \in \mathcal{N}_i \setminus \{1\} \cup \{N_i^d + 1, \dots, N_i\}, i \in \mathcal{I}$. If $v_{in}^m > 0$, then no stopping is required, and thus $\delta_{in} = \delta_{in}^{\text{ns}}$. Otherwise, a stopping section should be added. Let δ_{in}^s be the obtained δ_{in} with a stopping section that is determined as

$$\delta_{in}^s = l_{in}^{s, \text{offset}} - \frac{\bar{v}^2}{a_{in}}, \forall n \in \mathcal{N}_i \setminus \{1\} \cup \{N_i^d + 1, \dots, N_i\}, i \in \mathcal{I}. \quad (5.21)$$

Therefore, we obtain

$$\delta_{in} = \begin{cases} \delta_{in}^{\text{ns}}, & \text{if } v_{in}^{\text{m}} > 0; \\ \delta_{in}^{\text{s}}, & \text{if } v_{in}^{\text{m}} \leq 0; \end{cases}, \forall n \in \mathcal{N}_i \setminus \{N_i^{\text{d}} + 1, \dots, N_i\}, i \in \mathcal{I}. \quad (5.22)$$

With Equations (5.11) and (5.16)-(5.22), $x_{in}(t) \in \mathcal{X}_i^{\text{NO}}$ are determined. This study simplifies the objective function in the following sub-section.

5.3.1.2 Macroscopic Fuel Consumption Function

In addition to making simplifications in the CAV trajectory function shapes, this study proposes a macroscopic fuel consumption to further simplify the PO problem. Given $\mathcal{X}_i^{\text{NO}}$ at each direction i , the fuel consumption model formulated in Equation (5.9) is a function of \mathcal{S} , or more specifically, the excessive delay imposed by R_i . This fuel consumption includes two components: a minimum constant fuel consumption (assuming that $R_i = 0$ and CAVs move with maximum constant speed), and a marginal fuel consumption that is impacted by the delay caused by R_i . Let $F_i^{\text{marginal}}(R_i)$ denote the marginal fuel consumption at direction $i \in \mathcal{I}$. The $F_i^{\text{marginal}}(R_i)$ values are plotted against different R_i values for a specific direction i as shown in Figure 5.6. Interestingly, these scatter points could be well-fitted with a polynomial curve, which implies that the complex fuel consumption function can be represented with a very simple quadratic function of R_i . Let $F_i^{\text{NO}}(\mathcal{S})$ denote the simplified fuel consumption function. With this, we obtain $F_i(\mathcal{X}_i^{\text{NO}}, \mathcal{S}) \approx F_i^{\text{NO}}(\mathcal{S}) := f(R_i) + \Phi$, where Φ is the aforementioned constant fuel consumption component.

5.3.1.3 SMO Formulation

With these two simplifications and with Equations (5.2)-(5.9), PO problem (5.10) can be reformulated as a simple function of R_1 and C :

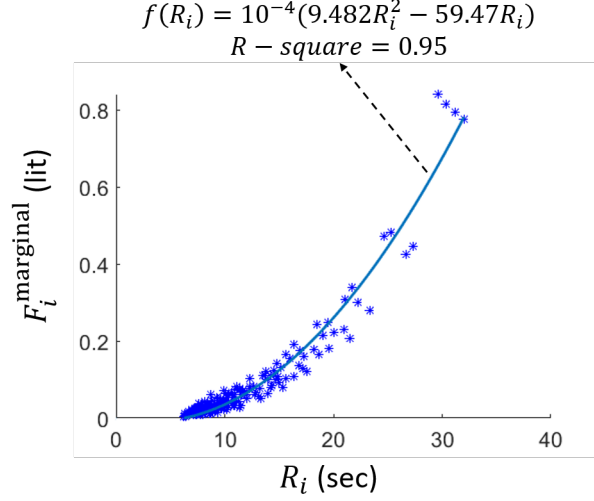


Figure 5.6: $F_i^{\text{marginal}}(R_i)$ vs. R_i .

$$\text{SMO} : \min_{R_1, C} O^{\text{simp}}(R_1, C) := \frac{\alpha R_1^2 + \beta(C) R_1 + \gamma(C)}{2C\gamma_1\gamma_2\lambda_1\lambda_2}, \quad (5.23)$$

$$\alpha = 4w\phi_1\gamma_1\gamma_2\lambda_1\lambda_2 + \gamma_1\lambda_1 + \gamma_2\lambda_2,$$

$$\beta(C) = -4\gamma_1\lambda_1 \left(w\gamma_2\lambda_2\phi_1(C-L) - \frac{1}{2}(C+L) \right),$$

$$\gamma(C) = \gamma_1\lambda_1 (2w\gamma_2\lambda_2(\phi_1(C+L) + \phi_2) + C+L)(C+L),$$

where $\phi_1 = 0.0009482$ and $\phi_2 = -0.005947$ are regression coefficients. Note that given R_1 and C , R_2 can be determined, and thus excluded in SMO formulation and the following analyses. Next, the analytical solution to SMO problem is presented in the following sub-section.

5.3.2 Analytical Solution

This sub-section presents the analytical solution to the SMO problem. Let R_i^{opt} denote the optimal solution to $R_i, \forall i \in \mathcal{I}$. This solution algorithm first solves R_1^{opt} as a

function of C . Then, with that SMO problem (5.23) can be reformulated as a EOQ-shaped function with the single decision variable C that could be analytically solved.

Given C and with SMO problem (5.23), unbounded optimal R_1 , denoted by $R_1^*(C)$, can be determined as:

$$R_1^*(C) = \frac{-\beta(C)}{2\alpha}.$$

$R_1^{\text{opt}}(C)$ is basically the minimum feasible R_1 value. Thus to derive $R_1^{\text{opt}}(C)$, we need to determine the bounds to R_1 . Let R_1^- and R_1^+ denote the lower and upper bounds to R_1 . Given the unsaturated traffic assumption, we obtain

$$R_1^- = \frac{\mu - \lambda_1}{\mu - \lambda_1 - \lambda_2} L,$$

$$R_1^+(C) = C + L - \frac{\mu - \lambda_2}{\mu - \lambda_1 - \lambda_2} L,$$

where L is the signal lost time that is determined by the CAV characteristics and the conflict zone geometric properties. Then, $R_1^{\text{opt}}(C)$ can be derived as:

$$R_1^{\text{opt}}(C) = \max\left(\min\left(R_1^*(C), R_1^+(C)\right), R_1^-\right). \quad (5.24)$$

Let C^{opt} denote the optimal solution to C . With Equations (5.23)-(5.24), C^{opt} and R_2^{opt} can be determined as:

$$C^{\text{opt}} = \text{argmin}\left(O^{\text{simp}}\left(R_1^{\text{opt}}(C)\right)\right),$$

$$R_2^{\text{opt}} = C^{\text{opt}} - R_1^{\text{opt}} + L.$$

Finally, let $\mathcal{S}^{\text{opt}} := \{R_1^{\text{opt}}, R_2^{\text{opt}}, C^{\text{opt}}\}$ define the optimal solution to signal timing plan \mathcal{S} . Figure 5.7 illustrates the analytical solution to SMO problem. In this figure, C_0 , C_1 , and

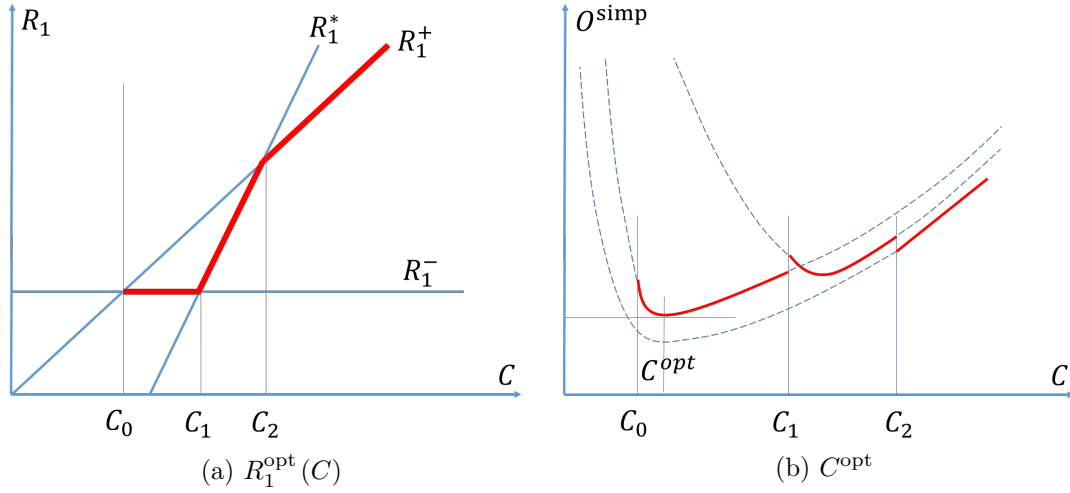


Figure 5.7: Analytical solution to SMO.

C_2 are the break points in the piecewise $R_1^{\text{opt}}(C)$ function. This ends the SMO problem formulation and analytical solution section.

5.4 Numerical Experiments

This section presents the numerical experiments to assess our model performance. First, a numerical experiment is conducted to compare the algorithm results with benchmark cases for a signalized intersection. Second, to show the extendability of our algorithm to the other types of crossing points, an example is provided for a signalized work-zone. Third, sensitivity analyses are performed on the impacts of traffic demand, length of the control zone, length of the crossing point, and speed limit changes on the algorithm solutions. In these experiments, we set $w = 40$ sec/lit, $\tau = 0.6$ sec, and $s_0 = 6$ m. Further, a set of default parameters are defined for the sensitivity analyses. The default parameter values are set as: $\lambda_1 = 2000$ vph, $\lambda_2 = 1500$ vph, $\bar{v} = 20$ m/sec, $l_1 = l_2 = 500$ m, $\mu = 3600 / \left(\tau + \frac{s_0}{\bar{v}} \right) = 4000$ vph, $l^C = 7$ m, and $L = 2.7$ sec.

Figure 5.8 shows the simulation results for a signalized intersection with the default parameter values. To evaluate the algorithm solutions, the results are compared with two

benchmark cases. In the first case, CAV trajectories are solved with our near-optimum trajectory construction model explained in Sub-section 5.3.1.1. However, instead of setting \mathcal{S}^{opt} , a fixed signal timing plan of $\mathcal{S} := \{16.4, 16.4, 30\}$ is used. Figure 5.9 shows the simulation results for this case. In the second benchmark case, no control is implemented and the CAVs trajectories are simulated with IDM car-following model. This car-following model is formulated as

$$a = \bar{a} \left(1 - \left(\frac{v}{\bar{v}} \right)^\delta - \left(\frac{s^*}{s_0} \right)^2 \right),$$

$$s^* = s_0 - s^{\text{car}} + \max \left(0, vT + \frac{v \cdot \Delta v}{2\sqrt{\bar{a}b}} \right),$$

where v and a are the vehicle speed and acceleration, respectively, \bar{a} and b are the maximum acceleration and comfortable deceleration, respectively, s^* is the desired space gap, s^{car} is the vehicle length, T is the time gap, Δv is the speed difference between the preceding and the current vehicle, and δ is the acceleration exponent. In this example, these parameters are set as: $\bar{a} = b = 1.5 \text{ m/s}^2$, $s^{\text{car}} = 5 \text{ m}$, $T = 0.6 \text{ sec}$, $\delta = 4$, and the other parameters are set to their default values. The results for this case are shown in Figure 5.10.

To quantify the benefits, the results of these cases are compared using three measures: throughput at the intersection, travel time delay per vehicle, and fuel consumption per unit of time. These measures are denoted by Q , \hat{D} , and \hat{F} , respectively. In all of the following experiments, \hat{D} is determined by dividing the total delay to the total number of vehicles that pass the crossing point during one C . Moreover, \hat{F} is calculated by dividing the total fuel consumption to the total travel time of all vehicles that pass the crossing point during one C . Table 5.1 presents these measures as well as the signal timing plan and the value of objective function O^{simp} . These results indicate that the proposed SMO problem can significantly improve the performance measures. Note that since O^{simp} is formulated as a function of signal timing plan \mathcal{S} , both benchmark cases obtain the same O^{simp} value. As the

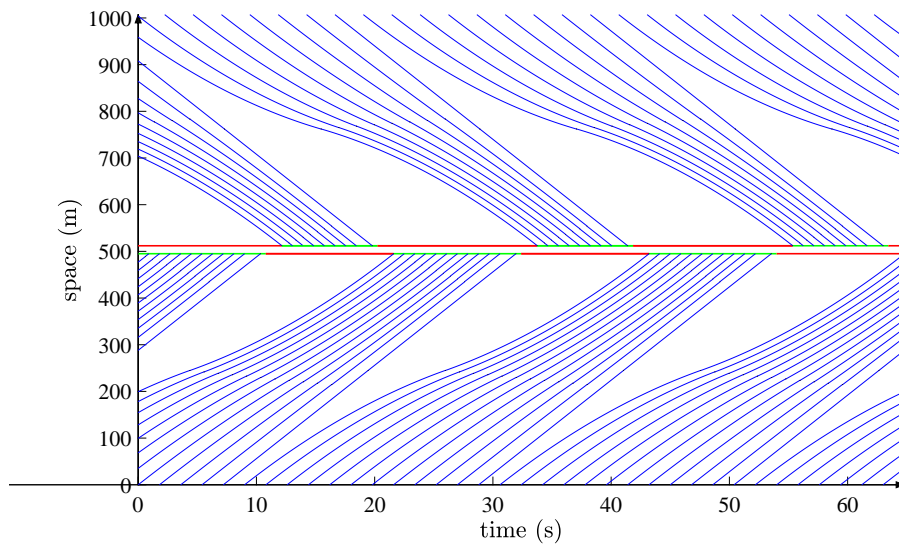


Figure 5.8: Simulation results for a signalized intersection.

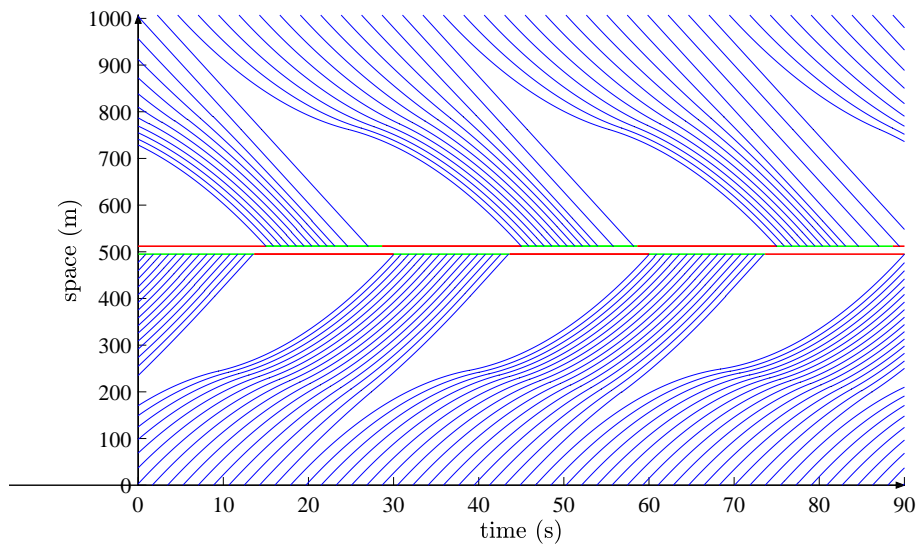


Figure 5.9: Simulation results for a signalized intersection with a fixed \mathcal{S} .

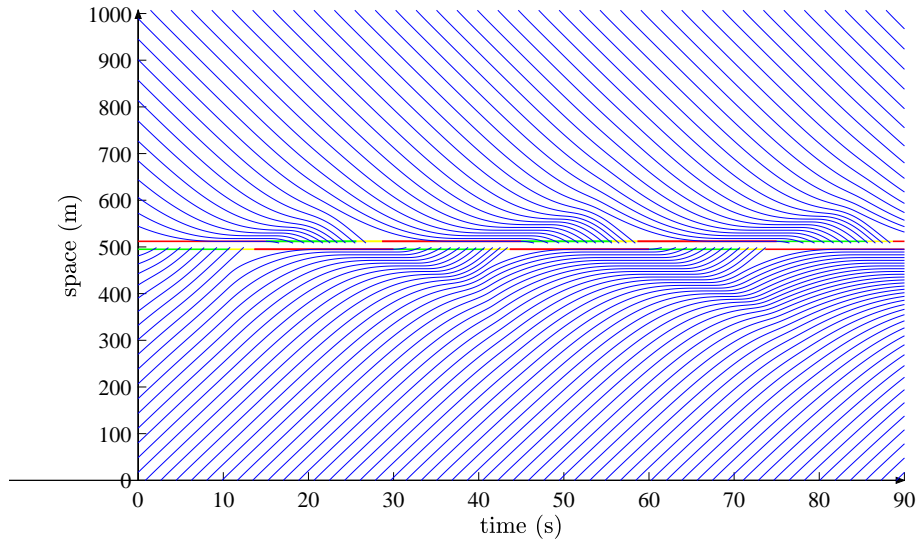


Figure 5.10: Simulation results for a signalized intersection with no control.

Table 5.1: Simulation quantitative results.

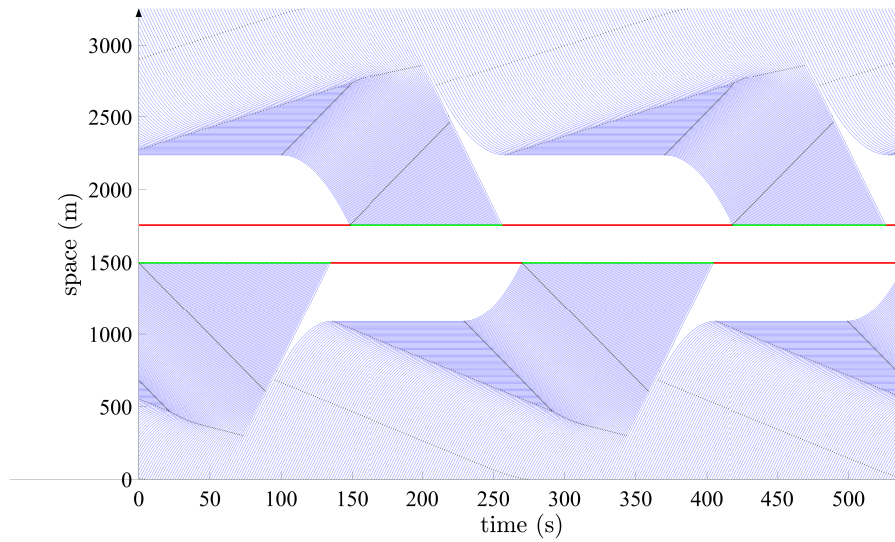
	R_1 (sec)	R_2 (sec)	C (sec)	Q (vph)	\hat{D} (sec)	\hat{F} (ml/sec)	O^{simp} (sec)
Trajectory and signal control	10.8	13.5	21.6	4000	5.0	1.8	12.41
Trajectory control	16.4	16.4	30	3692	7.4	1.9	16.46
No control	16.4	16.4	30	3165	20.7	10.4	16.46

\hat{D} and \hat{F} values indicate, this does not mean that both cases yield the same delay and fuel consumption. Therefore, the comparisons that based on O^{simp} is valid only when the same trajectory control method is applied.

To demonstrate the extendability of our model to the other types of crossing points, the model is applied on a signalized work-zone, and the results are shown in Figure 5.11. In this example, $l^C = 250$ m (the length of the work-zone section), $L = 27$ sec, $l_1 = l_2 = 1500$ m, and the other parameters are set to their default values.



(a) An illustration to signaled work-zone.



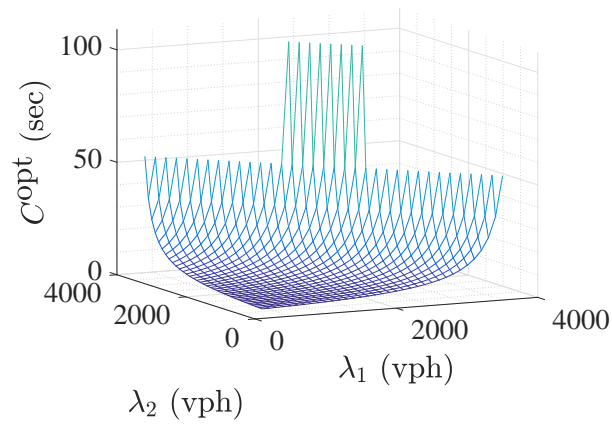
(b) Simulation results.

Figure 5.11: Simulation results for a signaled work-zone.

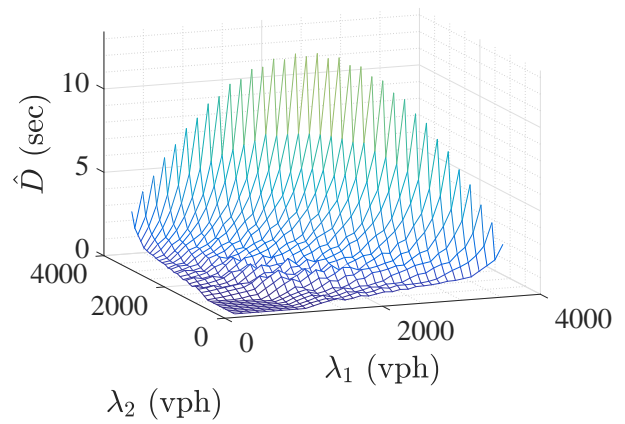
Figure 5.12 shows the results of the sensitivity analysis on $\lambda_i, i \in \mathcal{I}$. In this analysis, $\lambda_i, i \in \mathcal{I}$ varies between 200 to $\mu = 4000$ with the interval of 200 vph, and the other parameters are set to their default values. Since the proposed model assume that the traffic is under-saturated, the (λ_1, λ_2) pairs that yield saturated traffic are excluded. Thus all (λ_1, λ_2) pairs satisfy $\lambda_1 + \lambda_2 \leq \mu$. Note that although the traffic is assumed to be under-saturated, CAV technologies in pure-automated traffic shall provide significantly high highway capacity (Ghiasi et al., 2017) and thus the proposed control strategy shall cover a broad range of traffic conditions. The sensitivity analysis results indicate that the measures convexly increase with $\lambda_i, i \in \mathcal{I}$. However, even for relatively $\lambda_i, i \in \mathcal{I}$ values, the measures are bounded to significantly low values. This implies that our model improve the traffic performance even when the demand is very close to the capacity.

Next, we perform a sensitivity analysis on $l_i, i \in \mathcal{I}$ and l^C values, and the results are shown in Figure 5.13. In this analysis, it is assumed that $l_1 = l_2$ and for simplicity this parameter value is shown as l in the figure. We let l vary from 100 m to 2000 m with the interval of 100 m. Further, the minimum and maximum l^C values are set to 7 m and 500 m and the intervals between each two consecutive values are assumed to be 25.9 m. The results indicate that C^{opt} , \hat{D} , and O^{simp} values linearly increase with l^C , but insensitive to l . However, \hat{F} decreases with l^C and l that is because the total traffic delay increases with l^C and l with greater rates, and thus the unit time fuel consumption decreases.

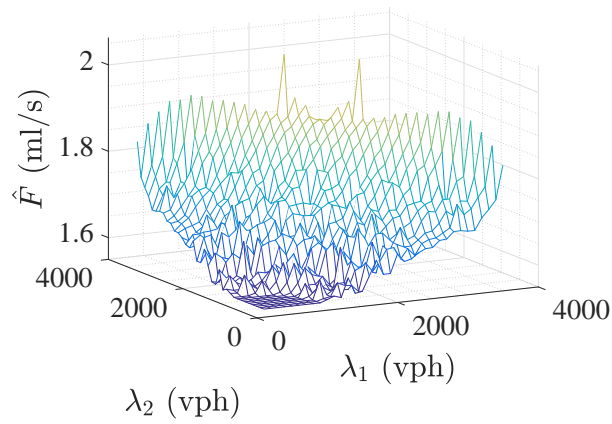
Finally, the results of the sensitivity analysis on \bar{v} are shown in Figure 5.14. In this experiment, the \bar{v} values vary from 10 m/s to 25 m/s with the interval of 1 m/s and the other parameters are kept to their default values. Figure 5.14(a) and Figure 5.14(b) show the \hat{F} values and the total fuel consumption of all vehicles that pass the intersection during one C^{opt} , respectively. The results indicate that \hat{F} increases with \bar{v} , however, the optimum total fuel consumption is obtained at $\bar{v} = 14$ m/s. It is also found that \hat{D} is relatively insensitive to \bar{v} and ranges around 5 sec for all \bar{v} values with very low variations. Overall, these numerical



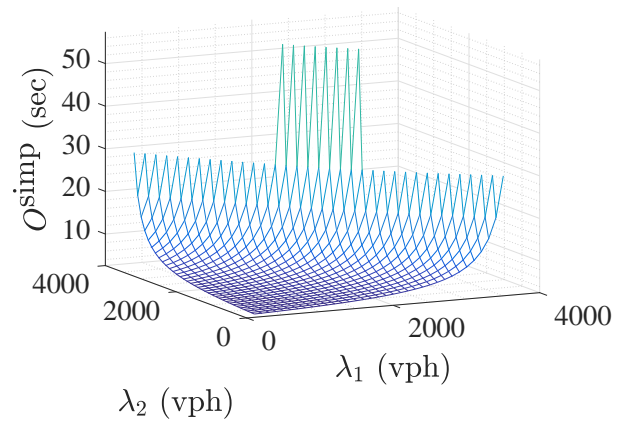
(a)



(b)

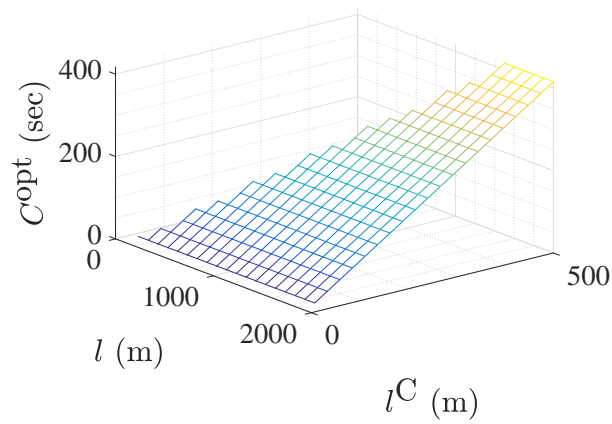


(c)

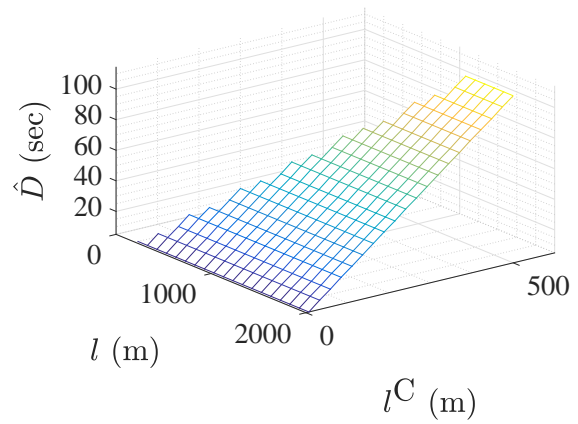


(d)

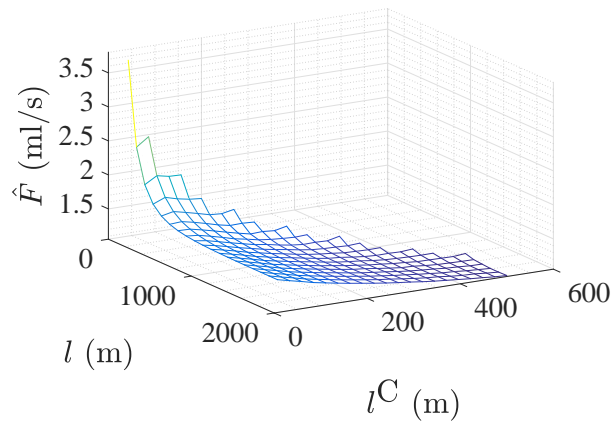
Figure 5.12: Sensitivity analysis results on $\lambda_i, i = 1, 2$.



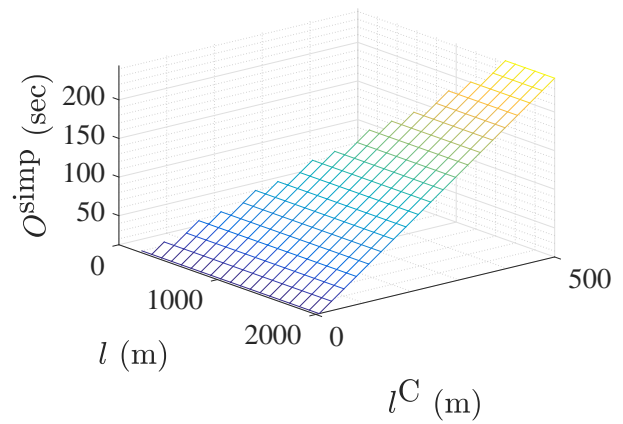
(a)



(b)



(c)



(d)

Figure 5.13: Sensitivity analysis results on $l_i, i = 1, 2$ and l^{C} .

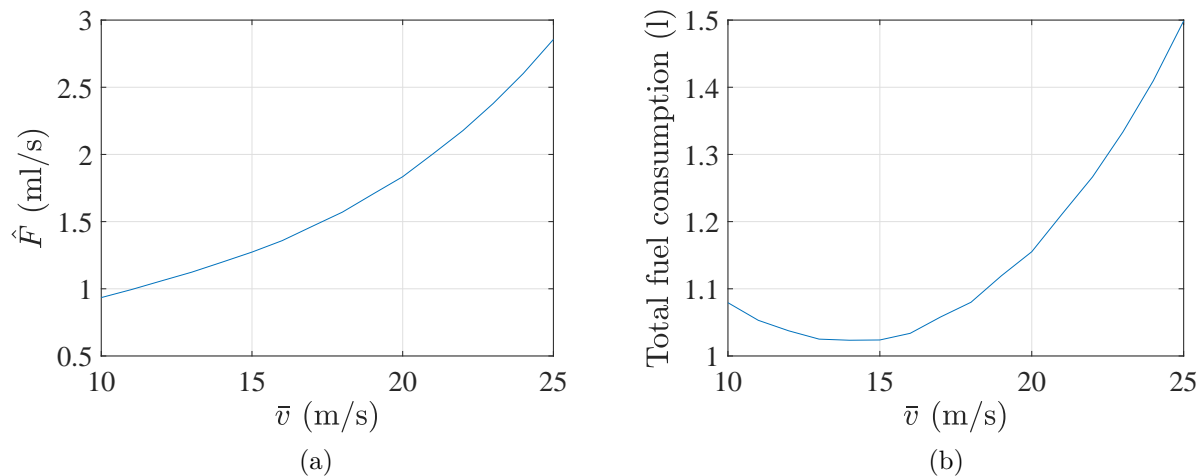


Figure 5.14: Sensitivity analysis results on \bar{v} .

experiments provide insightful information about the impacts of different traffic conditions and roadway geometries on the model outcomes.

5.5 Chapter Summary

This study proposes a joint trajectory and signal optimization problem for a signalized crossing point in pure automated traffic. This study makes two simplifications that lead to a simplified model, which can be efficiently solved to the exact solutions. First, each vehicle's trajectory is approximated with no more than five pieces of consecutive quadratic segments. Therefore, the feasible region of the optimization problem is significantly reduced, which led to the development of an exact solution algorithm. Second, this study proposes a macroscopic near-optimum fuel consumption function that can be replaced with the highly non-linear functions of the instantaneous fuel consumption. The proposed formulation is presented as a simple quadratic function of signal red interval. With these two modifications in vehicle trajectory and fuel consumption functions, a simplified joint trajectory and signal optimization model is developed that provides an exact solution algorithm that efficiently solves to the true optimum. Numerical experiments are performed to evaluate the

algorithm performance and to illustrate the applications of this algorithm on signalized intersections and work-zones. Further, the numerical analyses test the algorithm on various traffic conditions and roadway geometries.

CHAPTER 6: SPEED HARMONIZATION¹

This chapter proposes a new speed harmonization algorithm that can be applied in mixed traffic freeways. The proposed speed harmonization model is described as follows.

6.1 Problem Setting

This section describes the real-time traffic control algorithm. The problem setting is described below.

- Roadway geometry

We consider a section of a single-lane freeway without any inflow or outflow ramps. A longitudinal coordinate system is defined along the freeway that increases downstream, and the origin of the coordinate system is set somewhere upstream of a bottleneck such that the bottleneck occurs at location $l^B > 0$. Figure 6.1 illustrates the one-lane freeway geometry. It is worth mentioning that although we consider a one-lane freeway for the presented algorithm, this development can be easily extended to multi-lane freeways by scaling up the traffic proportionally.

- Vehicles

We consider a stream of vehicles that move along the single-lane freeway. In this study, three vehicle types are considered, i.e., HV (human-driven vehicles), CV (connected vehicles), and

¹This chapter is submitted for publication: Ghiasi, A., Li, X., Ma, J., Qu, X., 2018. A mixed traffic speed harmonization model with connected autonomous vehicles.

CAV (connected autonomous vehicles). We assume that HVs are regular human-driven vehicles with no communication or automation technologies. CVs are equipped with connected vehicle technologies and thus can transmit their real-time status to the other connected vehicles. However, these vehicles do not have automated technologies and thus cannot be controlled. Finally, we assume that CAVs include both connected and autonomous vehicle technologies, and thus can communicate with other CVs and CAVs and also are capable of being controlled by a computer program. We assume that both CVs and CAVs are equipped with necessary sensors (e.g., GPS devices for location and speed, accelerometers) and thus both CVs and CAVs are capable of recording and broadcasting its real-time trajectory. Further, we assume that a CAV is equipped with distance sensors, so it can measure the real-time trajectory of its immediate preceding vehicle. We call the collection of CVs and CAVs as probe vehicles for simplicity. We assume that N probe vehicles indexed as $n \in \mathcal{N} := 1, 2, \dots, N$ are distributed among HVs. Let $Y_n \in \{1, 2\}$ denote the vehicle n th type, i.e., $Y_n = 1$ if vehicle n is a CV, and $Y_n = 2$ if vehicle n is a CAV, and $\mathcal{A} := \{n | Y_n = 2\}_{\forall n \in \mathcal{N}}$ denote the set of CAV indices. We let P_1 and P_2 denote the expected market penetration rates of CVs and CAVs among all vehicles, respectively.

Let $p_n^{\text{probe}}(t) \in \mathcal{P}_t^{\text{probe}}$ and $p_i^{\text{CAV}}(t) \in \mathcal{P}_t^{\text{probe}}$ denote the locations of probe vehicle n ($\forall n \in \mathcal{N}$) and CAV i ($\forall i \in \mathcal{A}$) at time t , respectively, and $p_i^{\text{pre}}(t) \in \mathcal{P}_t^{\text{pre}}$ denote the locations of the vehicles immediately preceding to CAV i at time t , $\forall i \in \mathcal{A}$. The speed limit on this freeway section is v^f , and we do not allow the vehicles to back up. Thus, the speed range for all vehicles is $[0, v^f]$. Moreover, the minimum and maximum accelerations for all vehicles at any time are a^{\min} and a^{\max} , respectively.

- Traffic sensors

We deploy a number of S traffic sensors at locations $l_s, \forall s = 1, \dots, S$ to measure traffic density and flow information. To have these traffic sensors provide relevant information about the downstream traffic status, we deploy these traffic sensors around the bottleneck,

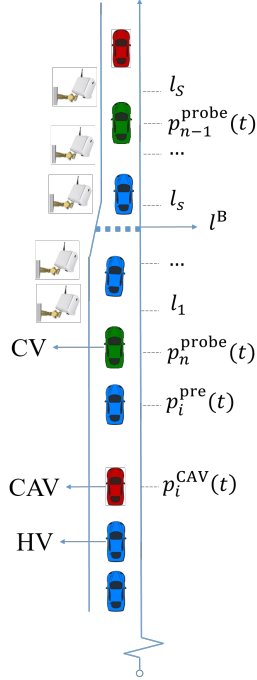


Figure 6.1: Problem setting.

i.e., $l_1 < l^B < l_S$ (as illustrated in Figure 6.1). After every ΔT time period, the sensors aggregate the measured traffic states and then share them with CAVs (e.g., through either broadcasting or a centralized server).

6.2 Algorithm Design

The problem investigated in this study is a real-time control strategy to harmonize traffic using CAVs. Basically, the information provided by the traffic sensors and the probe vehicles (i.e., CVs and CAVs) are used to detect a downstream speed drop or oscillation and predict its propagation to the upstream traffic. Then the trajectories of the CAVs upstream of the bottleneck are controlled to dampen traffic oscillation propagation and smooth the movements of the following vehicles. Ideally, the CAV trajectories shall hold the upstream traffic to proceed smoothly and steadily in the upstream segment of the bottleneck until the queue at the bottleneck dissipates and the traffic speed recovers (and so does the bottleneck

capacity). The proposed algorithm consists of three main steps. In the first step, we update the traffic flow and density collected by each traffic sensor s at the current time t , which we denote as $q_s(t)$ and $\rho_s(t)$, respectively. Since the information is updated at each decision time point with interval ΔT , the algorithm runs iteratively at the same discrete time points to update the trajectory control. The information provided by the traffic sensors and the probe vehicles are then used in the second step to predict the future status of the downstream queue. Note that we essentially only need to predict the vehicle trajectories immediately preceding to the CAVs, denoted by $r_{ti}(t'), \forall t' \geq t, i \in \mathcal{A}$. In the third step, we plan the future CAV trajectories, denoted by $f_{ti}(t'), \forall t' \geq t, i \in \mathcal{A}$, based on $r_{ti}(t'), \forall t' \geq t, i \in \mathcal{A}$ to harmonize the following traffic. For this, at each iteration, we control the CAVs upstream of the bottleneck, and thus, we exclude the CAVs that already passed a downstream location P^{end} , where negative impacts of the bottleneck are likely recovered. We let \mathcal{A}^- denote the set of excluded CAVs from the control strategy. Figure 6.2 shows the algorithm flowchart. The algorithm steps are described in detail in the following paragraphs.

6.2.1 Information Update

In the first step of the algorithm, the data input from the traffic sensors and the probe vehicles are updated. Traffic sensors located downstream will measure $q_s(t^-)$ and $\rho_s(t^-)$ and relay this information to the server (or each individual CAV) at a time interval of ΔT , where $t^- := t - \Delta T/2$. Note that since traffic sensors report the aggregated data with time interval ΔT , we represent these data in the middle of time interval $[t - \Delta T, t]$ (i.e., time $t^- = t - \Delta T/2$). We also update $\mathcal{P}_t^{\text{probe}}$, and the current speed of the CAVs (i.e., $\dot{p}_i^{\text{CAV}}(t), \forall i \in \mathcal{A}$) in this step. Further, we need the current location of the preceding vehicles to all CAVs, i.e., $\mathcal{P}_t^{\text{pre}}$. In estimating $p_i^{\text{pre}}(t)$, two scenarios are possible for each CAV i . The first case is that the vehicle preceding to CAV i is a probe vehicle. In this scenario, the preceding vehicle can send back the location information to the server and we have accurate

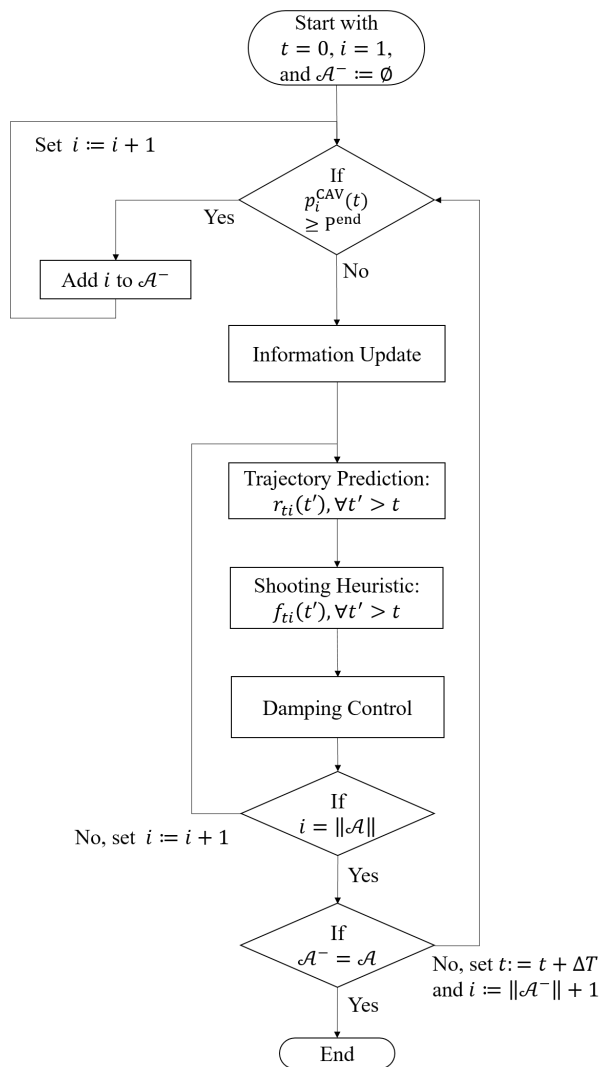


Figure 6.2: Algorithm flowchart.

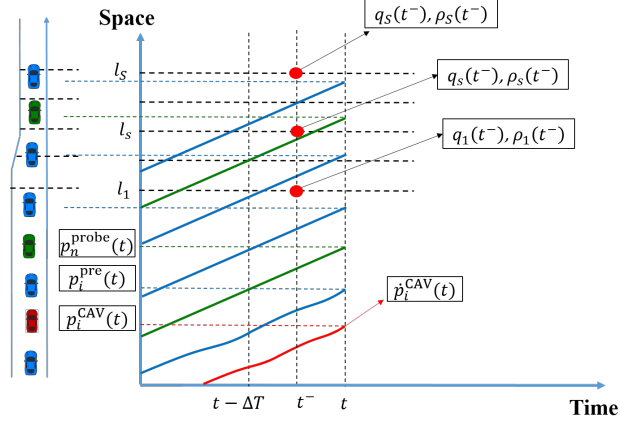


Figure 6.3: Information update.

estimation of $p_i^{\text{pre}}(t)$. In the second case, the preceding vehicle is an HV, and thus, we need to use the traffic sensor or the deployed distance sensor information to measure the traffic density surrounding the probe vehicles to estimate $p_i^{\text{pre}}(t)$. The outputs of this step are the current time traffic status that are shown in Figure 6.3.

Next, we predict the future downstream queue status using the updated information.

6.2.2 Trajectory Prediction

In the second step of the algorithm, we predict the future downstream queue status using the traffic sensors and probe vehicles information. The outputs of this step are T_{ti} and v_{ti} ($\forall i \in \mathcal{A}$), which respectively denote the predicted time and the speed at which the vehicle preceding to CAV i passes the fixed exit point, P^{end} . We assume that the macroscopic traffic evolution follows a triangular fundamental diagram which has been validated with field data (Dervisoglu et al., 2009). With the triangular fundamental diagram, we use a simplified version of the kinematic wave theory proposed by Newell (2002) and the LWR model (Whitham, 1955) to make the predictions. First, we need to estimate the boundary conditions that are explained in the following sub-section.

6.2.2.1 Boundary Condition Estimation

In the prediction algorithm, we use vehicle numbers as the boundary information. Let $m_s(t)$ denote the estimated vehicle number at l_s at time t . In this sub-step, we first estimate $m_s(t), \forall s = 1, \dots, S$, which then can be used to estimate the numbers associated with the probe vehicles, CAVs, and the preceding vehicles to the CAVs, denoted by $m_n^{\text{probe}}(t), \forall n \in \mathcal{N}$, $m_i^{\text{CAV}}(t), \forall i \in \mathcal{A}$, and $m_i^{\text{pre}}(t), \forall i \in \mathcal{A}$, respectively. For computational convenience, we allow an estimated number to be a fractional number. Note that since these continuous numbers are relative to the first vehicle's number at l_S , we obtain $m_S(\Delta T/2) = q_S(\Delta T/2) \Delta T/2$. Then $m_s(t^-)$ can then be estimated in two ways: (1) using the previous and the current iteration flow information from the same traffic sensor, $m_s^q(t^-)$ (see Equation (6.1)) or (2) using the current captured densities from the neighboring traffic sensor, $m_s^p(t^-)$ (see Equation (6.2)):

$$m_s^q(t^-) = m_s(t^- - \Delta T) + \frac{q_s(t^- - \Delta T) + q_s(t^-)}{2} \Delta T, \forall s = 1, \dots, S, \forall t^- \geq 3\Delta T/2. \quad (6.1)$$

$$m_s^p(t^-) = m_{s+1}(t^-) + \frac{\rho_s(t^-) + \rho_{s+1}(t^-)}{2} (l_{s+1} - l_s), \forall s = 1, \dots, S-1. \quad (6.2)$$

Then, we set $m_S(t^-) = m_S^q(t^-)$. For all $s = 1, 2, \dots, S-1$, we found that the average number of the values estimated by the two ways obtain better results, thus we use

$$m_s(t^-) = \begin{cases} m_s^p(t^-), & \text{if } t^- = \Delta T/2, \\ \frac{m_s^q(t^-) + m_s^p(t^-)}{2}, & \text{otherwise,} \end{cases}, \forall s = 1, \dots, S-1.$$

Note that for the first iteration we can only use the second way to estimate $m_s(\Delta T/2)$. We use a similar approach to estimate $m_s(t)$ using the following equations:

$$m_s^q(t) = m_s^q(t^-) + \frac{\Delta T}{2} q_s(t^-), \forall s = 1, \dots, S,$$

$$m_s^{\rho}(t) = m_s^{\rho}(t^-) + \frac{\rho_s(t^-) + \rho_{s+1}(t^-)}{2} (l_{s+1} - l_s), \forall s = 1, \dots, S-1,$$

$$m_s(t) = \frac{m_s^{\text{q}}(t) + m_s^{\rho}(t)}{2}, \forall s = 1, \dots, S-1,$$

$$m_S(t) = m_S^{\text{q}}(t).$$

Next, we estimate $m_n^{\text{probe}}(t), \forall n \in \mathcal{N}$, $m_i^{\text{CAV}}(t)$, and $m_i^{\text{pre}}(t), \forall i \in \mathcal{A}$. We find the first traffic sensor downstream of the first probe vehicle at current time t and assign the corresponding index to s' . If no traffic sensor exists downstream of the vehicle, then we set $s' := S$. Then, $m_1^{\text{probe}}(t)$ is estimated using the number and density information corresponding to traffic sensor s' at time t , i.e.,

$$m_1^{\text{probe}}(t) = m_{s'}(t) + (l_{s'} - p_1^{\text{probe}}(t)) \rho_{s'}(t^-).$$

To estimate $m_n^{\text{probe}}(t), \forall n \in \mathcal{N} \setminus \{1\}$, we consider the location difference between each pair of consecutive probe vehicles ($n-1$ and $n, \forall n \in \mathcal{N} \setminus \{1\}$) and the density neighboring the probe vehicle. Let $d_n^{\text{f}}(t)$ and $d_n^{\text{p}}(t)$ denote the spacing between probe n and its following and preceding vehicles for all $n \in \mathcal{N}$, respectively. Then $m_n^{\text{probe}}(t)$ and $m_n^{\text{pre}}(t)$ are estimated as follows.

$$m_n^{\text{probe}}(t) = m_{n-1}^{\text{probe}}(t) + \frac{p_{n-1}^{\text{probe}}(t) - p_n^{\text{probe}}(t) - d_n^{\text{f}}(t)}{d_{n-1}^{\text{p}}(t)} + 1, \forall n \in \mathcal{N} \setminus \{1\},$$

$$m_i^{\text{CAV}}(t) = \{m_n^{\text{probe}}(t) \mid p_n^{\text{probe}}(t) = p_i^{\text{CAV}}(t)\}, \forall i \in \mathcal{A},$$

$$m_i^{\text{pre}}(t) = m_i^{\text{CAV}}(t) - 1, \forall i \in \mathcal{A}.$$

Figure 6.4 illustrates the estimated boundary outputs. Next, we describe the prediction algorithm using traffic sensor information as follows.

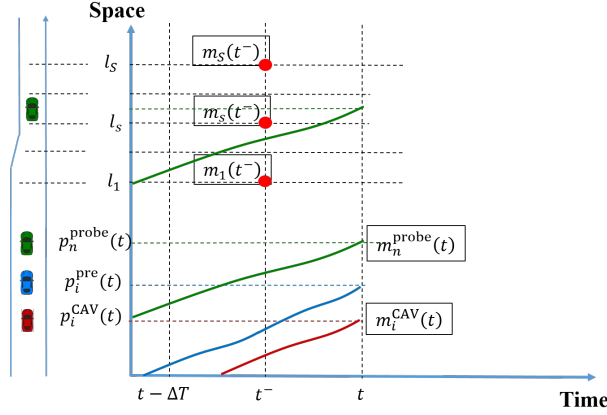


Figure 6.4: Boundary index estimation.

6.2.2.2 Sensor-based Prediction

This sub-section presents the steps to predict the trajectories of the preceding vehicles to the CAVs using the updated sensor information. Let $r_{ti}^s(t'), \forall t' \geq t, i \in \mathcal{A}$ denote the sensor-based predictions. This sub-section includes the following sub-steps to predict $r_{ti}^s(t'), \forall t' \geq t, i \in \mathcal{A}$.

- Backward wave lower-bound index prediction: In this sub-step we will find a lower-bound index for each CAV preceding vehicle, which indicates the lowest position of vehicle index. In other words, vehicle indices will not be lower than these points. First, in the time-space diagram, starting from each traffic sensor point (t^-, l_s) , we generate a backward shockwave at speed $-w$. This shockwave function is $y_{ts}^{\text{wave}}(t') := l_s - w(t' - t^-), \forall t' \geq t^-$. Second, we index each point on this shockwave to represent a vehicle index that increases along the shockwave with the rate of $1/s_0$ where s_0 is the traffic jam spacing. The indexing function is $m_{ts}^{\text{wave}}(t') := m_s(t^-) + w(t' - t^-)/s_0, \forall t' \geq t^-$. This index is a lower bound to the actual vehicle index at point $(t', y_{ts}^{\text{wave}}(t'))$. With this, we index every point along each wave as illustrated in Figure 6.5.

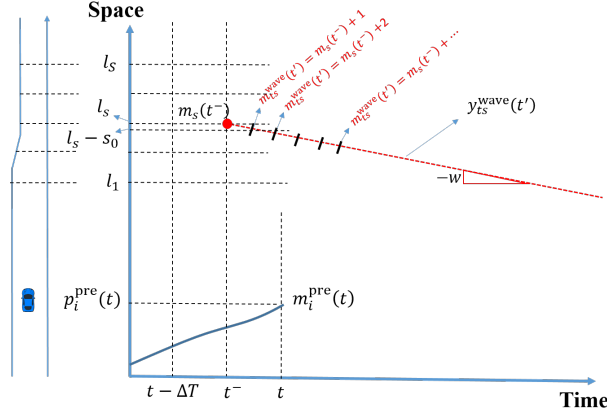
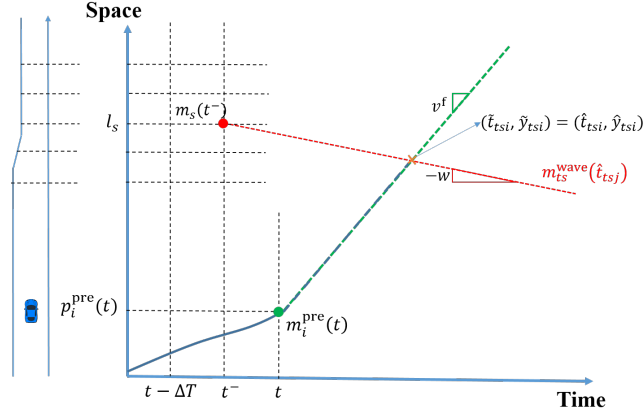
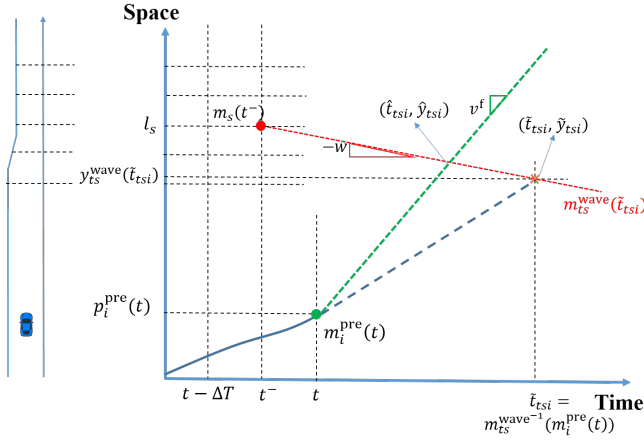


Figure 6.5: Sensor-based prediction: backward wave lower-bound index prediction.

- Trajectory reconstruction: In the previous sub-step, we found the lower-bound for the vehicle indices along the shockwave. In this sub-step, we find the actual indices that will not be lower than the obtained lower-bound. We first investigate how each CAV preceding vehicle go to the first wave (i.e., setting $s = 1$) at current point (i.e., setting current time $\bar{t}_i = t$ and $\bar{y}_i = p_i^{\text{pre}}(t), \forall i \in \mathcal{A}$). Since the vehicle's speed cannot exceed v^f , starting from point (\bar{t}_i, \bar{y}_i) , we shoot an upper bound trajectory at speed v^f for each $i \in \mathcal{A}$. We define this trajectory function as $y_{ti}^p(t') := \bar{y}_i + v^f(t' - \bar{t}_i), \forall t' > t, i \in \mathcal{A}$. We then find the intersection time between $y_{ts}^{\text{wave}}(t')$ and $y_{ti}^p(t')$, which we denote by \hat{t}_{tsi} and is calculated as $\hat{t}_{tsi} = (l_s - \bar{y}_i + v^f \bar{t}_i + wt^-) / (v^f + w), \forall s = 1, \dots, S, i \in \mathcal{A}$. Let \hat{y}_{tsi} be the location of the intersection between $y_{tsi}^{\text{wave}}(t')$ and $y_{ti}^p(t')$. Then, we compare lower-bound index $m_{ts}^{\text{wave}}(\hat{t}_{tsi})$ and $m_i^{\text{pre}}(t)$. As illustrated in Figure 6.6(a), if $m_{ts}^{\text{wave}}(\hat{t}_{tsi}) \geq m_i^{\text{pre}}(t)$, then traffic from the current preceding vehicle to wave s is not congested, and preceding vehicle i drives at v^f to reach point $(\hat{t}_{tsi}, y_{ts}^{\text{wave}}(\hat{t}_{tsi}))$. Then its future presence time on wave s , denoted by \tilde{t}_{tsi} , is exactly identical to \hat{t}_{tsi} . Otherwise, if $m_{ts}^{\text{wave}}(\hat{t}_{tsi}) < m_i^{\text{pre}}(t)$ as illustrated in Figure 6.6(b), then traffic is congested and this preceding vehicle cannot drive at v^f to reach point $(\hat{t}_{tsi}, y_{ts}^{\text{wave}}(\hat{t}_{tsi}))$. Instead, its presence on wave s is pushed off to time $\tilde{t}_{tsi} := m_{tsi}^{\text{wave}-1}(m_i^{\text{pre}}(t)), \forall s = 1, \dots, S, i \in \mathcal{A}$,



(a) Free-flow traffic



(b) Congested traffic

Figure 6.6: Sensor-based prediction: trajectory reconstruction for (a) free-flow traffic, (b) congested traffic.

where $m_{tsi}^{\text{wave}^{-1}}(\cdot)$ denote the inverse function of $m_{tsi}^{\text{wave}}(\cdot)$. This way, we connect the current point (\bar{t}_i, \bar{y}_i) to the wave s 's future presence point $(\tilde{t}_{tsi}, \tilde{y}_{tsi} := y_{tsi}^{\text{wave}}(\tilde{t}_{tsi}))$ and obtain a new trajectory section for each $i \in \mathcal{A}$, as illustrated in Figure 6.7(a) (for $s = 1$). Then we can move the current point to the new future presence point we solved above (i.e., setting $\bar{t}_i = \tilde{t}_{tsi}$ and $\bar{y}_i = \tilde{y}_{tsi}, \forall i \in \mathcal{A}$) and we move the next future presence point to the next wave (i.e., setting $s := s + 1$) to construct the next trajectory section by repeating the same operations. This is illustrated in Figure 6.7(b) (for $s = 2$) and

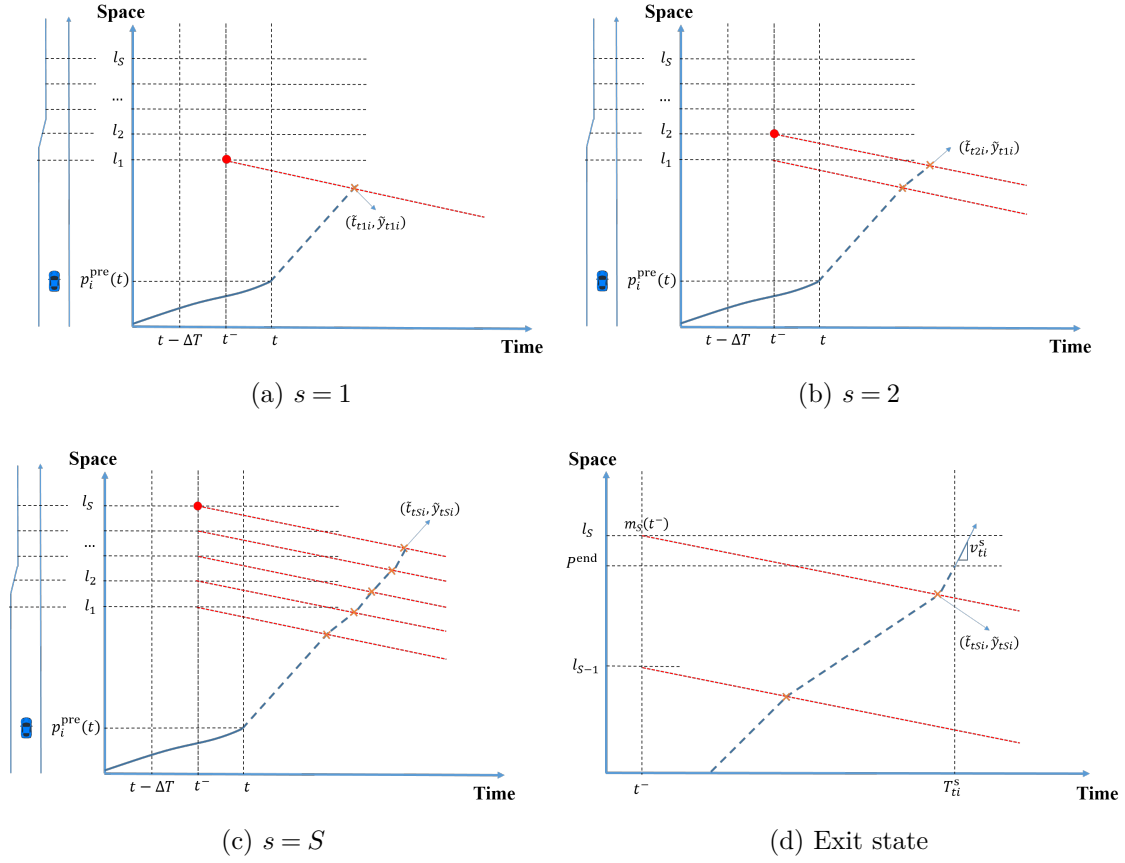


Figure 6.7: Sensor-based prediction: an illustration of trajectory reconstruction for (a) $s = 1$, (b) $s = 2$, (c) $s = S$, and (d) exit state prediction.

Figure 6.7(c) (for $s = S$). This way, we obtain the predicted preceding vehicle trajectory as a piece-wise linear curve illustrated in Figure 6.7(c).

- Exit state prediction: This sub-step solves the trajectory exit time, denoted by T_{ti}^S , $\forall i \in \mathcal{A}$. The constructed piece-wise linear functions continue up to the last point that may be lower than P^{end} . Since there is no other point greater than $(\tilde{t}_{tSi}, \tilde{y}_{tSi})$, we simply use the last traffic sensor data to calculate the exit speed denoted by v_{ti}^S , i.e., $v_{ti}^S = q_S(t^-) / \rho_S(t^-)$. Therefore, after $(\tilde{t}_{tSi}, \tilde{y}_{tSi})$ the trajectory continues with v_{ti}^S up to P^{end} . With this, we obtain a piece-wise linear function for $r_{ti}^S(t'), \forall t' \geq t, i \in \mathcal{A}$, and $T_{ti}^S, \forall i \in \mathcal{A}$ can be easily determined. Figure 6.7(d) illustrates exit state T_{ti}^S .

- Prediction smoothing: The outputs of the previous sub-step are piece-wise linear functions $r_{ti}^s(t'), \forall t' \geq t, i \in \mathcal{A}$ that are obtained based the sensor information and boundary conditions (Sub-sections 6.2.1 and 6.2.2.1) at current time t . Since the information updates at each decision time point, the boundary conditions may change, and thus the shapes of functions $r_{ti}^s(t'), \forall t' \geq t, i \in \mathcal{A}$ may be altered accordingly at each time point. Significant alterations in trajectory prediction may result in notable and unnatural fluctuations in the CAVs control strategy decisions. To overcome this issue, we smooth the trajectory prediction results (i.e., T_{ti}^s and $r_{ti}^s(t'), \forall t' \geq t, i \in \mathcal{A}$) based on the historical sensor information. First, we smooth $T_{ti}^s, \forall i \in \mathcal{A}$ with a weighted moving average filter. Let \bar{T}_{ti}^s denote the smooth $T_{ti}^s, \forall i \in \mathcal{A}$ value that is calculated as

$$\bar{T}_{ti}^s := \frac{\sum_{k=0}^{K-1} u_k T_{(t-k \cdot \Delta T)i}^s}{\sum_{k=0}^{K-1} u_k}, \forall i \in \mathcal{A},$$

where K is the moving average filter parameter and u_k is the weight coefficient at time point k . Then, we need to make sure that \bar{T}_{ti}^s results in a feasible predicted trajectory according to the speed range. We define $T_{ti}^{s, \text{mod}}$ as the modified exit time at time t for all $i \in \mathcal{A}$, which is calculated as

$$T_{ti}^{s, \text{mod}} := \max\left(\bar{T}_{ti}^s, t + \left(P^{\text{end}} - s_0 - r_{ti}^{\text{sh}}(t)\right) / v^{\text{f}}\right), \forall i \in \mathcal{A}.$$

We define $\delta_{ti}^{\text{T}} := T_{ti}^s - \bar{T}_{ti}^s$ as the time difference between T_{ti}^s and \bar{T}_{ti}^s , for all $i \in \mathcal{A}$. Then, we modify the breaking time points in piece-wise function $r_{ti}^s(t'), \forall t' \geq t, i \in \mathcal{A}$ according to δ_{ti}^{T} . Let $(\tilde{t}_{t_{si}}^s, \tilde{y}_{t_{si}}^s), \forall s \in \{1, \dots, S\}, i \in \mathcal{A}$ denote the breaking time-space points in $r_{ti}^s(t'), \forall t' \geq t, i \in \mathcal{A}$ function. Basically, for each break time point $(\tilde{t}_{t_{si}}^s, \tilde{y}_{t_{si}}^s), \forall s \in$

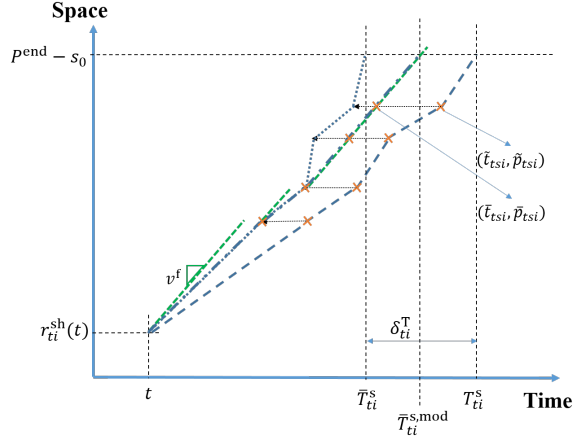


Figure 6.8: Sensor-based trajectory: prediction smoothing.

$\{1, \dots, S\}$, we shift \tilde{t}_{tsi}^s to a new time, denoted by \bar{t}_{tsi}^s , as formulated below.

$$\bar{t}_{t1i}^s := \max \left(t + (\tilde{y}_{t1i}^s - r_{t1i}^{sh}(t)) / v^f, \tilde{t}_{t1i}^s - \delta_{t1i}^T \left(\frac{\tilde{y}_{t1i}^s - r_{t1i}^s(t)}{P^{end} - s_0 - r_{t1i}^s(t)} \right) \right),$$

$$\bar{t}_{tsi}^s := \max \left(\bar{t}_{t(s-1)i}^s + (\tilde{y}_{tsi}^s - \tilde{y}_{t(s-1)i}^s) / v^f, \tilde{t}_{tsi}^s - \delta_{tsi}^T \left(\frac{\tilde{y}_{tsi}^s - r_{tsi}^s(t)}{P^{end} - s_0 - r_{tsi}^s(t)} \right) \right),$$

$$\forall s \in \{2, \dots, S\}, i \in \mathcal{A}.$$

Let $\bar{r}_{ti}^s(t'), \forall t' \geq t, i \in \mathcal{A}$ denote the modified trajectories that are reformulated using the new breaking points, i.e., $(\bar{t}_{tsi}^s, \tilde{y}_{tsi}^s), s \in \{1, \dots, S\}, i \in \mathcal{A}$. Figure 6.8 illustrates the trajectory modification procedure.

6.2.2.3 Probe-based Prediction

The previous sub-section provides the algorithm description for predicting the trajectory of the vehicles immediately preceding to the CAVs using the sensor information. However, sensor information may not be always accurate or available. In such cases, we rely on the probe vehicle information to predict the downstream traffic. Even if the sensor

information is available, such predictions can be further enhanced by combining the sensor-based predictions with the probe-based ones, which is explained in the next sub-section. This sub-section presents the procedure to predict the preceding vehicles' trajectories using only the real-time information provided by the probe vehicles.

Let $r_{ti}^p(t'), \forall t' \geq t, i \in \mathcal{A}$ denote the probe-based predictions. We group vehicles into different clusters such that each cluster is led by a CAV. To predict the trajectory of the preceding vehicle to each cluster, we use the information of the probe vehicles in the preceding cluster. The following sub-step explains the derivation of the probe offset trajectories.

- Offset trajectories: Basically, we assume that traffic status propagates upstream with wave speed w , thus we use an offset of the probe vehicle trajectories and shift them along the backward wave in the time-space diagram. We let $p_{tni}^{\text{offset}}(t'), \forall t' \geq t$ denote the offset trajectory of each probe vehicle n ($\forall n \in \mathcal{N}$) in cluster i ($\forall i \in \mathcal{A}$) at the current time t . This set of trajectories is calculated using Simplified Newell's model, $m_n^{\text{probe}}(t), \forall n \in \mathcal{N}$ and $m_i^{\text{pre}}(t), \forall i \in \mathcal{A}$ estimated in Sub-section 6.2.2.1 as:

$$p_{tni}^{\text{offset}}(t') := p_n^{\text{probe}}\left(t' - \left(m_i^{\text{pre}}(t) - m_n^{\text{probe}}(t)\right) \frac{s_0}{w}\right) - \left(m_i^{\text{pre}}(t) - m_n^{\text{probe}}(t)\right) s_0,$$

$$\forall t' \geq t, i = \min \{i \in \mathcal{A} \mid i > n, n \in \mathcal{N}\}.$$

In addition to the available probe vehicle trajectories up to current time t , for each $r_{ti}^p(t'), \forall t' \geq t, i \in \mathcal{A}$, we offset the current planned downstream CAV trajectory (i.e., $f_{tj}(t'), \forall t' \geq t, j = \max \{j \in \mathcal{A} \mid j < i, i \in \mathcal{A}\}$). The derivation of $f_{ti}(t'), \forall t' \geq t, i \in \mathcal{A}$ is explained in Sub-section 6.2.3. Let $p_{ti}^{\text{offset,f}}(t')$ denote the offset trajectory of

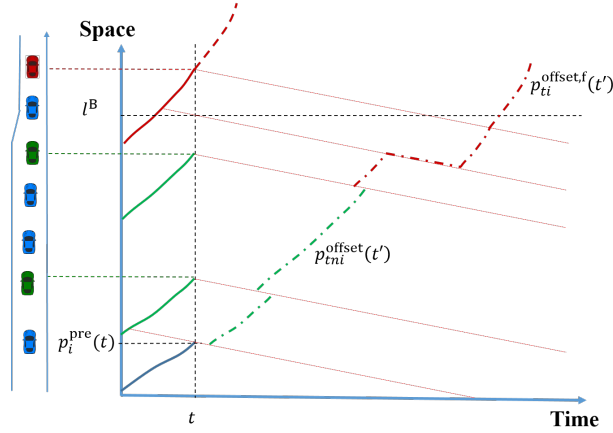


Figure 6.9: Probe-based prediction: an illustration to offset trajectories.

$f_{tj}(t'), \forall t' \geq t, j = \max\{j \in \mathcal{A} \mid j < i, i \in \mathcal{A}\}$ that is calculated as:

$$p_{ti}^{\text{offset},f}(t') := f_{tj}\left(t' - \left(m_i^{\text{pre}}(t) - m_j^{\text{CAV}}(t)\right) \frac{s_0}{w}\right) - \left(m_i^{\text{pre}}(t) - m_j^{\text{CAV}}(t)\right) s_0,$$

$$\forall t' \geq t, i \in \mathcal{A}, j = \max\{j \in \mathcal{A} \mid j < i, i \in \mathcal{A}\}.$$

Then, depending on the number of probe vehicles at each cluster, a number of $p_{tni}^{\text{offset}}(t')$ and one $p_{ti}^{\text{offset},f}(t')$ are available to be used in the prediction for each $r_{ti}^{\text{P}}(t'), \forall t' \geq t, i \in \mathcal{A}$. Figure 6.9 illustrates the offset trajectories for a cluster.

- Offset modification: In this study, we use Triangular Fundamental diagrams in modeling the traffic upstream and downstream of the bottleneck, and thus, the s_0 value in the upstream segment is less than the downstream one. This results in a jump in some sections of the offset trajectories (as shown in Figure 6.9). To overcome this issue, we implement the LWR model to estimate a near-bottleneck traffic speed, and replace these sections with a linear continuous segment. Let v^{B} denote the near-bottleneck traffic speed that is calculated as

$$v^{\text{B}} := \frac{wv^{\text{f}}Q^{\text{down}}}{wQ^{\text{down}} + v^{\text{f}}(Q^{\text{up}} - Q^{\text{down}})},$$

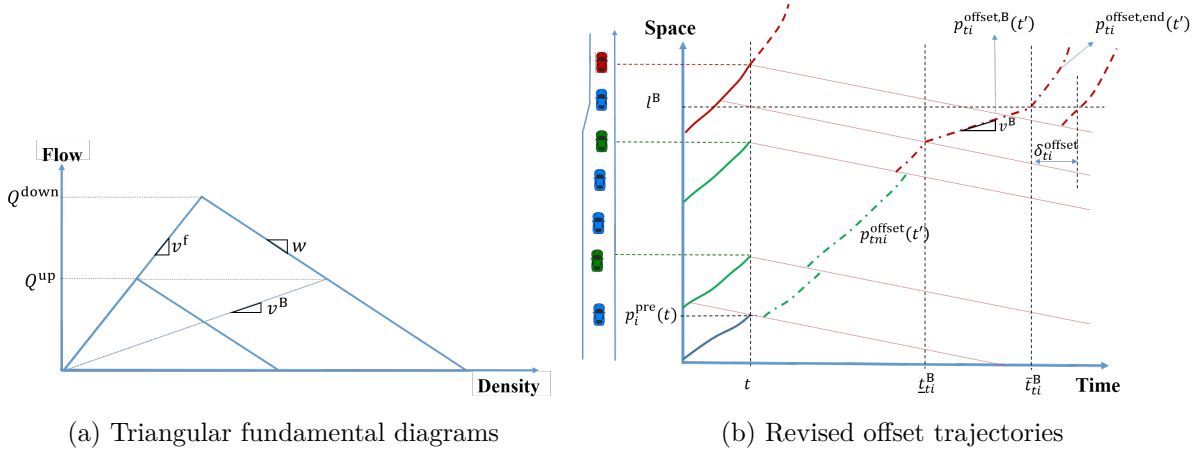


Figure 6.10: Probe-based prediction: an illustration to (a) triangular fundamental diagrams and v^B derivation and (b) the revised offset trajectories.

where Q^{up} and Q^{down} are the capacities of the upstream and downstream segments, respectively. We let $p_{ti}^{\text{offset,B}}(t'), t_{ti}^B \leq t' \leq \bar{t}_{ti}^B$ define this linear section function with the slope of v^B , where t_{ti}^B and \bar{t}_{ti}^B are the start and end time domain, respectively. For the sections of the offset trajectories after l^B , we just shift them in time to connect them with $p_{ti}^{\text{offset,B}}(\bar{t}_{ti}^B)$ and denote this section by $p_{ti}^{\text{offset,end}}(t'), \forall t' \geq \bar{t}_{ti}^B, i \in \mathcal{A}$. Figure 6.10(a) and Figure 6.10(b) illustrate the Triangular Fundamental diagrams with v^B derivation and revised offset trajectories $p_{ti}^{\text{offset,B}}(t'), t_{ti}^B \leq t' \leq \bar{t}_{ti}^B$ and $p_{ti}^{\text{offset,end}}(t'), \forall t' \geq \bar{t}_{ti}^B$ for all $i \in \mathcal{A}$.

The obtained offset trajectories for each vehicle cluster $i \in \mathcal{A}$ are actually a set of functions that may overlap in some time points (as illustrated in Figure 6.10). To construct probe-based prediction function $r_{ti}^{\text{p}}(t'), \forall t' \geq t$, we simply remove the overlapping section of the second trajectory for each two consecutive offset trajectories, and connect them together to form a continuous $r_{ti}^{\text{p}}(t'), \forall t' \geq t$ function for each $i \in \mathcal{A}$. Next, we combine the probe-based offset trajectories with sensor-based prediction results (i.e., $\bar{r}_{ti}^{\text{s}}(t'), \forall t' \geq t, i \in \mathcal{A}$) to further improve the prediction outcomes. If for any $i \in \mathcal{A}$, sensor-based prediction $\bar{r}_{ti}^{\text{s}}(t'), \forall t' \geq t$ is

available, we simply integrate the probe-based prediction offset trajectories and the sensor-based predictions together in the next sub-section.

6.2.2.4 Prediction Integration

This sub-section presents the algorithm to integrate $\bar{r}_{ti}^s(t')$ and $r_{ti}^p(t')$, $\forall t' \geq t$ to construct $r_{ti}(t')$, $\forall t' \geq t, i \in \mathcal{A}$. For each point in $r_{ti}^p(t')$, $\forall i \in \mathcal{A}$, we can find a point at the corresponding source probe vehicle trajectory with the same location. We define ω_{ni}^p as the time difference between t' and the corresponding point at the source probe trajectory n , and $\omega_i^s := t' - t^-$ (see Figure 6.11(a)). Then, for each cluster $i \in \mathcal{A}$, we integrate $\bar{r}_{ti}^s(t')$ and $r_{ti}^p(t')$, $\forall t' \geq t$ with a weighted average proportional to the inverse of the time difference between the predicted points and their source times as:

$$r_{ti}(t') := \frac{(\omega_{ni}^p)^{-1} \bar{r}_{ti}^s(t') + (\omega_i^s)^{-1} r_{ti}^p(t')}{(\omega_{ni}^p)^{-1} + (\omega_i^s)^{-1}}, \forall t' \geq t, i \in \mathcal{A}.$$

Note that in some cases, sensor information is not available or not applicable for the prediction due to the upstream CAV control strategy. Further, our experiments indicate that when sufficient sensor information is not available, it would be better to just ignore the sensor-based prediction results. Without much loss of generality, we assume that the distances between all traffic sensors are equal and denote it by Δl^S . Then, based on our numerical experiments, we define two criteria for sufficiency of the sensor information: $p_{i-1}^{\text{CAV}}(t) > l_{\lfloor S/2 \rfloor}$ and $p_{i-1}^{\text{CAV}}(t) - p_i^{\text{CAV}}(t) > \left(\frac{S}{2} + 1\right) \Delta l^S, \forall i \in \mathcal{A} \setminus \{1\}$. The first criterion requires that the vehicles in the preceding CAV cluster (i.e., $i - 1$) have already passed sufficient number of traffic sensors locations. The second criterion is met only if the number of vehicles existing in the preceding CAV cluster is large enough to cover a sufficient number of traffic sensors. For example, for a relatively large P_2 value, there may not be a large enough number of vehicles in each CAV cluster to cover more than one or two traffic sensors. In such a case, sensor

information may not be very reliable, and thus according to the second criterion, we ignore the sensor information. If these criteria are met, we set simply set $r_{ti}(t') := \bar{r}_{ti}^s(t')$.

For safety concerns, instead of considering the real predicted trajectory $r_{ti}(t')$, we define a shadow trajectory by shifting $r_{ti}(t'), \forall t' \geq t, i \in \mathcal{A}$ rightward by τ and downward by s_0 where τ is reaction time. We denote shadow trajectory as $r_{ti}^{\text{sh}}(t'), \forall t' \geq t, i \in \mathcal{A}$, which can be obtained as $r_{ti}^{\text{sh}}(t') := r_{ti}(t' - \tau) - s_0, \forall t' \geq t, i \in \mathcal{A}$. With this, we update the exit states as

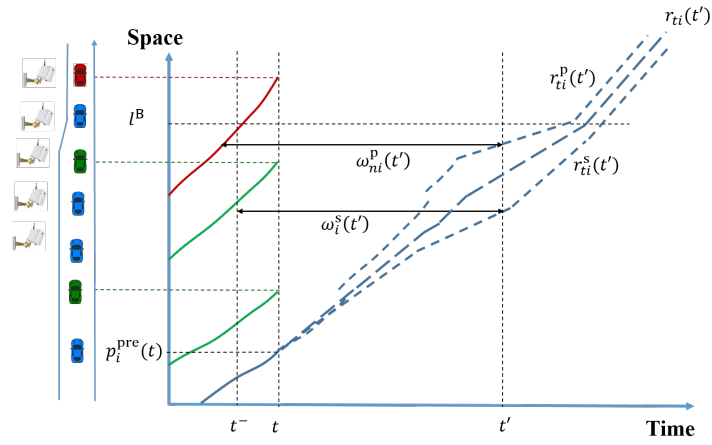
$$T_{ti}^{\text{end}} := \{t' \geq t \mid r_{ti}(t') = P^{\text{end}}\} + H_i^{\text{down}}, \forall i \in \mathcal{A},$$

$$v_{ti}^{\text{end}} := \max(\dot{r}_{ti}^{\text{sh}}(T_{ti}^{\text{end}}), \dot{p}_i^{\text{CAV}}(t)),$$

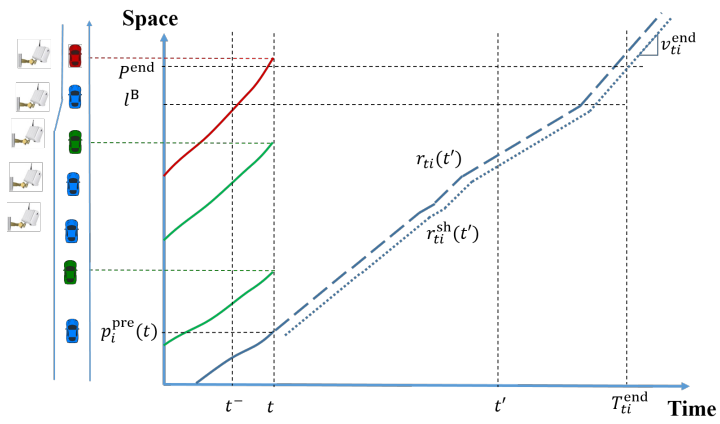
where T_{ti}^{end} and v_{ti}^{end} are the final exit states using the integrated trajectory prediction, $\dot{r}_{ti}^{\text{sh}}(t')$ denotes the derivative of $r_{ti}^{\text{sh}}(t')$ with respect to t' , and H_i^{down} is a time gap parameter that depends on the type of the preceding vehicle to CAV $i, \forall i \in \mathcal{A}$. Let H^{CV} and H^{HV} denote the time gap for the cases where the preceding vehicle is a probe vehicle and an HV, respectively. As such, if the preceding vehicle to CAV i is a CV or a CAV, then $H_i^{\text{down}} = H^{\text{CV}}$, otherwise $H_i^{\text{down}} = H^{\text{HV}}$. Note that the time gap for the latter case could be lower than the former one, i.e., $H^{\text{CV}} < H^{\text{HV}}$ (Ghiasi et al., 2017). For simplicity of the shooting heuristic algorithm (presented in Subsection 6.2.3), we do not allow the exit speed to drop below $\dot{p}_i^{\text{CAV}}(t)$; otherwise, it would require a more complex shooting heuristic. This is a reasonable assumption since as noted before, we set P^{end} to a location where traffic speed is expected to be recovered. Figure 6.11 illustrates the prediction integration algorithm and outputs.

6.2.3 Shooting Heuristic

With $T_{ti}^{\text{end}}, v_{ti}^{\text{end}}, p_i^{\text{CAV}}(t)$ and $\dot{p}_i^{\text{CAV}}(t), \forall i \in \mathcal{A}$, we are able to plan the CAV trajectories for the future that can smoothly pass P^{end} . This step of the algorithm is called a



(a) Integration of the sensor-based and probe-based predictions



(b) Exit state at the integrated prediction

Figure 6.11: Prediction integration.

shooting heuristic, and its output are $f_{ti}(t'), \forall t' \geq t, j \in \mathcal{A}$. In addition to the mentioned inputs, we also need the estimated preceding vehicle shadow trajectories $r_{ti}^{\text{sh}}(t'), \forall t' \geq t$ to check the feasibility of the $f_{ti}(t')$ for all $i \in \mathcal{A}$ during the shooting heuristic algorithm. This algorithm is divided into three sub-steps that together form the shooting heuristic algorithm.

6.2.3.1 CAV Shooting Equations

In this sub-step, we formulate $f_{ti}(t'), \forall t' \geq t, i \in \mathcal{A}$. The basic idea of the shooting heuristic is to partition each future CAV trajectory into a maximum of four consecutive parabolic sections. We call these four sections deceleration, stopping, acceleration, and cruising. We let the deceleration and acceleration sections have the same absolute acceleration values. With this, we can analytically find the connecting points between each consecutive sections. To prevent having a negative slope at the connecting point of the CAV trajectory, we add a stopping section if needed. Finally, when the trajectory speed recovers to v_{ti}^{end} , we connect this section to the cruising section and let the CAV proceed at constant speed v_{ti}^{end} (with zero acceleration) up to the exit time-space point $(T_{ti}^{\text{end}}, P^{\text{end}}), \forall i \in \mathcal{A}$. In the shooting heuristic, we first consider the case that $f_{ti}(t')$ has no stopping section. In this case, we will find five variables that together form $f_{ti}(t')$. These variables are shown with outlines in Figure 6.12.

To solve these five variables, we first fix t_{ti}^{cr} . Let α_i denotes the ratio of the cruising section length to the entire shooting length, i.e., $\alpha_i := \frac{P^{\text{end}} - p_{ti}^{\text{cr}}}{P^{\text{end}} - p_i^{\text{CAV}}(t)}, \forall i \in \mathcal{A}$. With α_i , we can indirectly fix t_{ti}^{cr} and p_{ti}^{cr} as the follows:

$$t_{ti}^{\text{cr}} = T_{ti}^{\text{end}} - \frac{\alpha_i (P^{\text{end}} - p_i^{\text{CAV}}(t))}{v_{ti}^{\text{end}}}, \forall i \in \mathcal{A}, \quad (6.3)$$

$$p_{ti}^{\text{cr}} = P^{\text{end}} - \alpha_i (P^{\text{end}} - p_i^{\text{CAV}}(t)), \forall i \in \mathcal{A}. \quad (6.4)$$

With this, we can find the remaining decision variables $\{a_{ti}, t_{ti}^c, p_{ti}^c, v_{ti}^c\}_{i \in \mathcal{A}}$ as follows.

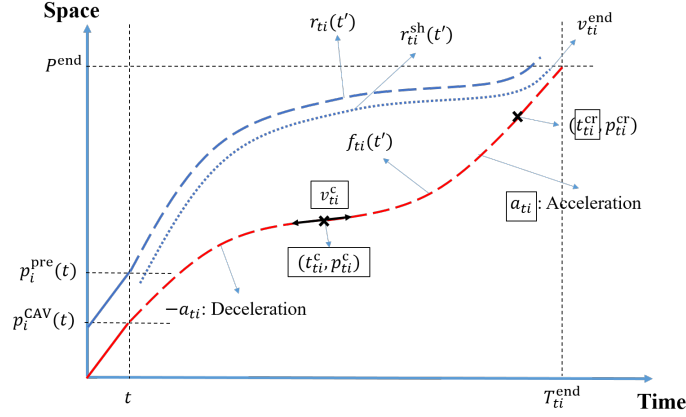


Figure 6.12: Shooting heuristic: case 1.

$$\begin{aligned}
 a_{ti} &= \frac{\dot{p}_i^{\text{CAV}}(t) + v_{ti}^{\text{end}}}{t_{ti}^{\text{cr}} - t} + \frac{\beta_{ti} - 2(p_{ti}^{\text{cr}} - p_i^{\text{CAV}}(t))}{(t_{ti}^{\text{cr}} - t)^2}, i \in \mathcal{A}, \\
 t_{ti}^c &= \frac{1}{2} \left(t + t_{ti}^{\text{cr}} + \frac{\dot{p}_i^{\text{CAV}}(t) - v_{ti}^{\text{end}}}{a_{ti}} \right), i \in \mathcal{A}, \\
 p_{ti}^c &= -\frac{1}{2} a_{ti} (t_{ti}^{\text{cr}} - t)^2 + \dot{p}_i^{\text{CAV}}(t) (t_{ti}^{\text{cr}} - t) + p_i^{\text{CAV}}(t), i \in \mathcal{A}, \\
 v_{ti}^c &= \dot{p}_i^{\text{CAV}}(t) - a_{ti} (t_{ti}^{\text{cr}} - t)^2, i \in \mathcal{A},
 \end{aligned}$$

where

$$\begin{aligned}
 \beta_{ti} &= 2 \left(\frac{(t_{ti}^{\text{cr}} - t)^2}{2} \left((\dot{p}_i^{\text{CAV}}(t))^2 + (v_{ti}^{\text{end}})^2 \right) - (t_{ti}^{\text{cr}} - t) (p_{ti}^{\text{cr}} - p_i^{\text{CAV}}(t)) (\dot{p}_i^{\text{CAV}}(t) + v_{ti}^{\text{end}}) + \right. \\
 &\quad \left. (p_{ti}^{\text{cr}} - p_i^{\text{CAV}}(t))^2 \right)^{1/2}, i \in \mathcal{A}.
 \end{aligned}$$

Calculating the decision variables concludes with the deceleration, acceleration, and cruising (that is determined by $\alpha_i, \forall i \in \mathcal{A}$) sections. However, in general the mentioned equations may result in a negative speed at the connecting point (i.e. $v_{ti}^c < 0$). If that happens, we need to switch to the second case to add a stopping section. In this case, we set

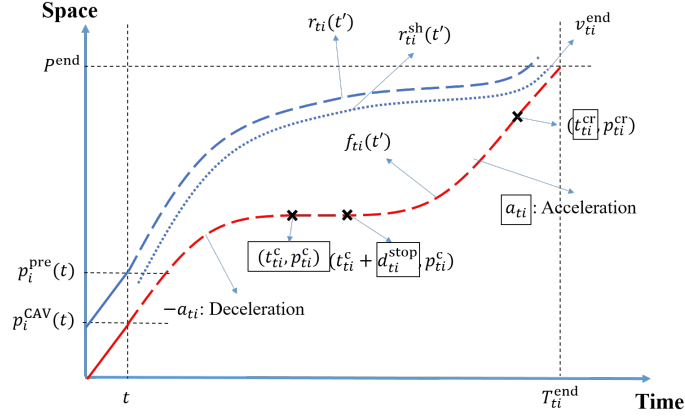


Figure 6.13: Shooting heuristic: case 2.

$v_{ti}^c = 0, \forall i \in \mathcal{A}$ and instead we solve the stopping section duration denoted by d_{ti}^{stop} . Again, we calculate t_{ti}^{cr} and p_{ti}^{cr} by fixing $\alpha_i, \forall i \in \mathcal{A}$ (Equations (6.3) and (6.4)). Thus the remaining variables are $\{a_{ti}, t_{ti}^c, p_{ti}^c, d_{ti}^{\text{stop}}\}_{i \in \mathcal{A}}$. These variables are in Figure 6.13 and are calculated as

$$a_{ti} = \frac{(\dot{p}_i^{\text{CAV}}(t))^2 + (v_{ti}^{\text{end}})^2}{2(1 - \alpha_i)(P^{\text{end}} - p_i^{\text{CAV}}(t))}, i \in \mathcal{A}$$

$$t_{ti}^c = t + \frac{\dot{p}_i^{\text{CAV}}(t)}{a_{ti}}, i \in \mathcal{A},$$

$$p_{ti}^c = p_i^{\text{CAV}}(t) + \frac{(\dot{p}_i^{\text{CAV}}(t))^2}{(\dot{p}_i^{\text{CAV}}(t))^2 + (v_{ti}^{\text{end}})^2} (p_{ti}^{\text{cr}} - p_i^{\text{CAV}}(t)), i \in \mathcal{A},$$

$$d_{ti}^{\text{stop}} = t_{ti}^{\text{cr}} - \frac{v_{ti}^{\text{end}}}{a_{ti}} - t_{ti}^c, i \in \mathcal{A}.$$

The mentioned two cases are applied for conditions where $p_i^{\text{CAV}}(t), i \in \mathcal{A}$ is relatively far from P^{end} . However, if $p_i^{\text{CAV}}(t)$ is too close to P^{end} , it is not efficient or even possible to include deceleration and stopping sections. In these third cases we only need acceleration and cruising sections. The decision variables in these cases are $\{a_{ti}, t_{ti}^{\text{cr}}, p_{ti}^{\text{cr}}\}_{i \in \mathcal{A}}$ that are shown with outlines in Figure 6.14, and calculated as

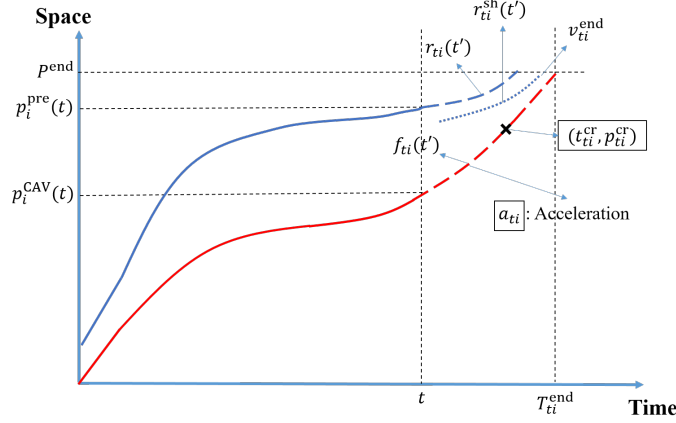


Figure 6.14: Shooting heuristic: case 3.

$$a_{ti} = \frac{(\dot{p}_i^{\text{CAV}}(t) - v_{ti}^{\text{end}})^2}{2(v_{ti}^{\text{end}}(T_{ti}^{\text{end}} - t) - (P^{\text{end}} - p_i^{\text{CAV}}(t)))}, i \in \mathcal{A}$$

$$t_{ti}^{\text{cr}} = \frac{t(\dot{p}_i^{\text{CAV}}(t) + v_{ti}^{\text{end}}) - 2T_{ti}^{\text{end}}v_{ti}^{\text{end}} + 2(P^{\text{end}} - p_i^{\text{CAV}}(t))}{\dot{p}_i^{\text{CAV}}(t) - v_{ti}^{\text{end}}}, i \in \mathcal{A},$$

$$p_{ti}^{\text{cr}} = P^{\text{end}} - v_{ti}^{\text{end}}(T_{ti}^{\text{end}} - t_{ti}^{\text{cr}}), i \in \mathcal{A}.$$

Note that if $v_{ti}^{\text{end}} = \dot{p}_i^{\text{CAV}}(t)$, then we simply set $t_{ti}^{\text{cr}} = t$, and thus, we obtain $f_{ti}(t') = p_i^{\text{CAV}}(t) + v_{ti}^{\text{end}}(t' - t)$, $t \leq t' \leq T_{ti}^{\text{end}}$.

Finally, the fourth case belongs to the conditions where $p_i^{\text{CAV}}(t)$ is so close to P^{end} and it may not be possible to merge $p_i^{\text{CAV}}(t)$ to point $(T_{ti}^{\text{end}}, P^{\text{end}})$ with v_{ti}^{end} for some $i \in \mathcal{A}$. In this case, we first only consider a short acceleration section that starts with the current states and ends at P^{end} at time T_{ti}^{end} (i.e., $f_{ti}(T_{ti}^{\text{end}}) = P^{\text{end}}$), but not necessarily with the speed of v_{ti}^{end} that yields $a_{ti} = \frac{2(P^{\text{end}} - p_i^{\text{CAV}}(t) - \dot{p}_i^{\text{CAV}}(t)(T_{ti}^{\text{end}} - t))}{(T_{ti}^{\text{end}} - t)^2}$, $i \in \mathcal{A}$. If $a_{ti} > a^{\text{max}}$, then we do not require $f_{ti}(t')$ to end at P^{end} at time T_{ti}^{end} , and set $a_{ti} = \min\left(a^{\text{max}}, \frac{v_{ti}^{\text{f}} - \dot{p}_i^{\text{CAV}}(t)}{T_{ti}^{\text{end}} - t}\right)$, $i \in \mathcal{A}$. Although this section may not end at point $(T_{ti}^{\text{end}}, P^{\text{end}})$ with v_{ti}^{end} , due to the shortness of this section, the difference is not significant. Figure 6.15 illustrates this case.

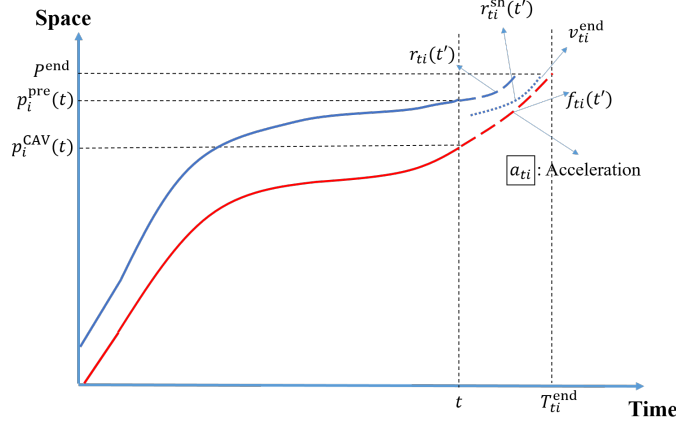


Figure 6.15: Shooting heuristic: case 4.

Using one of the four mentioned cases, calculation of the decision variables will result in the piece-wise quadratic function $f_{ti}(t'), \forall t' \geq t, i \in \mathcal{A}$ as follows.

- Case 1:

$$f_{ti}(t') = \begin{cases} -\frac{a_{ti}}{2}(t' - t)^2 + \dot{p}_i^{\text{CAV}}(t)(t' - t) + p_i^{\text{CAV}}(t), & t \leq t' < t_{ti}^c; \\ \frac{a_{ti}}{2}(t' - t_{ti}^c)^2 + v_{ti}^c(t' - t_{ti}^c) + p_{ti}^c, & t_{ti}^c \leq t' < t_{ti}^{\text{cr}}; \\ v_{ti}^{\text{end}}(t' - t_{ti}^{\text{cr}}) + p_{ti}^{\text{cr}}, & t_{ti}^{\text{cr}} \leq t' \leq T_{ti}^{\text{end}}. \end{cases}$$

- Case 2:

$$f_{ti}(t') = \begin{cases} -\frac{a_{ti}}{2}(t' - t)^2 + \dot{p}_i^{\text{CAV}}(t)(t' - t) + p_i^{\text{CAV}}(t), & t \leq t' < t_{ti}^c; \\ p_{ti}^c, & t_{ti}^c \leq t' < t_{ti}^c + d_{ti}^{\text{stop}}; \\ \frac{a_{ti}}{2}(t' - t_{ti}^c - d_{ti}^{\text{stop}})^2 + p_{ti}^c, & t_{ti}^c + d_{ti}^{\text{stop}} \leq t' < t_{ti}^{\text{cr}}; \\ v_{ti}^{\text{end}}(t' - t_{ti}^{\text{cr}}) + p_{ti}^{\text{cr}}, & t_{ti}^{\text{cr}} \leq t' \leq T_{ti}^{\text{end}}. \end{cases}$$

- Case 3:

$$f_{ti}(t') = \begin{cases} \frac{a_{ti}}{2}(t' - t)^2 + \dot{p}_i^{\text{CAV}}(t)(t' - t) + p_i^{\text{CAV}}(t), & t \leq t' < t_{ti}^{\text{cr}}; \\ v_{ti}^{\text{end}}(t' - t_{ti}^{\text{cr}}) + p_{ti}^{\text{cr}}, & t_{ti}^{\text{cr}} \leq t' \leq T_{ti}^{\text{end}}. \end{cases}$$

- Case 4: $f_{ti}(t') = \frac{a_{ti}}{2}(t' - t)^2 + \dot{p}_i^{\text{CAV}}(t)(t' - t) + p_i^{\text{CAV}}(t)$.

6.2.3.2 Feasibility Constraints

Once we calculate $f_{ti}(t'), \forall t' \geq t, i \in \mathcal{A}$, we need to check whether the planned trajectories meet the feasibility constraints or not. We define two feasibility constraints as follows.

- Kinematic constraint: We require that $a^{\min} \leq a_{ti} \leq a^{\max}, \forall i \in \mathcal{A}$. If this criterion holds for each $i \in \mathcal{A}$, then we conclude that $f_{ti}(t'), \forall t' \geq t$ is kinematically feasible.
- Safety constraint: For safety, we require that $f_{ti}(t') \leq r_{ti}^{\text{sh}}(t'), \forall t' \geq t, i \in \mathcal{A}$. Since we have the piece-wise functions for both $f_{ti}(t')$ and $r_{ti}^{\text{sh}}(t'), \forall i \in \mathcal{A}$, we can analytically find the feasibility status. In order to do so, for each $i \in \mathcal{A}$, we break the shooting duration into a number of sub-segments such that each $f_{ti}(t')$ and $r_{ti}^{\text{sh}}(t')$ consist of only one function equation, respectively. Therefore, we can easily calculate the feasibility status at each sub-segment. If $f_{ti}(t') \leq r_{ti}^{\text{sh}}(t')$ for all sub-segments, we conclude that $f_{ti}(t'), \forall t' \geq t$ is feasible.

6.2.3.3 α_i Solution

Given the decision variables, we formulated $f_{ti}(t')$ in each aforementioned case. The first two cases, however, fix t_{ti}^{cr} by $\alpha_i, \forall i \in \mathcal{A}$. In this sub-step, we finalize the shooting heuristic by finding the optimal α_i values that results in the smoothest CAV shooting. We found that as α_i increases, a_{ti} increases as well. Thus, we basically aim to find the minimum feasible α_i values for all $i \in \mathcal{A}$. We implement the Golden Section approach to find the minimum feasible $\alpha_i, \forall i \in \mathcal{A}$. We let $G = 0.618$ be the Golden Section ratio. The optimization problem is solved as follows. Let $\underline{\alpha}_i$ and $\bar{\alpha}_i$ denote the lower-bound and upper bound to $\alpha_i, \forall i \in \mathcal{A}$, respectively. $\bar{\alpha}_i, \forall i \in \mathcal{A}$ can be determined based on the a^{\min} and a^{\max} values or safely set to the maximum value (e.g., $\bar{\alpha}_i := 1, \forall i \in \mathcal{A}$). The value of $\underline{\alpha}_i$ should be found according to the safety constraint. For this we first set t_{ti}^{cr} to the tangent of $f_{ti}(t')$ and $\bar{r}_{ti}^{\text{s}}(t'), \forall t' \geq t, i \in \mathcal{A}$. De-

fine $c_{ti}(t') := \frac{\bar{r}_{ti}^s(t') - p_i^{\text{CAV}}(t)}{t' - t}$ and $\bar{\tau}^c := \{t' \mid \bar{r}_{ti}^s(t') = P^{\text{end}}\}, \forall t' \geq t, i \in \mathcal{A}$. If the maximum value for the $c_{ti}(t')$ function occurs at P^{end} (i.e., $\frac{P^{\text{end}} - p_i^{\text{CAV}}(t)}{\bar{\tau}^c - t} \geq \frac{\bar{r}_{ti}^s(t') - p_i^{\text{CAV}}(t)}{t' - t}, \forall t' \geq t$), then the tangent shall be at P^{end} , and thus $t_{ti}^{\text{cr}} := T_{ti}^{\text{end}}$ and $\underline{\alpha}_i := 0, i \in \mathcal{A}$. Otherwise, we numerically find the tangent between time points $\bar{\tau}^c$ and $\underline{\tau}^c := \arg \max_{t < t' < \bar{\tau}^c} (c_{ti}(t'))$, $\forall i \in \mathcal{A}$. Let g_{ti} denote the obtained tangent time. With that, we set $t_{ti}^{\text{cr}} := g_{ti}$ and thus $\underline{\alpha}_i = \frac{P^{\text{end}} - \bar{r}_{ti}^s(g_{ti})}{P^{\text{end}} - p_i^{\text{CAV}}(t)}, i \in \mathcal{A}$. For the initial iteration of the optimization problem, we set $\alpha_i := \underline{\alpha}_i$. Then, we calculate $f_{ti}(t'), \forall t' \geq t, i \in \mathcal{A}$, and check the feasibility constraints. If the feasibility constraints are met for each $i \in \mathcal{A}$, then the problem ends and $f_{ti}(t')$ is the smoothest trajectory. Otherwise, we increase α_i by $\alpha_i := \alpha_i + G(\bar{\alpha}_i - \underline{\alpha}_i)$, solve $f_{ti}(t')$, and check the feasibility. If $f_{ti}(t')$ is feasible for each $i \in \mathcal{A}$, we can set $\bar{\alpha}_i := \alpha_i$ and decrease α_i by $\alpha_i := \alpha_i - G(\bar{\alpha}_i - \underline{\alpha}_i)$; otherwise, we set $\underline{\alpha}_i := \alpha_i$ and increase α_i by the same equation. We iterate this procedure for each $i \in \mathcal{A}$ until $\bar{\alpha}_i \approx \underline{\alpha}_i$, and we set the solution as $\alpha_i = \bar{\alpha}_i$. By minimizing α_i , we actually find the minimum a_{ti} that will result in the smoothest $f_{ti}(t'), \forall t' \geq t, i \in \mathcal{A}$. With this, we end the shooting heuristic section.

6.2.4 Damping Control

When $p_i^{\text{CAV}}(t)$ is very close to $p_i^{\text{pre}}(t)$ for each $i \in \mathcal{A}$, the shooting heuristic algorithm may result in unnatural fluctuations in CAV trajectories that may also affect all the following vehicles trajectories. To avoid such perturbations, this sub-section proposes a damping control algorithm to smooth the CAV control when $p_i^{\text{pre}}(t) - p_i^{\text{CAV}}(t)$ is less than a distance threshold, denoted by ζ^{damp} , for each $i \in \mathcal{A}$ at time t . Basically, if for each $i \in \mathcal{A}$, $p_i^{\text{pre}}(t) - p_i^{\text{CAV}}(t) > \zeta^{\text{damp}}$, we do not apply the damping control and let CAV i follow $f_{ti}(t'), \forall t' \in (t, t + \Delta T]$. Otherwise, the damping control algorithm modifies the trajectory of CAV i for the following $(t, t + \Delta T]$ time period. This algorithm makes CAV i follow a combination of $f_{ti}(t')$ and $p_i^{\text{pre}}(t')$ rather than just $f_{ti}(t'), \forall t' \geq t$, for $\forall t < t' \leq t + \Delta T$. This combination is based on the Full Velocity Difference (FVD) car-following model (Jiang et al., 2001) that is

formulated as

$$\dot{v} = \frac{v^{\text{damp}}(\cdot) - v}{\tau} - \gamma \Delta v, \quad (6.5)$$

where v and \dot{v} are vehicle velocity and acceleration, respectively, $v^{\text{damp}}(\cdot)$ is the optimal velocity function, Δv is the velocity difference between the vehicle and its preceding vehicle, and τ and γ are the adaptation time and velocity difference sensitivity parameters, respectively. In the FVD model, $v^{\text{damp}}(\cdot)$ is an increasing linear function of the vehicle gap. However, in our damping control algorithm, we define $v^{\text{damp}}(\cdot)$ as a weighted average between the speed obtained from $f_{ti}(t')$ (i.e., $\dot{f}_{ti}(t') := \frac{df_{ti}(t')}{dt'}$) and $\dot{p}_i^{\text{pre}}(t' - \tau^{\text{CAV}})$ as follows

$$\begin{aligned} v^{\text{damp}}(t') := & \dot{f}_{ti}(t' - \Delta t) + \\ & \max\left(0, \dot{f}_{ti}(t' - \Delta t) - \dot{p}_i^{\text{pre}}(t' - \tau^{\text{CAV}} - \Delta t)\right) \times \\ & \frac{p_i^{\text{CAV}}(t' - \Delta t) - p_i^{\text{pre}}(t' - \Delta t) - \zeta^{\text{damp}}}{\zeta^{\text{damp}} - \zeta^{\text{terminate}}}, \forall t' \in (t, t + \Delta T], \end{aligned} \quad (6.6)$$

where Δt is a small time increment, τ^{CAV} is the CAV communication/reaction delay, and $\zeta^{\text{terminate}}$ is the control terminate parameter indicating that the control will be terminated if the spacing between the CAV and its preceding vehicles falls below this parameter. Therefore, if the damping control is applied, Equations (6.5) and (6.6) yield the CAV acceleration in real-time for any $t' \in (t, t + \Delta T]$. This ends our algorithm design section.

6.3 Numerical Experiments

This section presents simulation analyses to evaluate the performance of our algorithm. First, we conduct a numerical experiment to visualize the algorithm results and to compare them with a benchmark case. Second, we perform a sensitivity analysis on the impacts of traffic demand changes on the algorithm solutions. Finally, the effects of different CV and CAV market penetration rates on the algorithm outcomes are investigated.

In all of these examples, we consider a single-lane straight freeway with 80 vehicles driving downstream. We set coordinate 0 at the beginning of the control zone and the coordinate increases downstream. We set that bottleneck location to $l^B = 500$ m and deploy a set of traffic sensors around l^B . The default parameter values are set as: $S = 6$, $\Delta l^S = 40$ m ($l_1 = 400$ m), $\Delta T = 2$ sec, $v^f = 90$ km/h, and $P^{\text{end}} = l_S$. It is also assumed that each traffic sensor can capture the traffic information within 10 meters of its center location (i.e., 20 meters of coverage). For all numerical experiments, HVs and CVs follow a stochastic Optimal Velocity (OV) car-following model formulated as:

$$\dot{v} = \frac{v^{\text{opt}}(d) - v}{\tau} + \varepsilon,$$

$$v^{\text{opt}}(d) := \max\left(0, \min\left(v^f, \frac{d - s_0 + l^V}{h}\right)\right),$$

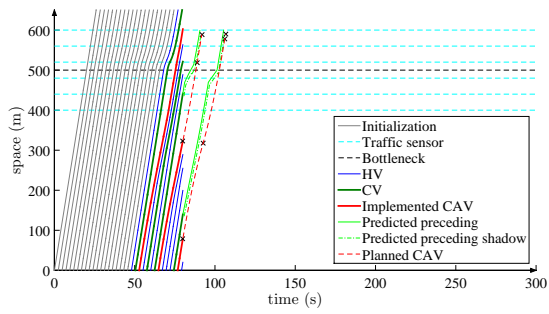
where ε is a zero-mean normally-distributed random term with a standard deviation of σ , d is the vehicle distance gap, h is the vehicle time gap at stationary conditions, l^V is the vehicle length, and the other variables and parameters are as previously defined. For simplicity, all vehicles are assumed to have the same length of $l^V = 5$ m and $\sigma := \sqrt{2}$ for all HVs and CVs (Li et al., 2018). To model different capacities for upstream and downstream of the bottleneck, different corresponding jam spacing parameters are set in the car-following model, i.e., $s_0 = 6.5$ and $s_0 = 10$ meters, respectively for upstream and downstream of the bottleneck. The other parameters are set as $\tau = 0.65$ s, $\gamma = 0.6$ s⁻¹, $\tau^{\text{CAV}} = 0.2$ s, $w = 4.64$ m/s, $a^{\text{min}} = -8$ m/s² (Kudarauskas, 2007), $a^{\text{max}} = 1.5$ m/s², $\zeta^{\text{damp}} = 50$ m, $\zeta^{\text{terminate}} = 10$ m, $H^{\text{CV}} = 1.22$ s, and $H^{\text{HV}} = 1.58$ s (Ghiasi et al., 2017). Let D denote the traffic demand entering the control zone, and set $D = 1500$ vehicles per hour for the following experiments.

To visualize the algorithm results, we perform a numerical example with $P_1 = 0.3$ and $P_2 = 0.2$. To feed the deployed sensor with a history of traffic information, we initialize the simulation with a platoon of 20 vehicles and assume that the first vehicle of this platoon is

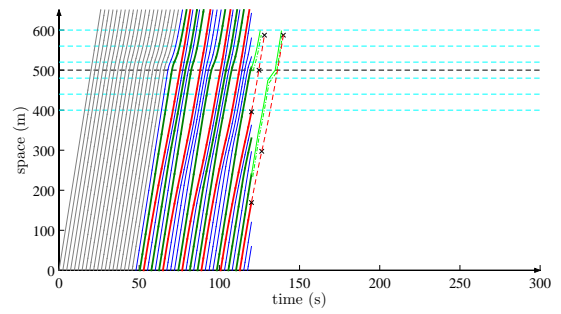
a probe vehicle. This initial vehicle platoon will serve as inputs to the prediction algorithm downstream of first CAV cluster. After this vehicle platoon, we allow 80 vehicles to enter the speed harmonization control zone. Thus, we consider 24 CVs and 16 CAVs ($N = 40$) that are distributed with a repeated pattern (as shown in Figure 6.17(b)). We plot the trajectories and related control information at four different time points along the simulation process in Figure 6.16. In this figure, the initialization vehicle platoon is shown with gray curves. Further, HVs, CVs and CAVs are shown with blue, green, and red trajectories, respectively. We can see that due to the bottleneck at 500 meters, a queue will be formed that is consistent with real-world observations. Further, each CAV form a vehicle cluster, in which the CAV is followed by a number of CVs and HVs. The solid and dashed light green curves represent $r_{ti}(t')$ and $r_{ti}^{\text{sh}}(t')$, $\forall t' > t, i \in \mathcal{A}$, respectively. And, the solid red curves are the implemented CAV trajectories under the proposed control algorithm up to the next decision time point, while the dashed red curve is the planned CAV trajectory $f_{ti}(t')$, $\forall t' > t, i \in \mathcal{A}$ that aims to smoothly merge into the $r_{ti}^{\text{sh}}(T_{ti}^{\text{end}})$ (the dashed green curve). Note that the CAVs only follow these planned trajectories up to the next decision point, and then the planned trajectory will be updated. As a result, we see that the CAVs can smartly adapt themselves along the process. Therefore, the CAV clusters smoothly hedge against the deceleration waves and gradually merge into the downstream traffic when the queue is about to dissipate.

To illustrate the merits of the results, we construct a benchmark example that simulates the human-driven traffic without any control. Figure 6.17(a) plots the benchmark human-driven trajectories generated with stochastic OV car-following model and compares it with the obtained control algorithm result shown in Figure 6.17(b).

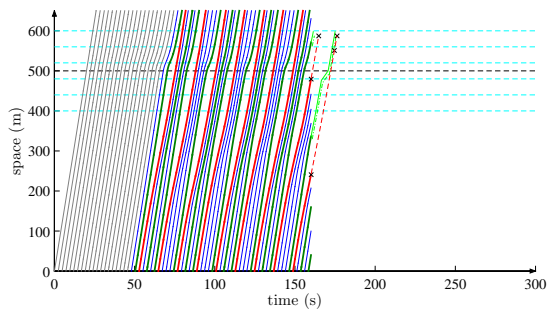
Comparing the two sets of results, we can see that the proposed CAV trajectory control significantly smooths not only the CAV trajectories but also the vehicles following the them. We have quantified the benefits based on four most important measures of effectiveness: throughput, speed standard deviation (as a proxy for driving comfort), fuel



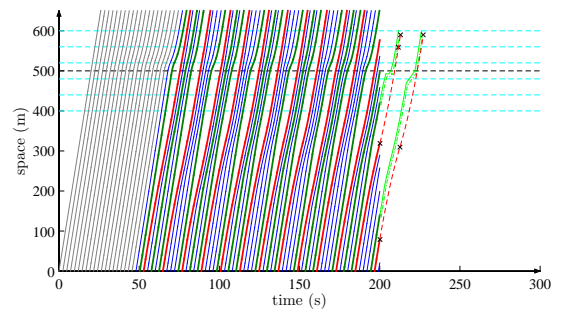
(a) $t = 80$ sec



(b) $t = 120$ sec

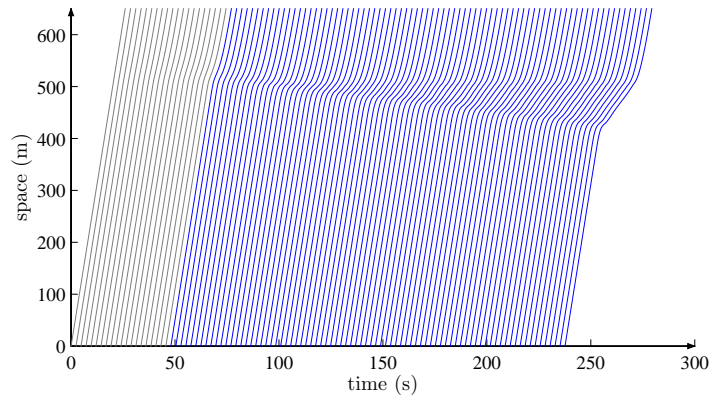


(c) $t = 160$ sec

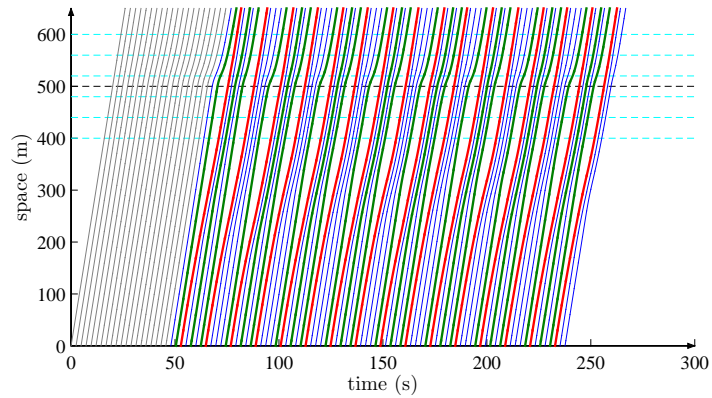


(d) $t = 200$ sec

Figure 6.16: Simulation results.



(a) Benchmark



(b) Implemented control

Figure 6.17: Simulation results: comparing the human-driven benchmark traffic with the implemented control.

consumption, and surrogate safety measure denoted by E^t , E^v , E^f , and E^s respectively. We have implemented the VT-micro model coefficients (Ahn, 1998; Ahn et al., 2002) to evaluate the fuel consumption improvements. Further, we use a surrogate measure based on the inverse time-to-collision (iTTC) measure (Balas and Balas, 2006). This measure is basically formulated as the integral over the travel time on the road segment for all following vehicles. Let index all the vehicles as $o \in \mathcal{O} := 1, 2, \dots, O$. Then, E^s can be formulated as

$$E^s := \sum_{o \in \mathcal{O} \setminus \{1\}} \int_{t_o^-}^{t_o^+} \frac{\dot{p}_o(t) - \dot{p}_{o-1}(t)}{p_{o-1}(t) - p_o(t)} dt,$$

where t_o^- , t_o^+ are the time when vehicle o enters and exits the control zone, respectively, and $p_o(t)$, and $\dot{p}_o(t)$ are the location and speed of vehicle o at time t , respectively. We evaluate evaluation measures E^t , E^v , E^f , and E^s within the control zone, i.e., 0 to P^{end} and E^t at P^{end} ($P^{\text{end}} = 600$ meters for the cases shown in Figure 6.17). Table 6.1 compares the benchmark case evaluation measures values with the controlled traffic. Moreover, to test the algorithm results with different sensor settings (i.e., S and Δl^S values), eight different instances are tested, and in each instance one of the S or Δl^S values is changed and the remaining parameters stay at their default values. Note that as we change either of these values, sensor locations may change, thus we report the l_1 values in Table 6.1 in addition to the changed parameter value. We define ΔE^t , ΔE^v , ΔE^f , and ΔE^s as the percentage of the E^t , E^v , E^f , and E^s improvements in different instances, respectively. Finally, to investigate the effects of v^f on the algorithm results, we perform numerical experiments with different v^f values and the results are shown in Table 6.2. Note that to capture the stochasticity nature of the car-following model, we run the simulation model 10 times for each scenario in all of the following examples and then report the average values.

The results shown in Table 6.1 indicate that our algorithm can improve the traffic performance with various sensor settings. Further, it is found that the E^t , E^v , E^f and E^s

Table 6.1: Comparison of the evaluation measures for different sensor settings.

	E^t (vph)	ΔE^t (%)	E^v (m/s)	ΔE^v (%)	E^f (L)	ΔE^f (%)	E^s (1/s)	ΔE^s (%)
Benchmark	1425	-	8.37	-	15.26	-	12.66	-
Default	1484	4.1	3.86	53.9	14.20	7.0	10.56	16.6
$S = 4$ ($l_1 = 480$ m)	1508	5.9	3.12	62.8	13.49	11.6	10.14	19.9
$S = 4$ ($l_1 = 440$ m)	1514	6.3	2.94	64.9	11.42	25.2	20.10	58.8
$S = 8$ ($l_1 = 400$ m)	1494	4.8	3.47	58.6	14.86	2.6	4.87	61.5
$S = 8$ ($l_1 = 360$ m)	1486	4.3	3.76	55.1	14.76	3.3	5.59	55.8
$S = 8$ ($l_1 = 320$ m)	1492	4.8	3.64	56.5	14.05	7.9	9.62	24.0
$\Delta l^S = 20$ m ($l_1 = 450$ m)	1482	4.0	4.14	50.6	11.75	23.0	22.19	75.3
$\Delta l^S = 80$ m ($l_1 = 300$ m)	1500	5.3	3.34	60.1	15.38	0.8	4.77	62.4

Table 6.2: Comparison of the evaluation measures for different v^f values.

		E^t (vph)	ΔE^t (%)	E^v (m/s)	ΔE^v (%)	E^f (L)	ΔE^f (%)	E^s (1/s)	ΔE^s (%)
$v^f = 70$ km/h	B**	1361	-	6.75	-	13.68	-	0.37	-
	C***	1437	5.6	4.05	40.0	11.96	12.6	3.08	736.7
$v^f = 90$ km/h*	B**	1425	-	8.37	-	15.26	-	12.66	-
	C***	1484	4.1	3.86	53.9	14.20	7.0	10.56	16.6
$v^f = 105$ km/h	B**	1458	-	8.71	-	15.55	-	22.99	-
	C***	1511	3.6	3.37	61.3	13.03	16.2	12.88	44.0
$v^f = 120$ km/h	B**	1487	-	7.18	-	13.51	-	33.65	-
	C***	1509	1.5	3.61	49.8	11.66	13.7	14.91	55.7

* Default case, ** Benchmark, *** Controlled

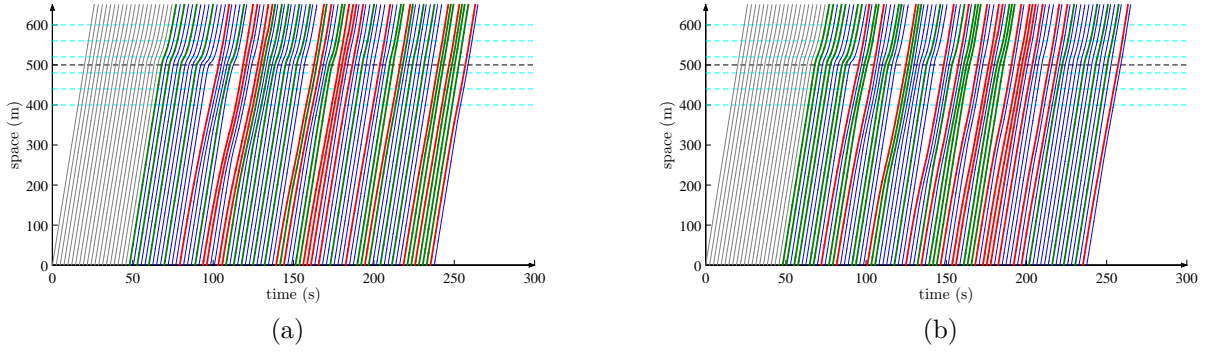


Figure 6.18: Simulation results: random distribution.

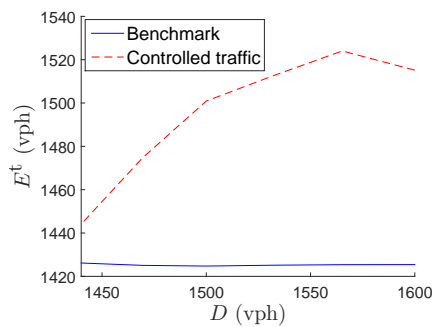
values mainly depend on the sensor spatial distribution around l^B and Δl^S rather than S . Actually, even the same number of S value may correspond to significantly different results. Therefore, to improve the sensor-based prediction effectiveness, it is important to locate a sufficient number of traffic sensors both upstream and downstream of the bottleneck. Overall, although our proposed control algorithm obtains promising improvements considering various parameter values, to further improve the algorithm outcomes, this study provides a tool to find the optimal traffic sensor settings according to traffic conditions, resources, etc. Finally, we compare the algorithm results for four v^f values in Table 6.2. Overall, the results indicate that this algorithm can improve the traffic performance at different v^f values.

The above numerical experiment is performed for a repeated vehicle spatial distribution pattern for CAV clusters. To demonstrate the robustness of our algorithm, we test the algorithm with random CV and CAV distributions with the same parameter settings. Figure 6.18 shows two examples of simulation analysis with random vehicle distributions. Both visual and quantitative results indicate that the proposed control algorithm can provide smoother traffic, with better fuel efficiency, less crash probabilities, and more driving comfort.

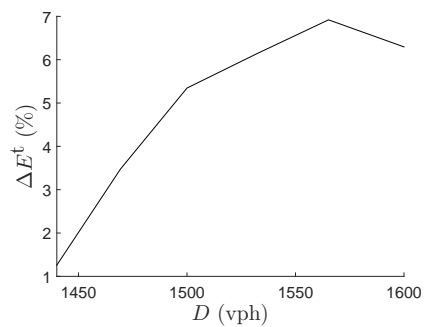
Next, we perform a sensitivity analysis on D parameter to investigate its effects on the evaluation measures as are shown in Figure 6.19. Figures 6.19(a), 6.19(c), 6.19(e),

and 6.19(g) plot the E^t , E^v , E^f , and E^s values and for both the benchmark case and the controlled traffic with the default parameter settings, respectively. Further, Figures 6.19(b), 6.19(d), 6.19(f), and 6.19(h) show the ΔE^t , ΔE^v , ΔE^f , and ΔE^s values, respectively. Note that since in unsaturated traffic with $D < Q^{\text{down}}$, simulation analysis obtains $E^t = D$, $E^v = 0$ and minimum E^f and E^s values for both benchmark and controlled traffic, and thus traffic control may not be as necessary. Therefore, we only investigate the saturated traffic with $D > Q^{\text{down}}$ in this numerical experiment. Further, numerical experiments reveal that for $D > 1600$ vph, traffic spills back to upstream segments of the control zone (i.e., negative coordinates). Therefore, longer control zones are needed for greater D values. Actually, to assure a specific improvement level, the length of the control zone shall increase with D . However, for the sake of consistency with the default parameter settings, the control zone is not changed in this analysis and the $D > 1600$ vph cases are excluded. With the default parameter setting, we obtain $Q^{\text{down}} = 1410$ and $Q^{\text{up}} = 2169$ vph. Thus in this sensitivity analysis, we let D vary from 1440 to 1600 vph. The results indicate that the proposed control strategy improves the evaluation measures for various D values in saturated traffic. However, as D increases, some of the improvements decrease, which is related to the length of the control zone, and therefore, shall be resolved with setting longer control zones. Overall, these tests confirm that the proposed speed harmonization algorithm could yield greater mobility, smoother traffic, more driving comfort, more fuel efficiency, and less crash risks in most common traffic conditions.

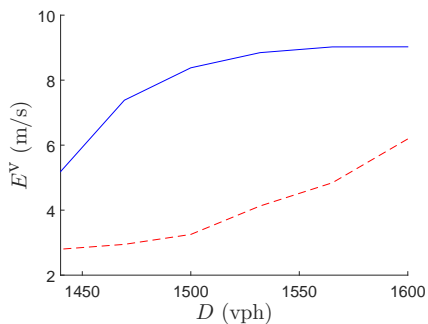
Finally, we perform numerical experiments to investigate the result of our algorithm under different P_1 and P_2 values. Figure 6.20 shows the ΔE^t , ΔE^v , ΔE^f , and ΔE^s values for the P_1 and P_2 spectra. We let P_1 and P_2 vary between 0 to 0.9 and 0.1 to 1 with an interval of 0.1, respectively. In this experiment, we randomly distribute CVs and CAVs and run the simulation 20 times for each for each (P_1, P_2) pair. Then, we set ΔE^t , ΔE^v , ΔE^f , and ΔE^s to the average of the obtained values for each (P_1, P_2) pair. As it is shown in this



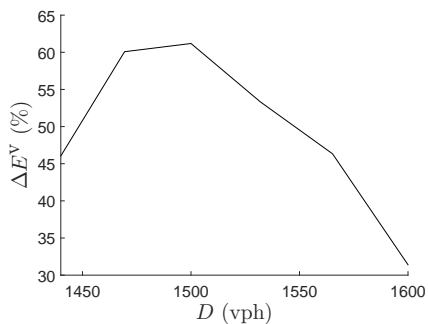
(a) E^t



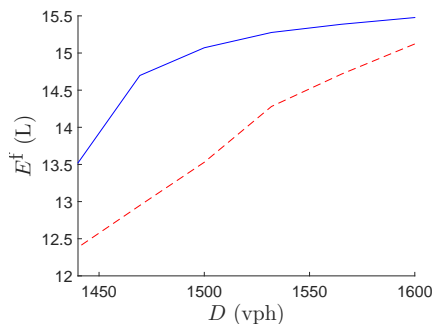
(b) ΔE^t



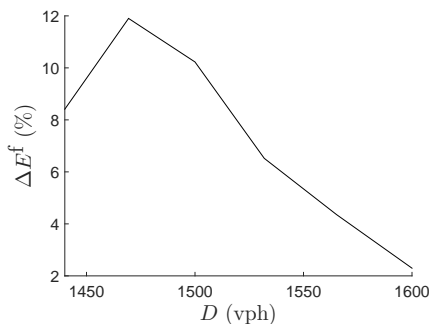
(c) E^v



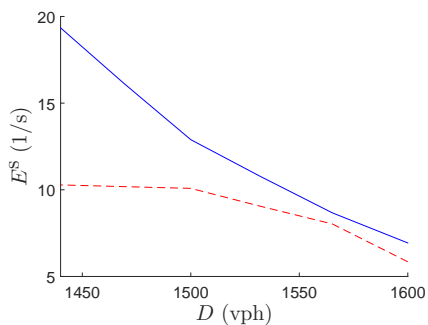
(d) ΔE^v



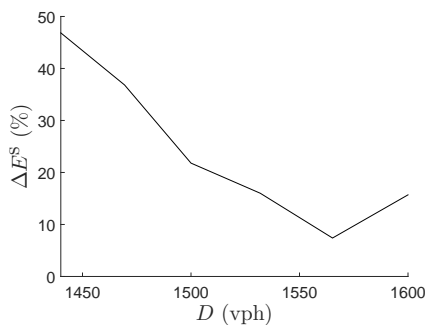
(e) E^f



(f) ΔE^f



(g) E^s



(h) ΔE^s

Figure 6.19: Sensitivity analyses on the D values.

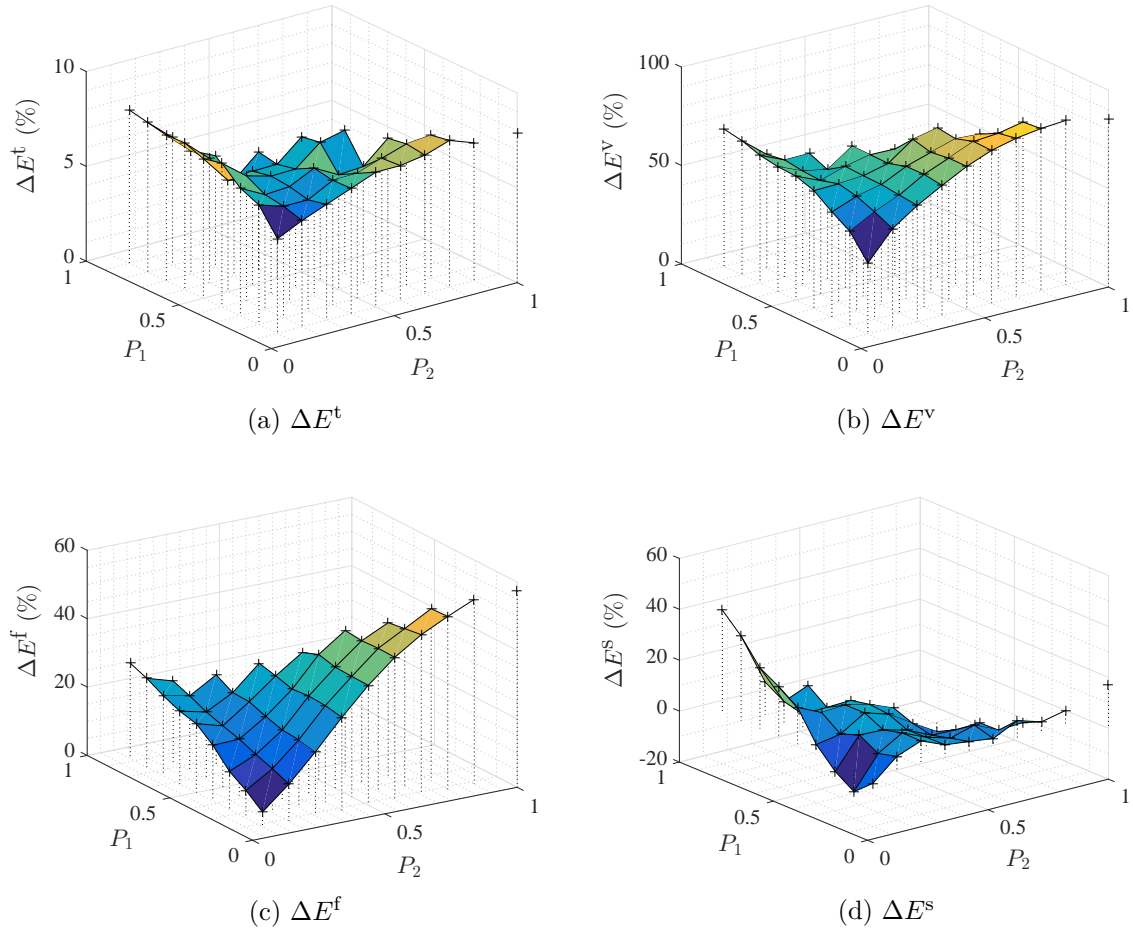


Figure 6.20: Sensitivity analyses on the P_1 and P_2 values.

figure, ΔE^t , ΔE^v , ΔE^f , and ΔE^s generally increase with P_1 and P_2 , which implies that our control strategy can improve the performance of the future mixed traffic highway. Further, the results indicate that the ΔE^v and ΔE^f values are more sensitive to P_2 than the P_1 values. That is due to the fact that CAVs play more effective role in our control strategy than CVs. This is not the case for ΔE^s as CAVs tend to merge the downstream clusters with shorter time gaps. However, this shall not create any safety concern because these vehicles are designed to safely operate with shorter headways (Ghiasi et al., 2017).

6.4 Chapter Summary

This chapter develops a traffic control strategy based on an innovative speed harmonization concept using CAV technologies. The proposed algorithm is applicable to a mixed traffic freeway with HVs, CVs, and CAVs. Basically, this algorithm controls the CAVs upstream of the bottleneck to effectively hedge against the backward shockwaves and smooth the traffic. This algorithm includes four main steps: information update, trajectory prediction, shooting heuristic, and damping control. The aforementioned steps of the algorithm are updated at every decision time point (i.e., ΔT). As a result, the proposed speed harmonization algorithm is modified using the new information that is received from the deployed traffic sensors and/or the downstream probe vehicle at the first step of algorithm. In the second step, we propose a prediction framework to predict the trajectories of the immediate preceding vehicles to the CAVs. The outputs of this step are the times (i.e., T_{ti}^{end}) and the corresponding speeds (i.e., v_{ti}^{end}) at which the preceding vehicles pass a predefined target zone (i.e., P^{end}), in which the negative impacts of the bottleneck are recovered. Considering the two second step outputs as the inputs of the third step, the shooting heuristic efficiently plans the future CAV trajectories. Based on the outputs of the first two steps of the algorithm at every time increment, we construct the functions of the future CAV trajectories. These piece-wise quadratic functions allow us to prevent any speed jump in CAV trajectories. Moreover, we consider physical limits as well as the safety constraints in constructing the CAV trajectory function. Further, to avoid any sudden CAV speed variation when CAVs are within a distance threshold to the preceding vehicle, CAV speed profiles are dampened with the proposed damping control algorithm.

Numerical experiments are conducted to illustrate the performance of the algorithm and to test it with various parameters and traffic conditions. The numerical experiment results indicate that presented speed harmonization algorithm is capable of not only smoothing

CAV movements but also harmonizing the following human-driven traffic. To quantify the benefits, four of the most important objective functions in traffic flow analyses are considered: throughput, speed variations, fuel consumption, and surrogate safety measure. The quantitative results show improvements in all four measures for most of the test cases compared with the benchmark case.

CHAPTER 7: CONCLUSION

Traffic congestion and stop-and-go maneuvers are inevitable experiences that play massive role in human's daily lives. Most of these issues are linked to the limitations in human behaviors. First, due to the limitations in human's reaction time, every consecutive pair of vehicles have to be spaced by a relatively long distance. As a result, the maximum possible capacity of a highway is limited to a relatively low value. Second, human-driven traffic is usually accompanied with frequent deceleration and acceleration cycles that are known as traffic oscillation or stop-and-go traffic. These issues impose adverse impacts on our society's prosperity and sustainability. Emerging connected and automated vehicle (CAV) technologies can potentially solve or at least reduce these problems through sensing the local environment, sharing information, and applying appropriate control measures. To realize the potential benefits of CAV technologies, this dissertation provides insightful methodological and managerial tools in microscopic and macroscopic traffic scales.

In the macroscopic scale, this dissertation investigates how distributed CAVs can impact mixed traffic highway capacity. CHAPTER 3 develops an analytical stochastic formulation to mixed traffic highway capacity based on a Markov-chain model. This model describes the vehicle spatial and headway distributions along a highway segment as a function of three critical factors: CAV penetration rate, CAV platooning intensity, and mixed traffic headway settings. The results of the analytical and numerical analyses reveal that the proposed Markov chain model can estimate the ground-truth mixed traffic highway capacity very accurately. Moreover, it is found that contrary to the ubiquitous assumption that higher CAV penetration rates and platooning intensities always help improve highway

capacity, these two factors may not always yield greater mixed traffic capacity. This finding warns the traffic operators to be aware of possible impacts of different CAV technology settings on highway capacity.

In the microscopic scale, this dissertation aims to use CAV technologies to dampen traffic oscillations and smooth traffic. CHAPTER 4 presents a simplified trajectory optimization model for a pure-automated traffic environment where all vehicles are assumed to be CAVs. In this problem, each CAV's trajectory is approximated with no more than five pieces of consecutive quadratic functions with identical trajectories acceleration and deceleration rates in the same platoon. The elegant theoretical properties in the objective shape and the feasible region lead to an exact solution algorithm that efficiently solves the true optimum to the proposed problem. This efficiency achievement is demonstrated with a number of numerical experiments on signalized segments and at non-stop intersections. The numerical analyses also reveal that the proposed simplified trajectory optimization problem reduces the queue length or confine traffic slowdown within a local area without further propagation.

The trajectory optimization concept is extended to a joint trajectory and signal optimization model in CHAPTER 5 to simultaneously design CAV trajectories and signal timing plan near signalized crossing points. In this problem, each CAV's trajectory is approximated with no more than five consecutive quadratic segment pieces. Moreover, instead of applying the original highly non-linear functions of the instantaneous fuel consumption, this chapter proposes a macroscopic near-optimum fuel consumption function that describes fuel consumption as a simple quadratic relationship with signal red interval. With these two modifications, the formulated simplified joint trajectory and signal optimization model can be analytically solved to the exact solution. Numerical experiments are conducted to evaluate the algorithm performance and to illustrate the applications of this model on signalized intersections and work-zones. Finally, this model is tested on various traffic conditions and roadway geometries.

CHAPTER 6 extends the trajectory optimization concept to a mixed traffic environment by proposing a CAV-based mixed traffic speed harmonization algorithm. This model effectively hedges against the backward shockwaves and smooth the traffic by controlling the CAVs upstream of the bottleneck. The proposed algorithm could be applied in real-time traffic management by iteratively predicting the downstream traffic and updating the upstream CAV controls in real-time. We use two information sources to estimate the downstream traffic: the real-time traffic sensor data and the information provided by the downstream connected vehicles (CVs) and CAVs. With this prediction, this study constructs the future piece-wise quadratic CAV trajectory functions considering safety and kinematic constraints. Finally, to avoid any sudden jump in CAV speed profiles, their movements may be dampened with the proposed damping control algorithm. The numerical experiment results reveal that the proposed speed harmonization algorithm is capable of not only smoothing CAV trajectories but also the following human-driven traffic.

This dissertation can be extended in a number of directions. Regarding the proposed capacity analysis model, it is interesting to investigate how lane changing maneuvers impact highway capacity in mixed traffic. Moreover, it is possible to analytically quantify the traffic flow rate across the full spectrum of traffic densities in both undersaturated and congested conditions for mixed traffic. In the simplified trajectory optimization problem, although we conjecture that the optimal solution to the simplified problem is likely near-optimum to the primary optimization problem, rigorous optimization models need to be built to quantify the optimality of the simplified solution. Further, some minor restrictions (e.g., identical speeds at the entrance and the exit of the highway segment) can be relaxed in future studies to suit more flexible problem settings. In the proposed joint trajectory and signal optimization problem, it is assumed that the traffic arrival pattern is homogeneous. Therefore, investigating the dynamic heterogeneous traffic can be a potential future study direction. Further, it will be worth extending this problem into multi-directional signalized crossing points.

Finally, the proposed CAV-based speed harmonization algorithm also considers the homogeneous traffic arrival pattern, thus it will be worth investigating a dynamic heterogeneous traffic in the future. Moreover, real world data can be incorporated to this model framework when detailed trajectory data are available for a long span of freeway around a bottleneck. Further, the presented approach framework is developed for one-lane freeway, which can be extended to multi-lane conditions, e.g., through forming a wall of synchronized CAVs across all lanes or effective management of lane changes.

REFERENCES

- Ahn, K., 1998. Microscopic Fuel Consumption and Emission Modeling. Master's thesis, Virginia Polytechnic Institute and State University, US.
- Ahn, K., Rakha, H., Park, S., 2013. Ecodrive application: Algorithmic development and preliminary testing. *Transportation Research Record: Journal of the Transportation Research Board* (2341), 1–11.
- Ahn, K., Rakha, H., Trani, A., Van Aerde, M., 2002. Estimating vehicle fuel consumption and emissions based on instantaneous speed and acceleration levels. *Journal of Transportation Engineering* 128 (2), 182–190.
- Ahn, K., Rakha, H. A., Kang, K., Vadakpat, G., 2016. Multimodal intelligent traffic signal system simulation model development and assessment. *Transportation Research Record: Journal of the Transportation Research Board* (2558), 92–102.
- Alessandri, A., Di Febbraro, A., Ferrara, A., Punta, E., 1999. Nonlinear optimization for freeway control using variable-speed signaling. *IEEE Transactions on Vehicular Technology* 48 (6), 2042–2052.
- Allam Ahmed, P., Kumar, R., Parida, P., Saleh, W., 2014. Effect of type of lead vehicle on following headway behaviour in mixed traffic. *World Journal of Science, Technology and Sustainable Development* 11 (1), 28–43.
- Altay, I., Aksun Güvenç, B., Güvenç, L., 2013. Lidar data analysis for time to headway determination in the drivesafe project field tests. *International journal of vehicular technology* 2013.
- Amoozadeh, M., Deng, H., Chuah, C.-N., Zhang, H. M., Ghosal, D., 2015. Platoon management with cooperative adaptive cruise control enabled by vanet. *Vehicular Communications* 2 (2), 110–123.

- Arnaout, G. M., Arnaout, J.-P., 2014. Exploring the effects of cooperative adaptive cruise control on highway traffic flow using microscopic traffic simulation. *Transportation Planning and Technology* 37 (2), 186–199.
- Arnaout, G. M., Bowling, S., 2014. A progressive deployment strategy for cooperative adaptive cruise control to improve traffic dynamics. *International Journal of Automation and Computing* 11 (1), 10–18.
- Azizi, L., Iqbal, M. S., Hadi, M. A., 2018. Estimation of freeway platooning measures using surrogate measures based on connected vehicle data. In: 97th Annual Meeting of the Transportation Research Board.
- Balas, V. E., Balas, M. M., 2006. Driver assisting by inverse time to collision. In: Automation Congress, 2006. WAC'06. World. IEEE.
- Bansal, P., Kockelman, K. M., 2017. Forecasting Americans long-term adoption of connected and autonomous vehicle technologies. *Transportation Research Part A: Policy and Practice* 95, 49–63.
- Barth, M., An, F., Younglove, T., Scora, G., Levine, C., Ross, M., Wenzel, T., 2000. Development of a comprehensive modal emissions model: Final report. University of California, Riverside, US.
- Barth, M., Boriboonsomsin, K., 2009. Energy and emissions impacts of a freeway-based dynamic eco-driving system. *Transportation Research Part D: Transport and Environment* 14 (6), 400–410.
- Bertini, R., Boice, S., Bogenberger, K., 2006. Dynamics of variable speed limit system surrounding bottleneck on german autobahn. *Transportation Research Record: Journal of the Transportation Research Board* (1978), 149–159.
- Bertini, R. L., Boice, S., Bogenberger, K., 2005. Using its data fusion to examine traffic dynamics on a freeway with variable speed limits. In: *Intelligent Transportation Systems, 2005. Proceedings. 2005 IEEE*. IEEE.
- Bose, A., Ioannou, P. A., 2003. Analysis of traffic flow with mixed manual and semiautomated vehicles. *IEEE Transactions on Intelligent Transportation Systems* 4 (4), 173–188.

- Calvert, S. C., van den Broek, T. A., van Noort, M., 2012. Cooperative driving in mixed traffic networks - optimizing for performance. In: Intelligent Vehicles Symposium (IV), 2012 IEEE.
- Chang, G.-L., Park, S., Paracha, J., 2011. Intelligent transportation system field demonstration: integration of variable speed limit control and travel time estimation for a recurrently congested highway. *Transportation Research Record: Journal of the Transportation Research Board* (2243), 55–66.
- Chen, D., Ahn, S., Chitturi, M., Noyce, D. A., 2017. Towards vehicle automation: Roadway capacity formulation for traffic mixed with regular and automated vehicles. *Transportation research part B: methodological* 100, 196–221.
- Chen, S., Du, L., 2017. Simulation study of the impact of local real-time traffic information provision strategy in connected vehicle systems. *International Journal of Transportation Science and Technology* 6 (4), 229–239.
- Chen, Z., He, F., Zhang, L., Yin, Y., 2016. Optimal deployment of autonomous vehicle lanes with endogenous market penetration. *Transportation Research Part C: Emerging Technologies* 72, 143–156.
- Day, C., Haseman, R., Premachandra, H., Brennan Jr, T., Wasson, J., Sturdevant, J., Bullock, D., 2010. Evaluation of arterial signal coordination: methodologies for visualizing high-resolution event data and measuring travel time. *Transportation Research Record: Journal of the Transportation Research Board* (2192), 37–49.
- De Nunzio, G., Canudas de Wit, C., Moulin, P., Di Domenico, D., 2013. Eco-driving in urban traffic networks using traffic signal information. In: *Decision and Control (CDC), 2013 IEEE 52nd Annual Conference*.
- Dervisoglu, G., Gomes, G., Kwon, J., Horowitz, R., Varaiya, P., 2009. Automatic calibration of the fundamental diagram and empirical observations on capacity. In: *Transportation Research Board 88th Annual Meeting*. Vol. 15.
- Dresner, K., Stone, P., 2008. A multiagent approach to autonomous intersection management. *Journal of Artificial Intelligence Research* 31, 591–656.
- Fancher, P., Bareket, Z., Ervin, R., 2001. Human-centered design of an ACC-with-braking and forward-crash-warning system. *Vehicle System Dynamics* 36 (2-3), 203–223.

Feng, Y., Khoshmaghan, S., Zamanipour, M., Head, K. L., 2015. A real-time adaptive signal phase allocation algorithm in a connected vehicle environment. In: 94th Annual Meeting of the Transportation Research Board.

Fernandes, P., Nunes, U., 2012. Platooning with IVC-enabled autonomous vehicles: Strategies to mitigate communication delays, improve safety and traffic flow. *IEEE Transactions on Intelligent Transportation Systems* 13 (1), 91–106.

Frey, H., Unal, A., Chen, J., Li, S., Xuan, C., 2002. Methodology for developing modal emission rates for EPA's multi-scale motor vehicle and equipment emission estimation system, prepared by North Carolina State University for the Office of Transportation and Air Quality, US Environmental Protection Agency. Ann Arbor, MI.

Gao, Y., Cao, Y., Zhao, S., 2015. The ergonomics application research on differences between adaptive cruise control system and drivers. In: *Proceedings of the 14th International Conference on Man-Machine-Environment System Engineering*. Springer.

Ghiasi, A., Hussain, O., Qian, Z. S., Li, X., 2017. A mixed traffic capacity analysis and lane management model for connected automated vehicles: A Markov chain method. *Transportation Research Part B: Methodological* 106, 266–292.

Goodall, N., Smith, B., Park, B., 2013. Traffic signal control with connected vehicles. *Transportation Research Record: Journal of the Transportation Research Board* (2381), 65–72.

Guan, T., Frey, C. W., 2013. Predictive fuel efficiency optimization using traffic light timings and fuel consumption model. In: *Intelligent Transportation Systems-(ITSC), 2013 16th International IEEE Conference*.

Hadiuzzaman, M., Qiu, T. Z., 2013. Cell transmission model based variable speed limit control for freeways. *Canadian Journal of Civil Engineering* 40 (1), 46–56.

Harwood, N., Reed, N., Oct 2014. Modelling the impact of platooning on motorway capacity. In: *Road Transport Information and Control Conference 2014 (RTIC 2014)*.

He, Q., Head, K. L., Ding, J., 2012. Pamscod: Platoon-based arterial multi-modal signal control with online data. *Transportation Research Part C: Emerging Technologies* 20 (1), 164–184.

- He, Q., Head, K. L., Ding, J., 2014. Multi-modal traffic signal control with priority, signal actuation and coordination. *Transportation research part C: emerging technologies* 46, 65–82.
- Hegyi, A., De Schutter, B., Hellendoorn, H., 2005a. Model predictive control for optimal coordination of ramp metering and variable speed limits. *Transportation Research Part C: Emerging Technologies* 13 (3), 185–209.
- Hegyi, A., De Schutter, B., Hellendoorn, H., Van Den Boom, T., 2002. Optimal coordination of ramp metering and variable speed control-an MPC approach. In: *American Control Conference, 2002. Proceedings of the 2002.* Vol. 5. IEEE.
- Hegyi, A., De Schutter, B., Hellendoorn, J., 2005b. Optimal coordination of variable speed limits to suppress shock waves. *IEEE Transactions on intelligent transportation systems* 6 (1), 102–112.
- Hussain, O., Ghiasi, A., Li, X., 2016. Freeway lane management approach in mixed traffic environment with connected autonomous vehicles. *arXiv preprint arXiv:1609.02946*.
- Iglesias, I., Isasi, L., Larburu, M., Martinez, V., Molinete, B., 2008. I2v communication driving assistance system: on-board traffic light assistant. In: *68th Vehicular Technology Conference, IEEE*.
- Ioannou, P. A., Chien, C.-C., 1993. Autonomous intelligent cruise control. *IEEE Transactions on Vehicular technology* 42 (4), 657–672.
- Jensen, J. L. W. V., 1906. Sur les fonctions convexes et les inégalités entre les valeurs moyennes. *Acta mathematica* 30 (1), 175–193.
- Jiang, R., Hu, M.-B., Zhang, H., Gao, Z.-Y., Jia, B., Wu, Q.-S., 2015. On some experimental features of car-following behavior and how to model them. *Transportation Research Part B* 80, 338–354.
- Jiang, R., Wu, Q., Zhu, Z., 2001. Full velocity difference model for a car-following theory. *Physical Review E* 64 (1), 017101.
- Kamalanathsharma, R. K., Rakha, H., et al., 2013. Multi-stage dynamic programming algorithm for eco-speed control at traffic signalized intersections. In: *Intelligent Transportation Systems-(ITSC), 2013 16th International IEEE Conference*.

- Kamrani, M., Wali, B., Khattak, A. J., 2017. Can data generated by connected vehicles enhance safety? proactive approach to intersection safety management. *Transportation Research Record: Journal of the Transportation Research Board* (2659), 80–90.
- Kanaris, A., Ioannou, P., Ho, F.-S., 1997. Spacing and capacity evaluations for different AHS concepts. In: *Automated Highway Systems*. Springer, 125–171.
- Kaths, J., 2016. Integrating reliable speed advisory information and adaptive urban traffic control for connected vehicles. In: *Transportation Research Board 95th Annual Meeting*.
- Kesting, A., Treiber, M., Helbing, D., 2010. Enhanced intelligent driver model to access the impact of driving strategies on traffic capacity. *Philosophical Transactions of the Royal Society of London A: Mathematical, Physical and Engineering Sciences* 368 (1928), 4585– 4605.
- Kesting, A., Treiber, M., Schönhof, M., Helbing, D., 2008. Adaptive cruise control design for active congestion avoidance. *Transportation Research Part C: Emerging Technologies* 16 (6), 668–683.
- Koupal, J., Michaels, H., Cumberworth, M., Bailey, C., Brzezinski, D., 2002. Epa’s plan for moves: a comprehensive mobile source emissions model. In: *Proceedings of the 12th CRC On-Road Vehicle Emissions Workshop, San Diego, CA*.
- Kudarauskas, N., 2007. Analysis of emergency braking of a vehicle. *Transport* 22 (3), 154–159.
- Larsson, A. F., 2012. Driver usage and understanding of adaptive cruise control. *Applied ergonomics* 43 (3), 501–506.
- Lavasani, M., Jin, X., Du, Y., 2016. Market penetration model for autonomous vehicles on the basis of earlier technology adoption experience. *Transportation Research Record: Journal of the Transportation Research Board* (2597), 67–74.
- Lee, J., 2010. Assessing the potential benefits of IntelliDrive-based intersection control algorithms. Vol. 72.
- Lee, J., Park, B., 2012. Development and evaluation of a cooperative vehicle intersection control algorithm under the connected vehicles environment. *Intelligent Transportation Systems, IEEE Transactions on* 13 (1), 81–90.

- Levin, M. W., Boyles, S. D., 2015. Effects of autonomous vehicle ownership on trip, mode, and route choice. *Transportation Research Record: Journal of the Transportation Research Board* (2493), 29–38.
- Levin, M. W., Boyles, S. D., 2016. A multiclass cell transmission model for shared human and autonomous vehicle roads. *Transportation Research Part C: Emerging Technologies* 62, 103–116.
- Li, L., Wang, F.-Y., 2006. Cooperative driving at blind crossings using intervehicle communication, *IEEE Transactions on Vehicular technology* 55 (6), 1712–1724.
- Li, X., Ghiasi, A., Xu, Z., 2017. Exact method for a simplified trajectory smoothing problem with connected automated vehicles. In: *96th Annual Meeting of the Transportation Research Board*.
- Li, X., Ouyang, Y., 2011. Characterization of traffic oscillation propagation under nonlinear car-following laws. *Transportation research part B: methodological* 45 (9), 1346–1361.
- Li, X., Wang, X., Ouyang, Y., 2012. Prediction and field validation of traffic oscillation propagation under nonlinear car-following laws. *Transportation research part B: methodological* 46 (3), 409–423.
- Li, X., Wang, Y., Tian, J., Jiang, R., 2018. Stability analysis of stochastic linear car-following models, <https://www.researchgate.net>.
- Lin, P.-W., Kang, K.-P., Chang, G.-L., 2004. Exploring the effectiveness of variable speed limit controls on highway work-zone operations. In: *Intelligent transportation systems*. Vol. 8. Taylor & Francis.
- Lu, S., Hillmanssen, S., Ho, T. K., Roberts, C., 2013. Single-train trajectory optimization, *IEEE Transactions on Intelligent Transportation Systems* 14 (2), 743–750.
- Lu, X.-Y., Shladover, S., 2014. Review of variable speed limits and advisories: Theory, algorithms, and practice. *Transportation Research Record: Journal of the Transportation Research Board* (2423), 15–23.
- Lu, X.-Y., Shladover, S. E., Jawad, I., Jagannathan, R., Phillips, T., 2015. A novel speedmeasurement based variable speed limit/advisory algorithm for a freeway corridor with multiple bottlenecks. In: *Transportation Research Board 94th Annual Meeting*.

- Ma, J., Li, X., Shladover, S., Rakha, H. A., Lu, X.-Y., Jagannathan, R., Dailey, D. J., 2016. Freeway speed harmonization. *IEEE Transactions on Intelligent Vehicles* 1 (1), 78–89.
- Ma, J., Li, X., Zhou, F., Hu, J., Park, B. B., 2017. Parsimonious shooting heuristic for trajectory design of connected automated traffic part ii: computational issues and optimization. *Transportation Research Part B: Methodological* 95, 421–441.
- Mandava, S., Boriboonsomsin, K., Barth, M., 2009. Arterial velocity planning based on traffic signal information under light traffic conditions. In: *Intelligent Transportation Systems, 2009. ITSC'09. 12th International IEEE Conference*.
- Mensing, F., Trigui, R., Bideaux, E., 2011. Vehicle trajectory optimization for application in eco-driving. In: *Vehicle Power and Propulsion Conference (VPPC), IEEE*.
- Minderhoud, M., Botma, H., Bovy, P., 1997. Assessment of roadway capacity estimation methods. *Transportation Research Record: Journal of the Transportation Research Board* (1572), 59–67.
- Neubert, L., Santen, L., Schadschneider, A., Schreckenberg, M., 1999. Single-vehicle data of highway traffic: A statistical analysis. *Physical Review E* 60 (6), 6480.
- Newell, G. F., 2002. A simplified car-following theory: a lower order model. *Transportation Research Part B* 36 (3), 195 – 205.
- Nikolos, I. K., Delis, A. I., Papageorgiou, M., 2015. Macroscopic modelling and simulation of acc and cacc traffic. In: *2015 IEEE 18th International Conference on Intelligent Transportation Systems, IEEE*.
- Norris, J. R., 1998. *Markov chains*. No. 2. Cambridge university press.
- Nowakowski, C., O'Connell, J., Shladover, S. E., Cody, D., 2010. Cooperative adaptive cruise control: Driver acceptance of following gap settings less than one second. In: *Proceedings of the Human Factors and Ergonomics Society Annual Meeting*. Vol. 54. SAGE Publications.
- Ntousakis, I. A., Nikolos, I. K., Papageorgiou, M., 2015. On microscopic modelling of adaptive cruise control systems. *Transportation Research Procedia* 6, 111–127.

- Pourmehrab, M., Elefteriadou, L., Ranka, S., Martin-Gasulla, M., 2017. Optimizing signalized intersections performance under conventional and automated vehicles traffic. arXiv preprint arXiv:1707.01748.
- Rao, B., Varaiya, P., 1993. Flow benefits of autonomous intelligent cruise control in mixed manual and automated traffic. *Transportation Research Record* (1408), 36–43.
- Roncoli, C., Papamichail, I., Papageorgiou, M., 2015. Model Predictive Control for Motorway Traffic with Mixed Manual and VACS-equipped Vehicles. *Transportation Research Procedia* 10, 452–461.
- Saboochi, Y., Farzaneh, H., 2009. Model for developing an eco-driving strategy of a passenger vehicle based on the least fuel consumption. *Applied Energy* 86 (10), 1925–1932.
- Sanchez, M., Cano, J.-C., Kim, D., 2006. Predicting traffic lights to improve urban traffic fuel consumption. In: 2006 6th International Conference on ITS Telecommunications.
- Schakel, W. J., van Arem, B., Netten, B. D., 2010. Effects of cooperative adaptive cruise control on traffic flow stability. In: *Intelligent Transportation Systems (ITSC), 2010 13th International IEEE Conference on*. IEEE.
- Shladover, S., Su, D., Lu, X.-Y., 2012. Impacts of cooperative adaptive cruise control on freeway traffic flow. *Transportation Research Record: Journal of the Transportation Research Board* (2324), 63–70.
- Shladover, S., VanderWerf, J., Miller, M. A., Kourjanskaia, N., Krishnan, H., 2001. Development and performance evaluation of avcss deployment sequences to advance from today's driving environment to full automation. Tech. rep., California Partners for Advanced Transit and Highways (PATH).
- Shladover, S. E., Nowakowski, C., Lu, X.-Y., Hoogendoorn, R., 2014. Using cooperative adaptive cruise control (CACC) to form high-performance vehicle streams. Tech. rep., California PATH Program, University of California, Berkeley.
- Smith, C. C., McGehee, D. Y., Healey, A. J., 1978. The prediction of passenger riding comfort from acceleration data. *Journal of Dynamic Systems, Measurement, and Control* 100 (1), 34–41.
- Spiliopoulou, A. D., Papamichail, I., Papageorgiou, M., 2009. Toll plaza merging traffic control for throughput maximization. *Journal of Transportation Engineering* 136 (1), 67–76.

Stevens, W., Harding, J., Lay, R., McHale, G., 1996. Summary and assessment of findings from the precursor systems analyses of automated highway systems. Tech. rep., Turner-Fairbank Highway Research Center, Federal Highway Administration.

Swaroop, D., Hedrick, J., Chien, C., Ioannou, P., 1994. A comparison of spacing and headway control laws for automatically controlled vehicles¹. *Vehicle System Dynamics* 23 (1), 597–625.

Talebpoor, A., Mahmassani, H., Hamdar, S., 2013. Speed harmonization: evaluation of effectiveness under congested conditions. *Transportation Research Record: Journal of the Transportation Research Board* (2391), 69–79.

Tielert, T., Killat, M., Hartenstein, H., Luz, R., Hausberger, S., Benz, T., 2010. The impact of traffic-light-to-vehicle communication on fuel consumption and emissions. In: *Internet of Things (IOT)*, 2010. IEEE.

Tientrakool, P., Ho, Y.-C., Maxemchuk, N. F., 2011. Highway capacity benefits from using vehicle-to-vehicle communication and sensors for collision avoidance. In: *Vehicular Technology Conference (VTC Fall)*. IEEE.

Trayford, R., Doughty, B., van der Touw, J., 1984a. Fuel economy investigation of dynamic advisory speeds from an experiment in arterial traffic. *Transportation Research Part A: General* 18 (5), 415–419.

Trayford, R., Doughty, B., Wooldridge, M., 1984b. Fuel saving and other benefits of dynamic advisory speeds on a multi-lane arterial road. *Transportation Research Part A: General* 18 (5), 421–429.

Ulfarsson, G. F., Shankar, V. N., Vu, P., 2005. The effect of variable message and speed limit signs on mean speeds and speed deviations. *International journal of vehicle information and communication systems* 1 (1-2), 69–87.

Van Arem, B., De Vos, A., Vanderschuren, M. J., 1997. The effect of a special lane for intelligent vehicles on traffic flows; an exploratory study using the microscopic traffic simulation model mixic. Tech. rep., Institute of Infrastructure, Transport and Regional Development.

Van Arem, B., Van Driel, C. J., Visser, R., 2006. The impact of cooperative adaptive cruise control on traffic-flow characteristics. *IEEE Transactions on Intelligent Transportation Systems* 7 (4), 429–436.

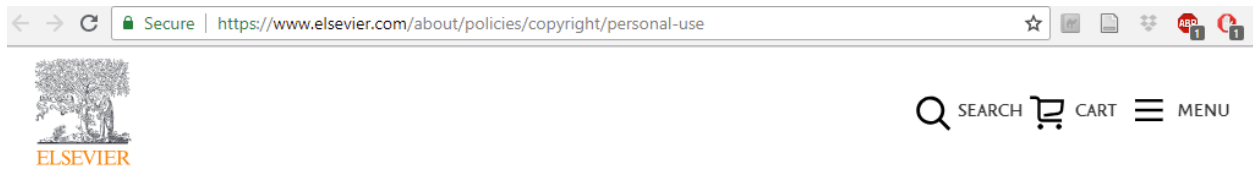
- van den Berg, V. A., Verhoef, E. T., 2016. Autonomous cars and dynamic bottleneck congestion: The effects on capacity, value of time and preference heterogeneity. *Transportation Research Part B: Methodological* 94, 43 – 60.
- Vander Werf, J., Shladover, S., Miller, M., Kourjanskaia, N., 2002. Effects of adaptive cruise control systems on highway traffic flow capacity. *Transportation Research Record: Journal of the Transportation Research Board* (1800), 78–84.
- VanderWerf, J., Shladover, S., Kourjanskaia, N., Miller, M., Krishnan, H., 2001. Modeling effects of driver control assistance systems on traffic. *Transportation Research Record: Journal of the Transportation Research Board* (1748), 167–174.
- Von Stryk, O., Bulirsch, R., 1992. Direct and indirect methods for trajectory optimization. *Annals of operations research* 37 (1), 357–373.
- Wang, M., Daamen, W., Hoogendoorn, S. P., van Arem, B., 2014a. Rolling horizon control framework for driver assistance systems. part i: Mathematical formulation and noncooperative systems. *Transportation Research Part C: Emerging Technologies* 40, 271–289.
- Wang, M., Daamen, W., Hoogendoorn, S. P., van Arem, B., 2014b. Rolling horizon control framework for driver assistance systems. part ii: Cooperative sensing and cooperative control. *Transportation Research Part C: Emerging Technologies* 40, 290–311.
- Wang, M., Daamen, W., Hoogendoorn, S. P., van Arem, B., 2015a. Connected variable speed limits control and vehicle acceleration control to resolve moving jams. In: *Transportation Research Board 94th Annual Meeting*.
- Wang, M., Daamen, W., Hoogendoorn, S. P., van Arem, B., 2016. Connected variable speed limits control and car-following control with vehicle-infrastructure communication to resolve stop-and-go waves. *Journal of Intelligent Transportation Systems*, 1–14.
- Wang, Z., Chen, X. M., Ouyang, Y., Li, M., 2015b. Emission Mitigation via longitudinal control of intelligent vehicles in a congested platoon. *Computer-Aided Civil and Infrastructure Engineering* 30 (6), 490–506.
- Wei, Y., Liu, J., Li, P., Zhou, X., 2016. Longitude trajectory optimization for autonomous vehicles: An approach based on simplified car-following model. In: *Transportation Research Board 95th Annual Meeting*.

- Weikl, S., Bogenberger, K., Bertini, R., 2013. Traffic management effects of variable speed limit system on a German autobahn: Empirical assessment before and after system implementation. *Transportation Research Record: Journal of the Transportation Research Board* (2380), 48–60.
- Whitham, G., 1955. On kinematic waves ii. a theory of traffic flow on long crowded roads. In: *Proc. R. Soc. Lond. A. Vol. 229*. The Royal Society.
- Wickramasinghe, N. K., Harada, A., Miyazawa, Y., 2012. Flight trajectory optimization for an efficient air transportation system. In: *28th International Congress of the Aeronautical Science (ICAS 2012)*.
- Wu, C., Zhao, G., Ou, B., 2011. A fuel economy optimization system with applications in vehicles with human drivers and autonomous vehicles. *Transportation Research Part D: Transport and Environment* 16 (7), 515–524.
- Wu, G., Boriboonsomsin, K., Zhang, W.-B., Li, M., Barth, M., 2010. Energy and emission benefit comparison of stationary and in-vehicle advanced driving alert systems. *Transportation Research Record: Journal of the Transportation Research Board* (2189), 98–106.
- Wu, X., He, X., Yu, G., Harmandayan, A., Wang, Y., 2015. Energy-optimal speed control for electric vehicles on signalized arterials. *Intelligent Transportation Systems, IEEE Transactions on PP* (99), 1–11.
- Xu, Y., Jia, B., Ghiasi, A., Li, X., 2017. Train routing and timetabling problem for heterogeneous train traffic with switchable scheduling rules. *Transportation Research Part C: Emerging Technologies* 84, 196–218.
- Yang, H., Jin, W.-L., 2014. A control theoretic formulation of green driving strategies based on inter-vehicle communications. *Transportation Research Part C: Emerging Technologies* 41, 48–60.
- Zhao, L., Sun, J., 2013. Simulation framework for vehicle platooning and car-following behaviors under connected-vehicle environment. *Procedia-Social and Behavioral Sciences* 96, 914–924.
- Zhou, F., Li, X., Ma, J., 2017. Parsimonious shooting heuristic for trajectory design of connected automated traffic part i: theoretical analysis with generalized time geography. *Transportation Research Part B: Methodological* 95, 394–420.

Zohdy, I. H., Rakha, H. A., 2014. Intersection management via vehicle connectivity: The intersection cooperative adaptive cruise control system concept. *Journal of Intelligent Transportation Systems* 20(1), 17–32.

APPENDIX A: COPYRIGHT PERMISSIONS

The permission from ELSEVIER for material in CHAPTERS 2 and 3 is below.



The screenshot shows a web browser window with the URL <https://www.elsevier.com/about/policies/copyright/personal-use>. The page features the Elsevier logo on the left and navigation links for SEARCH, CART, and MENU on the right. The main heading is 'Personal use'.

Personal use

Authors can use their articles, in full or in part, for a wide range of scholarly, non-commercial purposes as outlined below:

- Use by an author in the author's classroom teaching (including distribution of copies, paper or electronic)
- Distribution of copies (including through e-mail) to known research colleagues for their personal use (but not for Commercial Use)
- Inclusion in a thesis or dissertation (provided that this is not to be published commercially)
- Use in a subsequent compilation of the author's works
- Extending the Article to book-length form
- Preparation of other derivative works (but not for Commercial Use)
- Otherwise using or re-using portions or excerpts in other works

These rights apply for all Elsevier authors who publish their article as either a subscription article or an open access article. In all cases we require that all Elsevier authors always include a full acknowledgement and, if appropriate, a link to the final published version hosted on Science Direct.



Journal author rights

In order for Elsevier to publish and disseminate research articles, we need publishing rights. This is determined by a publishing agreement between the author and Elsevier. This agreement deals with the transfer or license of the copyright to Elsevier and authors retain significant rights to use and share their own published articles. Elsevier supports the need for authors to share, disseminate and maximize the impact of their research and these rights, in Elsevier proprietary journals* are defined below:

For subscription articles	For open access articles
<p>Authors transfer copyright to the publisher as part of a journal publishing agreement, but have the right to:</p> <ul style="list-style-type: none"> • Share their article for Personal Use, Internal Institutional Use and Scholarly Sharing purposes, with a DOI link to the version of record on ScienceDirect (and with the Creative Commons CC-BY-NC-ND license for author manuscript versions) • Retain patent, trademark and other intellectual property rights (including research data). • Proper attribution and credit for the published work. 	<p>Authors sign an exclusive license agreement, where authors have copyright but license exclusive rights in their article to the publisher**. In this case authors have the right to:</p> <ul style="list-style-type: none"> • Share their article in the same ways permitted to third parties under the relevant user license (together with Personal Use rights) so long as it contains a CrossMark logo, the end user license, and a DOI link to the version of record on ScienceDirect. • Retain patent, trademark and other intellectual property rights (including research data). • Proper attribution and credit for the published work.

*Please note that society or third party owned journals may have different publishing agreements. Please see the journal's guide for authors for journal specific copyright information.

**This includes the right for the publisher to make and authorize commercial use, please see "[Rights granted to Elsevier](#)" for more details.